Well Integrity: A Multi-Scale Approach

Zur Erlangung des akademischen Grades eines

DOKTORS DER NATURWISSENSCHAFTEN (Dr. rer. nat.)

von der KIT Fakultät für

Bauingenieur-, Geo- und Umweltwissenschaften

des Karlsruher Instituts für Technologie (KIT)

genehmigte

DISSERTATION

von

Marcel Schulz

Tag der mündlichen Prüfung: 09.10.2026

Referent: Prof. Dr. Frank Schilling

Korreferent: Prof. Dr. Andreas Henk

Karlsruhe (2026)

Abstract

Deep wells are an essential component of the global energy infrastructure. However, well integrity issues — the failure of wells to effectively seal and isolate subsurface formations — are widespread and can lead to severe environmental consequences such as aquifer contamination and greenhouse gas emissions. Avoiding leakage by maintaining well integrity is therefore critical throughout the entire lifecycle of wells. In this context, the cement-filled annulus between steel casings represents a key barrier system, as the cement–steel compound constitutes a common weakness. The complexity of the processes governing well integrity suggests the need for a multi-scale approach. Accordingly, this study links material property characterization at the sub-millimeter scale, meter-scale cyclic loading experiments, and field-scale operational practices to improve the understanding of well integrity.

Understanding the mechanisms responsible for leakage is a prerequisite for well integrity management. These mechanisms were therefore investigated experimentally, with a focus on the cement–steel compound in wells used for underground gas storage. These wells experience cyclic loading due to repeated gas injection and extraction and may therefore be particularly susceptible to integrity degradation. To investigate this, a total of 256 large-scale autoclave experiments were conducted on five 2-meter-long cement-filled steel casings designed to represent the casing-cement interface in wells. These specimens were subjected to cyclic pressure and thermal loading simulating underground gas storage operations. The system permeability of the cement-filled casing and its evolution with successive loading cycles and over time were determined from pressure changes associated with gas flow through the casing. These large-scale experiments were complemented by small-scale laboratory investigations on cement samples to characterize properties such as matrix permeability, porosity, and mineralogy before and after cyclic loading.

To quantitatively interpret the experiments, a numerical finite-difference model was developed to simulate gas flow through an annular gap between cement and steel and to derive effective gap apertures after each loading cycle. The model accounts for Hagen–Poiseuille gas flow as well as pressure–temperature coupling. This coupling is important because adiabatic gas compression and expansion during flow cause temperature changes in the gas. The resulting temperature difference between the gas and the surrounding autoclave steel induces heat transfer between gas and steel under approximately isochoric conditions, which superimposes the adiabatic temperature evolution driven by gas flow. This heat transfer in turn affects the gas pressure, thereby changing pressure gradients and consequently influencing gas flow.

The results demonstrate that interpreting gas flow and pressure evolution requires consideration of pressure–temperature interactions, which are often neglected. Furthermore, repeated pressure loading resulted in increased system permeabilities, most likely due to progressive debonding at the cement–steel interface and the development of an annular gap. Gas flow through the cement matrix can be ruled out due to its low matrix permeability. Thermal loading caused temporary permeability reductions, which are interpreted as condensation of water within the gap. Consequently, maintaining a fluid column in the annulus and selecting fluids with appropriate density and viscosity may contribute to improved sealing performance. Generally, the modeled

annular gap apertures stabilized between approximately 25–45 µm after a limited number of loading cycles, indicating that the gap aperture approaches a quasi-stable maximum.

The numerical model is further applied to diagnostic well integrity testing scenarios, suggesting that annular gaps generated by cyclic loading alone are unlikely to produce major leaks as defined by the American Petroleum Institute (2006). These findings indicate that, under conditions of high-quality cementation, the likelihood of major leakage is low, although minor leaks may still pose long-term risks, particularly for abandoned wells that are not monitored. Ultimately, the use of hybrid sealing concepts that combine cement with additional barrier materials, such as bentonite, rock plugs, bitumen, or metallic alloys, could further enhance long-term well integrity.

Beyond insights into leakage mechanisms gained from laboratory and modeling investigations, maintaining well integrity also requires appropriate diagnostic procedures and regulatory frameworks for the detection and management of leakage in the field. Because downhole integrity is difficult to assess directly, regulations often focus on manifestations of leaks at the surface. A typical manifestation of leakage within an annulus is pressure build-up at the wellhead that reoccurs after pressure release. This phenomenon is known as sustained casing pressure (SCP). If the leaking annulus is open to the atmosphere, pressure cannot build up and instead gas continuously flows to the atmosphere, which is referred to as casing vent flow (CVF).

Consequently, SCP and CVF can be used to infer the integrity condition of a well from pressure build-up or gas flow measurements at the wellhead and therefore often form the basis of regulatory requirements. To evaluate how different countries address these phenomena, well integrity regulations as well as industry guidelines in major gas-producing countries are reviewed, including the United States, Russia, China, Canada, Norway, and Australia. The analysis reveals substantial differences in regulatory approaches. While the United States, Canada, and Russia mainly apply direct and prescriptive requirements, Norway and Australia rely on indirect, risk-based frameworks that place greater responsibility on operators. A common shortcoming of prescriptive regulations is the lack of comprehensive workflows that span the entire process from the detection of pressure or flow to effective remediation. A minimum workflow for SCP and CVF management is therefore proposed, beginning with monitoring, i.e., the measurement of pressure build-up or flow in annuli. If pressure build-up or flow is detected, diagnostic testing must be performed to determine whether leakage is present or if, for example, the pressure is induced by temperature variations. If leakage is confirmed, appropriate remediation measures must be implemented. Monitoring and follow-up actions should continue throughout the post-abandonment phase. In addition, well integrity data should be thoroughly documented and made publicly available whenever possible.

By adopting a holistic multi-scale approach, this study contributes to a more comprehensive understanding of well integrity in deep wells.

Kurzfassung

Tiefe Bohrungen sind ein wesentlicher Bestandteil der globalen Energieinfrastruktur. Integritätsprobleme von Bohrungen – das Versagen, Bohrungen wirksam abzudichten – sind jedoch weit verbreitet und können zu schwerwiegenden Folgen wie Grundwasserkontamination und Treibhausgasemissionen führen. Die Vermeidung von Leckagen durch die Aufrechterhaltung der Bohrungsintegrität ist daher über den gesamten Lebenszyklus von Bohrungen hinweg von entscheidender Bedeutung. In diesem Zusammenhang stellt der zementgefüllte Ringraum zwischen Stahlverrohrungen ein zentrales Barrieresystem dar, da der Zement–Stahl-Verbund eine häufige mechanische Schwachstelle bildet. Die Komplexität der Prozesse, die die Bohrungsintegrität bestimmen, erfordert einen Multi-Skalen-Ansatz. In dieser Studie werden Skalen von der Materialcharakterisierung im Labormaßstab über großskalige zyklische Belastungsexperimente bis hin zu Feldpraktiken und regulatorischen Rahmenbedingungen betrachtet.

Das Verständnis der für Leckagen verantwortlichen Mechanismen ist eine grundlegende Voraussetzung für ein zuverlässiges Bohrlochintegritätsmanagement. Daher wurden diese Mechanismen experimentell untersucht, wobei der Schwerpunkt auf dem Zement–Stahl-Verbund in Bohrungen für die Untergrundgasspeicherung lag. Aufgrund der wiederholten Gasinjektion und -entnahme sind diese Bohrungen zyklischen Belastungen ausgesetzt und könnten daher besonders anfällig für eine Verschlechterung der Integrität sein. Hierzu wurden insgesamt 256 großmaßstäbliche Autoklavenexperimente an fünf je zwei Meter langen, zementgefüllten Stahlrohren durchgeführt, die die Grenzfläche zwischen Stahlverrohrung und Zement repräsentieren. Die Versuchskörper wurden zyklischen Druck- und Temperaturbelastungen ausgesetzt, um den Betrieb von Untergrundgasspeichern zu simulieren. Die Systempermeabilität der zementgefüllten Stahlrohre sowie ihre Entwicklung während der Belastungszyklen wurden anhand von Druckänderungen infolge des Gasflusses durch das Rohr bestimmt. Ergänzend wurden Laboruntersuchungen an Zementproben durchgeführt, um Parameter wie Matrixpermeabilität, Porosität und Mineralogie vor und nach der zyklischen Belastung zu charakterisieren.

Zur quantitativen Interpretation der Experimente wurde ein numerisches Finite-Differenzen-Modell entwickelt, das den Gasfluss durch einen Ringspalt zwischen Zement und Stahl simuliert und die effektive Spaltweite nach jedem Belastungszyklus bestimmt. Das Modell berücksichtigt sowohl Hagen–Poiseuille-Gasfluss als auch Druck–Temperatur-Kopplung. Diese Kopplung entsteht, da die adiabatische Kompression und Expansion des Gases während des Flusses Temperaturänderungen verursacht. Die daraus resultierende Temperaturdifferenz zwischen Gas und umgebendem Autoklavenstahl führt unter näherungsweise isochoren Bedingungen zu einem Wärmeaustausch, der die adiabatische Temperaturentwicklung aus dem Gasfluss überlagert. Dadurch werden der Gasdruck, die Druckgradienten und folglich der Gasfluss beeinflusst.

Die Ergebnisse zeigen, dass die Interpretation von Gasfluss und Druckentwicklung die häufig vernachlässigte Druck–Temperatur-Kopplung erfordert. Wiederholte Druckbelastung erhöhte die Systempermeabilität, was höchstwahrscheinlich auf ein fortschreitendes Ablösen an der Zement–Stahl-Grenzfläche und die Ausbildung eines Ringspalts zurückzuführen ist. Ein Gasfluss durch die Zementmatrix kann aufgrund ihrer geringen Permeabilität ausgeschlossen werden. Temperaturbelastung verursachte vorübergehende Permeabilitätsverringerungen, die als Kondensation von

Wasser im Ringspalt interpretiert werden. Dementsprechend könnten die Aufrechterhaltung einer Flüssigkeitssäule im Ringraum sowie die Auswahl geeigneter Flüssigkeiten hinsichtlich Dichte und Viskosität die Dichtwirkung verbessern. Die modellierten Ringspaltweiten stabilisierten sich nach wenigen Belastungszyklen zwischen etwa 25 µm und 45 µm und näherten sich damit einem quasi-stabilen Maximalwert.

Das numerische Modell wurde zudem auf Szenarien diagnostischer Bohrlochintegritätstests angewendet. Die Ergebnisse deuten darauf hin, dass ausschließlich durch zyklische Belastungen entstandene Ringspalte mit geringer Wahrscheinlichkeit zu erheblichen ("major") Leckagen führen, wie sie vom American Petroleum Institute (2006) definiert werden. Bei qualitativ hochwertiger Zementation erscheint die Wahrscheinlichkeit erheblicher Leckagen daher gering, wenngleich auch geringfügige Leckagen langfristige Risiken darstellen können, insbesondere bei nicht überwachten stillgelegten Bohrungen. Hybride Dichtungskonzepte, die Zement mit zusätzlichen Barrierematerialien wie Bentonit, Gesteinsstopfen, Bitumen oder metallischen Legierungen kombinieren, könnten die langfristige Bohrlochintegrität weiter verbessern.

Neben den Erkenntnissen aus Laboruntersuchungen und numerischer Modellierung erfordert die Aufrechterhaltung der Bohrlochintegrität geeignete Diagnoseverfahren und regulatorische Rahmenbedingungen zur Erkennung und zum Management von Leckagen im Feld. Da die Integrität im Bohrlochinneren nur eingeschränkt beurteilt werden kann, konzentrieren sich regulatorische Vorschriften häufig auf Leckagemanifestationen an der Oberfläche. Eine typische Manifestation ist ein Druckaufbau am Bohrlochkopf, der nach einer Druckentlastung erneut auftritt (*sustained casing pressure*, SCP). Ist der undichte Ringraum zur Atmosphäre hin offen, baut sich kein Druck auf. Stattdessen strömt kontinuierlich Gas aus (*casing vent flow*, CVF).

SCP und CVF ermöglichen Rückschlüsse auf den Integritätszustand einer Bohrung anhand von Druckaufbau- beziehungsweise Gasflussmessungen am Bohrlochkopf und bilden daher häufig die Grundlage regulatorischer Anforderungen. Hierzu wurden Bohrlochintegritätsvorschriften und Industrierichtlinien bedeutender Gasförderländer, darunter die Vereinigten Staaten, Russland, China, Kanada, Norwegen und Australien, untersucht. Die Analyse zeigt erhebliche Unterschiede in den regulatorischen Ansätzen. Während die Vereinigten Staaten, Kanada und Russland überwiegend direkte und präskriptive Vorschriften anwenden, verfolgen Norwegen und Australien indirekte, risikobasierte regulatorische Ansätze mit größerer Betreiberverantwortung. Eine häufige Schwäche präskriptiver Vorschriften ist das Fehlen eines durchgängigen Arbeitsablaufs von der Leckageerkennung bis zur Sanierung. Daher wird ein Minimalstandard für das Management von SCP und CVF vorgeschlagen: Überwachung von Druckaufbau oder Gasfluss, diagnostische Untersuchungen zur Bestätigung einer Leckage und anschließende Sanierungsmaßnahmen. Überwachung und geeignete Folgemaßnahmen sollten auch nach der Stilllegung fortgeführt werden. Darüber hinaus sollten Bohrlochintegritätsdaten umfassend dokumentiert und möglichst öffentlich zugänglich gemacht werden.

Durch die Anwendung eines ganzheitlichen Multiskalenansatzes trägt diese Arbeit zu einem umfassenderen Verständnis der Integrität tiefer Bohrungen bei.

Declaration of reproduced content

The following parts of this work have been reproduced with modifications from Schulz et al. (2025), of which I am the first author, under the terms of the Creative Commons Attribution 4.0 International License: Sections 1.1, 1.4 and 4.2, as well as parts of section 1.6, 5.4 and 6. This includes Figures 1, 2, 27, 28, 29, 30, 31 and 52 as well as Tables 15 and 16. The reproduced Figures 1, 2, 27, 30 and 52 were modified for this work, while the other figures were reproduced without modifications. The license terms are available at: https://creativecommons.org/licenses/by/4.0/

I hereby declare that I have independently contributed a significant part of the work published in Schulz et al. (2025).

Declaration of funding

This research was conducted as part of the SUBI project (grant number 03G0869), funded by the German Federal Ministry of Research, Technology and Space (BMFTR, formerly BMBF). It was further supported by the SAMUH$_2$ project (grant number 03EI3051A), funded by the German Federal Ministry for Economic Affairs and Energy (BMWE, formerly BMWK).

Contents

1 Introduction **1**
- 1.1 Well integrity . . . 1
- 1.2 Well integrity failure . . . 3
  - 1.2.1 Physical reasons for well integrity failure . . . 3
  - 1.2.2 Chemical reasons for well integrity failure . . . 6
- 1.3 Underground gas storages in Germany . . . 7
- 1.4 Sustained casing pressure: A well integrity issue indicator . . . 9
  - 1.4.1 Mechanisms and consequences . . . 9
  - 1.4.2 Reported cases across regions . . . 10
  - 1.4.3 Collection of regulatory information . . . 12
- 1.5 State of the art . . . 13
- 1.6 Objectives . . . 16

2 Experimental procedure **18**
- 2.1 Autoclave system . . . 18
- 2.2 Sample preparation . . . 19
- 2.3 Cyclic loading experiments . . . 21
- 2.4 Determination of the system permeability . . . 22
- 2.5 Determination of cement properties . . . 22

3 Numerical modeling **33**
- 3.1 Conceptual model . . . 33
- 3.2 Numerical model . . . 38
  - 3.2.1 Hagen–Poiseuille flow . . . 38
  - 3.2.2 Thermal effects . . . 45
  - 3.2.3 Matrix permeability . . . 55
  - 3.2.4 Automated models . . . 56
- 3.3 Sensitivity analysis . . . 62
  - 3.3.1 Overview . . . 62
  - 3.3.2 Influence of the number of segments and time step width . . . 63
  - 3.3.3 Influence of the gap width . . . 65
  - 3.3.4 Temperature of the flowing gas . . . 67
  - 3.3.5 Temperature and pressure dependence of input parameters . . . 71
  - 3.3.6 Heat transfer factor c . . . 75
  - 3.3.7 Upper chamber volume . . . 77

4 Results **79**
- 4.1 Cyclic loading experiments and gap modeling . . . 79
  - 4.1.1 Cement properties . . . 79
  - 4.1.2 Annular gap development . . . 83
  - 4.1.3 Statistical analysis of cyclic loading effects . . . 88
- 4.2 Regulations and guidelines for annular pressure and vent flow . . . 91
  - 4.2.1 Overview . . . 91
  - 4.2.2 Annulus management . . . 94
  - 4.2.3 Monitoring . . . 96

4.2.4 Diagnostic testing . . . 98
4.2.5 Pressure and flow thresholds . . . 101
4.2.6 Barrier classification . . . 104

5 Discussion **105**
5.1 Overview . . . 105
5.2 Evaluation of autoclave experiment results . . . 105
5.2.1 Background and context . . . 105
5.2.2 Potential cement matrix flow . . . 106
5.2.3 Effects of thermal loading cycles . . . 109
5.2.4 Effects of pressure loading cycles . . . 112
5.2.5 Additional effects on the system permeability . . . 115
5.2.6 Implications for wells and future research . . . 119
5.3 Model considerations and uncertainties . . . 124
5.3.1 Scope and objectives . . . 124
5.3.2 Monolithic formulation and comparison to operator splitting . . . 124
5.3.3 Selection of the fitting parameters . . . 129
5.3.4 Iterations and initial gap aperture . . . 138
5.3.5 Agreement between measured and modeled data . . . 140
5.3.6 Applicability of the Hagen–Poiseuille equation to compressible, non-ideal fluids under unsteady flow conditions . . . 145
5.3.7 Laminar and turbulent flow . . . 146
5.3.8 Synthesis of model uncertainties and sensitivities . . . 150
5.4 Annular pressure and flow regulations . . . 151
5.4.1 From experimental insights to regulation . . . 151
5.4.2 Rationale for regulation . . . 151
5.4.3 Direct and indirect regulations . . . 152
5.4.4 Suggested minimum standard workflow . . . 154
5.4.5 Open and closed annuli . . . 156
5.4.6 Abandoned wells . . . 156
5.4.7 Relation to experimental observations . . . 157

6 Conclusions **159**

Glossary **165**

Acknowledgements **171**

References **174**

Appendix **210**

List of Figures

1 Well illustration with leakage paths . . . 2
2 Percentage of wells showing SCP . . . 11
3 COBRA autoclave system . . . 18
4 Simplified annular gap as used in the numerical model . . . 33
5 Conceptual model of adiabatic cooling . . . 35
6 Conceptual model of adiabatic heating . . . 36
7 Spatial discretization of the annular gap . . . 40
8 Gas flow and heating effects on pressure development . . . 47
9 c-values used in the model vs upper chamber volume . . . 51
10 Modeled offsets $P_{\max}$ . . . 57
11 Effect of shifting $P_{\min}$ on experiment 1 of casing 2 . . . 59
12 Effect of shifting $P_{\min}$ on experiment 58 of casing 2 . . . 61
13 Modeled pressure development for different interval counts and time step widths . . . 64
14 Pressure development at different temperatures of the inflowing gas . . . 69
15 Influence of different gas parameters on the modeled gap aperture . . . 74
16 Pressure and temperature development at different values of c . . . 76
17 Pressure development at different upper chamber volumes . . . 77
18 Mercury porosimetry results . . . 80
19 Modeling results for casing 0 . . . 83
20 Modeling results for casing 1 . . . 84
21 Modeling results for casing 2 . . . 85
22 Modeling results for casing 3 . . . 86
23 Modeling results for casing 4 . . . 86
24 Modeled annular gap apertures of all experiments . . . 87
25 Model-derived matrix permeabilities of all experiments . . . 88
26 Boxplots of modeled gap apertures for different cyclic loading types . . . 89
27 Map of global SCP/CVF regulation and guidelines . . . 94
28 Map of annulus management requirements . . . 95
29 Map of monitoring requirements . . . 97
30 Bleed-Down/Build-Up test cases . . . 99
31 Map of diagnostic testing requirements . . . 103
32 Cracks in the autoclave cement sample of casing 1 . . . 107
33 Cracks in the control cement sample of casing 3 . . . 107
34 Comparison of model-derived and measured permeabilities . . . 108

35 Modeling results of all casings . . . 113
36 Modeling results and curing times . . . 116
37 Cement of casing 2 before and after autoclave experiments . . . 118
38 Modeling results for monolithic and operator splitting models . . . 128
39 Modeling results with and without thermal effects . . . 131
40 h modeled with and without thermal effects and with different values of c . 132
41 Comparison of modeling results related to c . . . 133
42 Example of shifting $P_{\min}$ in model HP . . . 135
43 Modeled offsets of $P'_{\min}$ and $P'_{\max}$ . . . 136
44 Comparison of modeled gap apertures h between models H and HP . . . 137
45 WRMSE boxplots for all models . . . 138
46 Convergence of the gap aperture for different initial apertures . . . 139
47 Modeling results with and without thermal effects . . . 141
48 Examples of agreement between measured and modeled data . . . 142
49 WRMSE of all experiments . . . 143
50 Raw pressure data recorded by the sensors . . . 144
51 Experiment 60 of casing 2 . . . 150
52 Suggested SCP workflow . . . 155
53 Effect of annular gap aperture on B/B pressure build-up . . . 161

List of Tables

1 XRF composition of cement powder 19
2 Experimental boundary conditions for the used casings 20
3 Sample conditioning and testing parameters for matrix permeability measurements 31
4 Upper chamber volumes and c-values for all casings 50
5 Change in annular gap aperture for different gap widths 66
6 Effect of gas temperature assumptions on modeled annular gap aperture . 70
7 Properties of nitrogen at different P/T conditions 72
8 Effect of pressure and temperature dependent parameters on h 72
9 Effect of uncertainty in V_{uc} on modeled annular gap aperture 78
10 Densities, water content, porosity and carbonate content of cement samples 79
11 Matrix permeabilities of cement samples 81
12 Mineral phases in cement samples 82
13 Binomial test results for each cyclic loading type 90
14 Brunner-Munzel test results between cyclic loading types 91
15 Different countries' SCP/CVF regulations and guidelines 93
16 Barrier classifications 104
18 Comparison of monolithic and operator splitting model results 128
19 Fitting parameters used in the different model types 130
20 Maximum number of model iterations 139

1 Introduction

1.1 Well integrity

Deep wells are an essential component of the global energy infrastructure as they are required for most subsurface energy projects, including hydrocarbon production, geothermal energy operations and the geological storage of gases and liquids such as hydrocarbons, carbon dioxide and hydrogen (Economides and Wood, 2009). Wells are created by drilling boreholes into the Earth's crust with the aim of providing controlled access to deep subsurface formations. A properly functioning well provides zonal isolation along its depth, preventing the migration of fluids between formations along the wellbore (ISO 16530-1, 2017). This isolation is essential because leaks and unintended fluid migration inside or outside the well can lead to environmental contamination of groundwater or surface water, greenhouse gas emissions, or safety hazards, for example due to pressure build-up or the presence of sour gas (e.g., Goodwin et al., 2015; Ingraffea et al., 2014; Jackson and Dusseault, 2014; Kinik and Wojtanowicz, 2011; Morais et al., 2024; Wisen et al., 2020).

To prevent such unintended fluid migration, maintaining well integrity is essential. In this study, well integrity refers to the condition of a well in which all technical barriers remain functional and capable of fulfilling their intended purpose. As such, well integrity management ensures that fluids are contained within the well and do not leak into the surrounding environment by maintaining the condition of components such as steel pipes and cement (e.g., Colborn et al., 2014; Kiran et al., 2017). According to the NORSOK D-010 standard, achieving well integrity involves implementing technical, operational, and organizational measures to minimize the risk of uncontrolled release of formation fluids throughout the entire lifespan of the well (Norwegian Oil Industry Association and Federation of Norwegian Manufacturing Industries, 2021).

Ensuring the long-term integrity of oil and gas wells will continue to be crucial for maintaining a strong and reliable energy infrastructure, even with an expected decrease in natural gas and oil consumption (e.g., Claessens, 2023; Zhou et al., 2022). Subsurface energy applications such as geologic carbon dioxide storage, compressed air and hydrogen storage, and geothermal energy utilization play a key role in reducing greenhouse gas emissions, and all of them rely on robust well integrity management (e.g., Bai et al., 2016; Carroll et al., 2016; Iyer et al., 2022; Ugarte and Salehi, 2022; Wood, 2024). The sealing components of wells used in these operations will be exposed to fluids and subsurface conditions, which can lead to multiple leakage pathways.

Figure 1 illustrates the main components of a drilled and completed well with four casings, which are tubular pipes installed during drilling operations to stabilize the borehole and isolate geological formations, as shown for example by Feder (2001). Casings are typically manufactured from specialized steel. The *conductor casing* is a short pipe driven into the

ground to stabilize unconsolidated near-surface sediments, prevent collapse, and isolate shallow aquifers during the initial drilling stage. The next inner casing string is referred to as the *surface casing*. The innermost casing is the *production casing*. Any casing strings installed between the surface casing and the production casing are referred to as *intermediate casings*. Inside the production casing lies the *tubing*, a slim steel pipe used to transport fluids either to or from the reservoir during production or injection operations. The commonly used term *tubular* refers collectively to all steel pipes installed in the well, including all casing strings and the tubing.

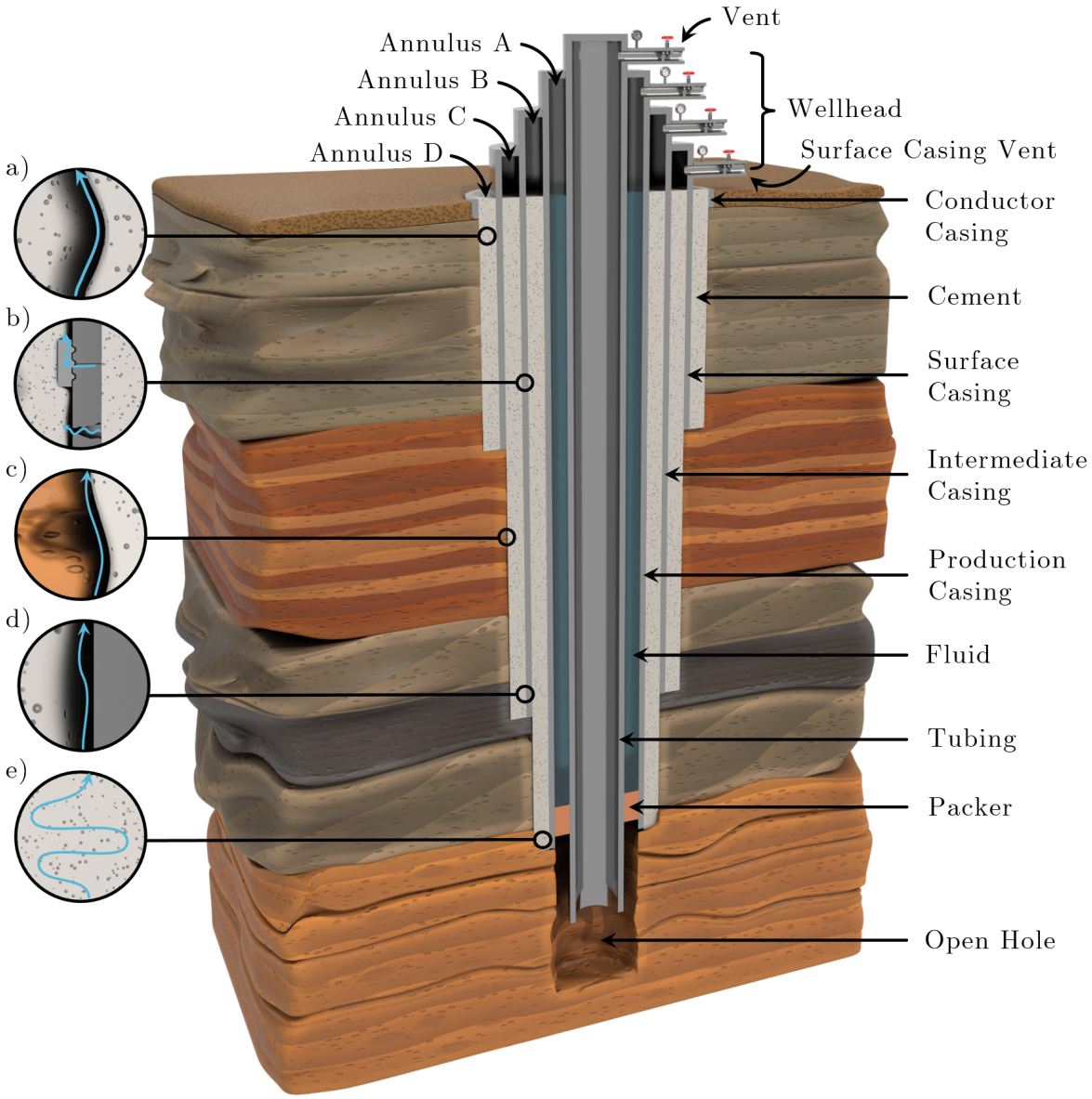


Figure 1: Illustration of a borehole and potential leakage pathways based on Feder (2001) and Gasda et al. (2004), modified after Schulz et al. (2025). The fluid leakage pathways shown are: a) fractures or mud channels in the cement, b) casing corrosion and thread leak, c) microannulus between rock and cement, d) microannulus between cement and steel, and e) cement matrix flow.

The spaces between adjacent casings, between tubing and casing, and between borehole wall and casing are referred to as annuli. Annuli are conventionally designated alphabetically from the inside outward, beginning with *annulus A* for the innermost annulus, followed by *annulus B*, and so forth. In order to seal the annular space and thereby prevent uncontrolled fluid migration along the wellbore, annuli are typically fully or partially filled with cement (Figure 1).

However, the space between the tubing and the production casing (*annulus A*) is typically filled with a corrosion-inhibiting liquid instead of cement, so the tubing can be exchanged when necessary, for example due to corrosion (e.g., Ma et al., 2022). A seal (the *packer*) is placed at the bottom of annulus A to prevent reservoir fluids from entering this annulus (e.g., Bellarby, 2009).

Although Figure 1 depicts a typical well configuration, actual well designs vary considerably depending on geological conditions and operational requirements, with substantial differences between onshore and deepwater wells (e.g., American Petroleum Institute, 2006; Jiang, 2021; Wan, 2011). For instance, wells may contain more or fewer casing strings. In addition, annuli are not always fully cemented. In some designs, only the lower sections are cemented, whereas the upper sections are filled with a liquid (e.g., Nelson, 2006, ch. 6-2.3.2, 9-6.1, C-3.6).[1] Furthermore, *hanging liners* are used in some wells, which are casing strings that do not extend to the surface but are instead hung from the next outermost casing string. In line with API RP 90, a liner is considered part of the casing into which it is installed in this study, since the annulus between the liner and the casing does not extend to the wellhead (American Petroleum Institute, 2006). Figure 1 further highlights several types of structural failures within the well barrier system that may potentially act as leakage pathways for reservoir fluids.

1.2 Well integrity failure

1.2.1 Physical reasons for well integrity failure

Well integrity failure refers to the loss of a well's ability to sufficiently contain fluids, allowing them to migrate into surrounding formations or to the surface (King and King, 2013). Various factors can compromise the integrity of a well. However, some of the main causes of leakage during underground operations lie within the wellbore sealing system – either through cracks in the cement, the pore space of the cement, or through the interfaces between rock, cement and steel (e.g., Opedal et al., 2014), as depicted in Figure 1. As one of the main reasons for cement failure is poor cement design, the composition must be selected carefully so that the cement fulfills both rheological and mechanical requirements

[1] *ch.* refers to chapters in the cited literature.

(Yousuf et al., 2021). In most wells, Class G cement or its coarser variant, Class H cement, are used (Nelson, 2006, ch. 2-7). Class G cement is based on the four Portland cement clinker phases[2] (Ghabezloo, 2011):

a) Alite: Ca_3SiO_5 (C_3S)

b) Belite: Ca_2SiO_4 (C_2S)

c) Tricalcium aluminate: $Ca_3Al_2O_6$ (C_3A)

d) Brownmillerite: $Ca_2(Al, Fe)_2O_5$ (C_4AF)

When water is added to the ground cement powder, hydration occurs. The following hydration reactions of the four clinker phases are described by Stark and Wicht (2013): Alite and Belite react to form calcium silicate hydrates (the amorphous C–S–H phases) and portlandite ($Ca(OH)_2$). The reaction of C_3A, the fastest-reacting clinker phase, depends on the presence of sulfate. Without sulfate, thin plates of calcium aluminate hydrates are formed. With sulfate, ettringite is formed first. Once the sulfate is consumed, ettringite slowly transforms into monosulfate, depending on pressure and temperature. C_4AF reacts in a similar manner, but more slowly, and additionally forms iron-containing compounds.

A wide range of additives is available to fine-tune the properties of cement according to specific rheological and mechanical needs (e.g., Broni-Bediako et al., 2016; Fink, 2011; Nelson, 2006, ch. 3). Given the complexity and sensitivity of cement behavior under downhole conditions[3], the formulation must be carefully tailored to the specific geological and operational context. An improper cement formulation increases the likelihood of failure (Yousuf et al., 2021).

Another critical factor besides the composition is the water-cement ratio during mixing. According to Dusseault et al. (2000), cement slurry with an excessively high water content can lose water to the surrounding porous rock because the hydrostatic pressure gradient in the cement column is typically higher than the adjacent pore pressure gradient. Since the cement suspension has already developed a small shear strength, this water loss may not be compensated by settling, which in turn causes shrinkage. This may lead to debonding between the cement and either the casing or the rock. In turn, debonding results in the formation of an annular gap[4] (Figure 1c,d), creating a potential flow path (Hachem and Kang, 2023). Similarly, salt-rich formation brines or rock salt can cause water to be

[2]The abbreviations in brackets follow the cement chemistry (Bogue) notation, in which C = CaO, S = SiO_2, A = Al_2O_3, and F = Fe_2O_3.

[3]For example, downhole conditions may involve high pressures, high temperatures, and complex fluid chemistries.

[4]An *annular gap* refers to a separation between the cement and the adjacent surface (casing or rock) with an aperture on the order of micrometers, while its lateral extent may be much larger. This feature is also commonly referred to as a *microannulus*.

withdrawn from the cement slurry, leading to shrinkage of the cement and the formation of fractures or a gap between rock and cement, as shown in Figure 1a,c (e.g., Chenevert and Shrestha, 1991; Dusseault et al., 2000; van Kleef, 1989).

Additionally, Portland cement shrinks during the curing phase because hydration products require less volume than the original slurry (e.g., Nelson, 2006, ch. 8-3.10; Powers, 1935). While this shrinkage can be partially compensated by additives (e.g., Dusseault et al., 2000; Fink, 2011), it may still lead to debonding (e.g., Yousuf et al., 2021). Finally, debonding between the cement and the formation may also occur if the filter or mud cake, which prevents drilling fluid from entering the formation, is not removed properly before cementation (e.g., Kremieniewski et al., 2021; Siddig et al., 2020).

Another common issue during cementation is the formation of mud channels (e.g., Bittleston et al., 2002; Pelipenko and Frigaard, 2004). If the drilling mud is not properly displaced, residual mud can create channels within the cement sheath. This issue is particularly common when a casing is eccentrically positioned, as the mud tends to accumulate on the narrower side of the annulus, forming a potential leakage path (Daccord et al., 2006).

Apart from issues during or shortly after cement slurry placement, leakage pathways may also form after the cement has cured. One frequent cause of leakage is the formation of cracks in the hardened cement (e.g., Hachem and Kang, 2023; Yousuf et al., 2021). Radial or longitudinal cracks may develop as a result of cyclic loading over time, or due to sudden pressure changes, such as those occurring during hydraulic stimulation (Yousuf et al., 2021). Radial cracking and debonding can also be triggered by temperature increases (e.g., Goodwin and Crook, 1992; Yousuf et al., 2021). Eccentric casings also increase the risk of crack development during hydraulic fracturing or other high-pressure operations, as stress concentrates at the thinnest sections of the cement, and even comparatively low pressures can lead to cement failure (Liu et al., 2018a).

Generally, cements with a higher Young's modulus or greater compressive strength are also more prone to fracturing due to pressure or temperature fluctuations than more elastic formulations (e.g., Goodwin and Crook, 1992; Yousuf et al., 2021). According to Nygaard et al. (2014), cements with higher Young's modulus or Poisson's ratio are also more susceptible to debonding and tensile fracturing due to cooling induced reductions in near-wellbore compressive stress. However, cements with a lower Young's modulus may facilitate the upward propagation of failures (Kim et al., 2016).

Although leakage is often caused by the previously described cracks in the cement or debonding at the cement–casing or cement–formation interface (e.g., Bachu, 2017; Hachem and Kang, 2023; Watson and Bachu, 2009), additional well integrity failure mechanisms can also contribute to leakage. Packer and tubing failures are relatively common in injection wells due to the high pressures involved, but these are typically straightforward to detect and remediate when appropriate monitoring systems are in place (Bachu and Watson, 2009). Casing failure is another potential leakage cause, with around 90% of such failures

occurring at the connection joints between individual casing sections, primarily driven by high thermal and mechanical loads (Cirimello et al., 2017; Maharaj, 1996). Casing wear can also contribute to structural failure, as during drilling operations, tool joints may abrade the casing wall and reduce its mechanical integrity (Lin et al., 2016). Finally, fractures in the caprock can create pathways for fluid migration. Although such fractures may occur due to natural processes (Tao et al., 2023), drilling-induced fractures in the near-well zone can also lead to leakage pathways (Opedal et al., 2018).

1.2.2 Chemical reasons for well integrity failure

In addition to the physical failure mechanisms related to pressure, stress, and temperature variations, chemical reactions can also compromise the integrity of casings and cement.

Casing corrosion is often caused by corrosive fluids containing carbon dioxide (CO_2), hydrogen sulfide (H_2S), oxygen, salts, or organic acids (Bertness et al., 1989). Corrosion due to microbiological activity, particularly involving sulfate-reducing bacteria such as *Desulfovibrio*[5] species, is also common (Baumgartner, 1962). However, CO_2 and H_2S are generally considered the most critical agents for casing corrosion (Obot et al., 2023).

Mubarak et al. (2023) describe the mechanism of CO_2-induced corrosion as follows, which is still subject of ongoing research. When CO_2 comes into contact with water, carbonic acid (H_2CO_3) forms. Depending on the pH value, H_2CO_3 dissociates into hydrogen ions (H^+) and either bicarbonate (HCO_3^-) or carbonate ions (CO_3^{2-}). The H^+ ions can subsequently be reduced to molecular hydrogen (H_2), consuming electrons, while iron (Fe) is oxidized to Fe^{2+}, releasing electrons and forming iron carbonate or hydroxycarbonate phases.

While the mechanisms of H_2S-induced casing corrosion are not yet fully understood as well, the following reactions are widely accepted (Mubarak et al., 2023): Fe is oxidized to Fe^{2+}, which reacts with H_2S to form iron sulfide (FeS) and H^+. The generated H^+ ions are then reduced to H_2. This overall process can be expressed as $Fe + H_2S \longrightarrow FeS + H_2$.

However, as H_2S hampers the formation of molecular hydrogen, some hydrogen ions may diffuse into the steel and form molecular hydrogen there. This can, for example, lead to hydrogen-induced cracking or hydrogen blistering (Mubarak et al., 2023).

Beyond casing corrosion, cement degradation due to chemical interactions can also lead to the formation of leakage pathways. CO_2 not only corrodes casing steel but also reacts with cement. These reactions are described by Song et al. (2024) as follows: The carbonic acid (H_2CO_3) generated from CO_2 and water dissociates into H^+ and carbonate (CO_3^{2-})

[5]Besides *Desulfovibrio*, numerous other species and mechanisms contribute to microbiologically influenced corrosion. For example, sulfur-oxidizing bacteria can oxidize sulfide or sulfur to highly corrosive sulfuric acid (Gao and Fan, 2023). Nevertheless, H_2S-producing *Desulfovibrio* species are considered responsible for the majority of microbiological casing corrosion (Baumgartner, 1962).

or bicarbonate (HCO_3^-) ions, creating an acidic environment. Portlandite in the cement renders the pore solution alkaline, which neutralizes the acid and causes calcium carbonate ($CaCO_3$) to precipitate. In parallel, the C–S–H gel reacts with hydrogen and carbonate ions to form $CaCO_3$ as well, which leaches calcium out of the C–S–H gel. The calcium carbonate can further react in the acidic environment to form more soluble calcium bicarbonate. Song et al. (2024) emphasize that these reactions weaken the mechanical stability of the cement and increase its permeability.

Another common cement degradation process is known as *sulfate attack*. This occurs when sulfate-rich fluids, for example from anhydrite-bearing formations, penetrate the cement matrix (Loizzo et al., 2020). Sulfate ions react with calcium to form gypsum, which subsequently reacts with hydrated calcium aluminates (such as monosulfate phases) to form secondary ettringite (Sun et al., 2019). This process results in volumetric expansion, which may induce fracturing and create potential leakage paths (Zhang et al., 2024a).

1.3 Underground gas storages in Germany

One application in which well integrity considerations are particularly relevant is underground gas storage (UGS), where large quantities of natural gas or other gases are injected into the subsurface and withdrawn when required. Globally, two main types of UGS account for almost all storage capacity (e.g., Cornot-Gandolphe, 2019; Al-Shafi et al., 2023):

1. **Pore storages:** Gas can be stored in porous rock formations provided the reservoir has sufficient permeability and is sealed by a geological trap[6]. The vast majority of global pore storages, and UGS in general, are depleted gas or oil fields repurposed for gas storage (e.g., Cornot-Gandolphe, 2019; Al-Shafi et al., 2023). Since these reservoirs have already been proven to be tight for millions of years while being porous, permeable and well explored, they are relatively straightforward to operate while providing large storage volumes. In addition to depleted reservoirs, (saline) aquifers are also used as UGS sites, provided they are sufficiently permeable and adequately sealed by a geological trap (e.g., Uliasz-Misiak and Misiak, 2024; Witherspoon et al., 1962).

2. **Caverns:** Almost all operational cavern-type UGS are salt caverns (e.g., Cornot-Gandolphe, 2019; Al-Shafi et al., 2023). These are created by drilling into a salt formation and leaching the salt with freshwater, gradually forming caverns that can

[6] A *geological trap* is a combination of impermeable boundaries and structural or stratigraphic features that confine hydrocarbons both vertically and, to some extent, laterally. For example, gas can be trapped in an anticline structure if a permeable reservoir layer is overlain by an impermeable cap rock layer (Grotzinger and Jordan, 2017).

reach several hundred meters in height and typically measure 50–100 m in diameter (Michalski et al., 2017). Because salt is highly impermeable and self-healing, salt caverns – which offer high injection and extraction rates and maintain high gas purity – are an attractive alternative to pore storages (Fibbi et al., 2022).

The wells for these UGS facilities are not fundamentally different in concept from those used in conventional oil and gas operations. However, the cyclic injection and withdrawal of gas impose additional challenges, as the wells must withstand repeated loading cycles. A specific high-frequency cycling application is currently being discussed and investigated in Germany ($SAMUH_2$ consortium, 2022; SUBI consortium, 2017). With the planned decarbonisation and the expansion of wind and solar power, the ability to supply constant baseload power is diminishing. Consequently, it becomes increasingly important to store and withdraw energy on demand. While batteries might seem the obvious choice for such buffering, Germany's stationary battery capacity by the end of 2022 was estimated at only 7 GWh, with an additional 65 GWh stored in electric vehicles (Figgener et al., 2022). To put these numbers into perspective: Germany's annual energy consumption is approximately 2.3 PWh, of which around 1.2 PWh is used for heating and approximately 0.5 PWh for electricity (Umweltbundesamt, 2025a,b,c).

UGS could instead play an important role as large-scale buffer systems, particularly since Germany possesses the fifth largest working gas[7] volume worldwide, corresponding to a natural-gas energy content of 251 TWh (Cornot-Gandolphe, 2019; Gas Infrastructure Europe, 2026). The simplest buffering concept involves injecting and withdrawing natural gas according to demand. There are also innovative concepts, such as power-to-gas, where excess electricity – e.g., from wind or solar power – is used to produce hydrogen via electrolysis, enabling chemical energy storage and potential injection into UGS facilities (Ozturk and Dincer, 2021).

Historically, UGS were typically filled during the warm months and gas was withdrawn during the cold months, resulting in an annual loading cycle (Federal Network Agency, 2026). Driven by the need to balance fluctuating renewable energy supply, future operation may involve significantly increased cycling frequencies, with frequent short-term injection and withdrawal cycles superimposed on the seasonal cycle. Since most of Germany's existing UGS facilities are several decades old (DVV Media Group GmbH, 2023) and were not designed for such cycling, their suitability for this purpose has to be evaluated. While the failure rates of rocks and well infrastructure are comparable for UGS, the discharge rate in the event of an infrastructure failure is approximately 10^6 times higher (Keeley,

[7]The *working gas volume* is the amount of gas that can be withdrawn and reinjected during operation, as opposed to the *cushion gas* that must remain in the storage for stability. In Germany, pore storages contain about 8.6×10^9 m^3 and cavern storages about 14.1×10^9 m^3 of working gas (DVV Media Group GmbH, 2025). These values are given for standard conditions (surface pressure and temperature).

2008), placing particular emphasis on the integrity of cement and steel components within the well.

Thus, experimental investigations and numerical modeling are carried out in this study to assess the effects of cyclic loading on a cement–steel composite, represented by a casing filled with cement. This configuration can be interpreted either as a plugged well in a depleted oil or gas reservoir repurposed for UGS, which must remain leak-tight under cyclic loading as well, or as the outer cement–steel interface of a cement-filled annulus.

1.4 Sustained casing pressure: A well integrity issue indicator

1.4.1 Mechanisms and consequences

Although underground gas storage represents one application in which well integrity is of particular importance, integrity failures are a widespread concern throughout the oil and gas industry and affect many wells worldwide. It is estimated that there are approximately six million active and inactive oil and gas wells in the United States and Canada alone (WellDatabase, 2025; WellWiki, 2021). Managing the integrity of these wells, along with millions of others worldwide, is a major challenge, as each well represents a potential pathway for fluid migration and requires ongoing monitoring.

While there are many methods for monitoring the integrity of a well, jurisdictions[8] with regional well integrity management programs typically rely on operators to report the occurrence of sustained casing pressure (SCP). This phenomenon refers to the build-up of annular pressure from leaking well components and is an indicator of integrity issues (Yao and Wojtanowicz, 2017). By definition, SCP rebuilds after it has been vented[9], distinguishing it from operator-induced pressures and those caused by temperature fluctuations (American Petroleum Institute, 2006).

When the annulus between two casings is open to the atmosphere, SCP cannot build up. Instead, the gas flows out of the annulus, which is referred to as casing vent flow (CVF), or more specifically surface casing vent flow (SCVF) when occurring in the annulus between the surface casing and the next innermost casing. Both SCP and CVF result from undesirable gas leakage through a well annulus and may indicate either developing or already existing well integrity issues.

Pressure build-up associated with SCP is particularly concerning, as it can cause failure at reservoir depth or at the surface, potentially resulting in a catastrophic well blowout,

[8] In this study, the term *jurisdiction* refers to the geographical area in which a regulation applies. It may correspond to a sub-national unit (e.g., a state, province, or territory) or to an entire country.

[9] Venting refers to the intentional release of gas and associated pressure from an annulus through the designated wellhead vent (Figure 1).

especially in offshore wells (Kinik and Wojtanowicz, 2011). For onshore wells with lower pressures, SCP can lead to the contamination of aquifers: If there is a leakage path that causes gas to escape from the well to the surrounding subsurface, this is referred to as gas migration (Lackey et al., 2022). Gas migration can pollute aquifers, surface waters, and the atmosphere (e.g., Ingraffea et al., 2014; Jackson and Dusseault, 2014; Morais et al., 2024; Wisen et al., 2020).

In contrast, CVF usually leads to direct greenhouse gas emissions into the atmosphere, exacerbating global warming. This also applies when SCP is released to the atmosphere to avoid the aforementioned risks. Sherwin et al. (2024) estimated that, on average, 3% of the natural gas produced from wells in the USA is lost through controlled (venting) or uncontrolled (leakage) emissions. These so-called fugitive emissions from the oil and gas sector contributed 4% of global greenhouse gas emissions in 2016 (Ritchie, 2020). Although it is difficult to estimate the contribution from specific sources, such as SCP/CVF from leaking wells (Boettcher et al., 2019), Bowman et al. (2023) estimated methane emissions from abandoned wells in Canada to be 85–93 kilotonnes per year, of which SCVF emissions accounted for 75–82%. Since SCP and (S)CVF are both indicators for well integrity issues, regulatory monitoring and testing requirements can be part of an effective risk reduction strategy.

1.4.2 Reported cases across regions

Reports of SCP and CVF are widely documented in oil and gas wells worldwide. Based on a review, Davies et al. (2014) concluded that 1.9% to 75% of wells experience barrier element failure, with 6.3% of wells in Pennsylvania affected by such failures. Furthermore, a high incidence of SCP is documented in offshore wells. In the Gulf of Mexico, up to 30% of wells exhibited SCP in some areas (Bourgoyne et al., 1999). In Norway, well integrity issues were documented in up to 18% of the offshore wells (Vignes and Aadnoy, 2008) and 31.3% of all wells on the Northern Continental Shelf (Rød, 2017). Due to differences between the studies, their results are not necessarily directly comparable.

The occurrence of SCP and/or CVF varies widely in onshore wells (Figure 2). Lackey et al. (2021) identified integrity problems in wells across Colorado, New Mexico, and Pennsylvania. Currently, monitoring for SCP or CVF is mandatory for all wells in Pennsylvania (Pennsylvania Department of Environmental Protection, 2017). While compliance issues have been identified in this state, it is estimated that 14.1% of Pennsylvania wells monitored prior to 2018 experienced SCP and/or CVF (Lackey et al., 2021; Figure 2). The percentage of wells that exhibited SCP varied between 0.2% and 26.5% among five regions considered in Colorado and New Mexico.

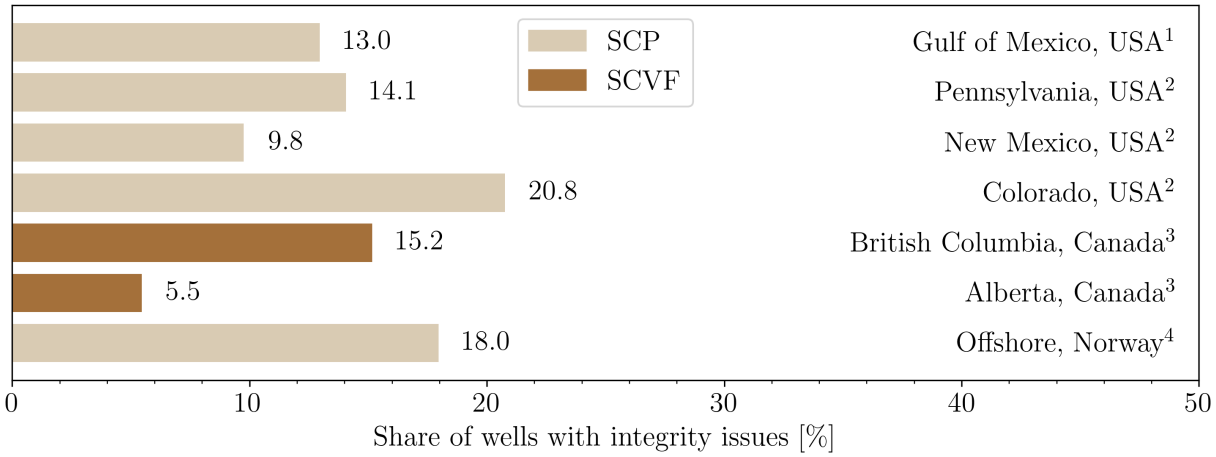


Figure 2: The percentage of wells showing SCP was up to 30% in some locations of the Gulf of Mexico, such as the Mississippi Canyon ([1]Bourgoyne et al., 1999), while 20.8% of wells in Colorado, 9.8% in New Mexico, and 14.1% in Pennsylvania showed SCP or CFV ([2]Lackey et al., 2021). The reported percentage of wells with SCVF in Alberta and British Colombia are 5.5% and 15.2%, respectively ([3]Seymour et al., 2024). However, Bowman et al. (2023) estimated that 32% of the abandoned wells in Alberta show SCVF based on 238 wells. A survey of seven companies, 12 facilities and 406 wells in Norway revealed that 18% of offshore wells showed integrity issues or uncertainties ([4]Vignes and Aadnøy, 2010). Due to differences in sample sizes and study designs, the results are not necessarily directly comparable. Figure modified after Schulz et al. (2025).

Similar observations are available for Canada. In British Columbia, a study of 21,525 wells found that 10.8% (2,329 wells) experienced leakage during their operational lifespan (Wisen et al., 2020). In Alberta, 4.9% of wells experienced SCVF, while 0.7% showed gas migration (Bachu, 2017). Seymour et al. (2024) estimated that 2.8% of wells in Alberta and 12% of wells in British Columbia exhibited SCVF. Despite testing requirements for 58.2% of wells in Alberta, only 6.2% had reported SCVF data, indicating compliance issues (Abboud et al., 2021). The focus of these studies is on SCP and CVF because detecting and measuring gas migration outside the casing is more challenging than measuring gas flow or pressure inside the casing. This is because, outside the casings, gas may disperse over a large area in the shallow subsurface around the well (Bachu, 2017).

Studies estimating greenhouse gas emissions from SCVF have primarily focused on Canadian jurisdictions. In British Columbia, SCVF emissions have been estimated at approximately 75 kt per year (Bowman et al., 2023). In contrast, Seymour et al. (2024) estimate methane emissions from SCVF at 1–10 kt in British Columbia and 22–166 kt in Alberta. Combined, this corresponds to approximately 1.7–11.4% of methane emissions from the upstream sector in both provinces (Seymour et al., 2024). However, such estimates remain highly uncertain as SCVF emission are likely underreported (Bowman et al., 2023).

1.4.3 Collection of regulatory information

As SCP and CVF are important well integrity issue indicators, regulations and industry practices from different countries were compared to complement the experiments on various scales with a regulatory perspective. To review SCP and CVF regulations, publicly available documents were collected. Where documents were not publicly accessible or difficult to locate, government agencies, researchers, and industry specialists were contacted. Chinese and Russian documents were translated either by native speakers or using neural machine translation tools, with native speakers consulted for quality assurance. Among the evaluated materials, the documents considered relevant and used in this study are:

- Title 30 of the U.S. Code of Federal Regulations (CFR), Part 250, Subpart E – Casing Pressure Management (Bureau of Safety and Environmental Enforcement, 2010)
- USA regulations for individual states (Supplementary Material 2 of Schulz et al., 2025)[10]
- API RP 90 (American Petroleum Institute, 2006)
- API RP 90-2 (American Petroleum Institute, 2016)
- Russian Federal Service for Environmental, Technological and Nuclear Supervision: Safety Rules in the Oil and Gas Industry (Rostekhnadzor, 2020)
- Standards of Chinese state-owned oil and gas companies (China National Offshore Oil Corporation, 2018; China National Petroleum Corporation, 2022)
- Directive 087 – Well Integrity Management (Alberta Energy Regulator, 2022)
- British Columbia Oil and Gas Activities Act – Drilling and Production Regulation (Government of British Columbia, 2023)
- Oil and Gas Activity Operations Manual (British Columbia Energy Regulator, 2023)
- Canadian regulations for individual provinces and territories (Supplementary Material 2 of Schulz et al., 2025)[10]
- DACC IRP 27: Wellbore Decommissioning (Energy Safety Canada, 2022)
- Petroleum and Geothermal Energy Resources Regulations 2015 of Western Australia (Government of Western Australia, 2015)

[10]On the journal homepage, the download link for Supplementary Material 2 is currently mislabeled as Supplementary Material 1, which may be corrected in the future. Here, the material is referred to as Supplementary Material 2, consistent with the designation in the table header.

- NOPSEMA Guidance Notes on Well Operations Management Plans (NOPSEMA, 2020a,b)
- Offshore Petroleum and Greenhouse Gas Storage Regulations 2011 of Australia (Office of Parliamentary Counsel, Canberra, 2023)
- Petroleum and Gas (Production and Safety) Act 2004 of Queensland (Queensland Government, 2004)
- Norwegian Regulations Relating to Petroleum Activities (Petroleum Safety Authority Norway, 2023a,b,c)
- NORSOK Standard D-010 (Norwegian Oil Industry Association and Federation of Norwegian Manufacturing Industries, 2021)
- Offshore Norge (117) - Recommended Guidelines for Well Integrity (Norwegian Oil and Gas Association, 2017)
- ISO 16530-1 (2017) and ISO 16530-2 (2014)

1.5 State of the art

Effects of cyclic loading on annular gaps

Regarding experimental work, Jackson and Murphey (1993) investigated how cyclic variations in casing pressure affect the development of an annular gap between the pressurized casing and a cement sheath surrounding the casing. Chu et al. (2015) modeled the development of such gaps using the Mohr–Coulomb yield criterion, based on the experiments by Jackson and Murphey (1993). Li et al. (2021) conducted similar experiments, cyclically pressurizing a casing inside a cement sheath. While Jackson and Murphey (1993) observed gap formation after high differential pressure loading, Li et al. (2021) reported only cracking within the cement sheath and no gap formation, likely because compressive stresses acted continuously on the interfaces during their tests. These configurations, however, are only loosely comparable to the experiments in this work, where gas pressure is applied directly to the cement rather than via casing pressurization.

Xi et al. (2021) performed related cyclic casing pressure experiments combined with numerical modeling to simulate multistage hydraulic fracturing. They also investigated pre-stressed cementation, in which additional pressure is applied to the cement slurry during curing through wellhead and casing pressure. They concluded that this approach can prevent the formation of an annular gap and SCP, and found that gas leakage typically initiates once the gap opening reaches approximately 40 µm. However, the observation period for gas flow was not specified, which is relevant because low volumetric flow rates

may remain undetected over short durations. Li et al. (2020) used the same autoclave system and observed annular gap formation between cement and casing under cyclic loading. The same setup was also used in cyclic loading tests by Zeng et al. (2019), who reported cement failure under repeated high pressure loading applied to the inside of the casing.

Zhang et al. (2017) modeled annular gap formation between cement and rock under cyclic thermal loading. They identified the temperature difference between the injected fluid and the formation and the sequence of loading cycles as key parameters, and derived gap apertures on the order of tens of micrometers.

Effects of cyclic loading on cement

While the previous studies focus on annular gaps at the cement–casing interface, other work investigated the behavior of bulk cement under cyclic loading to understand microcrack accumulation and mechanical failure. In addition to their annular cement sheath experiments, Li et al. (2021) conducted triaxial cyclic loading tests on cuboidal well cement specimens. They observed that cyclic loading led to microcrack accumulation, subsequent macrocrack formation, and ultimately cement failure. Zhou et al. (2019) performed cyclic loading tests on cylindrical well cement samples under both high and low temperature conditions, concluding that low temperatures increased stiffness and brittleness with limited deformation capacity, while high temperatures reduced stiffness but enhanced deformability, resulting in a more elastoplastic-like behavior.

Well integrity experiments without cyclic loading

In contrast to the cyclic loading studies discussed above, several experimental investigations have examined annular gap behavior under static or quasi-static pressure conditions. Schilling et al. (2015, 2016) evaluated three experiments conducted with the same autoclave system used in this work, but with CO_2 and without cyclic loading. They modeled the experiments using a pure Hagen–Poiseuille approach and obtained a gap aperture of approximately 13 µm. Klose et al. (2021) analyzed the same three experiments using three numerical models: one based on Hagen–Poiseuille flow, one based on Darcy flow, and one combining both. Their analysis yielded gap apertures of approximately 5 µm.

Moghadam et al. (2022) carried out large-scale experiments on a 2-meter-long cemented annulus between casing and a rock analogue. Although cyclic loading was not applied, they tested various casing pressures from 0 to 40 MPa and found that the annular gap between cement and casing remained open under all applied pressures. Similarly, Stormont et al. (2018) applied both internal casing pressure and external confining pressure to a cement sheath surrounding a casing and observed that the gap aperture between cement

and casing decreased with increasing confining and casing pressures. However, the gap never fully closed in their experiments once debonding had occurred.

Manceau et al. (2015) performed in-situ well integrity experiments under varying temperatures and pressures, without cyclic loading. They observed well permeability from the start, likely due to an existing annular gap between rock and cement, which increased with higher pressures and decreased with elevated temperatures.

Other related experiments

Additional studies share certain similarities with the experimental configuration used in this work (e.g., Anya et al., 2023; Gomez et al., 2017; Kuanhai et al., 2020; Meng et al., 2024; Moghadam et al., 2022; Wang et al., 2024; Xi et al., 2020). However, as illustrated by the examples above, experimental and modeling efforts on cyclic loading often focus on casing pressure. In other cases, cyclic loading is applied to cement specimens without particular attention to annular gap formation (e.g., Hao et al., 2024; Yang et al., 2024; Yuan et al., 2013; Zhang et al., 2022; Zhang et al., 2024b).

Beyond cement and steel, the effect of cyclic loading on the geological formations surrounding wells is a well-established research topic (see, e.g., Chen et al., 2016; Fan et al., 2017, 2016; Fuenkajorn and Phueakphum, 2010; Khaledi et al., 2016; Liang et al., 2012; Song et al., 2016; Wang et al., 2015). Other related studies examine the behavior of cement–steel composites in above-ground infrastructure (e.g., Cao et al., 2020; Koloo et al., 2018; Liu et al., 2018b). Since wellbore environments differ fundamentally from surface conditions, such results cannot be directly transferred to downhole applications.

Well integrity reviews

With respect to SCP, most reviews focus on technical aspects, such as integrity challenges associated with SCP (Ibukun et al., 2024), as well as its diagnosis and remediation (Wojtanowicz et al., 2001). Other reviews address broader topics, such well integrity issues and failure mechanisms (e.g., Ahmed and Salehi, 2021; Allahvirdizadeh, 2020; Jackson, 2014; Kiran et al., 2017; Ugarte and Salehi, 2022), well integrity technology (Ma et al., 2020), active integrity management processes (Wallace et al., 2008), post-abandonment integrity (Vrålstad et al., 2019), among other technical aspects.

Regulatory reviews on well integrity mainly focus on specific contexts or applications. For example, Thomas and Johnson (2019) reviewed well integrity regulations for unconventional wells. Yakoot et al. (2021) examined common well integrity practices for mature oil and gas fields, partly referencing widely adopted guidelines. Syed and Cutler (2010) analyzed regulations for CO_2 injection wells, while Morais et al. (2019) investigated the influence of non-prescriptive, indirect regulations on well integrity practices.

Research gap and contribution

Most laboratory studies on annular gap formation under cyclic loading apply pressure through the inside of the casing, thereby loading the cement sheath indirectly. In contrast, cyclic loading that acts directly on the cement-casing interface, as occurs for example during gas storage operation, has received little attention.

Moreover, thermal effects associated with gas pressurization and depressurization are usually not considered in the interpretation of pressure evolution, despite their measurable influence. For example, depressurization in a constant-volume vessel not only decreases pressure but also lowers the gas temperature. Conversely, pressurization increases both pressure and temperature. Likewise, heat transfer processes do not only affect temperature, but also influence pressure. Due to this bidirectional coupling between pressure and temperature, changes in one variable inevitably affect the other. Consequently, a correct interpretation of pressure evolution might require that pressure–temperature interactions are taken into account. These aspects are neglected in models developed for comparable experiments (Klose et al., 2021; Schilling et al., 2015), but are explicitly addressed in the numerical models developed in this thesis.

Finally, while numerous regulatory reviews address specific well types, a comprehensive global assessment of SCP regulations had been lacking. This gap was addressed by Schulz et al. (2025), which is incorporated into this thesis.

1.6 Objectives

Ensuring the long-term integrity of wells, including beyond their active operational lifetime, represents a major challenge for subsurface energy extraction, storage, and utilization. This challenge is closely linked to environmental protection and climate-change mitigation, which contribute to maintaining conditions favorable for human societies. Against this background, this study investigates how cyclic thermo-mechanical loading influences well integrity and which approaches may contribute to improving the long-term safety of wells. Because the mechanisms governing well integrity span multiple spatial and temporal scales, a holistic multi-scale approach is adopted, with particular focus on the cyclic thermo-mechanical loading of cement–steel barrier systems and regulatory aspects. The following hypotheses are tested:

- First hypothesis: *Cyclic thermo-mechanical loading of cement–steel composites alters the effective permeability of the composite more strongly than it would be expected from aging of cement alone.*

  To test this hypothesis, processes acting on different spatial and temporal scales are investigated. Small-scale laboratory experiments were conducted on cement samples to characterize age-dependent changes in material properties, particularly permeability. These observations were subsequently compared with large-scale experiments on cement–steel composite samples subjected to cyclic loading under representative underground gas storage conditions.

- Second hypothesis: *Thermally and mechanically coupled processes must be considered when evaluating leakage behavior in large-scale experiments.*

  While existing interpretation methods often account for gas compressibility, they neglect the temperature changes that pressure changes during gas flow inevitably induce through gas compression and expansion. These temperature changes lead to heat transfer between the surrounding autoclave system and the gas inside, which affects both temperature and pressure evolution. To account for these coupled thermo-mechanical processes, a finite-difference model was developed to simulate gas flow through annular gaps at the cement–steel interface and to explicitly incorporate bidirectional pressure–temperature coupling. Simulations with and without thermo-mechanical coupling were compared to assess the impact of thermal effects on pressure evolution.

- Third hypothesis: *Sustained casing pressure (SCP) and casing vent flow (CVF) can serve as effective indicators for assessing well integrity if appropriate monitoring, diagnostic, and evaluation procedures are applied.*

  To investigate this hypothesis, international regulations and industry practices related to SCP and CVF were reviewed and compared. Based on the advantages and limitations of different regulatory and industry approaches, a minimum workflow for SCP and CVF management was developed to support systematic well integrity assessment strategies. This challenge is closely linked to environmental protection and climate-change mitigation, which contribute to maintaining conditions favourable for human societies.

2 Experimental procedure

2.1 Autoclave system

In order to simulate cyclic loading on cement-filled casings, the CO_2 borehole research apparatus (COBRA) autoclave system type I was modified and used (Schilling et al., 2015, 2016). This autoclave system was originally designed in the context of geological CO_2 storage to investigate the influence of chemical reactions on cement aging (Schilling et al., 2015, 2016) and repurposed for cyclic loading experiments.

As used in this work, the autoclave system mainly consists of an upper chamber, a lower chamber, a cement-filled casing connecting these chambers, and an inflow control system (Figure 3b). The inflow control system comprises a piping assembly connected to exchangeable gas cylinders equipped with a pressure reducer. From there, the gas passes through a controlled compressor (pressure booster) and enters the lower chamber of the autoclave. The target pressure is defined via a computer-controlled system, and the gas inflow into the lower chamber is automatically controlled using a pneumatic needle valve.

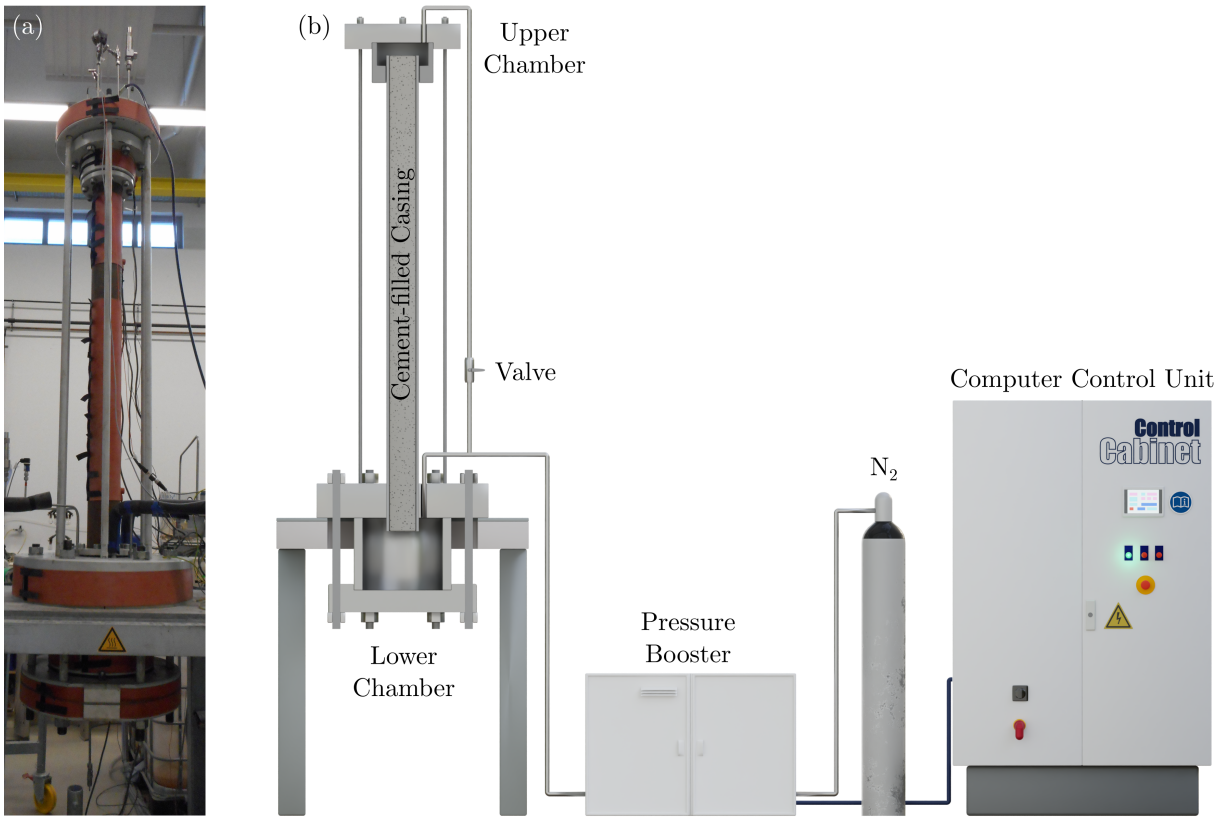


Figure 3: COBRA autoclave system used in the experimental study. (a) Photograph of the setup without thermal insulation, showing the externally mounted orange heating mats. (b) Schematic rendering of the system, illustrating the lower and upper pressure chambers, the connecting flow path (2-meter-long casing), the gas pressure booster, and the nitrogen supply. The schematic is simplified and does not include gaskets, detailed fittings, sensors or other auxiliary components.

A connecting pipe links the lower chamber to the upper chamber, enabling simultaneous pressurization of both chambers as well as pressure equilibration. This connection can be closed using a valve. At full capacity, pressure build-up rates of up to 6 bar/min can be achieved, while the lowest electronically controllable pressurization rate is 0.1 bar/min. The maximum allowable operating pressure of the autoclave system is 100 bar. Both chambers are equipped with spring-loaded emergency relief valves and additional rupture discs set to 100 bar to ensure safe operation. Furthermore, the lower chamber is connected to an electronically controlled valve that automatically releases pressure when a user-defined threshold is exceeded.

Both chambers and the casing are equipped with external heating mats (Figure 3a), allowing temperatures of up to 100 °C. The temperature of each of the seven heating mats is controlled within ±1 °C and can be adjusted individually to achieve either uniform temperature conditions or temperature gradients within the system (Schilling et al., 2015). In addition, the autoclave system is thermally insulated to promote homogeneous temperature distribution and reduce heat loss. Pressure and temperature are continuously monitored and automatically recorded for each chamber at a minimum sampling interval of 2 s. The system is sealed using rubber O-rings and annular PTFE plug seals.

2.2 Sample preparation

A total of five casings were used in the experiments described here, which were installed sequentially in the autoclave system and tested one after another. These casings were 2-meter-long K55 steel casings with an outer diameter of approximately 139.7 mm (5.5 inches) and a wall thickness of approximately 6.2 mm. The only exception was casing 0 with a wall thickness of approximately 9.2 mm. Casing 0 had been used during the former COBRA project and was therefore already filled with cement (Schilling et al., 2015, 2016). Casings 1–4 were newly prepared from sections cut from a single 9-meter-long casing originally manufactured for field applications. These casings were filled with fresh cement slurry immediately prior to each experimental series.

Casings 1–4 were filled with a slurry made from deionized water and Dyckerhoff Class G deep drilling cement powder from the same batch. The oxide composition of cement powder from this batch is given in Table 1, as determined by *Dyckerhoff GmbH*.

Table 1: Major oxide composition of the cement powder determined by X-ray fluorescence (XRF). The analysis was performed by *Dyckerhoff GmbH*.

SO_3	SiO_2	Al_2O_3	Fe_2O_3	CaO	P_2O_5	MgO	K_2O	Na_2O
2.7%	20.6%	4.5%	5.7%	63.0%	0.09%	0.9%	0.71%	0.10%

Water, cement powder and casing were stored in the room where the casings were filled with cement to ensure a comparable temperature. The same quantity of components with a water/cement powder ratio of 0.44 was used to fill casings 1–4 with cement. To achieve good homogeneity, the slurries for casings 1–4 were mixed in an *IS-38-E* colloidal mixer from *GERTEC Maschinen- und Anlagenbau GmbH*. The casings were filled from bottom to top to minimize air entrapment, following a procedure comparable to standard field cementation practices. In contrast, casing 0 had been filled three years prior with a Class G-based cement slurry optimized for minimal shrinkage (Schilling et al., 2016).

For later comparison with the casing samples, cylindrical 1-liter containers were filled with the same slurry. To maintain high and constant humidity during curing, these samples were stored in sealed containers together with water, without direct contact between water and cement. The casings were sealed with foam rubber on the bottom and a combination of plastic foil and adhesive tape on the top to prevent moisture loss of the cement. The cement, both inside the casings and 1-liter containers, cured according to Table 2. After completion of the respective curing period, each casing was installed in the autoclave system, and the corresponding experimental series was initiated on the same day.

Table 2: Experimental boundary conditions for the used casings. *Curing time* refers to the period during which the cement cured before being placed into the autoclave system. *Total time* denotes the duration from filling the casing with cement until completion of the experimental series.

Sample	Curing time	Total time	Additional treatment
Casing 0	>3 years	>3 years	Reused casing from former project[a]
Casing 1	154 days	312 days	-
Casing 2	28 days	304 days	-
Casing 3	28 days	683 days	Scale layer inside the casing removed[b]
Casing 4	28 days	479 days	-

[a] Casing 0 was filled with cement during the former COBRA project (Schilling et al., 2015, 2016). The cement was optimized for minimal shrinkage and more than 3 years old when the experiments of this study were performed. The casing and cement had already been heated and pressurized. Previous experiments involved CO_2 and saline fluids.

[b] Mill scale is a layer of iron oxides that forms on steel surfaces during hot rolling in the manufacturing process (Benchiheub et al., 2010). This scale layer on the inner surface of casing 3 was removed by sandblasting to study whether cement bonding improves on a cleaner and slightly roughened steel surface.

2.3 Cyclic loading experiments

With the autoclave setup described in Section 2.1, system permeability changes of the cement-filled casing after cyclic pressure and thermal loading were studied. In this context, *system permeability* includes any flowpath inside the casing between lower and upper chamber (Figure 3). This definition is distinct from the term *matrix permeability* as introduced in Section 2.5, which refers exclusively to flow through the cement matrix itself. The two terms are used consistently throughout this thesis to clearly differentiate between flow through the bulk material and flow through the overall system, including potential interfacial leakage paths. These definitions of system and matrix permeability are specific to the experimental framework and may differ from terminology used in other studies.

In order to simulate pressure variations in an UGS, pressure can be released and rebuilt within the autoclave system (pressure loading). Similarly, temperature variations can be imposed by controlling the heating mats (thermal loading). For the cyclic loading experiments, each cement-filled casing was installed in the autoclave system after the respective curing time listed in Table 2 had elapsed. Immediately after installation, the entire system was pressurized with N_2 to approximately 60 bar (gauge pressure) and heated to approximately 70 °C. Both pressure and temperature increases were applied gradually over several hours while the valve connecting the upper and lower chambers (Figure 3b) remained open. All five cement-filled casings listed in Table 2 subsequently underwent cyclic loading phases. In this thesis, *cyclic loading* refers to repeated variations in gas pressure (a), temperature (b), or a combination of both.

(a) **Pressure loading:** A pressure loading cycle was initiated by opening a vent valve in the lower chamber while both chambers were connected. The pressure was reduced over several hours from 60 bar gauge pressure to atmospheric pressure. Subsequently, the pressure was rebuilt by pumping nitrogen into the lower chamber while both chambers were connected. The build-up rate was typically set to 0.2 bar/min. A pressure loading cycle was considered complete once the pressure had rebuilt to 60 bar.

(b) **Thermal loading:** A thermal loading cycle was initiated by deactivating all heating mats while both chambers remained connected. The temperature then decreased from approximately 70 °C to approximately 30 °C over the course of several hours, typically overnight. As the system cooled, thermal contraction of the gas resulted in a pressure decrease of approximately 7 bar. Subsequently, the heating mats were reactivated, causing the temperature to increase again to approximately 70 °C within a similar timeframe. During reheating, the pressure also returned to its pre-cooling level. A thermal loading cycle was considered complete once the temperature had stabilized again at approximately 70 °C.

2.4 Determination of the system permeability

After each loading cycle (pressure and/or thermal), and occasionally after periods without loading, the system permeability of the cement-filled casing was evaluated to assess the impact of the preceding loading or aging. To determine the system permeability, gas flow through the cement-filled casing was deliberately induced:

First, the valve connecting the upper and lower chambers was closed. Then, a small amount of gas was released from the upper chamber by opening a needle valve for 1–2 s. This resulted in a pressure drop of approximately 3 bar in the upper chamber, thereby creating a pressure difference between the lower and upper chambers. Gas then flowed from the lower chamber to the upper chamber through the cement-filled casing, which constituted the only available flow path, in order to equilibrate the pressure difference. Depending on the system permeability of the cement-filled casing, the resulting pressure build-up in the upper chamber occurred at a faster or slower rate.

Pressure and temperature in both chambers were recorded at intervals of 2–3 s. During permeability testing, the pressure in the lower chamber was actively controlled to compensate for pressure loss caused by gas flow towards the upper chamber. In most system permeability testing experiments, the objective was to restore the upper chamber pressure to its pre-release level. These experiments were conducted only after pressure and temperature had stabilized following the preceding loading cycle.

The experiments did not directly yield system permeability values, but instead produced pressure–time data for the upper chamber, i.e., the pressure evolution, due to gas flow through the cement filled casing. This already provides qualitative insight, as faster pressure increases indicate higher system permeabilities.[11] For quantitative evaluation, the pressure evolution was further analyzed using a finite difference model (see Section 3).

2.5 Determination of cement properties

To support the interpretation of the cyclic loading experiments, key properties of the cement slurry and the hardened cement were determined. In this context, the term *cement slurry* refers to the freshly mixed suspension of water and cement powder, while *hardened cement* or *cured cement* describes the hardened material that forms from the hydration of the cement powder over several days. Throughout this work, the term *cement* refers exclusively to hardened cement that has cured for at least 28 days.

[11] For example, if an experiment conducted after a loading cycle exhibits a faster pressure increase than the corresponding experiment conducted before loading, this may indicate that the loading cycle increased the system permeability.

Cement slurry properties

First, the properties of the cement slurry used for casing 1 were determined to characterize the material prior to curing. Immediately after casing 1 was filled with cement, the spreading rate, density, and air content of the remaining slurry were measured. These measurements were performed by personnel of the *Institute of Concrete Structures and Building Materials* of the *Karlsruhe Institute of Technology*.

For the spreading rate, DIN EN 1015-3 (2007) was used as a guideline. A truncated cone funnel with a height of 6 cm, an upper diameter of 7 cm, and a lower diameter of 10 cm was placed on a flat table and filled with the sample slurry. The funnel was then lifted, allowing the slurry to spread, and the spreading diameter was measured twice with a 90° offset.

The slurry density was determined based on DIN EN 1015-6 (2006). The slurry was filled into a 1-liter container without compaction and weighed. The density was calculated from the measured mass and the known container volume.

The air content was determined using the pressure equalization method described in DIN EN 12350-7 (2022). The slurry was filled into a 5-liter pressure vessel, compacted, and leveled flush with the rim. Water was then injected through a valve until it exited through a second valve to ensure complete removal of residual air. Subsequently, air pressure was applied until a reading was obtained on the manometer. The pressure was adjusted to atmospheric level by releasing or injecting air as necessary. After tapping the vessel to release entrapped air, the resulting pressure was read from the gauge and recorded as the air content.

Properties of the hardened cement

Simultaneously with the installation of a casing in the autoclave system, the following properties of the corresponding 1-liter cured cement samples (see Section 2.2) were determined: Mineralogy, carbonate content, dry, wet and grain density, water content, porosity, pore size distribution and matrix permeability. These samples represent the cement properties prior to exposure to cyclic loading and are therefore referred to as *initial samples*.

While the cement in the casing was exposed to cyclic loading in the autoclave system as described in section 2.3, the remaining 1-liter samples[12] were stored at atmospheric pressure and approximately 20 °C without any loading. After completion of the cyclic loading experiments, the same properties as for the initial samples were determined for both the casing cement samples from the autoclave system (*autoclave samples*) and some

[12]The preparation of the 1-liter samples is described in Section 2.2.

of the remaining 1-liter samples (*control samples*) stored outside the autoclave. The autoclave samples represent cement that was exposed to cyclic loading, while the control samples serve as a reference representing cement that has experienced the same aging as the autoclave samples, but at atmospheric pressure, at a temperature of approximately 20 °C, and without cyclic loading.

To determine the cured cement properties, the initial, autoclave, and control samples of casings 1–4 underwent an identical testing routine described in the following paragraphs.

Sample processing

Before the determination of the cement properties, the cylindrical cement samples (see Section 2.2) were first crushed and dried, and then measured at different stages of processing. The cylinders underwent the following stages:

S1) **Cylinder (wet)**: Cylindrical cement sample as described in Section 2.2, freshly removed from the sealed container (initial and control samples) or from the autoclave system (autoclave samples).

S2) **Coarse fragments (wet)**: The cylinder (S1) was broken into coarse fragments using a bench vise.

S3) **Fine fragments (wet)**: The fragments (S2) were further reduced to finer fragments using a jaw crusher.

S4) **Fine fragments (dry)**: The fragmented sample material (S3) was dried at 105 °C to constant weight.

S5) **Coarse powder (dry)**: Fine fragments (S4) were ground by hand to a coarse powder using a ceramic mortar.

S6) **Fine powder (dry)**: Fine fragments (S4) were milled to a fine powder in a disc mill (*Siebtechnik GmbH Scheibenschwingmühle TS*) equipped with an agate grinder.

To determine the cement properties, two cylinders were used per sample type[13]. One cylinder was used exclusively for determining the matrix permeability and did not undergo stages S2–S6 described above. The other cylinder underwent stages S1–S6 and was used to determine the remaining properties (mineralogy, carbonate content, dry, wet, and grain density, water content, porosity, and pore size distribution). Each measurement was performed on all twelve sample types, i.e., casings 1–4 with an initial, autoclave, and control sample each.

[13]In this context, *sample type* refers to a specific combination of casing and treatment condition (initial, control, or autoclave). For example, the control samples of casing 2 represent one sample type.

Mineralogy

For X-ray diffraction (XRD) analysis, 1.8 g of the powder sample (S6) was mixed with 0.2 g of a 99.5% pure crystalline silicon powder (-325 mesh), used as an internal standard, in a planetary ball mill with agate grinding jars and balls. A *Bruker D8 Discover* instrument with a *LYNXEYE XE-T* detector was used for the XRD measurement. The X-ray source was a copper tube powered by a generator operating at 40 kV and 40 mA. The scanning parameters included a dwell time of 0.6 seconds and a step width of 0.01° over a range of 2° to 82° 2θ. Samples were rotated during the measurement to obtain more representative diffraction data by averaging over particle orientation and local inhomogeneities. Air scattering was minimized by short beam paths, anti-scatter screens, and a compact, automatically aligned detector geometry. The measured data were analyzed using the Rietveld refinement method.

Carbonate content

In addition to the XRD measurement, the carbonate content of each sample was determined separately according to DIN 18129 (2011). 3.7 g of the powder sample (S6) and 10 mL hydrochloric acid (2 mol/L) were placed in a calcimeter according to Scheibler (referred to as a CO_2 gasometer in DIN 18129, 2011). Temperature and atmospheric pressure were documented before the experiment. Subsequently, the powder sample and the aqueous acid solution were mixed to trigger the reaction depicted in Equation 1, while a magnetic stirrer ensured proper mixing throughout the experiment.

$$\mathrm{CaCO_3\,(s) + 2\,HCl\,(aq) \rightarrow CaCl_2\,(aq) + H_2O\,(l) + CO_2\,(g)} \tag{1}$$

During the reaction, the carbon dioxide (CO_2) released from the carbonates of the sample was captured in the Scheibler apparatus. The produced CO_2 volume was determined and adjusted to standard conditions with temperature and atmospheric pressure readings. This allowed for the determination of the carbonate content in the sample according to Equations 2 and 3 (DIN 18129, 2011).

According to DIN 18129 (2011), calcite and dolomite content can be determined separately, as calcite reacts primarily within the first 30 seconds, while dolomite reacts more slowly. However, this was not possible for the tested cement samples due to an exothermic reaction at the start of the experiments, which altered the temperature conditions. As a result, only the total carbonate content was determined after 30 minutes. Further details regarding the experiment and its evaluation are provided in DIN 18129 (2011). For each sample type, two separate experiments were conducted on different powder subsamples of the same type,[14] and the arithmetic mean of the results was determined.

[14]For example, crushed material from an initial sample of casing 2 was first pulverized, and subsequently two experiments were conducted on different portions of that powder.

$$V_0 = \frac{p_{\text{abs}} \cdot V_{\text{G}}}{p_{\text{n}} \cdot (273 + T) \cdot \beta} \tag{2}$$

$$V_{\text{Ca}} = \frac{V_0 \cdot \rho_{\text{a}} \cdot M_{\text{mol}}}{m_{\text{d}}} = \frac{m_{\text{Ca}}}{m_{\text{d}}} \tag{3}$$

V_0	Released CO_2 volume at normalized conditions of 1 bar and 0 °C [cm^3]
p_{abs}	Absolute air pressure at the test site [hPa]
V_{G}	Measured gas volume [cm^3]
p_{n}	Standard air pressure of 1 bar = 1000 hPa
T	Temperature at the test site [°C]
β	Expansion coefficient for CO_2 with $\beta = \frac{1}{268.4} K^{-1}$
V_{Ca}	Mass fraction of total carbonates m_{Ca} in the sample [%]
ρ_{a}	Density of CO_2 at 1 bar and 0 °C with $\rho_{\text{a}} = 0.001977$ g/cm^3
M_{mol}	Ratio of the molar masses of $CaCO_3$ and CO_2 with $M_{\text{mol}} = 2.274$ [-]
m_{d}	Mass of the dry sample material [g]
m_{Ca}	Mass fraction of total carbonates [g]

Wet density

ISO 17892-2 (2014) was used as a guideline to determine the wet density of the cements. First, cylindrical (S1) cement samples (see Section 2.2) with heights and diameters of approximately 10 cm (initial and control samples) to 12.5 cm (autoclave samples) were weighed. Then, the height and diameter of each sample were measured four times, with height measurements taken at 90° intervals and diameter measurements taken at 45° intervals. The arithmetic means were used to determine each sample's volume, and the wet density was determined according to Equation 4.

$$\rho_{\text{wet}} = \frac{m_{\text{wet,cyl}}}{\pi \cdot r_{\text{cyl}}^2 \cdot h_{\text{cyl}}} = \frac{m_{\text{wet,cyl}}}{V_{\text{cyl}}} \tag{4}$$

ρ_{wet}	Wet density of the cement [g/cm^3]
$m_{\text{wet,cyl}}$	Wet mass of the cylindrical sample [g]
r_{cyl}	Radius of the base of the cylindrical sample [cm]
h_{cyl}	Height of the cylindrical sample [cm]
V_{cyl}	Volume of the cylindrical sample [cm^3]

Grain density

To determine the grain density, ISO 17892-3 (2015) was followed as a guideline. A series of weight measurements was performed using capillary pycnometers - plugged flasks with precisely defined internal volumes of approximately 100 mL. First, the empty pycnometer was weighed (m_p). Approximately 20 g (m_d) of the pulverized sample (S5) were then placed into the pycnometer, and both were weighed together (m_1). The pycnometer, still containing the sample, was partly filled with deionized and deaerated water. It was heated on a heating plate until the water boiled for at least 20 minutes, without losing sample material. After boiling, the pycnometer was stored unplugged in a desiccator below ambient pressure overnight to cool. Once cooled, the pycnometer was completely filled with deionized and deaerated water, weighed again (m_2), and the water temperature was recorded (T_2). The pycnometer was then emptied, cleaned, filled with deionized and deaerated water only, and weighed again (m_3), along with another water temperature recording (T_3). The grain density of the sample was then determined according to Equation 5 (ISO 17892-3, 2015). For each sample type (e.g., the initial samples of casing 2), two separate experiments were conducted on different powder subsamples of the same type[15], and the arithmetic mean of the results was determined.

$$\rho_\mathrm{grain} = \frac{m_\mathrm{d}}{\frac{(m_3 - m_\mathrm{p})}{\rho_\mathrm{w3}} - \frac{(m_2 - m_1)}{\rho_\mathrm{w2}}} \tag{5}$$

ρ_grain	Grain density of the sample [g/cm^3]
m_d	Mass of the dry sample material (m_1 - m_p) [g]
m_p	Mass of the empty pycnometer [g]
m_1	Mass of the pycnometer filled with the dry sample (m_p + m_d) [g]
m_2	Mass of the pycnometer completely filled with the sample and water [g]
m_3	Mass of the pycnometer completely filled with water [g]
ρ_w2	Density of water at temperature T_2 [g/cm^3]
ρ_w3	Density of water at temperature T_3 [g/cm^3]
T_2	Water temperature measured when m_2 was determined [°C]
T_3	Water temperature measured when m_3 was determined [°C]

[15]For example, crushed material from an initial sample of casing 2 was first pulverized, and subsequently two weight measurement series were performed on different portions of that powder.

Water content

Following the determination of the wet density, material was removed from the cylindrical cement sample (S1) with a bench vise and fragmented further by a jaw crusher. The resulting wet fragments (S3) were weighed, dried at 105 °C to a constant weight (S4) and weighed again according to ISO 17892-1 (2014). Then, the water content was determined according to Equation 6 (ISO 17892-1, 2014).

$$w_{H_2O} = \frac{m_{wet,frag} - m_{dry,frag}}{m_{wet,frag}} \cdot 100 \tag{6}$$

w_{H_2O}	Water content of the cement [%]
$m_{wet,frag}$	Wet mass of the sample fragments (S3) [g]
$m_{dry,frag}$	Dry mass of the sample fragments (S4) [g]

Dry density

The dry density of the cement was determined according to Equation 7 (DIN 18125-1, 2010), using the wet mass and volume of the cylindrical sample determined during the wet density calculation, as well as the water content (Equation 6). Since the sample needed to be fragmented for drying, the dry mass of the cylinder was determined indirectly from the wet mass of the cylinder using the water content (Equation 7), as it was impractical to measure the complementary volume of the fragmented sample.

$$\rho_{dry} = \frac{m_{dry,cyl}}{V_{cyl}} = \frac{m_{wet,cyl} - m_{wet,cyl} \cdot w_{H_2O} \cdot 0.01}{V_{cyl}} \tag{7}$$

ρ_{dry}	Dry density of the cement [g/cm^3]
$m_{wet,cyl}$	Wet mass of the cylindrical sample [g]
$m_{dry,cyl}$	Dry mass of the cylindrical sample [g]
w_{H_2O}	Water content of the cement [%]
V_{cyl}	Volume of the cylindrical sample [cm^3]

Porosity

The percentage of pore volume was calculated with the previously determined dry density and grain density of the cement according to Equation 8.

$$\phi = \left(1 - \frac{\rho_{\text{dry}}}{\rho_{\text{grain}}}\right) \cdot 100 \tag{8}$$

ϕ	Porosity of the cement [%]
ρ_{dry}	Dry density of the cement [g/cm^3]
ρ_{grain}	Grain density of the cement [g/cm^3]

Pore size distribution

The pore size distribution of the samples was determined using mercury porosimetry based on DIN 66139 (2012). First, sections of the fragmented cylindrical samples (S2) were dry-sawed into cuboids with an edge length of approximately 5 mm. Since the samples needed to be free of pore water for the measurement, they were freeze-dried by applying liquid nitrogen over them and storing them below ambient pressure for a week. The measurement was then conducted with an *Autopore III mercury porosimeter* from *Micromeritics Instruments Corporation*, which allows determination of pore diameters between 360 µm and 3 nm. During the measurement, mercury was forced into the pore structure under stepwise increasing pressure. The method relies on the principle that the pressure required to intrude mercury into a round pore is inversely proportional to the pore's diameter (Webb and Orr, 1997). Based on the applied pressures and mercury volumes, the pore size distribution was derived. For each sample type (e.g., the control samples of casing 2), two to three separate experiments were conducted on different subsamples of the same type[16].

Matrix permeability

In this work, the term *matrix permeability* refers to the permeability of the cured cement itself, including flow through the pore space and microcracks within the cement matrix. It explicitly excludes any leakage pathways along the cement–casing interface.

The matrix permeability measurements were conducted based on a German Committee for Reinforced Concrete standard (DAfStb, 1991). To prepare the cylindrical samples (S1) for matrix permeability measurement, cores with a diameter of 7.5 cm were drilled and then wet-sawed into discs with a thickness of 3 cm. Since water was used in the sawing process, the samples required conditioning at controlled humidity and temperature to equilibrate the pore water content. Conditioning until mass constancy ensures that the

[16]For example, material from a control sample of casing 2 was sawed into 15 cuboids, which were then divided into three subsets. Subsequently, one measurement was performed on each subset.

water content of all samples is comparable, which is essential for obtaining comparable matrix permeability measurements.[17]

The original objective was to continue conditioning until mass constancy was achieved. However, this process was time-consuming for some samples, and achieving mass constancy had to be balanced with concerns about cement aging during the drying phase. Due to the iterative nature of this process, conditioning times were not uniform across samples (Table 3). The conditioning time was reduced from 120–130 days to 3–5 days during the measurement of the autoclave and control samples of casing 2. On these two samples types, both old and new conditioning regimes were tested to detect potential deviations in results. The two samples first underwent the newer, shorter conditioning (3 days, Casing $2a$ samples) and then the original, longer conditioning (4 months, Casing $2b$ samples).

For the measurement, each sample was installed in an *S0 2000 H* test cell from *Sommer Meß- und Feinwerktechnik*. The sample was sealed laterally, and a defined inlet gas pressure P_i was applied to the underside of the sample using oxygen. Atmospheric pressure was maintained at the top of the sample, forcing the gas to flow upward through the sample. A bubble counter was connected to the top of the sample as a gas flow meter to measure the time required for a specific gas volume to pass through it. The capillary tubes for the bubble counter defining the specific gas volume were selected to measure the specific gas volume within 20–60 seconds. Once a steady gas flow was established, the time required to reach the specific gas volume was recorded three times. The volumetric flow rate $\dot{V}$ was then determined by dividing the specific gas volume by the arithmetic mean of the three recorded times. This procedure was repeated for two to three additional, higher inlet pressures. The inlet pressures were chosen based on the sample's matrix permeability $K_\mathrm{Darcy}^\mathrm{meas}$ to keep the measurement time within the 20–60 second range. For each inlet pressure, a separate matrix permeability was determined according to Equation 9 as shown in DAfStb (1991). As the final result for each sample type, the arithmetic mean of the resulting matrix permeability values was determined, as the matrix permeability showed negligible pressure dependence in these experiments.

$$K_\mathrm{Darcy}^\mathrm{meas} = \eta \cdot \frac{2 \cdot \dot{V} \cdot P_0 \cdot l}{A \cdot (P_\mathrm{i}^2 - P_\mathrm{o}^2)} \tag{9}$$

$K_\mathrm{Darcy}^\mathrm{meas}$	Specific matrix permeability coefficient [m^2]
A	Cross-sectional area of the test specimen [m^2]
$\dot{V}$	Volumetric flow rate of the oxygen gas [m^3/s]
l	Length (thickness) of the test specimen in flow direction [m]

[17] This is due to the fact that water occupying the pores must be displaced by gas flowing through the pore network, which requires more time than in the absence of water.

η	Dynamic viscosity of the gas (oxygen in this case) at the test temperature [Pa · s]
P_i	Inlet pressure applied to the bottom of the sample [Pa]
P_o	Outlet pressure applied to the top of the sample; here equal to the atmospheric pressure [Pa]
P_0	Pressure at which the flow rate is measured, here equal to P_o [Pa]

Table 3: Sample preparation and testing conditions for matrix permeability measurements. Samples were conditioned before the measurements for the specified duration at the indicated temperature and relative humidity. If no humidity is shown, the samples were dried in an oven. The listed pressure steps are the inlet overpressures applied to the bottom of each sample during the measurement. For example, a value of 0.5 bar represents an absolute inlet pressure of approximately 1.5 bar, accounting for the atmospheric pressure of ∼1 bar. *a* and *b* represent repeated measurements of the same sample at different times, while *1* and *2* indicate different samples from the same batch. The sample *Casing 2 Initial* broke during installation and could not be measured, therefore no pressure was applied.

Cement Samples		Sample conditioning			Measurement
		Duration [days]	Temperature [°C]	Humidity [%]	Pressure [bar]
Casing 1	Initial 1	40	20	65	0.5/1.0/1.5/2.0
	Initial 2	40	20	65	0.5/1.0/1.5/2.0
	Autoclave 1a	121	20	65	0.5/0.75/1.0
	Autoclave 1b	125	20	65	0.5/0.75/1.0
	Autoclave 2a	121	20	65	0.5/1.0/1.5
	Autoclave 2b	125	20	65	0.5/1.0/1.5
	Autoclave 3	121	20	65	0.5/1.0/1.5
	Control	121	20	65	1.0/1.5/2.0
Casing 2	Initial	121	20	65	-
	Autoclave a	3	40	-	1.0/1.5/2.0
	Autoclave b	130	20	65	1.0/1.5/2.0
	Control a	3	40	-	0.2/0.4/0.6
	Control b	130	20	65	0.5/1.0/1.5
Casing 3	Initial	3	40	-	0.2/0.4/0.6
	Autoclave	5	40	-	3.0/3.5/4.0
	Control	5	40	-	1.5/2.0/2.5
Casing 4	Initial a	3	40	-	0.5/1.0/1.5/2.0
	Initial b	7	40	-	0.5/1.0/1.5
	Autoclave	3	40	-	0.5/1.0/1.5
	Control	3	40	-	0.5/1.0/1.5

While the previously described determinations of cement properties were conducted largely by the author, the matrix permeability measurements were performed by personnel of the *Institute of Concrete Structures and Building Materials* of the *Karlsruhe Institute of Technology*.

3 Numerical modeling

3.1 Conceptual model

The pressure build-up experiments described in Sections 2.1–2.4 form the basis for the numerical modeling approach developed in this study. During the experiments, gas release from the upper chamber created a pressure difference between the lower and upper chamber, inducing gas flow through the cement-filled casing. As a result, the pressure in the upper chamber increased over time until it approached the pre-release level.

A one-dimensional finite-difference model was developed to simulate gas flow through the cement-filled casing and the associated pressure and temperature evolution in the upper chamber. It is assumed that gas flow from the lower chamber to the upper chamber occurs exclusively through an annular gap at the cement-casing interface (Figure 4a). This assumption is supported by previous experiments using CO_2, in which carbonation was observed along the cement-casing interface but not within the cement matrix itself (Schilling et al., 2016).

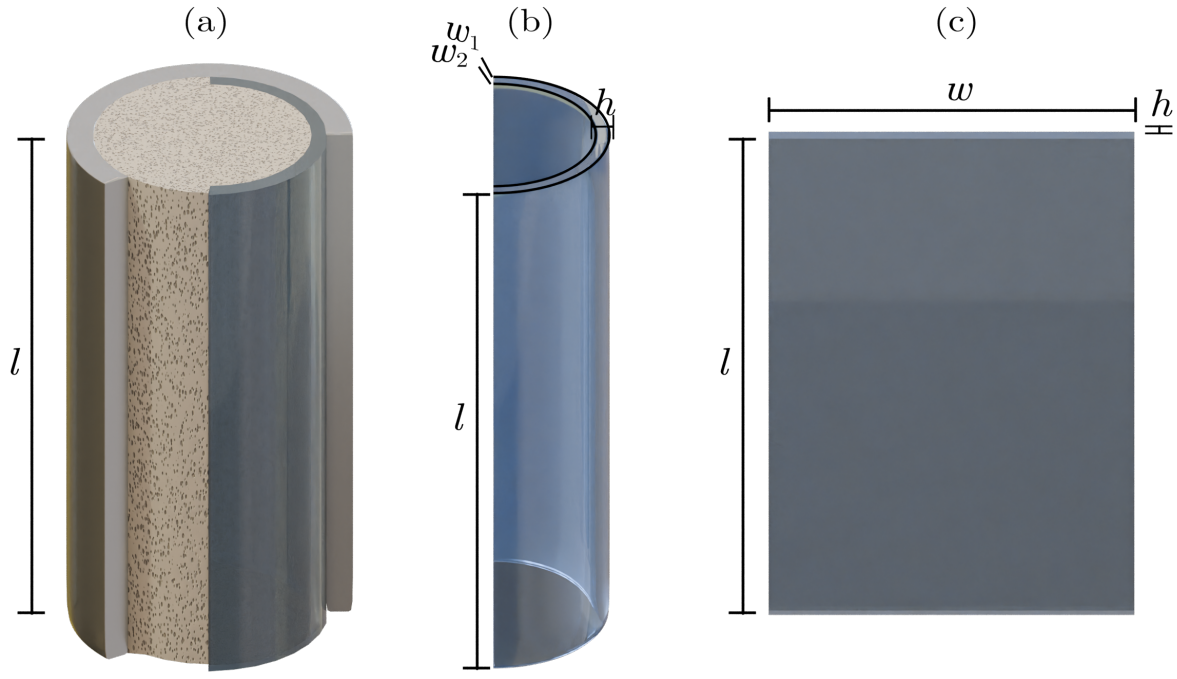


Figure 4: The annular gap (blue-grey volume) depicted as (a) a gap between the casing (sectioned for visibility) and cement; (b) an isolated gap; and (c) a straightened gap as used in the model. Dimensions are not to scale: $l \approx 2$ m, $w \approx 200$ mm, and h is on the order of µm. Due to the small values of h, the following assumption is made in the model: $w_1 = w_2 = w$. The gap is not assumed to span the entire width of the interface between cement and steel at full aperture. Instead, it is assumed to cover approximately 50% of the interface, as portrayed in the figure. Consequently, a width of $w \approx 200$ mm was adopted in the model.

Accordingly, the pressure build-up in the upper chamber at constant chamber volume is primarily controlled by the geometry of the annular gap and by thermal effects associated with gas flow. The objective of the model is to infer the effective annular gap aperture by calibrating the simulated upper-chamber pressure evolution to the experimentally measured pressure data.

The annular gap is represented as a three-dimensional domain characterized by an inner circumference w_1, an outer circumference w_2, and a length l, corresponding to the length of the cement column inside the casing (Figure 4b). The radial difference between the inner and outer circumferences defines the aperture h of the annular gap, which is assumed to vary, for example as a result of cyclic loading. Given circumferences of approximately 200 mm and apertures below 0.1 mm, the difference between the inner and outer circumferences is negligible. Therefore, the annular gap is approximated as a rectangular channel, in which one side of the base corresponds to the circumference w and the other to the aperture h (Figure 4c). The model allows simulation of either a continuous gap extending over the entire cement-casing interface or a partial gap covering only a specified fraction of the circumference, as illustrated in Figure 4. In this study, w represents half of the casing circumference, corresponding to a gap extending over 50% of the interface.

To simulate gas flow through the gap, the Hagen–Poiseuille equation for rectangular flow channels according to Bruus (2008) is applied (Equations 10 and 11). In the model, the annular gap is divided into multiple segments, and the flow from segment to segment, and finally into the upper chamber, is calculated step-wise in small time steps.

$$\dot{V} = \frac{K_{\mathrm{HP}} \cdot h^3 \cdot w}{12 \cdot \eta \cdot l} \cdot \Delta P_{\mathrm{cas}} \tag{10}$$

$$K_{\mathrm{HP}} = 1 - \sum_{n=1}^{\infty} \frac{1}{(2n-1)^5} \cdot \frac{192}{\pi^5} \cdot \frac{h}{w} \cdot \tanh\left((2n-1) \cdot \frac{\pi}{2} \cdot \frac{w}{h}\right) \tag{11}$$

$\dot{V}$	Volumetric flow rate [m^3/s]
K_{HP}	Shape factor accounting for the channel geometry [-]; since w is 4–5 orders of magnitude greater than h in this work, $K_{\mathrm{HP}} \approx 1$.
w	Width of the straightened annular gap [m], see Figure 4
h	Aperture of the annular gap [m], with $h \ll w$; see Figure 4
l	Length of the annular gap [m], see Figure 4; in the model, l is spatially discretized
η	Dynamic viscosity of the flowing fluid [Pa·s]
ΔP_{cas}	Pressure difference between both ends of the channel [Pa]

In addition to the Hagen–Poiseuille flow, pressure-temperature interactions in the gas phase are also considered in the model. All pressure and temperature changes resulting from different processes are calculated individually and then combined for each time step. These processes are:

(1) **Temperature decrease due to gas release:** When gas is released from the upper chamber, the remaining gas expands, and its temperature is consequently reduced. For this temperature decrease, it is assumed that the gas release occurs rapidly enough to neglect any heat exchange between the gas remaining in the upper chamber and the surrounding steel during the release phase. The process is modeled as an adiabatic[18] expansion of the gas, with a constant amount of substance and an expanding volume (Figure 5). This temperature decrease occurs only once at the start of an experiment and is therefore not recalculated during subsequent time steps.

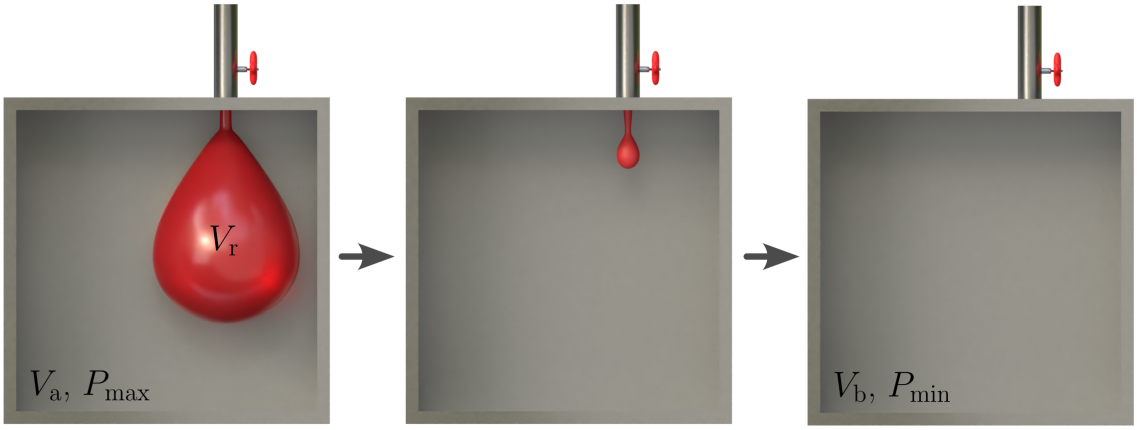


Figure 5: Conceptual model of the adiabatic cooling process in the upper chamber: To illustrate the process, a bag containing the gas to be released (V_r) is assumed. Once this gas is released, the gas remaining in the chamber expands from V_a to V_b, while the pressure drops from P_{max} to P_{min} and the amount of substance remains constant. It holds that $V_a + V_r = V_b$

(2) **Pressure increase due to gas flow:** Gas flow, calculated according to Equation 10, leads to pressure changes in the upper chamber and in the annular gap.

(3) **Temperature increase due to heat transfer from steel to gas:** The temperature decrease caused by the gas release (1) results in a lower gas temperature in the upper chamber at the start of the subsequent pressure build-up compared to the surrounding steel. This temperature difference leads to heat transfer from the autoclave steel to

[18] *Adiabatic* refers to a process without heat exchange. *Isentropic* refers to the reversible case of an adiabatic process in which no entropy is produced, i.e., there are no dissipative effects such as friction or turbulence. Since such effects are neglected in the present model, adiabatic temperature changes are approximated using isentropic relations.

the gas, heating the gas inside the upper chamber during the experiment. Due to the use of heating mats and the much larger thermal mass (total heat capacity) of the steel autoclave compared with the enclosed gas, the steel temperature is assumed to remain constant at the value prior to gas release.

(4) **Pressure increase due to heat transfer from steel to gas:** In addition to gas flow (2), heat transfer from steel to gas (3) causes a secondary pressure increase in the upper chamber. For this, isochoric heating is assumed, as the volume of the upper chamber remains constant. Only the pressure increase resulting from heating is considered in this step of the calculation, with the amount of substance assumed to remain constant in this step. The pressure increase due to gas flow (2) is excluded from this step of the calculation, as it is addressed independently in the model.

(5) **Temperature increase due to gas flow:** Additionally, the gas flow into the upper chamber increases the pressure, which in turn slightly increases the gas temperature due to compression. This temperature increase is considered in the model because it influences a) the heat transfer from the surrounding steel to the gas (3) and consequently b) the pressure inside the upper chamber. The temperature increase resulting from the pressure increase due to gas flow is calculated under the assumption of an isentropic volume change, following an approach analogous to the gas release process (Figure 5). However, in the case of the temperature increase, gas flows into the upper chamber rather than out of it (Figure 6).

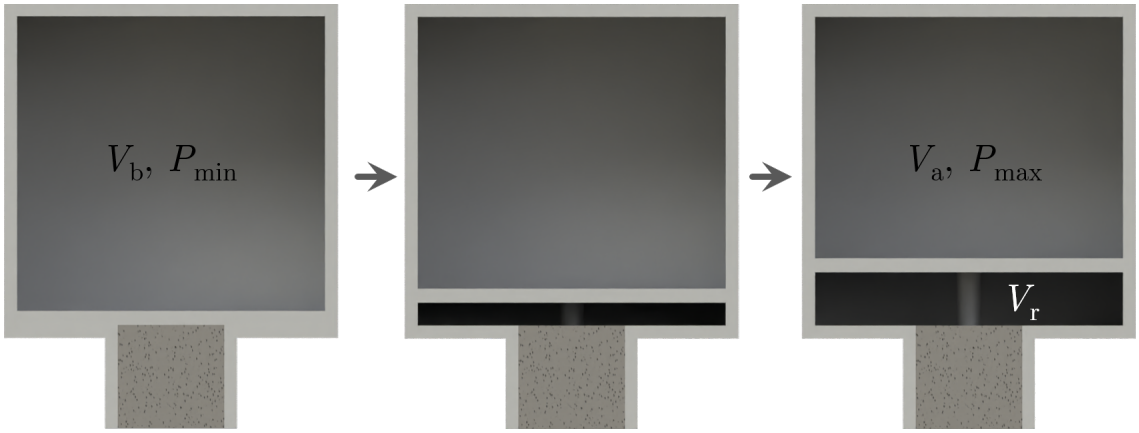


Figure 6: Conceptual model of the adiabatic heating process caused by gas flow into the upper chamber. As an illustration analogous to Figure 5, the inflowing gas is treated as a separate volume that pushes a piston into the chamber, while the amount of substance remains constant above the piston. With each time step, the piston advances incrementally. The process starts with volume V_b at pressure P_{min} and ends with volume V_a at pressure P_{max}. V_r is equivalent to the released gas volume, such that $V_a + V_r = V_b$.

In contrast to the relatively fast gas release (1), gas flow into the upper chamber occurs over a period of minutes to hours, making the process inherently non-adiabatic due to heat exchange with the surrounding steel and cement. Despite this, the temperature

change in the upper chamber due to the pressure increase caused by gas flow is calculated assuming adiabatic and isentropic conditions over a short time step. This result is then combined with the non-adiabatic temperature change due to heat transfer from steel to gas (3), which is calculated for the same time step. This ensures that the non-adiabatic nature of the process is represented in the model, even though one of the contributing sub-processes in each time step is treated as adiabatic.

The pressure change due to gas flow (2) is calculated both within the gap and the upper chamber. The thermal effects[19] (1 and 3–5), however, are only considered for the upper chamber in the main model. Within the gap, it is assumed that the temperature of the flowing gas equilibrates immediately with the surrounding steel and cement due to the relatively small gap volume and the large contact surface area. The temperatures of the surrounding cement and steel are assumed to remain unchanged because their thermal mass is much larger than that of the gas within the gap. It is further assumed that the cement and steel adjacent to the upper chamber have approximately the same temperature as the gas inside the upper chamber. Consequently, the gas entering the upper chamber is assumed to have the same temperature as the gas already present in the chamber. To assess the impact of this assumption, different scenarios for the temperature of the gas in the gap were evaluated, as described in Section 3.3.4. This sensitivity analysis indicates that gas temperature variations in the gap have a negligible influence on the results.

When considering the experiment as a whole, gas predominantly flows from the annular gap into the upper chamber, leading to increases in both temperature and pressure. Similarly, heat transfer between the steel of the upper chamber and the gas typically occurs from the steel to the gas, increasing the gas temperature and pressure. However, at specific points during an experiment, both processes can also occur in reverse: gas may flow from the upper chamber into the gap, and the steel may cool the gas in the upper chamber if the respective temperature and pressure differences occur.[20] The model explicitly allows for these reversed processes, but they have never dominated the overall system behavior. For the sake of readability, the following subsection therefore mainly describes the processes as if only the non-reversed gas and heat flow occured.

[19] In this work, the term *thermal effects* refers to all processes in which temperature changes influence the pressure evolution or pressure changes influence the temperature evolution in the upper chamber. In other words, thermal effects include all temperature–pressure couplings that contribute to the pressure evolution. If thermal effects are not considered, only the purely mechanical gas flow and the associated pressure changes are taken into account.

[20] For example, reversed gas flow may occur due to pressure variations in the lower chamber. If the lower chamber pressure falls below the upper chamber pressure, gas flows from the upper towards the lower chamber. A similar reversal can occur for heat flow. When gas flows rapidly into the upper chamber, the associated pressure increase causes gas heating. If the gas temperature then exceeds the steel temperature, heat flow will occur from gas to steel. Such conditions are more likely once the pressure and temperature in the upper chamber have largely equilibrated.

The conceptual model represents a first-order abstraction of the governing physical processes and forms the basis for the numerical implementation described in the following chapter. Consequently, both the conceptual and numerical models constitute approximations of the underlying physical processes. The associated assumptions, limitations, uncertainties, and sensitivities of the modeling approach are discussed in Sections 3.3 and 5.3.

3.2 Numerical model

3.2.1 Hagen–Poiseuille flow

Based on the conceptual framework described above, a numerical model was developed to simulate the pressure evolution within the system. This implementation requires the specification of several input parameters, including the viscosity and compressibility of the flowing fluid, the total simulation time, and the number of discrete segments used to represent the annular gap. In addition, geometric parameters such as the inner diameter of the casing, the length of the annular gap, and the volume of the upper chamber must be defined. Furthermore, the pressure in the upper chamber is required. The annular gap aperture h serves as the fitting parameter, allowing the modeled pressure build-up curve to be matched to the experimental observations.

The numerical model focuses on the pressure build-up phase, which begins immediately after the gas release has ended. For the simulation, all measured pressure values from the upper chamber are normalized according to Equation 12, scaling the pressure to a dimensionless value between 0 and 1. A normalized pressure of 0 corresponds to the minimum pressure reached during the gas release. A normalized pressure of 1 represents the equilibrium pressure of the system, after the pressure build-up has concluded, which is approximately equal to the pressure level prior to release. Intermediate values reflect the proportion of pressure rebuilt. For example, a value of 0.3 indicates that 30% of the released pressure has been rebuilt.

In the subsequent calculations, a pressure P always represents the physical pressure in pascals, whereas the complementary P' refers to the unitless, normalized pressure according to Equation 12. Outside the model and thus before normalization, the arithmetic mean of the measured pressure values was calculated, typically over groups of five, to reduce fluctuations in the measured data. Values temporally close to the pressure release were excluded from averaging to preserve the lowest measured minimum pressure, and to enhance the temporal resolution during the phase of rapid pressure build-up.

$$P' = \frac{P_{\text{phys}} - P_{\text{min}}}{P_{\text{max}} - P_{\text{min}}} \tag{12}$$

P'	Normalized, dimensionless pressure value [-]
P_{phys}	Physical, non-normalized pressure value [Pa]
P_{min}	Measured minimum pressure in the upper chamber reached due to the gas release [Pa]
P_{max}	Measured maximum pressure in the upper chamber reached during the pressure build-up [Pa]

In the model, calculations are performed over discrete spatial intervals. The annular gap is divided into N intervals for the calculation, with $N + 1$ grid points (representing segment volumes[21]) located at the interval boundaries (Figure 7). The gas flow is calculated from one point to the next, with i referring to the grid point (and thus segment volume) index, taking values from 0 to N. A value of $N = 2$ was used in this work, as it could be shown that this discretization yields almost identical results compared to finer spatial resolutions under certain conditions (see Section 3.3.2).

For example, for $i = 2$, $\dot{V}_{j,2}$ is the volumetric flow rate through flow interval 2, from grid point 1 to grid point 2, and thus from segment volume 1 to segment volume 2, at time step j (Figure 7). The pressure $P_{j,2}$ represents the pressure in segment 2 after gas flow during time step j has been completed.

The lowermost grid point 0 is located at the interface between the bottom end of the annular gap and the lower chamber. Accordingly, the pressure $P_{j,0}$ at grid point 0 represents the pressure in the lower chamber at the end of time step j. It is assumed that a small portion of the annular gap is strongly influenced by the lower chamber pressure. Therefore, the volume of half a gap segment adjacent to the lower chamber is considered to share the same pressure as the lower chamber (Figure 7). In principle, this half-segment volume should be added to the lower chamber volume. However, because the lower boundary is prescribed as a pressure boundary condition, only the lower chamber pressure enters the calculations. Since the lower chamber volume is not used in the model, this adjustment was omitted.

Similarly, the pressure $P_{j,N}$ corresponds to the pressure in the upper chamber at the end of time step j. Analogously, the volume of half a gap segment adjacent to the upper

[21] Flow calculations are performed between discrete *grid points*, which define the distances over which fluid transport is evaluated. As *grid points* themselves do not have a physical volume, the term *segment* is introduced to refer to the corresponding control volume used in pressure calculations. Each grid point i represents the center of segment i, and both share the same index. Consequently, the terms *grid point* and *segment* refer to closely related entities and may, where appropriate, be used interchangeably.

chamber is considered to share the same pressure as the upper chamber (Figure 7). Thus, this half-segment is added to the volume of the upper chamber for calculations within the model. Consequently, segment 0 can be referred to as the *lower chamber segment*, segment N as the *upper chamber segment*, and all intermediate segments as *gap segments*.

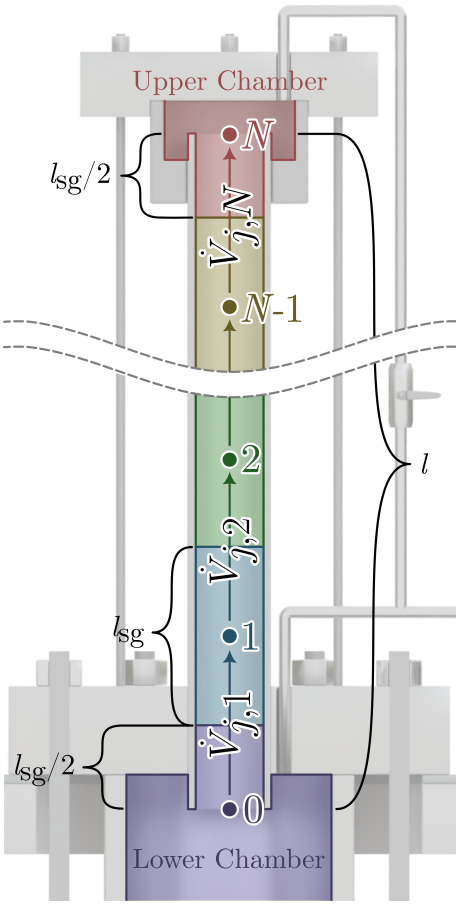


Figure 7: Spatial discretization of the annular gap. Numbers next to the points indicate the corresponding grid points and associated segment volumes. For example, the blue segment corresponds to $i = 1$ and is represented by grid point 1 located at its center. $\dot{V}_{j,i}$ denotes the volumetric flow rate at time step j between segments i and $i - 1$. l_{sg} is the length of a segment and l is the total length of the casing, with $l_{\mathrm{sg}} = l/N$. The distance between adjacent grid points is equal to l_{sg}.

Similar to the calculations performed across discrete spatial intervals, the model also operates in discrete time steps. In this context, t represents the time in seconds that has passed since the beginning of the experiment (after the gas release) at the integer time step j. In the model, an experiment is considered to begin once P_{min} is reached at $t = 0$ s and $j = 0$. All calculations then start at $j = 1$. For example, with a time step width Δt of 0.02 s, t would be 0.08 s at $j = 4$. J is the total number of time steps.

For each experiment, Δt is determined according to Equation 13 (derived from Equation 10). This ensures that the outflow per time step from a segment does not exceed its available volume, thereby preventing numerical instabilities and potential program termination due to unphysical flow rates resulting from excessively large time steps. The factor 0.25 in

Equation 13 serves as a fixed safety margin to reduce the risk of instabilities, while the variable $F_{\Delta t}$ allows for manual adjustment of Δt. The maximum allowed value for Δt was set to 0.1 s.

$$\Delta t = \frac{0.25}{F_{\Delta t}} \cdot \frac{12 \cdot \eta}{h^3 \cdot w} \cdot \frac{l}{N} \cdot V_{\text{sg}} \cdot \kappa \tag{13}$$

$$V_{\text{sg}} = w \cdot h \cdot \frac{l}{N} \tag{14}$$

Δt	Time step width [s]
$F_{\Delta t}$	Variable that can be set above 1 to manually decrease Δt [-]
h	Aperture of the annular gap [m]; see Figure 4
w	Width of the straightened gap [m]; see Figure 4
η	Dynamic viscosity of the flowing fluid [Pa·s]
l	Length of the annular gap [m]; see Figure 4
N	Number of flow intervals [-]
V_{sg}	Volume of a gap segment [m^3]
κ	Compressibility[22] of the flowing fluid [Pa^{-1}]

To initialize the flow calculation, $P'_{0,i}$ is set to 0 for the upper half of the segments, covering both the upper chamber and adjacent gap segments. This simulates the pressure drop caused by the bleed-down in the upper chamber at the start of the experiment. In contrast, $P'_{0,i}$ is set to 1 in the lower half of the gap, representing a higher initial pressure for grid points farther away from the upper chamber. In the lower chamber ($i = 0$), the pressure was intended to be maintained at a constant level ($P_{\max}$). Thus, $P'_{j,0}$ would ideally remain equal to 1 for all time steps j.

However, a constant pressure in the lower chamber was not always ideally achieved by the pressure control unit. Consequently, the measured pressure values from the lower chamber were utilized in the model. They were normalized according to Equation 12 and implemented as $P'_{j,0}$. Since pressure measurements were recorded at 2-second intervals, while a much smaller time step width is used in the model (e.g., 0.02 s), intermediate pressure values in the lower chamber need to be estimated for time steps between recorded intervals. For each time step, the pressure in the lower chamber is approximated by using the closest available recorded pressure value.

[22]Termination due to excessive flow is primarily an issue in gap segments, where the isothermal compressibility is used (see Section 3.1). A constant compressibility of $1.8 \cdot 10^{-7}$ Pa^{-1} is used in Equation 14, which approximately corresponds to the isothermal compressibility of nitrogen shortly after gas release. The time step width Δt is calculated with sufficient safety margins to ensure that volumetric flow rates remain low enough to prevent termination due to excessive flow - even if the actual compressibility deviates slightly from the constant value.

Next, the flow through each interval i and the corresponding pressure change at each grid point i (representing segment i), from bottom to top, are calculated for every time step j. The calculations begin with $P'_{1,1}$, followed sequentially by $P'_{1,2}$ and continue point by point until $P'_{1,N}$ is reached. After completing all calculations of the first time step, the algorithm advances to the next time step, beginning with $P'_{2,1}$. In this sequence, Equation 15 is applied to calculate the volumetric gas flow through each gap interval at each time step. Equation 15 is a modification of Equation 10, adapted for the finite difference approach.

$$\dot{V}'_{j,i} = K_{\mathrm{HP}} \cdot \frac{h^3 \cdot w}{12\eta} \cdot \frac{\Delta P'_{j,i}}{l_{\mathrm{sg}}} \tag{15}$$

- $\dot{V}'_{j,i}$ Volumetric gas flow rate (pressure-normalized) between point $i-1$ and point i during time step j; can be positive (gas flow from point $i-1$ to point i) or negative (gas flow from point i to point $i-1$) $[\frac{\mathrm{m}^3}{\mathrm{Pa \cdot s}}]$; $\dot{V}'_{j,i} \cdot (P_{\max} - P_{\min}) = \dot{V}_{j,i}$
- K_{HP} Shape factor accounting for the channel geometry according to Equation 11 [-]; in this study $K_{\mathrm{HP}} \approx 1$
- w Width (circumference) of the annular gap [m]; see Figure 4
- h Aperture of the annular gap [m]; see Figure 4
- l_{sg} Length of an annular gap segment, equals l/N [m]
- η Dynamic viscosity of the flowing fluid [Pa·s]
- $\Delta P'_{j,i}$ Normalized pressure difference between segment i and $i-1$ (point i and $i-1$) at the beginning of time step j [-]; equals $P'_{j,i-1} - P'_{j,i}$

After calculating $\dot{V}'_{j,i}$, the corresponding pressure changes resulting from gas flow between the grid points are determined according to Equations 16–18. Here, $\Delta P'^{\,\mathrm{inflow}}_{j,i}$ represents the pressure change in segment i (and thus at grid point i) due to gas inflow from segment $i-1$ at time step j. Analogously, $\Delta P'^{\,\mathrm{outflow}}_{j,i}$ denotes the pressure change in segment i due to gas outflow from segment i to segment $i+1$ at time step j. These two pressure changes, calculated according to Equations 16 and 17, are only determined for values of i ranging from 1 to $N-1$.

For the uppermost segment N, only the pressure change $\Delta P'^{\,\mathrm{inflow}}_{j,N}$ due to inflow from segment $N-1$ must be considered. Since the final segment N represents the upper chamber, there is no outflow from segment N to a subsequent segment. Furthermore, the upper chamber's volume is distinct from that of a gap segment and considerably larger. Thus, the upper chamber pressure change due to gas flow is calculated according to

Equation 18 instead of 16. Reverse flow from upper to lower segments is mathematically possible in the form of negative inflow and outflow values.

$$\Delta P'^{\,\text{inflow}}_{j,i} = \frac{\dot{V}'_{j,i} \cdot \Delta t}{V_{\text{sg}} \cdot \kappa^{(\text{T})}_{j,i}} \tag{16}$$

$$\Delta P'^{\,\text{outflow}}_{j,i} = \frac{\dot{V}'_{j,i+1} \cdot \Delta t}{V_{\text{sg}} \cdot \kappa^{(\text{T})}_{j,i}} \tag{17}$$

$$\Delta P'^{\,\text{inflow}}_{j,N} = \frac{\dot{V}'_{j,N} \cdot \Delta t}{V_{\text{uc}} \cdot \kappa^{(\text{S})}_{j,N}} \tag{18}$$

$\Delta P'^{\,\text{inflow}}_{j,i}$	Normalized pressure change in segment i due to gas flow from segment/grid point $i-1$ to i at time step j [-]
$\Delta P'^{\,\text{outflow}}_{j,i}$	Normalized pressure change in segment i due to gas flow from segment/grid point i to $i+1$ at time step j [-]
$\Delta P'^{\,\text{inflow}}_{j,N}$	Normalized pressure change in segment N (upper chamber) due to gas flow from segment/grid point $N-1$ to N at time step j [-]
$\dot{V}'_{j,i}$	Volumetric gas flow rate (pressure-normalized) between grid point $i-1$ and grid point i during time step j; can be positive (gas flow from point $i-1$ to point i) or negative (gas flow from point i to point $i-1$) $[\frac{\text{m}^3}{\text{Pa·s}}]$; $\dot{V}'_{j,i} \cdot (P_{\max} - P_{\min}) = \dot{V}_{j,i}$
Δt	Time step width used in the model [s]; e.g., 0.02 s
V_{sg}	Volume of a gap segment according to Equation 14 [m^3]
V_{uc}	Volume of the upper chamber segment [m^3]
$\kappa^{(\text{T})}_{j,i}$	Isothermal compressibility of the gas at grid point i (in segment i) and time step j [Pa^{-1}]
$\kappa^{(\text{S})}_{j,N}$	Isentropic compressibility of the gas at grid point N (in segment N) and time step j [Pa^{-1}]

The isothermal compressibility is used for calculations within the gap, because immediate heat exchange is assumed there. In contrast, the isentropic compressibility is applied in the upper chamber, where heat exchange is assumed to be non-instantaneous (see Section 3.1). The compressibilities $\kappa^{(\text{T})}_{j,i}$ and $\kappa^{(\text{S})}_{j,N}$ are calculated for each segment and time step. This was achieved by deriving a function to compute $\kappa^{(\text{T})}_{j,i}$ within the gap. For the upper chamber, $\kappa^{(\text{T})}_{j,N}$ can be converted into $\kappa^{(\text{S})}_{j,N}$, as both are directly related through the adiabatic index γ (Fleming, 2025). The following paragraphs provide a more detailed description of this procedure.

First, 22 isothermal compressibility values at typical pressure and temperature conditions observed in the experiments were determined outside of the model using Equation 19, which numerically approximates the isothermal compressibility from the compressibility factor (Dehli et al., 2023; Heintz, 2017). The required compressibility factors were obtained from Wischnewski (2007).

$$\kappa^{(\mathrm{T})} = \frac{1}{P_Z} - \frac{1}{Z}\left(\frac{\Delta Z}{\Delta P_Z}\right)_T \tag{19}$$

$\kappa^{(\mathrm{T})}$ Isothermal compressibility of nitrogen at pressure P_Z and temperature T [Pa^{-1}]

P_Z Pressure at which the compressibility is calculated [Pa]

Z Compressibility factor of nitrogen at the pressure P_Z and temperature T at which the compressibility is calculated [-]

ΔZ Change in compressibility factor of nitrogen corresponding to ΔP_Z [-]

ΔP_Z Pressure difference over which ΔZ is determined [Pa]

Within the small temperature range of the measurements, the temperature dependence of $\kappa^{(\mathrm{T})}$ is minor, while the pressure dependence dominates (see Section 3.3.5). Therefore, a function describing $\kappa^{(\mathrm{T})}_{j,i}$ at different pressures was derived from the 16 compressibility values[23] using a linear regression based on pressure alone. This approach was further justified by the uncertainty regarding the temperature in the gap and yielded a coefficient of determination of 0.998.

The resulting Equation 20 is used in the model to estimate $\kappa^{(\mathrm{T})}_{j,i}$ for all segments, while Equation 21 is subsequently applied to determine $\kappa^{(\mathrm{S})}_{j,N}$ specifically for the upper chamber. The adiabatic index γ is approximated according to Equation 22 (Çengel et al., 2019, ch. 7.9).

$$\kappa^{(\mathrm{T})}_{j,i} = -2.973239 \cdot 10^{-9}\,\mathrm{bar}^{-1}\,\mathrm{Pa}^{-1} \cdot P_{j-1,i} + 3.42476357 \cdot 10^{-7}\,\mathrm{Pa}^{-1} \tag{20}$$

$$\kappa^{(\mathrm{S})}_{j,N} = \frac{\kappa^{(\mathrm{T})}_{j,N}}{\gamma} \tag{21}$$

$$\gamma = \frac{c_\mathrm{p}}{c_\mathrm{v}} \tag{22}$$

$P_{j-1,i}$ Pressure in segment i at the end of time step $j-1$ and thus at the beginning of time step j [bar]

$\kappa^{(\mathrm{T})}_{j,i}$ Isothermal compressibility of the gas in segment i and time step j [Pa^{-1}]

[23] The compressibility values were determined at pressures between 55 bar and 62 bar, with temperatures at either 60 °C or 70 °C.

$\kappa_{j,N}^{(S)}$ Isentropic compressibility of the gas in segment N (the upper chamber) and time step j [Pa^{-1}]

γ Adiabatic index, heat capacity ratio of the gas [-]

c_p Heat capacity of the gas at constant pressure [J/(kg·K)]

c_v Heat capacity of the gas at constant volume [J/(kg·K)]

Following the calculation of pressure differences according to Equations 16 - 18, the pressure in segment i at the end of time step j is determined in the model using Equation 23. However, $P'_{j,N}$, the pressure in the upper chamber, cannot be fully determined at this stage, as it also depends on thermal effects (see Section 3.1). Consequently, Equation 23 is only applied for indices i ranging from 1 to $N-1$, which represent the annular gap where thermal effects are neglected. $P'_{j,N}$ is calculated separately at a later stage using Equation 35, which accounts for the pressure increase due to gas flow (Equation 18) as well as the pressure increase due to heat flow from the steel of the upper chamber to the gas within. Modeling the heat transfer requires considering several thermal effects, whose numerical implementation is described in the following sections.

$$P'_{j,i} = P'_{j-1,i} + \Delta P'^{\,\text{inflow}}_{j,i} - \Delta P'^{\,\text{outflow}}_{j,i} \tag{23}$$

$P'_{j,i}$ Normalized pressure in segment i at the end of time step j, after the gas flows $\dot{V}_{j,i}$ and $\dot{V}_{j,i+1}$ have concluded [-]

$P'_{j-1,i}$ Normalized pressure in segment i at the end of time step $j-1$, and thus at the beginning of time step j [-]

$\Delta P'^{\,\text{inflow}}_{j,i}$ Normalized pressure change in segment i due to gas flow from segment/grid point $i-1$ to i at time step j [-]

$\Delta P'^{\,\text{outflow}}_{j,i}$ Normalized pressure change in segment i due to gas flow from segment/grid point i to $i+1$ at time step j [-]

3.2.2 Thermal effects

The Hagen–Poiseuille flow and the resulting pressure changes are calculated for both the upper chamber and the annular gap. In contrast, thermal effects are treated differently. It is assumed that within the gap, the gas temperature equilibrates immediately with the surrounding materials (see Sections 3.1 and 3.3.4). Consequently, temperatures and temperature-related pressure changes are only calculated for the upper chamber.

Ideally, both temperature and pressure values before and after the gas release would be available for accurate temperature modeling. However, the temperature data recorded after the gas release cannot be interpreted quantitatively, as the relatively large thermal mass of the temperature sensor allows accurate temperature tracking only during slow

processes. For rapid gas temperature changes in the upper chamber, such as the decrease during gas release or the increase caused by the heating of the surrounding steel, the sensor response is too slow to capture the actual gas temperature. To compensate for this limitation, the temperature $T_{\min}$ of the gas in the upper chamber immediately after the gas release is estimated using the temperature-pressure relationship shown in Equation 24 (Çengel et al., 2019, ch. 7.9), assuming isentropic expansion (Figure 5).

$$T_{\min} = T_{\max} \left(\frac{P_{\max}}{P_{\min}} \right)^{\frac{1-\gamma}{\gamma}} \tag{24}$$

$T_{\min}$	Calculated temperature in the upper chamber immediately after gas release [K]
$T_{\max}$	Measured temperature in the upper chamber before the gas release [K]
$P_{\min}$	Measured pressure in the upper chamber immediately after gas release [Pa]
$P_{\max}$	Measured pressure in the upper chamber before gas release [Pa]
γ	Adiabatic index, (Equation 22), heat capacity ratio of the gas [-]

The temperature values following $T_{\min}$ are also necessary to model the temperature influence on the pressure curve. As the temperature sensor could not capture rapid temperature changes accurately, recorded temperature data during the heating process are not used in the model as they are considered highly incorrect. Instead, the temperature evolution in the upper chamber is modeled using fundamental thermodynamic principles. However, the temperature readings show a small dip shortly after gas release, confirming qualitatively that a short-term temperature decrease followed by an increase occurs after gas release.

To model the temperature evolution in the upper chamber, a factor that characterizes the rate of heat transfer from the steel to the gas over time was derived from experimental pressure data. The procedure is briefly outlined below in steps I-IV and described in more detail afterwards. To ensure methodological transparency and clarity, selected intermediate results and brief explanatory remarks are included in this section.

I **Derive temperatures from pressure changes:** During gas release, the remaining gas in the upper chamber cooled due to adiabatic expansion. Subsequently, heat flow occured from the warmer cement and steel to the gas inside the upper chamber. Experiments were identified where, due to low volumetric flow rates, the gas in the upper chamber was nearly fully heated by the surrounding steel before any substantial gas flow occurred. In other words, the amount of substance in the upper chamber stayed nearly constant during this short time span, while the pressure increase was almost exclusively caused by heat flow. This condition is met in ten experiments,

which allow the heating process caused by the temperature difference between steel and gas to be observed in near isolation. In these cases, pressure changes can be directly converted into temperature changes, resulting in ten temperature-time curves.

II **Derive heat transfer factor:** From each of these ten temperature curves, a factor c characterizing the rate of heat transfer from steel to gas over time was derived.

III **Transfer to other experiments:** Since the procedure described above was performed only for the ten experiments with low volumetric flow rates, c-values for experiments with higher flow rates were estimated based on the results.

IV **Transfer to model:** Steps I-III were performed as preparatory steps and are not part of the main model. Within the model, the heating of the gas caused by the warmer surrounding steel is simulated using the c-values derived in step III.

As described in step I, experiments were first identified in which the early measured pressure increase occurs almost exclusively due to the heat transfer from the steel to the gas, while the influence of gas flow is negligible. However, in most experiments, the pressure increase results from an overlap of these two processes, making it difficult to separate their individual contributions. Nevertheless, in experiments with low gas flow rates due to low permeabilities and thus generally slow pressure increases, a steep initial rise is observed (Figure 8a), which reaches a plateau after approximately 100–200 seconds (Figure 8b). This early plateau suggests that the initial steep pressure increase (e.g., up to 0.4 in Figure 8) is almost exclusively caused by heat flow from the surrounding steel to the gas, while the subsequent increase (from 0.4 to 1.0) is mainly attributed to gas flow into the upper chamber.

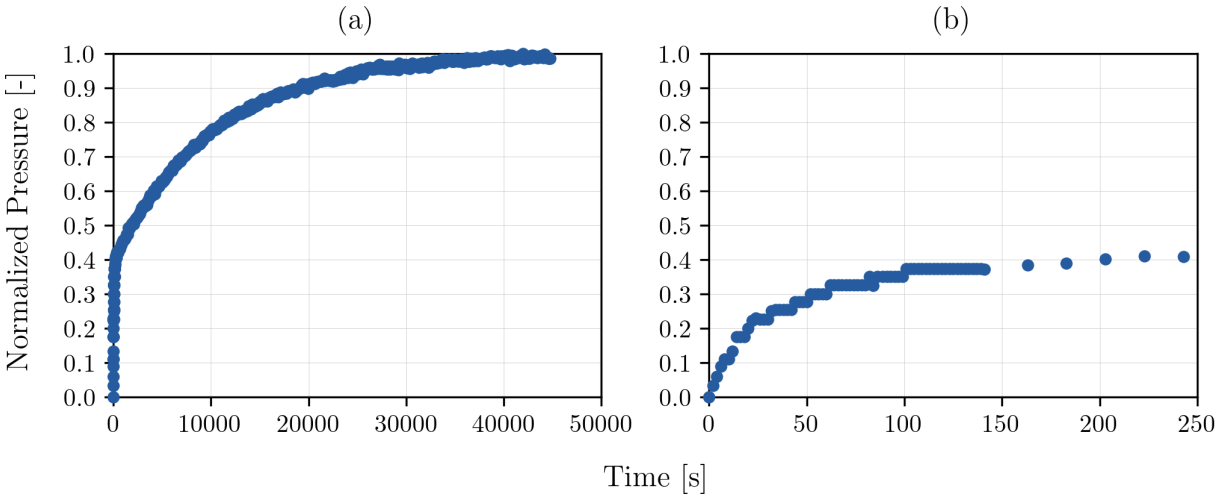


Figure 8: Measured and normalized experimental pressure data for Casing 3, Experiment 4: In (a), the entire runtime is shown. In (b), only the first 250 seconds are shown and a plateau is reached after approximately 150 seconds.

This behavior was observed in the first four experiments of casing 4, the first four experiments of casing 3, and experiments 8 and 10 of casing 1. For these ten experiments with low gas flow rates, the pressure induced temperature curve was derived according to Equation 25 (Çengel et al., 2019, ch. 3.6), which converts each pressure value during the initial steep increase into a temperature value under the assumption of isochoric conditions.

The time steps m used in Equation 25 differ from the time steps j used in the model, as the measured pressure data of Equation 25 use a different temporal resolution than the modeled data. The calculation begins at $m = 1$. Note that Equation 25 can only be applied if the measured pressure increase in the upper chamber is solely caused by heat transfer from the surrounding steel to the gas, with negligible influence from gas flow.

$$T_m = T_{m-1} \cdot \frac{P_m}{P_{m-1}} \tag{25}$$

T_m Calculated temperature in the upper chamber at time step m [K]; $T_0 = T_{\min}$

P_m Measured pressure in the upper chamber at time step m [Pa]; $P_0 = P_{\min}$

For each of the resulting ten calculated temperature curves, a factor was derived that characterizes the rate of heat transfer from the steel to the gas over time (step II). It is assumed that the temperature evolution of the gas heated by the surrounding steel follows a bounded growth behavior according to Equation 26 (Kreyszig et al., 2011). For each of the ten temperature curves derived from Equation 25, the parameters a and b were determined from the experimental data. Subsequently, a modeled curve based on Equation 26 was adjusted to best approximate each calculated curve from Equation 25, using c as the fitting parameter. The result was a c-value for each of the ten calculated curves. In this context, c represents the growth rate constant and thus determines the rate of thermal exchange between the steel of the upper chamber and the gas inside. Within the scope of this thesis, it is therefore interpreted as a heat transfer factor.

$$T(t) = a - b \cdot e^{-c \cdot t} \tag{26}$$

$T(t)$ Temperature in the upper chamber at time t [K]

a Maximum temperature that can be reached during the heating process as $t \to \infty$ [K]; equals the temperature before the gas release ($T_{\max}$) and after the full heating process is completed

b Difference between the temperatures immediately before and after gas release, defined as $b = a - T(0) = T_{\max} - T_{\min}$ [K]

c Growth rate constant/heat transfer factor [1/s]

t Time that has passed since $T(0) = T_{0,N} = T_{\min}$ at $t = 0$ s was reached [s]

Since c-values were derived for only ten of the 256 experiments so far, an approach was developed to estimate the missing c-values for the remaining 246 experiments (step III) based on the following assumptions. The parameter c reflects the rate of thermal exchange between the steel and the gas in the upper chamber. It is therefore assumed that c primarily depends on the geometry and volume of the upper chamber. The chamber itself remained unchanged. However, variations in cement filling height and the placement of additional material in the upper chamber caused differences in upper chamber volume and geometry between casings[24]. As long as the geometry of the upper chamber remains constant, c is assumed to be approximately constant as well.

Based on these considerations, the following procedure was used to determine a fixed c-value for each casing:

Casings where c could be directly derived from experiments

- **Casing 1:** Two experiments (8 and 10) exhibited low enough gas flow rates so that c-values could be derived from the initial pressure increase as described above. The arithmetic mean of these three c-values was used as the representative c-value for all experiments of casing 1, assuming c primarily depends on the upper chamber geometry.
- **Casing 3:** The same procedure as for casing 1 was applied (based on four experiments instead of two), resulting in one representative c-value for all experiments of casing 3.
- **Casing 4:** The same procedure as for casing 1 was applied (based on four experiments instead of two), resulting in one representative c-value for all experiments of casing 4.

  A cuboidal cement sample was placed in the upper chamber during this experimental series. This likely introduced additional heat flow from the cement sample to the gas. Consequently, the c-values of casing 4 are not directly comparable to the c-values of the other casings.

Casings where c could not be directly derived from experiments

- **Casing 2:** None of the experiments exhibited a sufficiently low volumetric flow rate to separate the pressure increase caused by heating from the pressure increase due to gas inflow. Consequently, no c-value could be derived directly for casing 2.

[24] In this context, a *casing* refers to the experimental series conducted on the casing, where experiments generally share identical geometries. For readability, the term is occasionally shortened to simply *casing* throughout the text, even though it technically denotes the experimental series.

To derive a representative c-value for casing 2, a regression-based approach was applied. The six c-values obtained from experiments with steep initial pressure increases in casings 1 and 3 were correlated with their respective upper chamber volumes, whereas casing 4 was excluded because of the cuboidal cement sample placed in the upper chamber during this experimental series. Assuming a linear dependence of c on the upper chamber volume, a linear regression was performed based on these six data pairs, each consisting of c-value and chamber volume (Figure 9). The resulting Equation 27 expresses c as a function of the upper chamber volume and was used to derive a single c-value for casing 2.

– **Casing 0:** As with casing 2, none of the experiments exhibited slow gas flow. Therefore, c was calculated analogously using Equation 27. However, a pipe connected to the upper chamber was replaced during the experimental series of casing 0. Consequently, the chamber volume changed, resulting in two slightly different c-values for the experiments of casing 0.

$$c = -0.00121\,\mathrm{s^{-1}\,L^{-1}} \cdot V_{\mathrm{uc}} + 0.036\,\mathrm{s^{-1}} \tag{27}$$

c Growth rate constant of the bounded growth equation (Equation 26); controls the rate at which heat is exchanged between the steel of the upper chamber and the gas inside and can therefore be regarded as a heat transfer factor [1/s]

V_{uc} Volume of the upper chamber, including the top volume of the casing not occupied by cement and adjacent pipes [L]

The c-values derived according to the described methods and used in the model are shown in Table 4 and Figure 9.

Table 4: Upper chamber volumes and c-values used in the model. The c-value of casing 4 is relatively high due to an additional cement sample placed in the upper chamber, which appears to enhance heat transfer to the gas. Two values are listed for Casing 0 because a pipe was exchanged during this experimental series, which caused a change in volume.

Casing	Volume [L]	c-value [1/s]
Casing 1	6.4554	0.0282[a]
Casing 3	5.9590	0.0288[a]
Casing 4	4.8650	0.0424[a]
Casing 0α	5.0605	0.0299[b]
Casing 0β	4.8382	0.0302[b]
Casing 2	4.9290	0.0300[b]

[a] c-values of casing 1, 3 and 4 were derived from experimental data.
[b] c-values of casing 0 and 2 were derived from Equation 27.

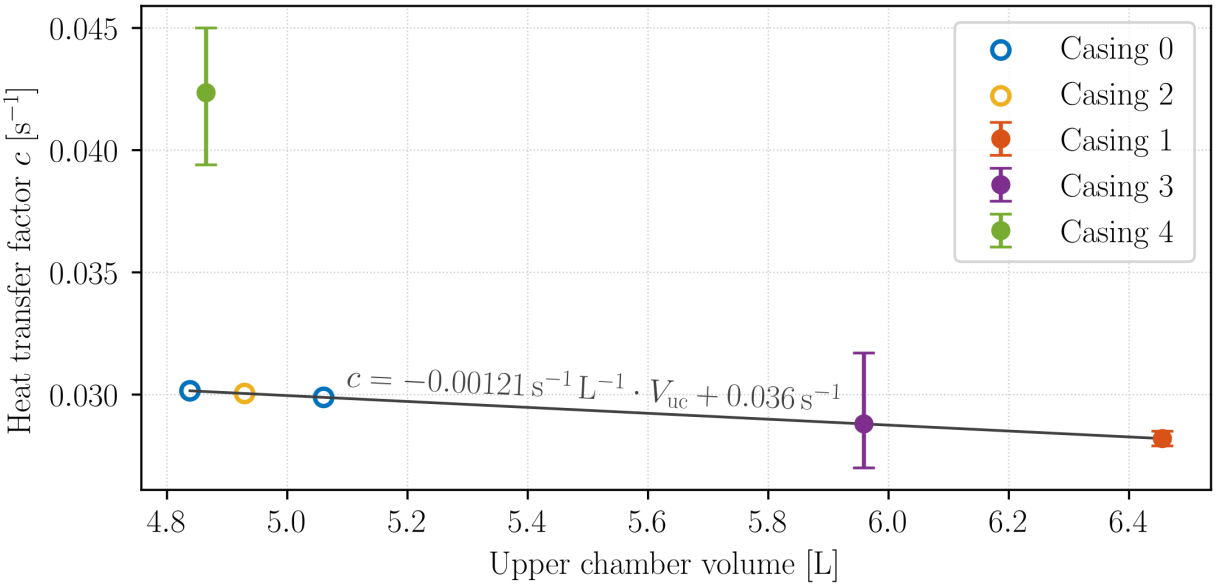


Figure 9: The six c-values used in the model are plotted against the volume of the upper chamber (V_{uc}). Filled symbols indicate values representing the arithmetic mean of multiple values originally derived from experimental data. The error bars denote the range of values used to calculate the mean. Open symbols indicate c-values calculated using Equation 27, based on c-values of casings 1 and 3. A cuboidal cement sample was placed in the upper chamber during the experimental series of casing 4, making the resulting c-values not directly comparable to those of the other casings.

While the previous paragraphs described how the c-values were determined outside of the model, the following paragraphs explain how c is incorporated into the internal model calculations (Step IV).

In principle, the temperature evolution for each experiment could be calculated using Equation 26, since the parameters a, b, and c are known. However, the stepwise temperature calculation within the numerical model is based on Equation 28. Although both equations produce identical temperature curves when the temperature in the upper chamber only depends on heat transfer between steel and gas, Equation 28 provides greater flexibility for incorporating additional thermal effects, such as temperature changes induced by gas flow into the upper chamber.

Equation 28 is advantageous because the temperature evolution depends on the temperature difference (Equation 29) rather than on time. The discrete heat transfer factor k is derived directly from the continuous heat transfer factor c and additionally accounts for the time step width Δt (Equation 30).

$$T_{j,N}^{\mathrm{warm}} = T_{j-1,N} + \Delta T_{j,N} \cdot k \tag{28}$$

$$\Delta T_{j,N} = T_{max} - T_{j-1,N} \tag{29}$$

$$k = 1 - e^{-c \cdot \Delta t} \tag{30}$$

$T_{j,N}^{\text{warm}}$ Gas temperature in the upper chamber (segment N) at time step j, accounting for heat flow from steel to gas during time step j. The temperature change caused by the gas flow at time step j is not included [K]

$T_{j-1,N}$ Gas temperature in the upper chamber at the end of time step $j-1$ and thus at the beginning of time step j, calculated according to Equation 36 [K]; $T_{0,N} = T_{\min}$

$\Delta T_{j,N}$ Difference between the saturation temperature $T_{\max}$ and the last modeled temperature $T_{j-1,N}$; decreases with increasing j [K]

k Discrete heat transfer factor based on c and Δt [-]

$T_{\max}$ Measured temperature in the upper chamber before the gas release [K]

c Growth rate constant of the bounded growth equation (Equation 26); controls the rate at which heat is exchanged between the steel of the upper chamber and the gas inside and can therefore be regarded as a continuous heat transfer factor [1/s]

Δt Time step width used in the model [s]; e.g., 0.02 s

The discrete heat transfer factor k describes the fraction of the remaining temperature difference that is transferred in a single time step Δt and can be derived as follows. If the bounded temperature growth (Equation 26) is expressed as

$$T_{j,N}^{\text{warm}} = a - b \cdot e^{-c\,t_j}, \quad t_j = j \cdot \Delta t,$$

the temperature change between two successive time steps is

$$T_{j,N}^{\text{warm}} - T_{j-1,N}^{\text{warm}} = (a - T_{j-1,N}^{\text{warm}}) \left(1 - e^{-c\,\Delta t}\right).$$

Comparing this with the following formulation derived from Equation 28,

$$T_{j,N}^{\text{warm}} = T_{j-1,N}^{\text{warm}} + (T_{\max} - T_{j-1,N}^{\text{warm}}) \cdot k,$$

and considering $a = T_{\max}$, it follows directly that

$$k = 1 - e^{-c\,\Delta t}.$$

The calculated temperature from Equation 28 is subsequently used to derive a corresponding pressure value using Equation 31, which is a modification of Equation 25. The resulting pressure value, $P_{j,N}^{\text{warm}}$, is then normalized according to Equation 12 and the corresponding normalized pressure change, $\Delta P'^{\text{warm}}_{j,N}$, is calculated according to Equation 32.

$$P_{j,N}^{\text{warm}} = \frac{T_{j,N}^{\text{warm}}}{T_{j-1,N}} \cdot P_{j-1,N} \tag{31}$$

$$\Delta P'^{\text{warm}}_{j,N} = P'^{\text{warm}}_{j,N} - P'_{j-1,N} \tag{32}$$

$P_{j,N}^{\text{warm}}$ Pressure in the upper chamber at time step j, including the pressure increase from heating at time step j, but not the pressure increase due to gas flow from the lower chamber at time step j [Pa]; the difference between $P_{j,N}^{\text{warm}}$ and $P_{j-1,N}$ is solely caused by the heating of the gas due to the warmer surrounding material; $P_{0,N}^{\text{warm}} = P_{\min}$

$T_{j,N}^{\text{warm}}$ Gas temperature at time step j, accounting for heating by the chamber steel during time step j. The temperature change caused by gas flow at time step j is not included. [K]

$T_{j-1,N}$ Gas temperature in the upper chamber at the end of time step $j-1$ and thus at the beginning of time step j [K]; $T_{0,N} = T_{\min}$

$P_{j-1,N}$ Pressure in the upper chamber at the end of time step $j-1$ and thus at the beginning of time step j [Pa]; $P_{0,N} = P_{\min}$

$\Delta P'^{\text{warm}}_{j,N}$ Normalized pressure increase in the upper chamber due to heat flow from steel to gas at time step j [-]

$P'^{\text{warm}}_{j,N}$ Normalized value of $P_{j,N}^{\text{warm}}$ [-]; $P'^{\text{warm}}_{0,N} = 0$

$P'_{j-1,N}$ Normalized pressure in the upper chamber at the end of time step $j-1$ and thus at the beginning of time step j [-]; $P_{0,N} = 0$

In the next step, the temperature in the upper chamber, attributed to the pressure change caused by gas flow during time step j, is determined according to Equation 33, assuming isentropic conditions within time step j (Çengel et al., 2019, ch. 7.9). Subsequently, the temperature change due to the pressure change resulting from gas flow during time step j, $\Delta T_{j,N}^{\text{flow}}$, is calculated according to Equation 34.

$$T_{j,N}^{\text{flow}} = T_{j-1,N} \cdot \left(\frac{P_{j-1,N}}{P_{j-1,N} + \Delta P_{j,N}^{\text{inflow}}} \right)^{\frac{1-\gamma}{\gamma}} \tag{33}$$

$$\Delta T_{j,N}^{\text{flow}} = T_{j,N}^{\text{flow}} - T_{j-1,N} \tag{34}$$

$T_{j,N}^{\text{flow}}$ Temperature in the upper chamber at time step j, including the temperature increase from gas flow at time step j, but not the temperature increase due to heat flow from steel to gas at time step j [K]; $T_{0,N}^{\text{flow}} = T_{\min}$

$T_{j-1,N}$ Gas temperature in the upper chamber at the end of time step $j-1$ and thus at the beginning of time step j [K]; $T_{0,N} = T_{\min}$

$P_{j-1,N}$ Pressure in the upper chamber at the end of time step $j-1$ and thus at the beginning of time step j [Pa]; $P_{0,N} = P_{\min}$

$\Delta P_{j,N}^{\text{inflow}}$ Pressure increase in the upper chamber solely due to $\dot{V}_{j,N}$, the gas flow from segment/grid point $N-1$ into the upper chamber at time step j [Pa]; see Equation 18 for normalized form

γ Adiabatic index according to Equation 22; heat capacity ratio of the gas [-]

$\Delta T_{j,N}^{\text{flow}}$ Temperature increase in the upper chamber at time step j, caused by gas flow into the chamber and the resulting pressure increase [K]

As the concluding step at the end of each time step j, the pressure $P'_{j,N}$ and temperature $T_{j,N}$ in the upper chamber are determined according to Equations 35 and 36. These equations account for the effects of gas and heat flow on both pressure and temperature in the upper chamber. All calculations are then repeated for the next time step.

$$P'_{j,N} = P'_{j-1,N} + \Delta P'^{\text{inflow}}_{j,N} + \Delta P'^{\text{warm}}_{j,N} \tag{35}$$

$P'_{j,N}$ Normalized pressure in the upper chamber at the end of time step j, including both heat flow and gas flow shares [-]

$\Delta P'^{\text{inflow}}_{j,N}$ Normalized pressure increase in the upper chamber due to gas inflow from the annular gap at time step j [-]

$\Delta P'^{\text{warm}}_{j,N}$ Normalized pressure increase in the upper chamber due to heat flow from steel to gas at time step j [-]

$$T_{j,N} = T_{j,N}^{\text{warm}} + \Delta T_{j,N}^{\text{flow}} \tag{36}$$

$T_{j,N}$ Temperature in the upper chamber at the end of time step j, including both heat flow and gas flow shares [K]

$T_{j,N}^{\text{warm}}$ Temperature at time step j, accounting for heat flow from steel to gas during time step j. The temperature change caused by the gas flow at time step j is not included [K]

$\Delta T_{j,N}^{\text{flow}}$ Temperature increase in the upper chamber at time step j, caused by gas flow into the chamber and the resulting pressure increase [K]

The code implementing the algorithm described above is provided in Appendix A.

3.2.3 Matrix permeability

Based on the previous calculations, a matrix permeability value $K_{\text{Darcy}}^{\text{model}}$ is derived in the model. This value represents the matrix permeability the sample would exhibit if gas flow occurred through the cement, either through the pore space or cracks, rather than through the annular gap. To determine the matrix permeability, the volumetric flow rate expressions from Hagen–Poiseuille (Bruus, 2008; Equation 10) and Darcy's law (Darcy, 1856; Wyckoff et al., 1933; Equation 37) were equated and rearranged to solve for $K_{\text{Darcy}}^{\text{model}}$. The resulting Equation 38 is used to derive matrix permeabilities from the model, which are intended to be compared to the measured matrix permeabilities of the initial, autoclave and control cement samples (see Section 2.5).

$$\dot{V} = \frac{K_{\text{Darcy}}^{\text{model}} \cdot A \cdot \Delta P_{\text{cas}}}{\eta \cdot l} \tag{37}$$

$\dot{V}$	Volumetric flow rate [m^3/s]
$K_{\text{Darcy}}^{\text{model}}$	Matrix permeability of the cement [m^2]
A	Base area of the cement column [m^2]
ΔP_{cas}	Pressure difference between both ends of the cement column [Pa]
η	Dynamic viscosity of the gas [$Pa \cdot s$]
l	Length of the cement column inside the casing [m]

$$K_{\text{Darcy}}^{\text{model}} = \frac{K_{\text{HP}} \cdot h^3 \cdot w}{12 \cdot \pi \cdot r^2} \tag{38}$$

$K_{\text{Darcy}}^{\text{model}}$	Modeled equivalent matrix permeability assuming only cross-sectional flow [m^2]
K_{HP}	Shape factor accounting for the channel geometry, close to 1 [-]
h	Aperture of the annular gap [m]
w	Width of the annular gap [m]
r	Inner radius of the casing [m]

3.2.4 Automated models

The model described in Sections 3.2.1–3.2.3 serves as a foundation for three different automated models. These automated models vary fitting parameter values within certain bounds to minimize the quadratic difference between the measured and modeled pressures. The first automated model, H, uses only the aperture of the annular gap, h, as a fitting parameter. In model H, h is allowed to vary between 1 µm and 100 µm, while c is set according to Table 4.

The second model, HC, uses both h and the heat transfer factor c (Equation 30) as fitting parameters. The factor c is used instead of k because k depends solely on c and Δt. By varying c, Δt can be set independently, while the change in c is still reflected in k. In model HC, h is allowed to vary between 1 µm and 100 µm, while c is allowed to vary between 0.001 s^{-1} and 0.25 s^{-1}.

The third model, HP, uses h, $P_{\min}$, and $P_{\max}$ as fitting parameters, with h allowed to vary between 1 µm and 100 µm, and c set according to Table 4. In contrast to the other models, $P_{\min}$ and $P_{\max}$ influence the normalized measured pressure data rather than the modeled data, as all measured pressure values are normalized based on $P_{\min}$ and $P_{\max}$ (Equation 12). Consequently, a decrease in $P_{\max}$ leads to a decrease in the normalized measured pressures, while a decrease in $P_{\min}$ results in an increase.

Optimization of $P_{\max}$ in model HP

$P_{\max}$ was selected as a fitting parameter to improve robustness against outliers, as the normalization process defines $P_{\max}$ based on a single measured value. If one of the pressure values recorded after the main pressure increase exhibits an anomalously high outlier, the normalization would be dominated by that outlier (Figure 10a). Allowing the model to adjust $P_{\max}$ counteracts this effect (Figure 10b): The model decreases $P_{\max}$ by $\Delta P_{\max}$, which is limited to the absolute value corresponding to a normalized value of 0.025. Consequently, the lower bound for shifting $P_{\max}$ in model HP is defined as

$$P_{\max}^{\text{lower}} = P_{\max}^{\text{original}} - 0.025 \cdot (P_{\max}^{\text{original}} - P_{\min}^{\text{original}}),$$

where $P_{\max}^{\text{original}}$ is the original measured maximum pressure value during the experiment, and $P_{\min}^{\text{original}}$ is the corresponding minimum. The upper bound of $P_{\max}$ equals $P_{\max}^{\text{original}}$.

In models H and HC, the adjustment of $P_{\max}$ is approximated by upscaling all measured pressure values by 1% after the normalization.

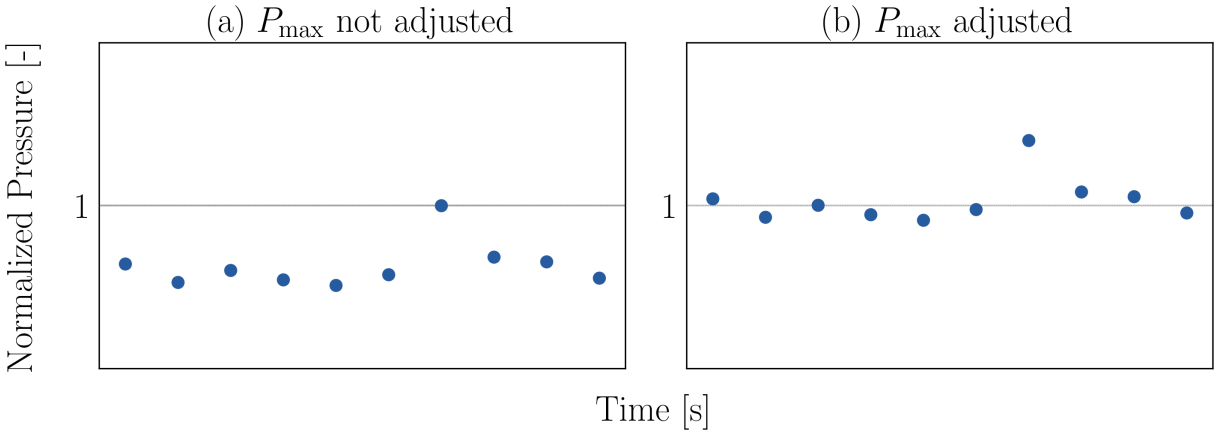


Figure 10: Effect of adjusting P_{max} to reduce the influence of outliers during normalization. This figure shows an idealized example of pressure values after the main pressure increase has concluded and is not based on real data. (a) Normalization dominated by an outlier; (b) optimal adjustment in model HP by shifting P_{max}, so that the normalization is not dominated by the outlier.

Optimization of P_{min} in model HP

P_{min} is used as a fitting parameter because the 2-second recording frequency is insufficient to ensure that the true minimum pressure is captured precisely. The actual minimum pressure may occur at any time between two measurements. Consequently, the recorded minimum pressure may already fall within the subsequent pressure increase and therefore exceed the true minimum pressure. In the worst case, the true minimum pressure might be missed by nearly two seconds. Depending on the experiment, 2 seconds can be sufficient for a significant normalized pressure increase of 0.1 or more. By treating P_{min} as a fitting parameter, the model can attempt to account for this effect.

However, if the measured minimum pressure fails to capture the true minimum pressure, the discrepancy would not only involve pressure but also time. The offsets of P_{min} in pressure and time are not independent but intrinsically linked, as a lower pressure corresponds to an earlier time along the pressure evolution curve. To account for this relationship, the model uses the first 20 measured pressure values of each experiment to derive a continuous pressure–time function by regression, using $P(t) = a - b \cdot e^{-c \cdot t}$ as the regression model. This bounded growth function is based on Equation 26, but describes pressure $P(t)$ instead of temperature $T(t)$. When the model adjusts P_{min}, the corresponding time associated with P_{min} is adjusted simultaneously according to this regression function.

In other words, treating P_{min} as a free fitting parameter allows the model to shift the starting point (P_{min} and its associated time) along the pressure–time regression curve within the constraints described below. This shift can improve the agreement between measured and modeled pressure data. Two different scenarios are implemented for model HP, each using a distinct regression approach:

(a) **The measured $P_{\mathbf{min}}$ lies within the pressure-increase phase:** This is the more common scenario, illustrated in Figure 11. In this case, the measured value of P_{min} can be regarded as a valid measurement, though not necessarily the absolute minimum. The measured P_{min} is therefore included in the regression as the origin of the bounded growth function. In the fitting algorithm, P_{min} is varied freely between the following bounds, until the best agreement between measured and modeled pressure data is reached.

As the true P_{min} corresponds to a lower pressure at an earlier time (compared to the measured P_{min}) in scenario (a), the upper bound for varying P_{min} is defined by the measured P_{min}. The lower bound is the pressure calculated using the regression curve at $t = -2\,\text{s}$. To avoid unrealistic bounds in cases of steep regression curves, the model additionally compares the lower bound to the originally measured P_{min}. If this difference exceeds 0.05 (normalized), the model adjusts the lower bound to limit the difference to 0.05.

With each variation of P_{min}, the starting time is also adjusted according to the regression curve. However, rather than shifting the newly modeled P_{min} to a negative time, all measured pressure values are shifted forward in time.

Figure 11 illustrates case (a). In this example, the model estimates a P_{min} significantly lower than the measured value, with a pressure difference of 0.17 bar. Consequently, the regression function applies the maximum time offset of 2 s, positioning the modeled P_{min} at $t = -2\,\text{s}$ with the the measured P_{min} still at $t = 0\,\text{s}$. However, while the regression in Figure 11a depicts this shift from measured to modeled P_{min} backward in time for the original dataset, the actual model uses the modeled P_{min} as starting point at $t = 0\,\text{s}$ (shifted dataset). Accordingly, all measured pressure values are shifted forward by 2 s in the depicted experiment, rather than shifting the modeled starting point backward. Furthermore, all normalized pressure values increase due to the lower P_{min}, as P_{min} affects the normalization.

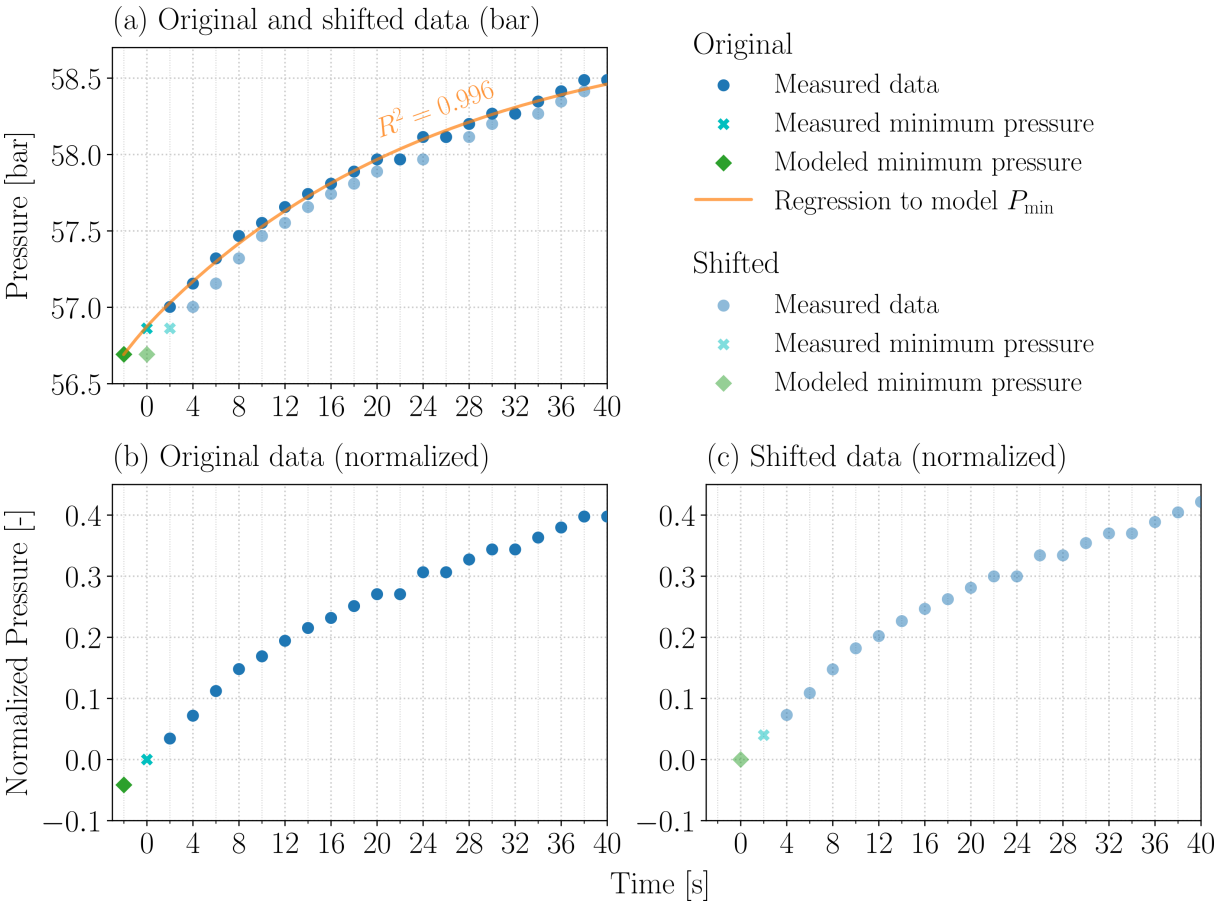


Figure 11: Effect of model HP determining a new $P_{\min}$ on the pressure data. For the depicted Experiment 1 of casing 2, the measured $P_{\min}$ lies within the pressure-increase phase. *Shifted* denotes the dataset after the adjustments in time and pressure performed by model HP, whereas *original* refers to the unshifted dataset. The *modeled minimum pressure* is the value of $P_{\min}$ for which model HP determined the best agreement between measured and modeled pressure data. The green point labeled as *modeled minimum pressure* therefore represents the new starting point of experiment 1, in both pressure and time.
(a) Comparison of original and shifted pressure data (not normalized).
(b) Normalized original dataset, with the modeled minimum pressure occurring at negative values of time and pressure.
(c) Normalized shifted dataset. Due to the new $P_{\min}$, all data are shifted in pressure (Equation 12) and time. The measured minimum pressure is still considered part of the pressure-increase phase.

(b) **The measured $P_{\min}$ lies within the final phase of the gas release:** This less common scenario (illustrated in Figure 12) occurs only when a pressure P_α is recorded near the end of the gas release, when the pressure is already close to the true minimum. If the pressure increase following the gas release is rapid enough that the next recorded value P_β exceeds P_α, P_α is registered as the measured $P_{\min}$.

In this case, the measured $P_{\min}$ cannot be considered part of the pressure-increase phase. The measured $P_{\min}$ is therefore excluded from the regression and not con-

sidered a measured pressure in the fitting algorithm.[25] Analogously to scenario (a), the fitting algorithm varies P_{min} freely between the following bounds, until the best agreement between measured and modeled pressure data is reached.

In scenario (b), the true P_{min} occurs at a lower pressure and at a later time compared to the measured P_{min}. Thus, the upper bound for varying P_{min} is defined by either the measured P_{min} or the pressure at $t = 1\,\text{s}$ on the regression curve, depending on which is lower. A 1-second interval was chosen because the pressure drop typically occurs more rapidly than the subsequent increase and the recording frequency is 2 seconds. Thus, if the remaining pressure drop after the measured P_{min} spans 1 second, the subsequent increase would require at least that amount of time - likely more - to rise above the measured value. Otherwise, the measured P_{min} would fall within the pressure-increase phase.

The lower bound for varying P_{min} is defined as the pressure derived from the regression curve at $t = 0\,\text{s}$. As case (b) applies to only 10 of the 256 experiments, restricting the lower bound of P_{min} by a normalized pressure difference of 0.05 was not necessary, as all shifted P_{min}-values remained within a realistic range.

With each variation of P_{min}, the starting time is also adjusted according to the regression curve. However, rather than shifting the newly modeled P_{min} forward in time, all measured pressure values are shifted backward in time.

Case (b) is illustrated in Figure 12. In this example, the model estimates a P_{min} 0.7 bar below the measured P_{min} and applies the maximum time offset of 1 s. Consequently, the modeled P_{min} is placed at $t = 1\,\text{s}$ with the the measured P_{min} still at $t = 0\,\text{s}$. However, while the regression in Figure 12a depicts this shift from measured to modeled P_{min} forward in time for the original dataset, the actual model uses the modeled P_{min} as starting point at $t = 0\,\text{s}$ (shifted dataset). Accordingly, all measured pressure values are shifted backward by 1 s in the depicted experiment, rather than shifting the modeled starting point forward. The measured P_{min} is removed from the shifted data, as it does not lie within the pressure-increase phase. Furthermore, all normalized pressure values increase due to the lower P_{min}, as P_{min} affects the normalization. The limitations of these methods are discussed in Section 5.3.3.

[25] In the algorithm, measured pressure values are compared to modeled pressure values to quantify the agreement between measured and modeled values, as explained in more detail later in this subsection. In scenario (b), the measured P_{min} is omitted from this comparison because it belongs to the gas release phase, whereas the model only considers the pressure-increase phase.

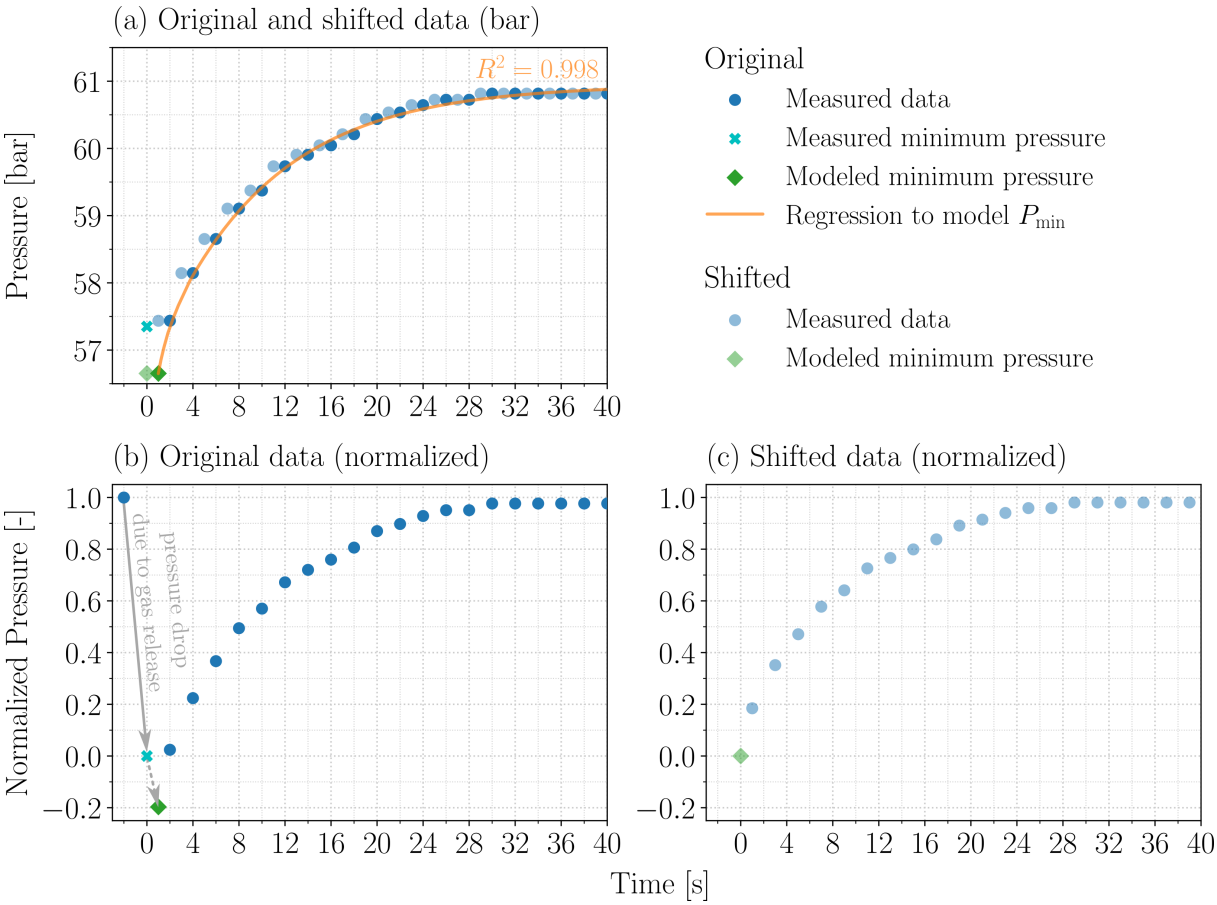


Figure 12: Effect of model HP determining a new P_{min} on the pressure data. For the depicted Experiment 58 of casing 2, the measured P_{min} lies within the final phase of gas release. *Shifted* denotes the dataset after the adjustments in time and pressure performed by model HP, whereas *original* refers to the unshifted dataset. The *modeled minimum pressure* is the value of P_{min} for which model HP determined the best agreement between measured and modeled pressure data. The green point labeled as *modeled minimum pressure* therefore represents the new starting point of experiment 58, in both pressure and time.
(a) Comparison of original and shifted pressure data (not normalized).
(b) Normalized original dataset, with an arrow indicating that the measured minimum pressure lies within the gas-release phase.
(c) Normalized shifted dataset. Due to the new P_{min}, all data are shifted in pressure (Equation 12) and time. The measured minimum pressure is not considered part of the pressure-increase phase and therefore not shown.

Error minimization

All models minimize the difference between the modeled and measured pressure in the form of the weighted root mean square error (WRMSE), as defined in Equation 39 (e.g., Chai and Draxler, 2014). The weighted RMSE was chosen over the regular RMSE to account for the merging of data points and variations in the recording frequency. Weighting factors w_m were assigned to each measured pressure data point based on the timespan it represents. For example, if the interval between consecutive measurements is 2 seconds, each data point is assumed to represent half of this interval before and after the measurement, resulting in

a total span of 2 seconds and a weighting factor of 2. If a merged value represents 10 such points, covering a timespan of 20 seconds, the corresponding weighting factor is 20.

$$\mathrm{WRMSE} = \sqrt{\frac{\sum_{m=1}^{M} w_m \cdot (y_m - \hat{y}_m)^2}{\sum_{m=1}^{M} w_m}} \tag{39}$$

WRMSE	Weighted root mean square error [-]
y_m	True (measured) normalized pressure in the upper chamber at time step m [-]
$\hat{y}_m$	Predicted (modeled) normalized pressure in the upper chamber at time step m [-]
M	Total number of time steps m [-]
w_m	Weight assigned to time step m [-]

Since the integer time values associated with time steps m of the measured data do not typically correspond exactly to floating-point time values associated with time steps j of the modeled data, an interpolated modeled pressure $\hat{y}_m$ is assigned to each measured pressure y_m in all three automated models. This is achieved by identifying the two modeled pressure values closest in time to y_m and interpolating between them to determine $\hat{y}_m$, ensuring that values are compared at the same point in time.

The same minimization methods from `scipy.optimize` are used in all three model versions (H, HC and HP) to automatically minimize the WRMSE. First, the `differential_evolution` method according to Storn and Price (1997) is used to approximately locate the global minimum of the WRMSE. The resulting fitting parameter value(s) at this minimum serve as initial guesses for the `L-BFGS-B` algorithm (Limited-memory Broyden–Fletcher–Goldfarb–Shanno with Bounds), which performs a refined local optimization (e.g., Byrd et al., 1995; Zhu et al., 1997). The motivation for this two-stage optimization strategy, combining global and local minimization, is discussed in Section 5.3.3 (page 137 ff.).

3.3 Sensitivity analysis

3.3.1 Overview

In the following sections, a sensitivity analysis of several model parameters and settings is presented. The goal is to identify the parameters and model settings that strongly affect the modeling results and to quantitatively assess their impact. For example, if the model is sensitive to a parameter that depends on pressure, it may be necessary to calculate this parameter separately for each time step and segment at the corresponding pressure, rather

than using a single fixed value for the entire experiment. The sensitivity analysis therefore provides the rationale for several modeling decisions described in Section 3.2.

All sensitivity analyses were carried out using model H, which only employs the annular gap aperture h as a fitting parameter and was also used to generate the main modeling results in Section 4.1.2. Two different types of representations are used throughout the sensitivity analysis for illustrative purposes:

1. Figures presenting pressure curves from generic modeled experiments. These simulations only use minimum and maximum pressures, initial temperatures, c-values, and lower chamber pressures from real experiments. In these cases, no fitting procedure is applied and the simulations are performed using a fixed modeled gap aperture h. Variations in the investigated parameters can therefore be visualized and compared through changes in the modeled pressure evolution curves.

2. Tables present modeling results based on the non-generic, measured dataset of experiments, for which the gap aperture h is treated as a variable fitting parameter. This corresponds to the regular modeling procedure described in Section 3.2, with the investigated parameters varied between individual model runs. In these cases, variations in the investigated parameters have a negligible effect on the shape of the modeled pressure curves, but instead influence the modeled value of h required to provide the closest approximation to the experimental data.

3.3.2 Influence of the number of segments and time step width

While a discretization into finite segments and time steps is necessary for the model, it introduces an error due to the more continuous nature of real processes. To assess this error, model runs with different segment counts[26] $(N + 1)$ and time step widths Δt were performed. While an arbitrarily fine discretization would in principle be possible, it would come at the cost of substantially increased computation time. Therefore, the aim was to choose a discretization that achieves the lowest possible computation time without significantly altering the pressure evolution curves and gap apertures compared to results from much finer resolutions.

With increasing values of N, the central portions of the pressure curves shift upward at fixed gap apertures h (Figure 13), indicating an increase in volumetric flow rate. As a result, models yield lower values of h for higher values of N. Since a higher number of segments should better approximate the more continuous reality, larger values of N are expected to be more accurate. Under this assumption, h tends to be overestimated for low values of N. Generally, differences between results decrease with increasing values

[26] N = Number of flow intervals, $N + 1$ = number of segments (see Section 3.2)

of N. For example, the discrepancy between $N = 2$ and $N = 4$ is more pronounced than between $N = 32$ and $N = 64$ (Figure 13). The results at $N = 32$ are considered sufficiently accurate, provided that the temporal discretization is sufficiently fine as well.

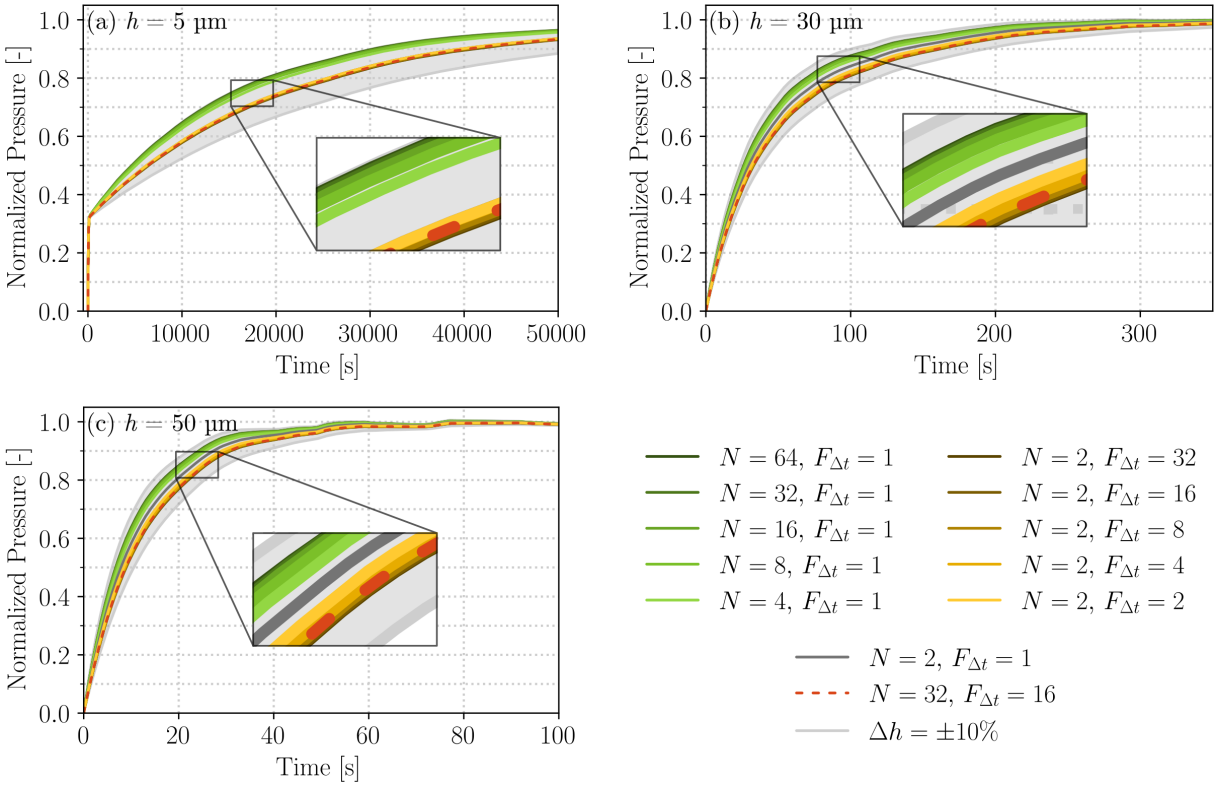


Figure 13: Modeled pressure development in the upper chamber for different interval counts N and time step scaling factors $F_{\Delta t}$. The experimental data provide the minimum and maximum pressures, initial temperatures, c-value, and the pressure in the lower chamber used as boundary and initial conditions for the model. Results are based on experiment 10 (a) and experiments 33 (b, c) of casing 1 with fixed annular gap apertures. As a reference, two curves with a 10% increase and decrease in the annular gap aperture are shown ($\Delta h = \pm 10\%$).

The influence of the temporal discretization is therefore examined by varying the time step width Δt, which is controlled by the time step scaling factor $F_{\Delta t}$ and decreases as $F_{\Delta t}$ increases (Equation 13). Smaller time steps are generally expected to provide a better approximation of the underlying processes, which are more continuous in reality.

Compared to increasing N, increasing values of $F_{\Delta t}$ have the opposite effect: the central portions of the pressure curves shift downward (Figure 13). Consequently, the modeled gap aperture h increases with increasing values of $F_{\Delta t}$. This implies that h is underestimated for low values of $F_{\Delta t}$. Similar to N, the difference between results decreases as $F_{\Delta t}$ increases. Thus, the results at $F_{\Delta t} = 16$ are considered sufficiently accurate, provided that the spatial discretization is sufficiently fine as well ($N = 32$). For small values of h (Figure 13a), the results for different values of $F_{\Delta t}$ are grouped closer than for larger values of h (Figure 13b,c).

However, when high values are chosen for both N and $F_{\Delta t}$, the resulting pressure curves are predominantly controlled by the time step width, with the influence of N becoming comparatively small. In other words, at sufficiently small time steps, further increases in the number of segments only marginally affect the curve position.

As a consequence, and generally because the numerical effects of increasing N and increasing $F_{\Delta t}$ act in opposite directions, an appropriate combination of segment count and time step width can be selected that yields results almost equivalent to those obtained with much finer discretizations, but at significantly reduced computational cost. As illustrated in Figure 13, the curves at $N = 32$ and $F_{\Delta t} = 16$ are nearly identical to those obtained with $N = 2$ and $F_{\Delta t} = 8$. Therefore, $N = 2$ and $F_{\Delta t} = 8$ were chosen for the final model runs to improve computational efficiency without a significant loss of accuracy.

3.3.3 Influence of the gap width

The width w of the annular gap is assumed to extend halfway around the circular interface between steel and cement (Figure 4). However, the actual circumferential extent w of the annular gap may differ from this assumption. The purpose of this section is to assess the sensitivity of the modeled annular gap aperture h to variations in the assumed gap width w.

It is important to note that the numerical model does not resolve the true three-dimensional geometry of the gap, but instead operates with an effective (or apparent) gap geometry that reproduces the observed pressure increase in the upper chamber. As a consequence, the assumed gap width w and the modeled gap aperture h are not independent parameters. For a given volumetric flow rate and unchanged gas properties, any change in the assumed gap width must be compensated by a corresponding change in the gap aperture (Equation 15). Due to the cubic dependence of the volumetric flow rate on the gap aperture, variations in the assumed gap width w require only relatively small adjustments of h to maintain the same flow rate. In other words, if the actual gap extends over a larger fraction of the circumference than assumed, the modeled aperture h would be slightly smaller.

Using Equation 40, which is derived from the Hagen–Poiseuille equation (Equation 15), the change in h can be determined for different assumptions of w. To describe the fraction of the full perimeter that the annular gap extends around, a scaling factor v is introduced. For example, $v = 0.9$ represents a gap width that extends around 90% of the circumference of the steel-cement interface. The ratio of two v-values, v_1/v_2, expresses the relative change in gap width, which is the only input needed for determining the corresponding percentage change in h.

$$\Delta h = \left(\left(\frac{v_1}{v_2} \right)^{-1/3} - 1 \right) \cdot 100 \tag{40}$$

Δh Percentage change in the annular gap aperture h when comparing two different gap widths represented by v_1 and v_2 [%]

v_1, v_2 Scaling factors representing the fraction of the perimeter occupied by the annular gap [-]; For example, with $v_1 = 0.9$ and $v_2 = 0.5$, the equation quantifies how h changes when increasing the gap width from 50% to 90%.

Table 5 summarizes values of Δh determined according to Equation 40 for different values of v_1 and v_2. Regarding the numerical model, v_2 represents the true value of v, while v_1 is the assumed value used in the model. Overall, the choice of v_1 has a considerable impact on the result. However, using $v_1 = 0.5$ in the model provides a common basis for comparing results and limits the potential error in h to $\pm 27\%$, provided the actual effective value of v_2 lies between 0.2 and 1. For smaller values of v_2, the error increases.

Table 5: Percentage change in annular gap aperture Δh for different gap width scaling factors v according to Equation 40

$v_2[-]$	Δh [%]	
	for $v_1 = 0.5$	for $v_1 = 1$
1.0	26.0	0.0
0.9	21.6	-3.5
0.8	17.0	-7.2
0.7	11.9	-11.2
0.6	6.3	-15.7
0.5	0.0	-20.6
0.4	-7.2	-26.3
0.3	-15.7	-33.1
0.2	-26.3	-41.5
0.1	-41.5	-53.6
0.05	-53.6	-63.2

It should be noted that changing the assumed gap width w (and the corresponding modeled aperture h) also alters the geometry and volume of the annular gap. In principle, this could affect the pressure evolution, as the pressure change within the gap depends on the segment volume (Equations 16 and 17). Deviations from the prediction of Equation 40 and Table 5 could therefore be expected.

However, model runs with different values of w (i.e., different scaling factors v) yielded the same changes in h as those predicted by Equation 40. This indicates that, for the investigated parameter range, the influence of the gap volume on the modeled pressure

evolution is negligible. Consequently, Equation 40 provides a robust approximation of the influence of the assumed gap width w on the modeled annular gap aperture h for the parameter range and modeling approach applied here.

3.3.4 Temperature of the flowing gas

Although the model already accounts for several thermal effects, the temperature of the gas entering the upper chamber may additionally influence the modeled pressure evolution and, consequently, the inferred annular gap aperture h. This section therefore evaluates the sensitivity of the modeled gap aperture to assumptions regarding the temperature of the gas entering the upper chamber. The working hypothesis is that the temperature of the inflowing gas does not significantly affect the results and can therefore be assumed to be equal to the temperature of the resident gas.

If the temperature of the inflowing gas differs from that of the gas already present in the upper chamber, both the temperature and pressure in the chamber are affected by mixing between the inflowing and resident gases. In this section, the term *mixing* refers to the spatial intermingling of the inflowing gas with the resident gas in the upper chamber and the subsequent establishment of a common equilibrium temperature due to heat exchange between them. Several approaches for estimating the temperature of the inflowing gas were implemented, and their influence on the modeled results was quantified. The applied calculation methods and their implications are summarized below.

Within the numerical model, the temperature of the gas flowing through the annular gap is determined at the moment it enters the upper chamber. Subsequently, the temperature change in the upper chamber due to mixing of the inflowing gas with the resident gas is determined. This mixing step accounts exclusively for temperature differences between the two gas volumes. Other temperature changes, such as those resulting from pressure variations or heat transfer through the chamber walls, are determined separately as described in Section 3.2 (page 45 ff.).

Since the temperature of the gas flowing through the gap cannot be measured directly and depends on various unknown factors, three limiting scenarios are considered to bound the physically plausible range:

(a) **Immediate heat exchange:** In this scenario, the temperature of gas flowing through the annular gap is assumed to equilibrate instantaneously with the temperature of the surrounding materials, i.e., casing and cement. This assumption is justified by the small gas volume within the gap, the large surface-to-volume ratio, and the moderate flow velocities, all of which promote rapid heat transfer. Furthermore, the casing and cement adjacent to the upper chamber are assumed to have approximately the same temperature as the gas already present in the upper chamber. Consequently,

the inflowing gas enters the upper chamber at essentially the same temperature as the resident gas, and no temperature difference occurs during mixing.

(b) **No heat exchange:** In this scenario, heat exchange between the gas and its surroundings is neglected entirely. The gas therefore enters the annular gap at the temperature of the lower chamber and subsequently undergoes temperature changes exclusively due to expansion associated with the pressure decrease along the flow path. Two alternative formulations were used to quantify this expansion-induced cooling. The Joule-Thomson effect (i) provides a limiting case for irreversible adiabatic expansion with entropy increase. As a complementary extreme, reversible adiabatic (isentropic) expansion of an ideal gas is considered in case (ii).

(i) **Joule-Thomson effect:** The temperature decrease of the flowing gas due to expansion is modeled according to the Joule-Thomson effect, as described by Equation 41 (Joule and Thomson, 1852; Maytal and Pfotenhauer, 2013). The resulting, typically negative, temperature difference $\Delta T_{j,N}^{\text{gap}}$ is then added to the temperature of the lower chamber to determine the temperature of the flowing gas. The required Joule-Thomson coefficient μ_{J} is determined at each time step based on the current pressure and temperature conditions using the Peng-Robinson Equation of State (Peng and Robinson, 1976). In this approach, the annular gap is idealized as a single throttling element, which is most likely inaccurate. Nevertheless, the Joule-Thomson effect is applied to estimate expansion-induced cooling under extreme assumptions.

$$\Delta T_{j,N}^{\text{gap}} = \mu_{\text{J}} \cdot (P_{j-1,N} - P_{j-1,0}) \tag{41}$$

$\Delta T_{j,N}^{\text{gap}}$ Temperature difference between the gas entering the upper chamber from the gap and the gas already present in the upper chamber at the moment of mixing during time step j [K]

μ_{J} Joule-Thomson coefficient: The rate of temperature change with respect to pressure during a throttling process at constant enthalpy [K/Pa]

$P_{j-1,N}$ Pressure in the upper chamber at the beginning of time step j [Pa]

$P_{j-1,0}$ Pressure in the lower chamber at the beginning of time step j [Pa]

(ii) **Isentropic cooling:** Additionally, the temperature evolution of the flowing gas is determined assuming isentropic expansion. To achieve this, Equation 33, which is normally used to calculate the gas temperature evolution in the upper chamber, is applied analogously to each individual segment of the annular gap. Consequently, the temperature evolution of the flowing gas could be resolved along the entire flow path.

(c) **Constant temperature difference:** In this purely hypothetical scenario, a constant temperature difference ΔT^{gap} between the inflowing gas and the resident gas in the upper chamber is assumed throughout the simulation. This approach was used to evaluate the sensitivity of the model to unrealistically large temperature differences and thereby establish an upper bound for the influence of temperature uncertainty.

After determining the temperature of the inflowing gas, the temperature in the upper chamber after mixing is determined at each time step using a pressure-weighted arithmetic mean. Specifically, the temperature of the inflowing gas is weighted by the pressure increase caused by the inflow, while the temperature of the resident gas is weighted by the chamber pressure prior to inflow. The resulting mixed temperature[27] is then used to determine the corresponding pressure change under isochoric conditions using Equation 25, rearranged for pressure and applied at each time step j (modeled data) instead of m (measured data). These temperature- and pressure-related contributions are subsequently combined with all other thermal and flow-related effects described in Section 3.2. Results for constant temperature differences are shown in Figure 14.

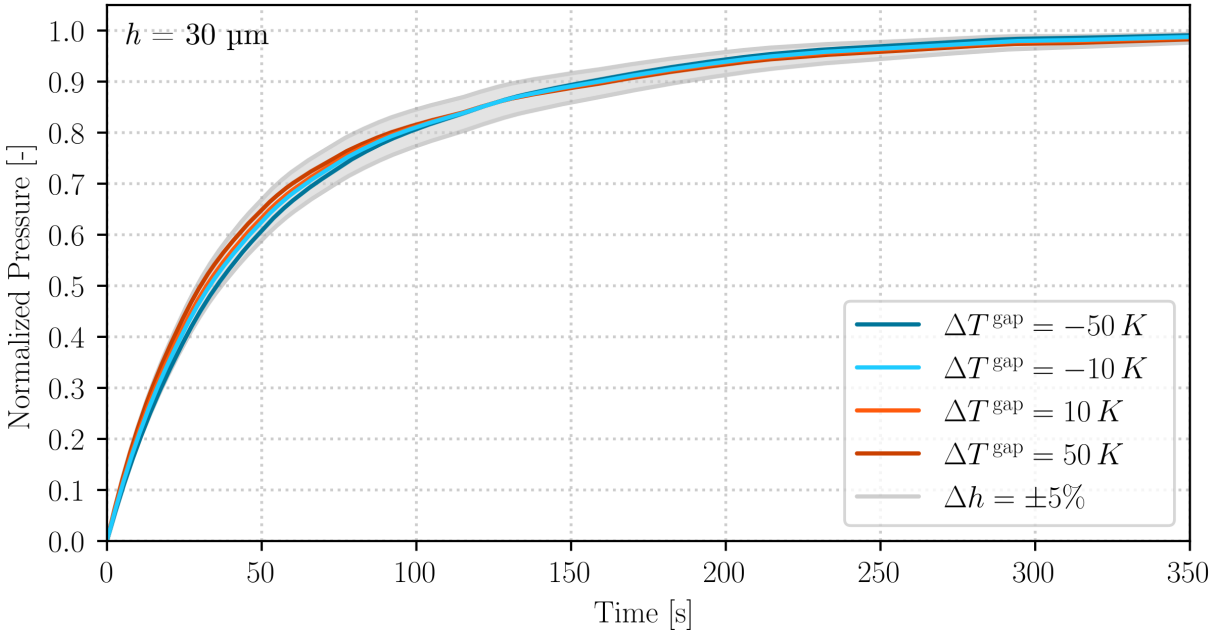


Figure 14: Modeled pressure development in the upper chamber for four extreme values of ΔT^{gap}, the constant temperature difference between the gas entering the upper chamber from the gap and the gas already present in the upper chamber at the moment the two gas volumes mix, based on experiment 33 of casing 1 with a constant annular gap aperture h of 30 µm. Similar behavior was observed for both smaller and larger apertures (Table 6). The experimental data provide the minimum and maximum pressures, initial temperature, c-value, and the pressure in the lower chamber used as boundary and initial conditions for the model. As a reference, two curves with a 5% increase and decrease in the annular gap aperture and no temperature difference are displayed ($\Delta h = \pm 5\%$).

[27] This mixing step accounts exclusively for the different temperatures of the two gas volumes. Other temperature changes, such as those caused by pressure changes due to the inflowing gas, are treated separately in the model according to Section 3.2, page 45 ff.

Overall, the influence of the inflowing gas temperature on the modeled pressure evolution is negligible unless unrealistically large temperature differences between inflowing and resident gas are imposed (Figure 14). Even for extreme temperature differences of ±10 K, the resulting pressure curves remain closely clustered. Consequently, the immediate heat exchange and no heat exchange scenarios yield nearly identical pressure curves and are therefore not shown separately. Likewise, the corresponding modeled gap apertures differ only marginally between the immediate heat exchange and no heat exchange scenario (Table 6), with average deviations on the order of 0.05%.

Given the negligible influence of gap temperature assumptions within realistic bounds and the physical plausibility of fast thermal equilibration, the immediate heat exchange scenario for the gas in the gap was selected for the generation of the results, assuming identical temperatures of the inflowing and resident gas. This assumption is supported by the small volume of the annular gap, the large contact area with surrounding materials, and the moderate flow velocities, all of which favor efficient heat transfer. Furthermore, the thermal mass (total heat capacity) of the surrounding steel and cement is substantially larger than that of the gas, such that any heat exchange is assumed to have a negligible effect on the steel and cement temperatures.

Table 6: Modeled annular gap apertures h obtained with model H under different assumptions for the temperature of the gas entering the upper chamber. *Cas.* denotes the casing number and *Exp.* the corresponding experiment number. h_{ref} denotes the reference gap aperture obtained with standard model H, assuming that the inflowing gas has the same temperature as the gas already present in the upper chamber (immediate heat exchange). For scenarios without heat exchange with the surroundings, *Joule–Thomson* assumes Joule–Thomson cooling of the gas during flow through the annular gap, while *Isentr. cool.* assumes isentropic expansion and cooling. The case $\Delta T = 2\,\mathrm{K}$ assumes that the inflowing gas is always 2 K warmer than the resident gas in the upper chamber. For each scenario, the modeled gap aperture h and the relative deviation $\Delta h = 100 \cdot (h - h_{\mathrm{ref}})/h_{\mathrm{ref}}$ are listed. The MAPE (Equation 56) corresponds to the arithmetic mean of $|\Delta h|$.

			Joule-Thomson		Isentr. cool.		$\Delta T = 2\,\mathrm{K}$	
Cas.	Exp.	h_{ref} [µm]	h [µm]	Δh [%]	h [µm]	Δh [%]	h [µm]	Δh [%]
0	2	23.00	23.00	-0.01	23.01	0.00	23.00	-0.03
0	28	30.71	30.71	-0.02	30.71	-0.02	30.71	-0.03
1	10	6.98	6.98	-0.05	6.98	-0.01	6.98	-0.04
1	17	14.13	14.13	-0.02	14.13	-0.02	14.13	0.01
1	18	21.43	21.43	0.00	21.43	0.02	21.43	0.00
1	33	31.14	31.14	-0.01	31.14	0.00	31.11	-0.12
2	3	38.10	38.07	-0.07	38.08	-0.05	38.07	-0.08
2	13	19.53	19.53	0.01	19.53	0.00	19.52	-0.02
2	23	42.01	41.97	-0.09	42.00	-0.02	41.96	-0.11
2	51	42.34	42.22	-0.27	42.29	-0.11	42.29	-0.11
3	8	13.75	13.76	0.07	13.75	0.03	13.75	0.05
4	14	28.14	28.16	0.06	28.16	0.09	28.15	0.04
MAPE [%]				0.06		0.03		0.05

3.3.5 Temperature and pressure dependence of input parameters

In the model, several parameters depend on pressure and temperature and would therefore, in principle, vary between time steps and along the discretized segments of the annular gap. However, treating these parameters as fixed values simplifies the model and reduces computational effort. It is therefore necessary to assess which pressure- and temperature-dependent parameters can be approximated as constants over the experimental pressure and temperature range without affecting the modeling results, and which parameters must be calculated at the pressure and temperature of each time step and segment.

To address this, a sensitivity analysis was performed for the following pressure- and temperature-dependent properties of nitrogen, using values taken from or calculated based on data from Wischnewski (2007):

(1) the heat capacity at constant pressure (c_p),

(2) the heat capacity at constant volume (c_v),

(3) the adiabatic index γ, calculated from c_p and c_v according to Equation 22,

(4) the dynamic viscosity η, and

(5) the compressibility[28] κ, calculated according to Equations 19 and 21.

For c_p, c_v, γ, η, and κ, values at 70 °C and 60 bar were initially used in the model, as pressure and temperature during the experiments typically fluctuate around these conditions. To evaluate the validity of this assumption, a sensitivity analysis was performed. Each parameter (c_p, c_v, γ, η, κ) was varied individually by using values at different pressure–temperature conditions, while the remaining four parameters were kept at their reference values (70 °C and 60 bar) and all other model settings (e.g., time step width Δt) were kept constant.

The maximum temperature and pressure in the upper chamber typically occur before an experiment is initiated by gas release, whereas the minimum values are reached immediately afterward. For this sensitivity analysis, 70 °C and 60 bar were chosen as the maximum conditions, while the minimum values were set to 60.6 °C and 55 bar, representing a pressure drop of 5 bar and thus a relatively large pressure and temperature variation. The parameter values at these two conditions are listed in Table 7.

[28]While Equation 19 approximates the isothermal compressibility $\kappa^{(\mathrm{T})}$ used within the gap, the corresponding isentropic compressibility $\kappa^{(\mathrm{S})}$ for the upper chamber can be obtained from $\kappa^{(\mathrm{T})}$ through the adiabatic index γ (Equation 21).

Table 7: Properties of nitrogen at different pressure (P) and temperature (T) conditions occurring during the experiments: heat capacities at constant pressure (c_p) and constant volume (c_v), adiabatic index (γ), dynamic viscosity η, isothermal compressibility $\kappa^{(\mathrm{T})}$, and isentropic compressibility $\kappa^{(\mathrm{S})}$. Values were taken from or calculated using data from Wischnewski (2007).

P [bar]	T [°C]	c_p $[\frac{\mathrm{kJ}}{\mathrm{kg \cdot K}}]$	c_v $[\frac{\mathrm{kJ}}{\mathrm{kg \cdot K}}]$	γ [-]	η [Pa · s]	$\kappa^{(\mathrm{T})}$ $[\frac{1}{\mathrm{Pa}}]$	$\kappa^{(\mathrm{S})}$ $[\frac{1}{\mathrm{Pa}}]$
60	70	1.1096	0.7544	1.4709	$2.07 \cdot 10^{-5}$	$1.639 \cdot 10^{-7}$	$1.114 \cdot 10^{-7}$
55	60.6	1.1084	0.7539	1.4703	$2.02 \cdot 10^{-5}$	$1.794 \cdot 10^{-7}$	$1.220 \cdot 10^{-7}$

Even between the maximum and minimum conditions (60 bar/70 °C and 55 bar/60.6 °C), the difference in heat capacities remains around 0.1%, while the resulting difference in the adiabatic index γ is below 0.04%. Consequently, the modeled annular gap apertures for both values of γ are almost identical (Table 8). As variations in c_p and c_v at the given temperature and pressure conditions have a negligible impact on the modeling results, constant values for c_p, c_v, and γ at 60 bar and 70 °C are used in the model.

Table 8: Modeled annular gap apertures h obtained with model H for parameters at different pressure and temperature conditions. *Cas.* denotes the casing number and *Exp.* the corresponding experiment number. $h_{60/70}$ denotes the reference gap aperture modeled with fixed values of γ (and thus c_p and c_v), η and κ at 60 bar and 70 °C. The subscript 55/60.6 indicates that the corresponding parameter is assigned its value at 55 bar and 60.6 °C, while the other parameters remain at 60 bar and 70 °C, analogous to Figure 15. κ refers to both $\kappa^{(\mathrm{T})}$ and $\kappa^{(\mathrm{S})}$. For each parameter variation, the modeled gap aperture h and the relative deviation $\Delta h = 100 \cdot (h - h_{60/70})/h_{60/70}$ are listed. The MAPE (Equation 56) corresponds to the arithmetic mean of $|\Delta h|$.

		Reference	$\gamma_{55/60.6}$		$\eta_{55/60.6}$		$\kappa_{55/60.6}$	
Cas.	Exp.	$h_{60/70}$ [µm]	h [µm]	Δh [%]	h [µm]	Δh [%]	h [µm]	Δh [%]
0	2	22.89	22.89	0.02	22.71	-0.75	23.59	3.05
0	28	30.61	30.61	0.02	30.38	-0.76	31.54	3.04
1	10	7.02	7.02	0.02	6.97	-0.73	7.24	3.09
1	17	14.07	14.08	0.01	13.96	-0.79	14.51	3.06
1	18	21.29	21.29	0.00	21.13	-0.75	21.94	3.06
1	33	30.81	30.82	0.04	30.58	-0.72	31.76	3.09
2	3	38.15	38.15	0.01	37.86	-0.76	39.32	3.07
2	13	19.58	19.58	0.02	19.43	-0.77	20.18	3.04
2	23	42.05	42.06	0.02	41.74	-0.73	43.35	3.08
2	51	41.98	41.99	0.02	41.66	-0.76	43.26	3.05
3	8	13.68	13.68	0.03	13.57	-0.75	14.09	3.07
4	14	27.97	27.98	0.01	27.76	-0.74	28.83	3.06
MAPE [%]				0.02		0.75		3.06

In contrast, using the compressibility values ($\kappa^{(\mathrm{T})}$ for the gap and $\kappa^{(\mathrm{S})}$ for the upper chamber) at minimum conditions results in a modeled gap aperture that is 3% smaller compared to calculations based on maximum-condition compressibilities (Table 8). Likewise, the

pressure curves corresponding to the compressibility at maximum and minimum conditions differ considerably for fixed gap apertures (Figure 15).

Therefore, $\kappa^{(T)}$ and $\kappa^{(S)}$ are not treated as constants in the final model. Instead, compressibilities are determined separately for each segment and time step according to Equations 20 and 21. Both compressibilities are primarily pressure-dependent under the experimental conditions, while their temperature dependence is minimal. For example, the isothermal compressibility determined according to Equation 19 differs by only 0.2% between 70 °C and 60.6 °C at constant 60 bar. Consequently, Equation 20 determines $\kappa^{(T)}$ solely as a function of pressure. Its applicability is therefore limited to the temperature range (60–70 °C) over which the regression was established.

With variable compressibilities according to Equation 20 and 21, the newly determined gap apertures deviate by an arithmetic mean of 0.5% from those obtained using fixed values of $\kappa^{(T)}$ and $\kappa^{(S)}$ at maximum conditions. This suggests that incorporating variable compressibilities eliminates an arithmetic mean error of approximately 0.5%. In these new simulations, the deviation is 0.5% instead of the 3% observed in the extreme scenario because the pressure and temperature in the upper chamber and gap increase over time, leading to a decrease in compressibility. This effect is not present in the extreme case calculations, where fixed maximum and minimum compressibility values were used. Additionally, pressure drops in real experiments are typically less than 5 bar, which reduces the deviation further.

Similarly, the variation of dynamic viscosity η leads to a slightly different pressure curve at minimum conditions compared to maximum conditions (Figure 15). The difference in the modeled gap apertures between both extreme scenarios remains below 1% (Table 8). However, the error due to assuming a constant viscosity is expected to be considerably smaller than the 1% deviation between the extreme cases. As pressures and temperatures increase over time, the difference between a fixed viscosity and a pressure- and temperature-dependent viscosity decreases. This would reduce the error caused by assuming a constant viscosity to less than 0.15%, assuming that the relative deviations between using a fixed viscosity at 60 bar/70 °C and using a variable viscosity are similar to the deviations observed for compressibility. In contrast to the compressibility, however, the viscosity depends not only on pressure but also on temperature. Since the temperature in gap segments can only be determined with relatively high uncertainty, and because a constant viscosity introduces a more negligible error than a constant compressibility, a fixed viscosity at 60 bar and 70 °C is used in the model. Although Figure 15 shows parameter-dependent curves only for an annular gap aperture of 30 µm, the same relative trends between the parameter variations are obtained for larger or smaller gap apertures as well (Table 8).

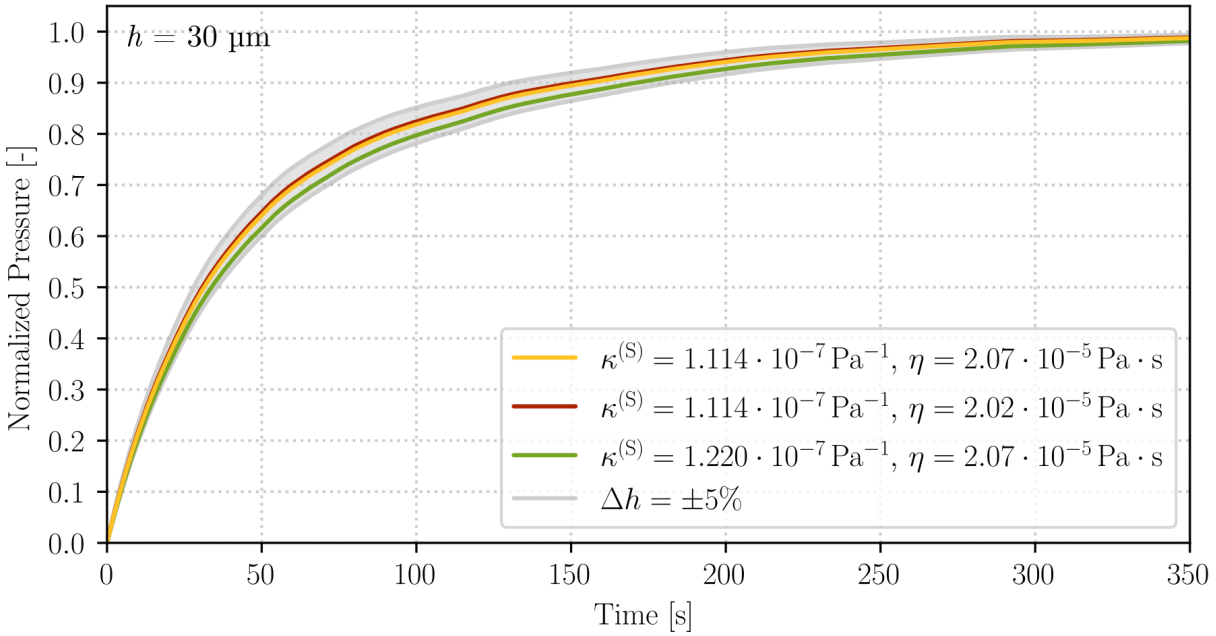


Figure 15: Modeled pressure development in the upper chamber for different parameter variations based on experiment 33 of casing 1 with a fixed annular gap aperture h of 30 µm. The experimental data provide the minimum and maximum pressures, initial temperature, c-value, and the pressure in the lower chamber used as boundary and initial conditions for the model. As a reference, two grey curves with a 5% increase and decrease in the annular gap aperture and all parameters at 60 bar and 70 °C are displayed ($\Delta h = \pm 5\%$). While the shown isentropic compressibility $\kappa^{(S)}$ was used in the upper chamber, the corresponding isothermal compressibility $\kappa^{(T)}$ at the same pressure and temperature (Table 7) was used in the gap. The yellow curve shows compressibility and viscosity at the reference conditions of 60 bar and 70 °C. The green curve shows the effect of varying compressibility (50 bar, 60.6 °C), while the red curve shows the effect of varying viscosity (50 bar, 60.6 °C).

Additionally, the isothermal compressibility $\kappa^{(T)}$ was determined using Equation 42 (Atkins and de Paula, 2006, p. 62)[29] instead of Equation 19 to assess potential differences between the results of these two equations. Both equations account for the non-ideal behavior of nitrogen at higher temperatures and pressures: Equation 19 achieves this by incorporating the compressibility factor Z, while Equation 42 uses real-gas densities according to Wischnewski (2007). The differences in $\kappa^{(T)}$ between Equation 19 and Equation 42 within the pressure and temperature range observed in the experiments range from 0.01% to 0.1%, making the choice of equation negligible.

[29] In Atkins and de Paula (2006, p. 62), the isothermal compressibility is defined as $\kappa^{(T)} = -\frac{1}{V}\left(\frac{\partial V}{\partial P}\right)_T$, with V = volume and P = pressure. Using the relation $\rho \propto 1/V$, where ρ is the density, this can be expressed as the discrete approximation given in Equation 42.

$$\kappa^{(\mathrm{T})} = \left(\frac{\rho_2 - \rho_1}{\frac{\rho_2+\rho_1}{2} \cdot \Delta P_\rho} \right)_T \tag{42}$$

$\kappa^{(\mathrm{T})}$ Isothermal compressibility of nitrogen at the mean pressure $\frac{P_{\rho 2}+P_{\rho 1}}{2}$ and constant temperature T [Pa^{-1}]

ρ_2 Density of nitrogen at pressure $P_{\rho 2}$ and temperature T [$\mathrm{g/cm^3}$]

ρ_1 Density of nitrogen at pressure $P_{\rho 1}$ and temperature T [$\mathrm{g/cm^3}$]

ΔP_ρ Pressure difference $P_{\rho 2} - P_{\rho 1}$ [Pa]

$P_{\rho 2}$ Pressure at which density ρ_2 was determined [Pa]

$P_{\rho 1}$ Pressure at which density ρ_1 was determined [Pa]

3.3.6 Heat transfer factor c

The heat transfer factor c (Equations 26 and 30) controls the rate of temperature increase due to heat transfer from the steel of the upper chamber to the gas within. Since values of c were derived from ten experiments and the model uses arithmetic means of these values, it carries inherent uncertainties. Similar uncertainties apply to model version HC, which treats c as a fitting parameter. To assess the impact on the results, c was varied within specific bounds: the minimum and maximum values derived from the ten experiments (0.025 s^{-1} and 0.045 s^{-1}), as well as the minimum and maximum values obtained when allowing model HC to vary c freely (0.001 s^{-1} and 0.14 s^{-1}).

The influence of c is most pronounced at the beginning of an experiment. In experiments with low gas flow rates and thus small modeled gap apertures h, most variations in c have little effect. An exception occurs only for extremely low values of c (0.001 s^{-1}), for which heat transfer from the steel is substantially delayed, which in turn delays the steep normalized pressure increase to approximately 0.3 at the beginning (Figure 16a). Since these extremely low values of c would introduce substantial WRMSE, model HC does not assign such low values of c in experiments with low gas flow rates.

In general, explicitly accounting for heat transfer from the steel to the gas is essential, particularly for experiments with low gas flow rates, as it is required to reproduce the initial steep pressure increase (Figure 16a). However, because heat transfer is largely completed within the first approximately 200 s (except for extremely low values of c), the exact value of c has only a minor influence on the pressure evolution in experiments with very low gas flow rates, where gas inflow into the upper chamber occurs on much longer timescales than the heat transfer.

In contrast, the influence of c is very strong during the first approximately 200 s of experiments with low gas flow rates, as only negligible gas inflow occurs over such short

time intervals in these experiments and therefore the pressure build-up is almost exclusively heat-flow controlled. While this does not affect the overall experiment, where the initial normalized pressure increase to 0.3 appears near-vertical (Figure 16a), it does justify deriving values of c from this initial steep pressure increase in suitable experiments.

In experiments with higher gas flow rates and thus generally faster pressure increases (Figure 16b,c), heat transfer from the steel to the gas temporally overlaps more strongly with gas inflow from the annular gap. As a result, the value of c has a more pronounced influence on the overall shape of the pressure and temperature curves in the upper chamber. This effect is particularly strong when heat transfer and gas inflow are completed on similar timescales, typically of approximately 200 s (Figure 16b), such that both processes overlap over most of the experiment duration.

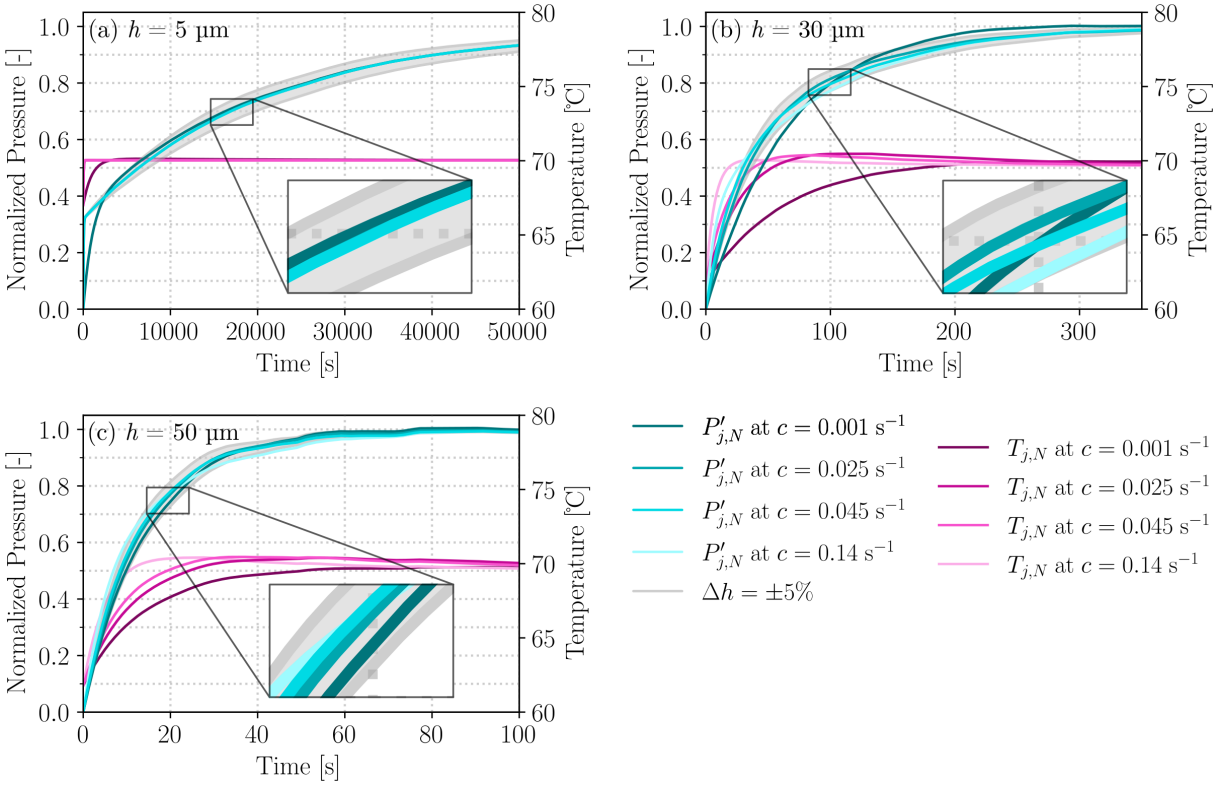


Figure 16: Modeled pressure and temperature development in the upper chamber for four values of the geometry parameter c, based on experiment 10 (a) and 33 (b, c) of casing 1 with fixed annular gap apertures h. The experimental data provide the minimum and maximum pressures, initial temperatures, and the pressure in the lower chamber used as boundary and initial conditions for the model. $P'_{j,N}$ denotes the normalized pressure in the upper chamber, while $T_{j,N}$ denotes the temperature in the upper chamber. As a reference, two curves with a 5% increase and decrease in the annular gap aperture at $c = 0.03$ s^{-1} are shown ($\Delta h = \pm 5\%$).

However, variations in c have only a limited impact on the main results of model H. Even the most extreme variations of c as determined by model HP (0.001 s^{-1} and 0.14 s^{-1}) primarily affect the inferred gap aperture h within a range of approximately ±5%. For the most widely separated values of c considered in model H ($c = 0.025$ s^{-1} and $c = 0.045$ s^{-1}),

the resulting curves remain relatively close to each other (Figure 16). Moreover, the arithmetic mean absolute difference in h between using $c = 0.025$ s^{-1} and $c = 0.045$ s^{-1}, calculated over all 256 experiments, is only 0.5% (0.1 µm). As these represent the most extreme values of c within model H, which is the primary model used for result generation, it can be concluded that the modeling results are only weakly sensitive to the value of c within the investigated parameter range.

Furthermore, model HC, treating c as a fitting parameter, requires an initial value for c. Similar to the initial gap aperture, earlier estimates of c were used as input values for the final model run, ensuring that the input is already close to the result. Likewise, the initial value of c has little effect on the final result. For example, the difference in h between model runs initialized with $c = 0.001$ s^{-1} and $c = 0.25$ s^{-1} is on the order of 0.02%.

3.3.7 Upper chamber volume

The volume V_{uc} of the upper chamber was determined based on a three-dimensional model of the autoclave. The cement height in the casing, additional sample material in the upper chamber, as well as pipes, sensors, and other attached components were incorporated into the calculation. However, particularly with the latter elements, minor uncertainties may have been introduced. To assess their impact, the influence of the upper chamber volume on the results was analyzed (Figure 17).

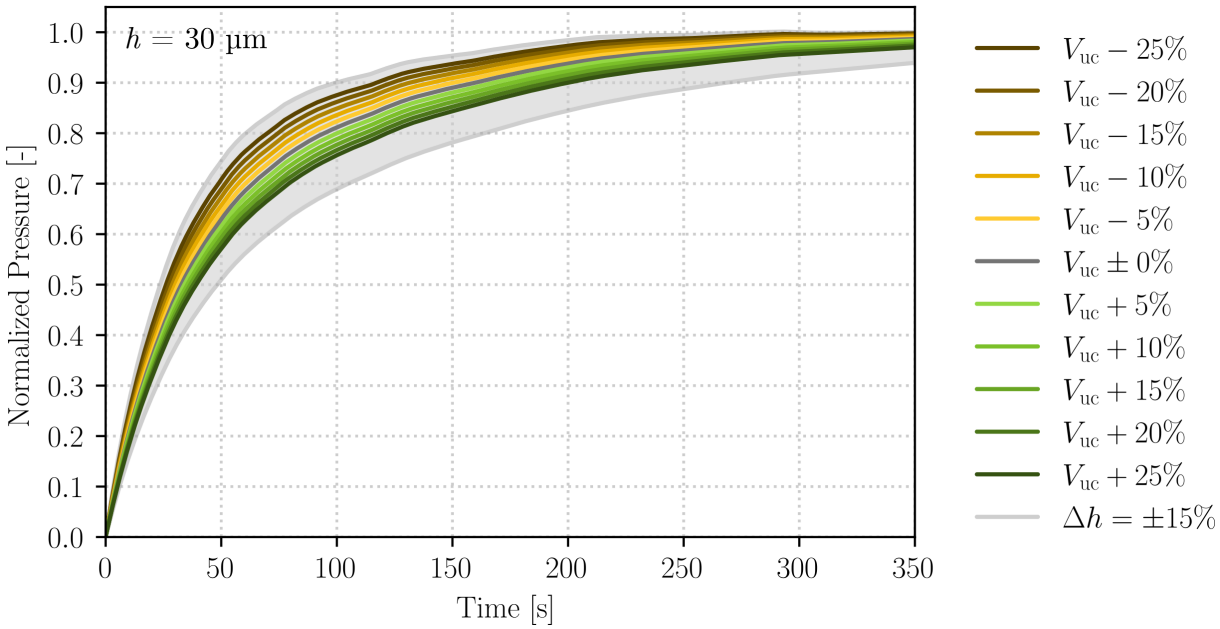


Figure 17: Modeled pressure development in the upper chamber for different volumes of the upper chamber (V_{uc}), based on experiment 33 of casing 1 with a fixed annular gap aperture h of 30 µm. The experimental data provide the minimum and maximum pressures, initial temperature, c-value, and the pressure in the lower chamber used as boundary and initial conditions for the model. For example, $V_{\text{uc}} + 10\%$ represents a 10% increase in V_{uc}. As a reference, two curves with a 15% increase and decrease in the annular gap aperture and no volume change are displayed ($\Delta h = \pm 15\%$).

In general, the volume considerably affects the modeled pressure curve at fixed annular gap apertures and, consequently, the modeled gap aperture h when h is treated as a variable fitting parameter. Varying V_{uc} by ±25% results in a maximum deviation of approximately 10% in h, which occurs when V_{uc} is underestimated by 25%. If V_{uc} is misestimated by 5%, the resulting error in h is on the order of 1.7% (Table 9). Thus, it cannot be ruled out that the assumed value of V_{uc} inherits an error that affects h.

However, the upper chamber volume is known with relatively high accuracy due to the precise manufacturing of the system. The main sources of uncertainty arise from the determination of the cement filling height in the casing and from the volume of connecting pipes, sensors and vents. Consequently, the resulting uncertainty in the estimated chamber volume is expected to be low. Furthermore, experiments on the same casing share the same value of V_{uc} and therefore exhibit the same systematic uncertainty, except for Casing 1, where a tube was exchanged during the experimental series. While Figure 17 presents modeled curves for an annular gap aperture of 30 µm, variations in V_{uc} lead to identical trends for larger or smaller gap apertures as well.

Nevertheless, these results highlight that the upper chamber volume is a critical parameter and should be determined with particular care, especially in cases where additional sample material is placed inside the chambers or where the effective volume is otherwise difficult to estimate.

Table 9: Modeled annular gap apertures h obtained with model H for different assumptions of the upper chamber volume V_{uc}. *Cas.* denotes the casing number and *Exp.* the corresponding experiment number. h_{ref} denotes the reference gap aperture determined without changes in V_{uc}. For each scenario, the modeled gap aperture h and the relative deviation $\Delta h = 100 \cdot (h - h_{\mathrm{ref}})/h_{\mathrm{ref}}$ are listed. The MAPE (Equation 56) corresponds to the arithmetic mean of $|\Delta h|$.

			$V_{\mathrm{uc}} - 1\%$		$V_{\mathrm{uc}} - 5\%$		$V_{\mathrm{uc}} + 1\%$		$V_{\mathrm{uc}} + 5\%$	
Cas.	Exp.	h_{ref} [µm]	h [µm]	Δh [%]	h [µm]	Δh [%]	h [µm]	Δh [%]	h [µm]	Δh [%]
0.00	2.00	23.00	22.93	-0.34	22.62	-1.69	23.08	0.33	23.38	1.64
0.00	28.00	30.71	30.62	-0.31	30.19	-1.69	30.82	0.34	31.22	1.66
1.00	10.00	6.98	6.95	-0.46	6.86	-1.74	7.00	0.29	7.10	1.65
1.00	17.00	14.13	14.08	-0.35	13.89	-1.70	14.18	0.35	14.36	1.62
1.00	18.00	21.43	21.35	-0.35	21.06	-1.71	21.50	0.33	21.78	1.64
1.00	33.00	31.14	31.03	-0.36	30.62	-1.69	31.24	0.31	31.65	1.63
2.00	3.00	38.10	37.97	-0.35	37.45	-1.71	38.22	0.32	38.72	1.63
2.00	13.00	19.53	19.46	-0.34	19.19	-1.71	19.59	0.34	19.85	1.64
2.00	23.00	42.01	41.86	-0.34	41.30	-1.68	42.15	0.35	42.69	1.64
2.00	51.00	42.34	42.20	-0.33	41.62	-1.70	42.48	0.33	43.03	1.64
3.00	8.00	13.75	13.70	-0.32	13.51	-1.68	13.79	0.36	13.97	1.64
4.00	14.00	28.14	28.05	-0.33	27.66	-1.70	28.24	0.34	28.60	1.64
MAPE [%]				0.35		1.70		0.33		1.64

4 Results

4.1 Cyclic loading experiments and gap modeling

4.1.1 Cement properties

Using the methodology described above, the results of the experiments and model evaluations are presented in the following sections, beginning with the cement properties.

After mixing the slurry for casing 1, its properties were determined. The spreading diameters measured in two orthogonal directions were 36 cm in both cases. A slurry density of 1.92 g/cm^3 and an air content of 0.4% were measured.

In parallel with the cyclic loading experiments, several properties of the hardened cement were determined as described in Section 2.5. The results are summarized in Table 10.

Table 10: Densities, water content, porosity and carbonate content of the cement samples obtained from experiments described in Section 2.5.

Cement samples		Dry density [g/cm^3]	Wet density [g/cm^3]	Grain density [g/cm^3]	Water content [%]	Porosity [%]	Carbonate content [%]
Casing 1	Initial	1.58	1.97	2.57	19.5	39	0.4
	Autoclave	1.58	1.93	2.48	18.2	36	0.3
	Control	1.67	2.01	2.45	16.9	32	0.3
Casing 2	Initial	1.58	1.94	2.56	18.6	38	0.4
	Autoclave	1.54	1.88	2.57	17.8	40	0.2
	Control	1.56	1.93	2.55	19.1	39	0.2
Casing 3	Initial	1.47	1.89	2.59	22.1	43	0.2
	Autoclave	1.54	1.83	2.65	16.1	42	0.3
	Control	1.54	1.93	2.67	20.2	42	0.3
Casing 4	Initial	1.52	1.92	2.58	21.0	41	0.3
	Autoclave	1.54	1.92	2.59	19.8	41	0.3
	Control	1.52	1.95	2.59	21.9	41	0.3

Samples typically show water contents of approximately 20%. Autoclave samples generally exhibit slightly lower water contents and correspondingly lower wet densities compared to initial and control samples. A notable exception is the control sample of casing 1, which shows the lowest water content overall. This sample also exhibits the highest dry and wet densities, as well as the lowest grain density and porosity.

Dry densities are largely comparable across all samples, with two exceptions: the control sample of casing 1, which shows the highest value, and the initial sample of casing 3, which exhibits the lowest. Wet densities and porosities display similarly limited variation among

most samples, again with the control sample of casing 1 deviating from the overall trend. Grain densities are generally consistent, except for the control and autoclave samples of casing 1, which exhibit slightly lower values than the remaining samples.

In addition to total porosity, the pore size distribution was characterized by mercury intrusion porosimetry, as described in Section 2.5. The results are presented in Figure 18.

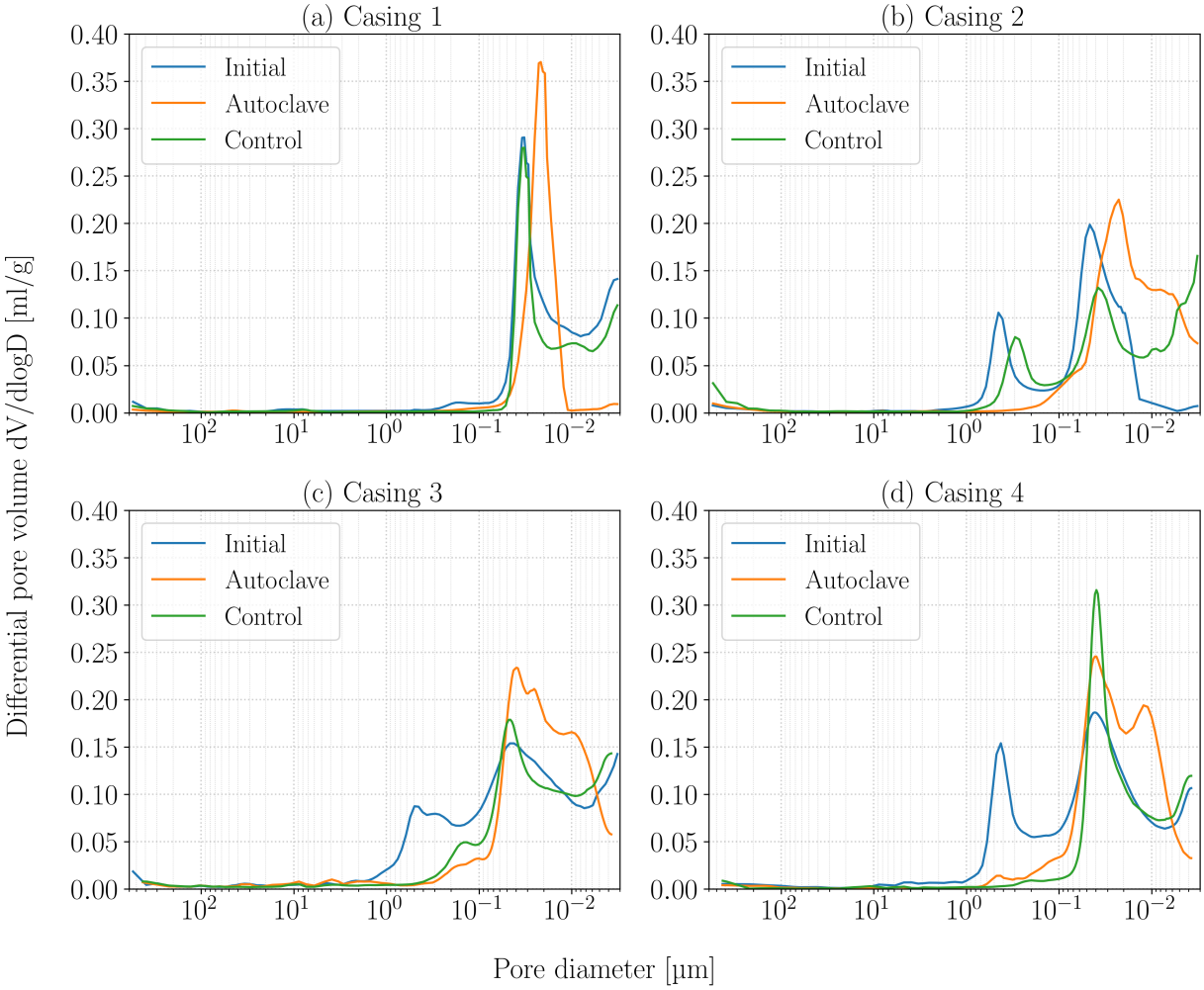


Figure 18: Mercury porosimetry results for different cement samples (see Section 2.5 for details). *dV/dlogD* is the incremental pore volume per logarithmic pore diameter interval, normalized by the sample mass. Thus, *dV/dlogD* indicates how much pore volume is associated with a specific range of pore diameters (on a logarithmic scale) per gram of cement. Consequently, peaks in the curves indicate the most common pore diameters in the respective sample. While multiple replicate measurements were conducted with different subsamples of each sample type[30], only one representative curve per type is shown, as the results are similar within each type.

All samples contain a small fraction of large pores with diameters on the order of 0.6 mm. However, the majority of the pore volume typically begins at pore diameters between

[30]In this context, *sample type* refers to a specific combination of casing and treatment condition (initial, control, or autoclave). For example, the autoclave samples of casing 2 represent one sample type.

approximately 0.1 µm and 1 µm. An exception is casing 1, where the main pore volume is associated with smaller pores, beginning at diameters around 0.05 µm.

Although differences are observable between casings and between samples within individual casings, no consistent overall trend exists. For casings 1 and 2, the dominant pore diameter peak of autoclave samples tends to shift slightly toward smaller diameters compared to the corresponding initial and control samples. For casings 2, 3, and 4, the earliest pore diameter peak (between 1 µm and 0.1 µm) is consistently observed in the initial sample.

Matrix permeabilities of the cement samples were determined as described in Section 2.5, and the results are summarized in Table 11.

Table 11: Measured matrix permeabilities of the cement samples. *Conditioning* refers to the duration of the sample preparation. Samples that underwent 3–7 days of conditioning were stored at 40 °C in an oven, while the others were stored at 20 °C and 65% relative humidity (Table 3). *a* and *b* represent repeated measurements of the same sample at different times, while *1*, *2* and *3* indicate different samples from the same batch. The initial sample of casing 2 was damaged during installation in the test cell and could not be measured.

Cement Samples		Matrix permeability [m^2]	Conditioning [days]	Annotations [-]
Casing 1	Initial 1	$8 \cdot 10^{-16}$	40	-
	Initial 2	$1 \cdot 10^{-15}$	40	-
	Autoclave 1a	$9 \cdot 10^{-15}$	121	-
	Autoclave 1b	$9 \cdot 10^{-15}$	125	-
	Autoclave 2a	$3 \cdot 10^{-15}$	121	-
	Autoclave 2b	$4 \cdot 10^{-15}$	125	-
	Autoclave 3	$5 \cdot 10^{-15}$	121	-
	Control	$3 \cdot 10^{-16}$	121	-
Casing 2	Initial	-	121	Broken sample
	Autoclave a	$3 \cdot 10^{-16}$	3	-
	Autoclave b	$6 \cdot 10^{-16}$	130	-
	Control a	$4 \cdot 10^{-14}$	3	-
	Control b	$2 \cdot 10^{-15}$	130	-
Casing 3	Initial	$4 \cdot 10^{-14}$	3	-
	Autoclave	$7 \cdot 10^{-18}$	5	-
	Control	$2 \cdot 10^{-16}$	5	-
Casing 4	Initial a	$3 \cdot 10^{-16}$	3	-
	Initial b	$2 \cdot 10^{-15}$	7	-
	Autoclave	$3 \cdot 10^{-16}$	3	-
	Control	$6 \cdot 10^{-15}$	3	-

After extended conditioning, the autoclave sample of casing 2 exhibits an increase in matrix permeability, whereas the control sample shows a decrease. For casing 4, the two initial samples differ by approximately one order of magnitude in matrix permeability: one value is closer to the autoclave sample, while the other is more similar to the control sample.

For casing 1, the autoclave samples exhibit the highest matrix permeabilities and the control sample the lowest. In contrast, this relationship is reversed for casing 2. For casing 3, the initial sample shows the highest matrix permeability, while the autoclave sample exhibits the lowest.

Repeated measurements of autoclave samples 1 and 2 from casing 1 show nearly identical matrix permeability values over short time intervals, indicating good measurement reproducibility.

The mineralogical composition of the cement samples was analyzed by X-ray diffraction (XRD) combined with Rietveld refinement, as described in Section 2.5. The results are summarized in Table 12. Initial samples generally contain higher amounts of alite and belite and lower amounts of portlandite compared to the control and autoclave samples. Likewise, all autoclave samples contain approximately twice the amount of hydrogarnet relative to their respective initial and control samples. Ettringite and calcite were detected exclusively in the initial sample of casing 1.

Table 12: Relative amounts of crystalline and amorphous phases in cement samples determined by X-ray diffraction using Rietveld refinement. Abbreviations: Am = Amorphous, Po = Portlandite, C_3S = Alite, C_2S = Belite, C_4AF = Brownmillerite, HG = Hydrogarnet, Qz = Quartz, Et = Ettringite, Cal = Calcite. Silicon, the added internal powder standard, was mathematically removed from the results.

Cement	Samples	Am [%]	Po [%]	C_3S [%]	C_2S [%]	C_4AF [%]	HG [%]	Qz [%]	Et [%]	Cal [%]
Casing 1	Initial	57.6	17.6	1.2	4.3	8.2	5.7	0.2	1.2	3.9
	Autoclave	55.8	20.0	0.7	1.7	7.0	14.8	0.2	-	-
	Control	61.7	17.6	0.8	3.7	8.7	7.6	0.2	-	-
Casing 2	Initial	51.7	15.8	4.4	10.0	9.9	6.9	1.3	-	-
	Autoclave	55.4	18.6	0.2	2.1	9.0	13.6	1.1	-	-
	Control	59.4	19.4	1.0	2.9	9.8	7.1	0.3	-	-
Casing 3	Initial	55.9	17.9	2.6	8.1	8.7	6.7	0.2	-	-
	Autoclave	52.3	19.7	0.2	1.0	9.8	15.1	1.9	-	-
	Control	59.1	19.9	1.9	0.8	10.7	7.4	0.2	-	-
Casing 4	Initial	59.9	16.6	2.6	8.2	7.2	5.3	0.2	-	-
	Autoclave	53.3	18.8	3.7	1.2	8.9	13.3	0.9	-	-
	Control	59.9	19.1	4.4	0.8	7.7	6.3	1.7	-	-

4.1.2 Annular gap development

The system permeability of the cement-filled casings was experimentally evaluated after each loading cycle and occasionally after periods without loading (see Section 2.4). This allows the effect of each loading type on the casing's system permeability to be assessed individually. The experimental data were evaluated using different models (see Section 3.2). The results shown in the figures below are based on model H, which was selected as the primary model according to the considerations discussed in Section 5.3.3. Model H uses the gap aperture h as its only fitting parameter, with values of c assigned according to Table 4. It is important to note that the *modeled* value of h is a rather apparent quantity, as it is model-derived and can be influenced by various factors besides the true aperture, as discussed in more detail in Sections 5.2 and 5.3.

Figure 19 displays the modeled annular gap apertures for casing 0 as a function of time. The cement inside this casing was used in earlier experiments and is therefore pre-aged (Table 2). Nevertheless, the modeled gap aperture h increases during the first 40 days, with no identifiable correlation to any specific loading type. After the pause around day 40, h shows minimal further increase, regardless of the loading type applied.

Before the first experiment, both pressure and temperature were increased, which effectively represents the second half of a combined pressure and thermal loading cycle. While the subsequent decrease in pressure and temperature of a full cycle is missing, it is still classified as a combined pressure and thermal loading cycle.

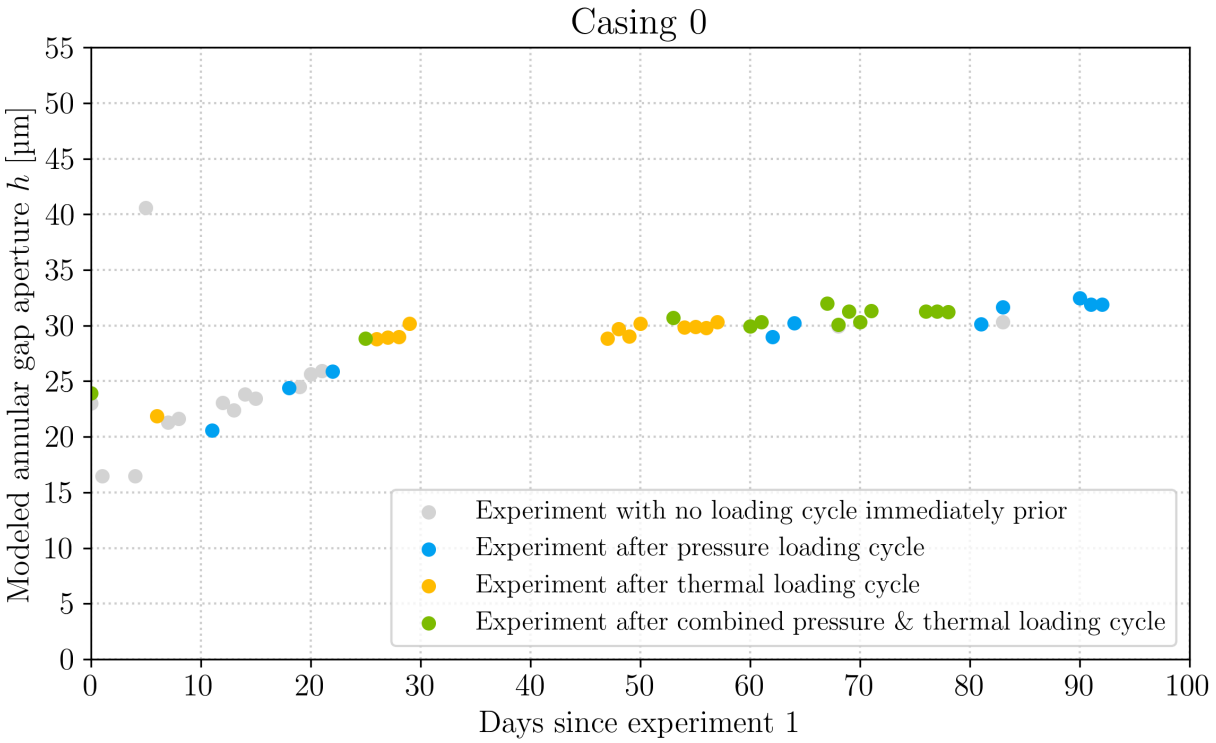


Figure 19: Results of model H based on the experiments that were carried out on casing 0

Figure 20 shows the temporal evolution of the modeled annular gap apertures for casing 1. Before day 80, no loading cycles were applied, resulting in a relatively constant modeled gap aperture. The two pauses around days 20 and 50 show little effect. The first three pressure loading cycles cause a steep increase in h. Afterwards, h remains within 25–35 µm, regardless of additional loading.

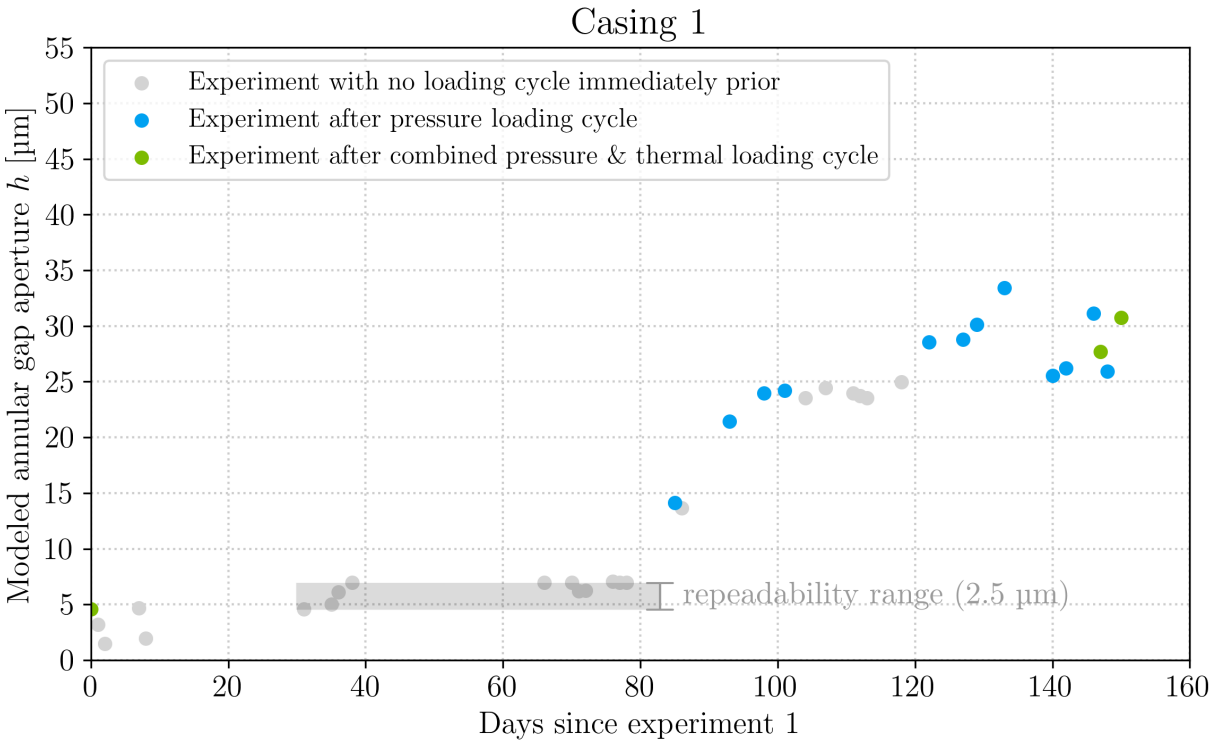


Figure 20: Results of model H based on the experiments that were carried out on casing 1. The repeatability range corresponds to repeated measurements performed under identical conditions over a time span of approximately 50 days without applied loading. The indicated range therefore reflects the measurement precision of repeated experiments.

For casing 2 (Figure 21), the main increase in h occurs after the first pressure loading. In this experimental series, pressure loading generally increases h, while thermal loading appears to show the opposite trend: following thermal loading, h often decreases and subsequently slowly increases again, even in the absence of further loading. After the pause around day 160, the h-values tend to increase slightly compared to the pre-pause level. Furthermore, repeated thermal loading does not appear to exert a strong impact after that pause.

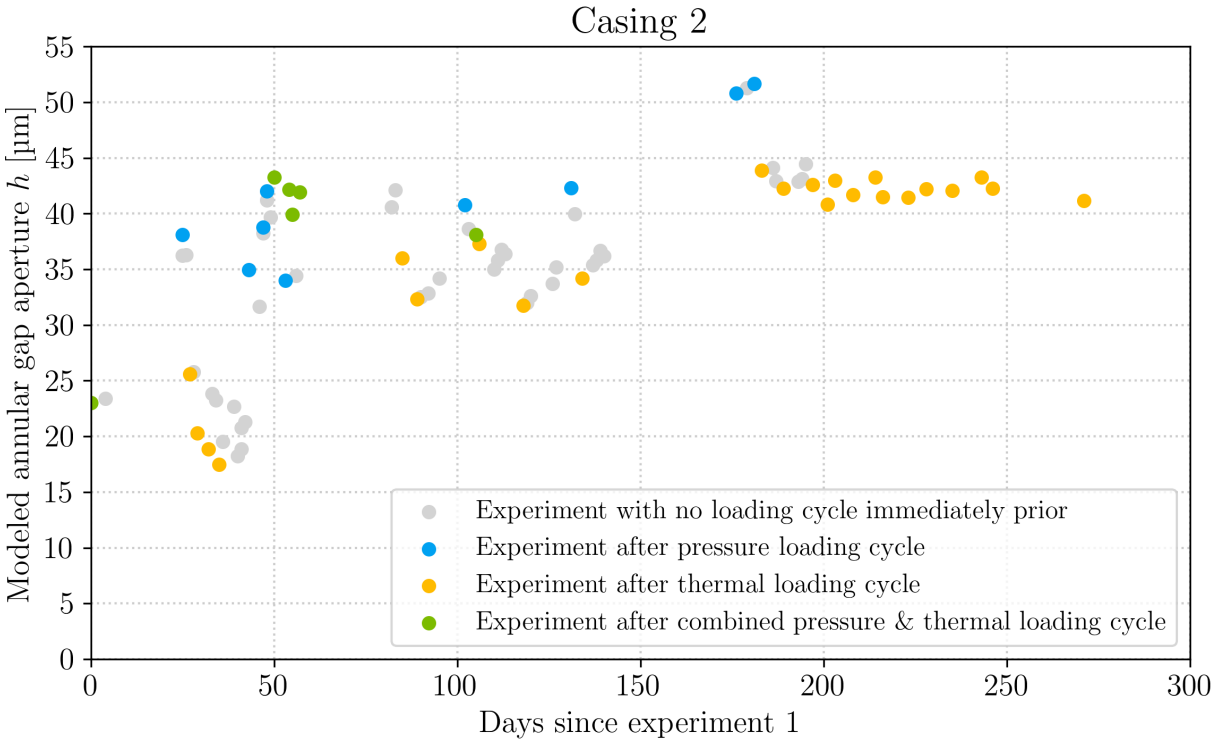


Figure 21: Results of model H based on the experiments that were carried out on casing 2

Casing 3 (Figure 22) shows a similar trend to the previous casings, with modeled h-values following pressure loading typically exceeding those following thermal loading. All values of h after the pause around day 200 are higher than those before the pause. This is particularly evident for post-pause h-values determined after pressure loading, which are consistently in the range of approximately 35–40 µm. In contrast, post-pause h-values determined after thermal loading predominantly lie between 25–30 µm, only slightly above the pre-pause level.

Casing 4 (Figure 23) follows a similar pattern to previous casings, with modeled h-values after pressure loading generally above those after thermal loading. Similar to casing 1, a sharp increase in h is observed during the three pressure loading cycles around day 100. As with casing 3, all h-values after the pause around day 250 are higher than those before the pause.

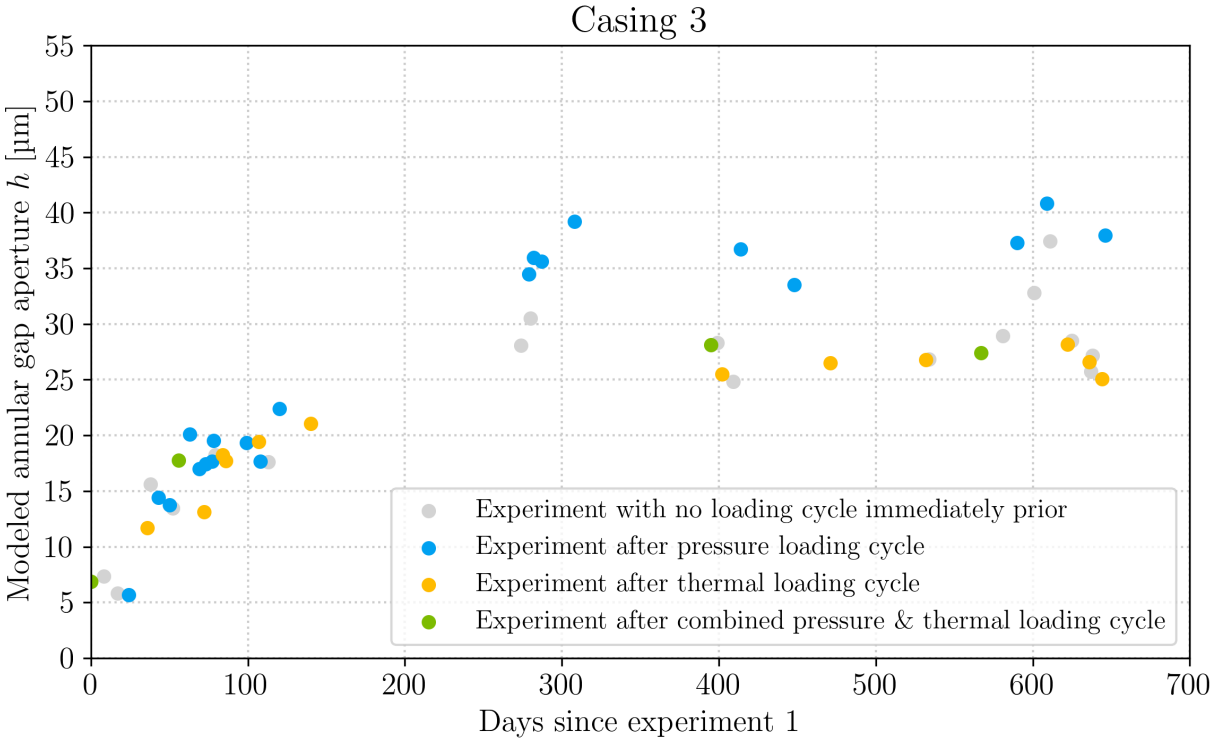


Figure 22: Results of model H based on the experiments that were carried out on casing 3

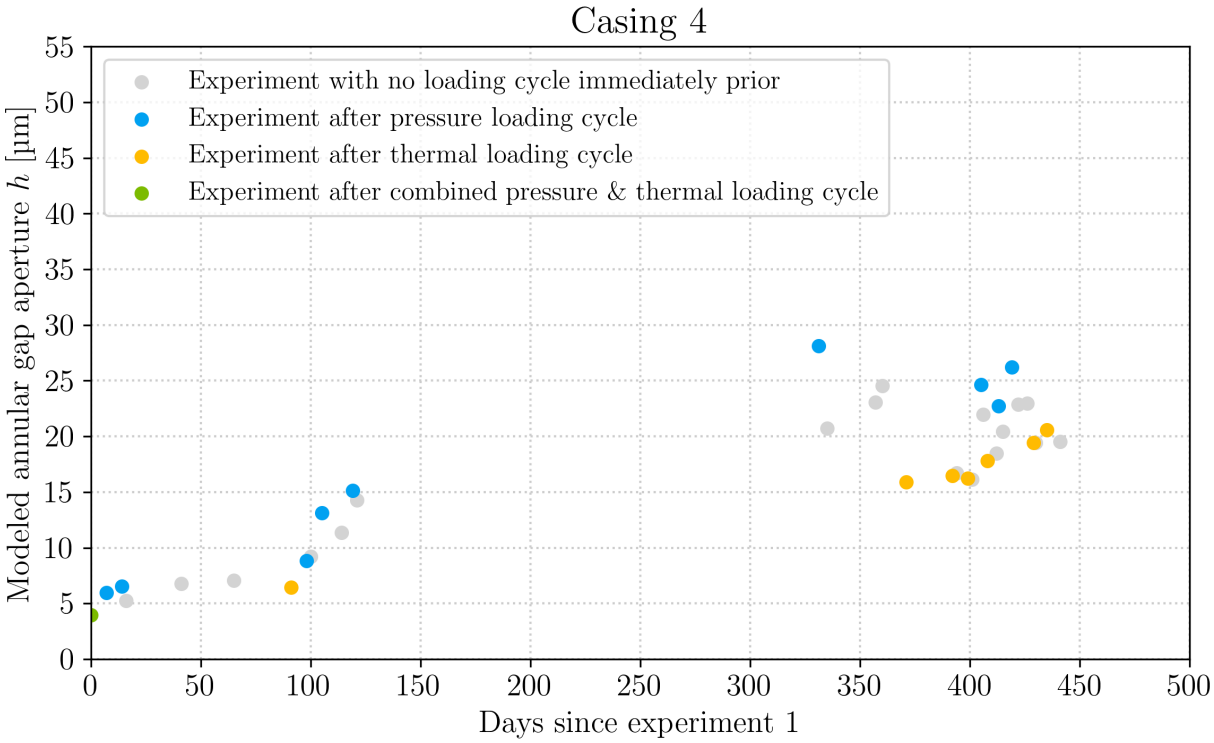


Figure 23: Results of model H based on the experiments that were carried out on casing 4

Figure 24 shows the modeled annular gap apertures for all casings for comparison. The initial h-values lie around 20 µm for casings 0 and 2, and below 10 µm for the other casings. Furthermore, h-values of casing 0 show less vertical variation in the plot than h-values of the other casings. Overall, casings 1, 3, and 4 display a similar pattern of h-values, with casing 3 showing slightly higher initial and final values than the others. Patterns for Casings 3 and 4 appear similar, although the final h-values for casing 4 are lower than those of casing 3. Toward the end of each experimental series, the results tend to scatter more.

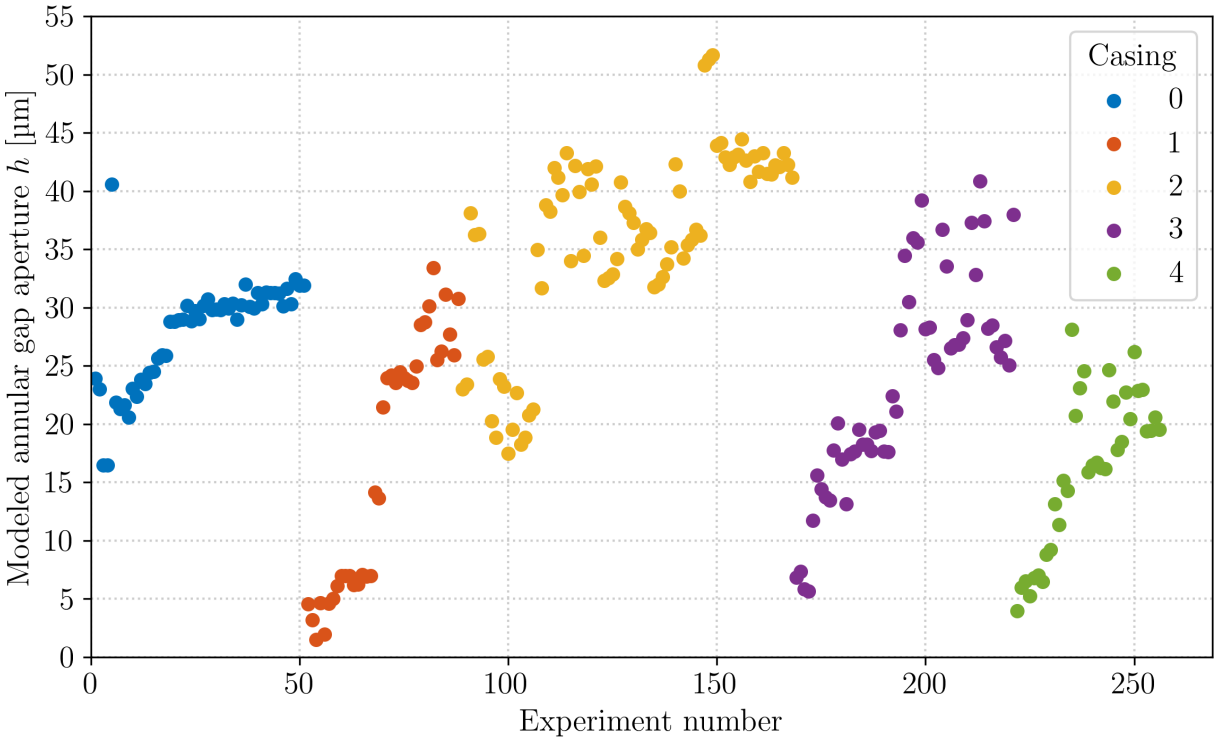


Figure 24: Modeled annular gap apertures of all experiments using model H; colors represent different casings

Similar trends are observed in Figure 25, which shows the matrix permeabilities derived from model H for all casings (Equation 38), under the assumption that gas flow occurs solely through the cement matrix rather than the annular gap. Most model-derived matrix permeabilities for casings 0 and 2 lie between 10^{-14} and 10^{-13} m^2, with occasional values slightly below or above this range.

In contrast, Casing 1 shows the widest range, spanning approximately four orders of magnitude and starting well below 10^{-17} m^2. Most matrix permeabilities for casings 3 and 4 lie between 10^{-16} and 10^{-13} m^2. These values represent the permeabilities that would be required to reproduce the volumetric gas flow rates observed in the experiments under the matrix-flow assumption.

The experimentally measured matrix permeabilities are summarized in Table 11 and compared to the model-derived permeabilities in Section 5.2.2.

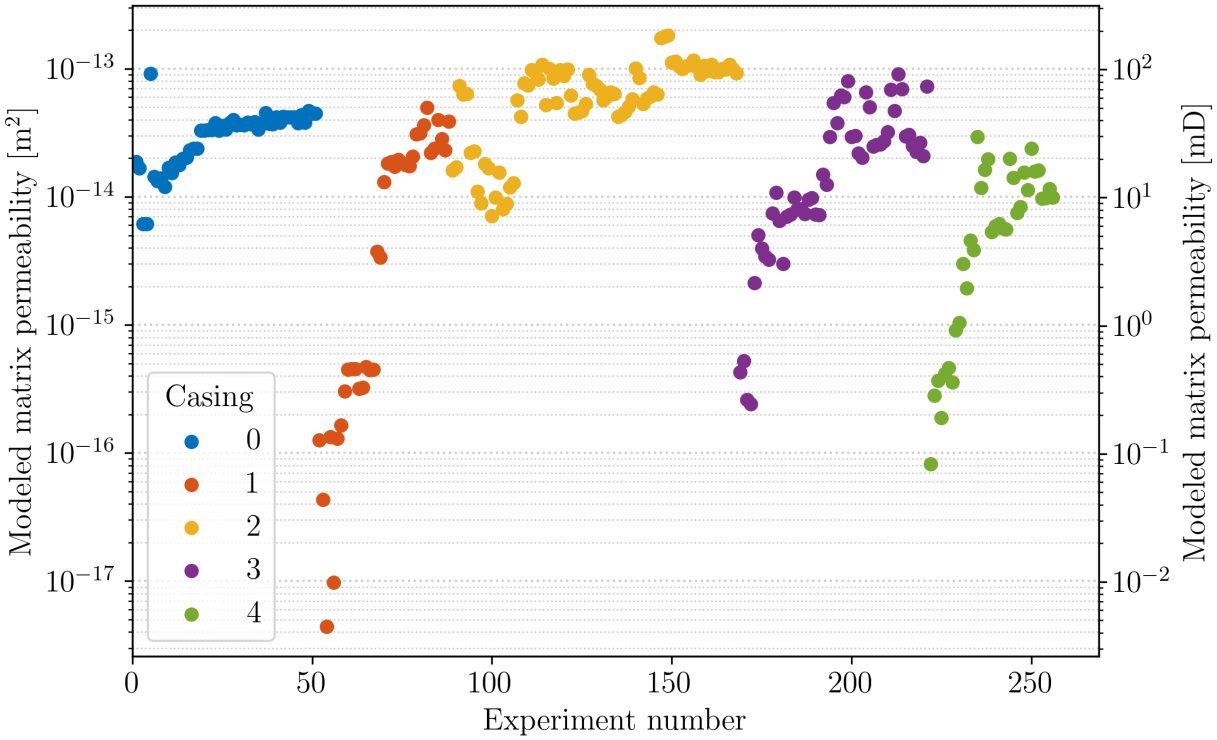


Figure 25: Matrix permeabilities for all experiments derived from model H, according to Equation 38, assuming gas flow through the cement instead of the annular gap

4.1.3 Statistical analysis of cyclic loading effects

To further assess the impact of each loading type on the modeled annular gap aperture h, the experiments were classified into four groups: Group N includes experiments without prior loading; group P includes experiments following pressure loading; group T includes experiments following thermal loading; and group PT includes experiments following combined pressure and thermal loading.

Accordingly, a value of h in group P, for example, represents the modeled annular gap aperture obtained from an experiment performed directly after a pressure loading cycle. Each Δh_{load} value denotes the change in the modeled gap aperture following the respective loading cycle. For instance, a Δh_{load} value of -2 µm in group T indicates a decrease in the modeled gap aperture by 2 µm following thermal loading.

In 75% of the experiments in group P, the modeled aperture h increases, whereas in 71% of the experiments in group T, h decreases (Figure 26, Table 13). In contrast, the Δh_{load} values in group N are approximately symmetrically distributed around 0 µm, with 55% of the values being positive and 45% negative. Group PT shows a similar pattern to group N, with 55% increases and 45% decreases in h.

A notable exception can be observed for casing 0. The modeled aperture h increases from 16 µm in experiment 4 to 41 µm in experiment 5, before decreasing again to 22 µm

in experiment 6.[31] Consequently, experiment 5 alone accounts for the two pronounced outliers in Figure 26a, at 24.1 µm and −18.8 µm. Most other experiments conducted shortly before and after experiment 5 yielded modeled apertures of approximately 22 µm.

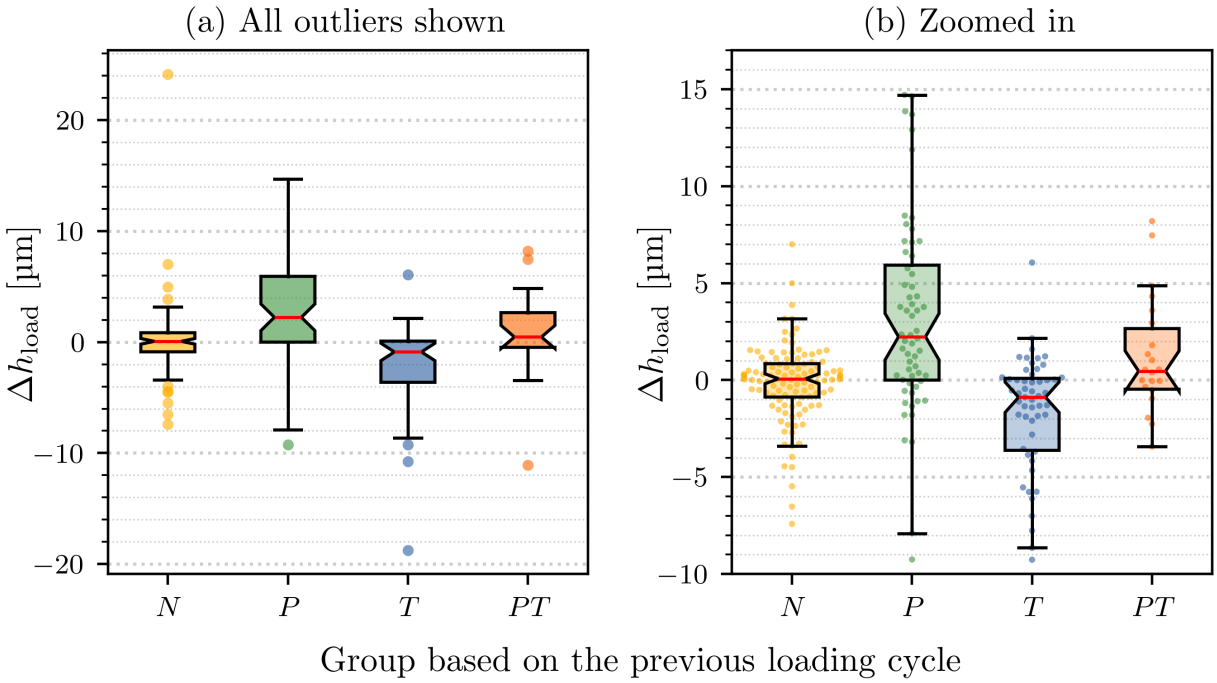


Figure 26: Boxplots showing the the distribution of changes in the modeled gap apertures for the different loading types. The red line denotes the median. The notches represent an approximate 95% confidence interval of the median. The box spans the interquartile range (IQR) between the first (Q1) and third quartile (Q3). The whiskers extend to the outermost data points within the range [Q1 − 1.5 · IQR, Q3 + 1.5 · IQR], while data outside this range are plotted as outliers (Iglewicz, 2025). Subfigure (a) displays all outliers. In subfigure (b), the plot is zoomed in along the y-axis, and a swarmplot of the full dataset is overlaid. As the boxplots for relative and absolute changes in h are similar, only absolute changes are shown here.

To further evaluate differences in Δh_{load} between groups, several statistical tests based on p-values were performed. A p-value quantifies the probability of observing differences in Δh_{load} between groups at least as large as those present in the data, assuming the null hypothesis is true (Habibzadeh, 2025). In this context, the null hypothesis states that no systematic differences in Δh_{load} exist between groups. A p-value below 0.05 indicates that the observed differences are unlikely under the null hypothesis and are therefore considered statistically significant.

First, a Shapiro–Wilk test (Shapiro and Wilk, 1965) was conducted to assess normality. The results show that neither the modeled h values nor the Δh_{load} values follow a normal distribution, whether examined across the entire dataset or within individual groups.

[31] One possible explanation is that the valve between the upper and lower chambers was not fully closed during experiment 5. This may have permitted gas flow through the connecting pipe rather than exclusively through the casing, resulting in an apparently higher system permeability.

Because the normality assumption required for parametric tests was therefore not met, the non-parametric Kruskal-Wallis test (Kruskal and Wallis, 1952) was applied. This test revealed statistically significant differences in Δh_{load} between groups ($H = 45.39$, $p < 0.0001$).

To further examine pairwise differences between groups, Dunn's test (Dunn, 1964) with Holm correction (Holm, 1979) was applied. Significant differences in Δh_{load} were identified for the following group pairs:

- Group N vs. group P ($p < 0.001$)
- Group N vs. group T ($p = 0.008$)
- Group P vs. group T ($p < 0.001$)
- Group T vs. group PT ($p = 0.008$)

No statistically significant differences were observed between group N and group PT ($p = 0.24$), or between group P and group PT ($p = 0.14$).

To assess the directional tendency of the Δh_{load}-values within each group, a binomial test (Wagner-Menghin, 2005) was conducted. The null hypothesis assumed an equal probability of positive and negative Δh_{load}-values. The results are summarized in Table 13.

Table 13: Results of the group wise binomial tests

Group	$\Delta h_{\text{group}} > 0$	p-value	Interpretation
N	55.3% (63/114)	0.303	Not significant
P	75.0% (45/60)	< 0.001	Significant (positive bias)
T	29.1% (16/55)	0.003	Significant (negative bias)
PT	54.5% (12/22)	0.832	Not significant

The binomial test confirms a statistically significant predominance of positive Δh_{load}-values in group P and a statistically significant predominance of negative values in group T. These results support the pairwise differences identified by Dunn's test and illustrated in Figure 26.

Lastly, a Brunner-Munzel test (Brunner and Munzel, 2000) was conducted to evaluate differences in the magnitude of Δh_{load}-values between groups. The results are presented in Table 14. A BM-value far from zero indicates a strong difference between groups. Positive BM-values indicate that the second group tends to exhibit larger Δh_{load}-values than the first group, whereas negative BM-values indicate the opposite.

Table 14: Results of the Brunner–Munzel test for pairwise comparisons of Δh_{load} between groups.

Groups	BM-value	p-value	Interpretation
N vs. P	4.9	< 0.001	Significant
N vs. T	-3.7	< 0.001	Significant
N vs. PT	1.2	0.254	Not significant
P vs. T	-8.0	< 0.001	Significant
P vs. PT	-2.1	0.043	Significant
T vs. PT	3.2	0.003	Significant

4.2 Regulations and guidelines for annular pressure and vent flow

4.2.1 Overview

Given the gas flow through the cement-filled casings identified in the experiments, which would manifest as sustained casing pressure (SCP) or casing vent flow (CVF) in field wells, it is essential to consider how such issues are addressed in practice. This section therefore summarizes procedures for managing SCP and CVF described in legally binding regulations and non-legally binding industry guidelines as of 2024 (Schulz et al., 2025). Legally binding regulations are defined by authorities, whereas industry guidelines are issued by oil and natural gas business associations, such as the American Petroleum Institute (API). Although industry guidelines are not legally binding, they are in some cases used as templates for regulations or even explicitly referenced therein.

In practice, regulations generally represent minimum compliance requirements. In many cases, operating companies adopt industry guidelines that exceed these legal requirements to align with corporate risk management policies and to manage financial and reputational risks associated with well integrity failures. Occasionally, regulations explicitly mandate compliance with specific guidelines. Regulators in some jurisdictions also inspect wells for SCP and/or CVF during routine compliance inspections. However, practices for these inspections vary widely.

This study based on Schulz et al. (2025) identifies four major aspects of SCP and CVF regulations and guidelines: (1) monitoring, (2) diagnostic testing, (3) pressure or flow rate thresholds, and (4) barrier classification.

Monitoring consists of regularly measuring annular pressure in the case of SCP, or flow rates in the case of CVF. Changes in pressure or flow detected during monitoring may indicate well integrity issues or result from other factors, such as temperature variations.

Diagnostic testing is required to differentiate between potentially harmful well integrity issues and harmless effects, such as temperature variations due to production rate changes.

The difference between monitoring and diagnostic testing can be subtle and subjective. For example, flow rate measurements may be considered diagnostic testing because measuring a constant flow rate over a specified time period diagnoses CVF. Note that this study classifies pure flow rate measurements and similar assessments as *monitoring* when performed routinely and as *testing* when conducted intermittently.

In addition to monitoring and diagnostic testing, some regulations and guidelines mention allowable pressure or flow rate thresholds in different annuli. An SCP threshold can, for example, be defined as the maximum pressure that can occur in an annulus without risking groundwater contamination or damage to well components. Exceeding this threshold indicates a potentially severe integrity issue. Some guidelines classify wells based on the integrity of both barriers, independent of diagnostic test results (Table 15, Column 4; Table 16). Likewise, the barrier classifications aim to mitigate undesired accidents and events. In Table 15, the presence of monitoring, diagnostic testing, pressure thresholds, and barrier classification in regulations and guidelines of different countries are summarized.

Jurisdictions in the USA and Canada, as well as Russia, have direct SCP and CVF management regulations (Figure 27). In Canada, these regulations vary between individual provinces and territories. Likewise, in the United States, they vary between states. In addition to these state-level regulations, U.S. federal regulations cover SCP for offshore wells in federal waters, and federal onshore regulations apply to wells on land owned or managed by the federal government. Supplementary Material 2 of Schulz et al. (2025) provides a detailed analysis of regulations by jurisdiction in the USA and Canada.

While SCP and CVF are not (or only minimally) regulated directly in China, Australia, and Norway, they are indirectly addressed through either guidelines, or indirect regulations that mainly specify risks to be avoided rather than detailed procedures. In China, operators follow guidelines of state-owned companies. In Australia, there are both national regulations and state-level regulations based on a risk-based approach. For example, in Western Australia, well integrity hazards (including SCP) must be "controlled". A well management plan is required, which must include a list of standards that the respective operator follows (Government of Western Australia, 2015). Norwegian regulations follow a similar risk-based approach (Petroleum Safety Authority Norway, 2023a,b,c). No information describing regulations in Middle Eastern countries was found (Schulz et al., 2025).

Table 15: Different countries' SCP and SCVF regulations and guidelines, sorted by gas production in 2023 (× indicates a topic is covered in a regulation or guideline and – suggests the topic is not covered). Reproduced from Schulz et al. (2025)

Country	Reference	Document Type	Monitoring	Diagn. testing	Thresholds	Classification
USA	Bureau of Safety and Environmental Enforcement (2010)	Regulation (offshore)	×	×	×	–
	American Petroleum Institute (2006)	Guideline (API RP 90, offshore)	×	×	×	–
	American Petroleum Institute (2016)	Guideline (API RP 90-2, onshore)	×	×	×	–
	State regulations (Supplementary Material 2 of Schulz et al., 2025)[d]	Regulation	State-dependent requirements			
Russia	Rostekhnadzor (2020)	Regulation	×	×	–	–
China	China National Offshore Oil Corporation (2018)	Guideline (state-owned company)	×	×	×	×
	China National Petroleum Corporation (2022)	Guideline (state-owned company)	×	×	×	×
Canada	Alberta Energy Regulator (2022)	Directive[a]	–	×	×	–
	Government of British Columbia (2023)	Regulation	–	×	×	–
	British Columbia Energy Regulator (2023)	Regulator Guideline[b]	×	×	×	–
	Other jurisdictions (Supplementary Material 2 of Schulz et al., 2025)[d]	Regulation	Requirements depending on province/territory			
	Energy Safety Canada (2022)	Guideline	×	–	–	–
Australia	Government of Western Australia (2015), NOPSEMA (2020a,b), Office of Parliamentary Counsel, Canberra (2023), and Queensland Government (2004)	Regulation	–	–	–	–
Norway	Petroleum Safety Authority Norway (2023a,b,c)	Regulation (offshore)	×	–	–	–
	Norwegian Oil Industry Association and Federation of Norwegian Manufacturing Industries (2021)	Guideline (offshore)	×	–	×	–
	Norwegian Oil and Gas Association (2017)	Guideline (offshore)	×	×	×	×
International	ISO 16530-1 (2017), ISO 16530-2 (2014)	Guidelines	×	×[c]	×	–

[a] Although not formal regulations, directives are authoritative and must be followed.
[b] While not a regulation itself, the Oil and Gas Activity Operations Manual is issued by the regulator as a guideline containing recommended practices to ensure compliance with the regulations.
[c] Bleed-down/build-up tests are suggested but not described. Instead, the American Petroleum Institute (2006) is referenced for a testing description.
[d] On the journal homepage, the download link for Supplementary Material 2 is currently mislabeled as Supplementary Material 1, which may be corrected in the future. Here, the material is referred to as Supplementary Material 2, consistent with the designation in the material header.

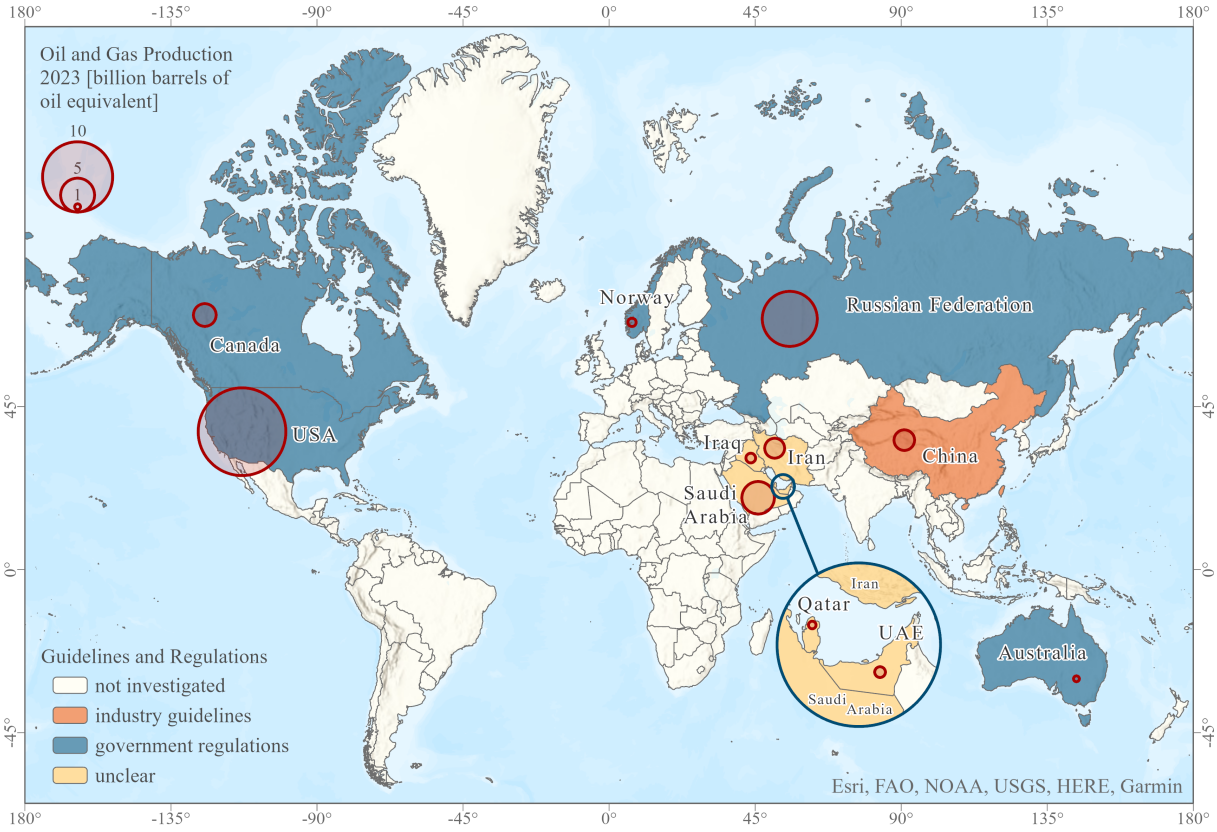


Figure 27: World map showing countries with guidelines and regulations for SCP and CVF. Modified after Schulz et al. (2025), oil and gas production data from Enerdata (2024), shapefiles from Esri (2022). Mercator projection

4.2.2 Annulus management

An annulus can be configured as either open to the atmosphere or closed at the wellhead. With closed annuli, a leak that causes fluids to migrate upwards within the annulus is contained, preventing methane from being directly emitted into the atmosphere by retaining it within the wellhead. Consequently, the build-up of SCP is possible in closed annuli. If SCP exceeds the formation's hydrostatic pressure and entry pressure at the bottom of the casing, gas migration into the surrounding subsurface can occur. However, if the bottom of the annulus is filled with cement, SCP build-up can stop gas leakage through the cement and lead to a steady state if the annular pressure at the wellhead becomes sufficiently high (Lackey and Rajaram, 2019; Xu and Wojtanowicz, 2017).

Conversely, open annuli prevent pressure build-up at the wellhead, thereby mitigating the build-up of unsafe pressures and protecting aquifers from SCP-induced gas migration. However, open annuli can lead to direct greenhouse gas emissions in case of a subsurface leak inside the well that causes CVF.

In Canada and the USA, the status of an annulus (open/closed) is often prescribed in regulations (Figure 28). In British Columbia, Canada, the surface casing annulus has to be open to the atmosphere (Government of British Columbia, 2023). However, SCVF emissions of natural gas have to be kept below 100 m^3/day for each well. Similarly, Alberta also requires open annuli (Alberta Energy Regulator, 2022). The surface casing annulus has to be open to the atmosphere unless the well has an absolute open flow gas deliverability below 28,000 m^3/day, the true vertical depth of the well is less than 1 km, no H_2S is present in the gas, and there is no evidence of SCVF.

In contrast, seven states in the USA require closed annuli (Figure 28). Jurisdictions with conditionally closed annuli in the USA only mandate annuli of certain well types (e.g., wells with uncemented annuli) or annulus A (Figure 1) to be closed. In four U.S. states, regulations require annuli to remain open under specific conditions. In Montana, Nebraska, and North Dakota, open annuli are mandated during hydraulic fracturing operations (Montana Secretary of State, 2011; Nebraska Oil and Gas Conservation Commission, 2017; North Dakota Industrial Commission, 2010). In contrast, Kentucky prescribes open annuli only for temporarily abandoned wells drilled through coal seams (Kentucky Energy and Environment Cabinet, 2020). Other jurisdictions, like Pennsylvania, leave annulus management to the operator's discretion (Pennsylvania Department of Environmental Protection, 2017).

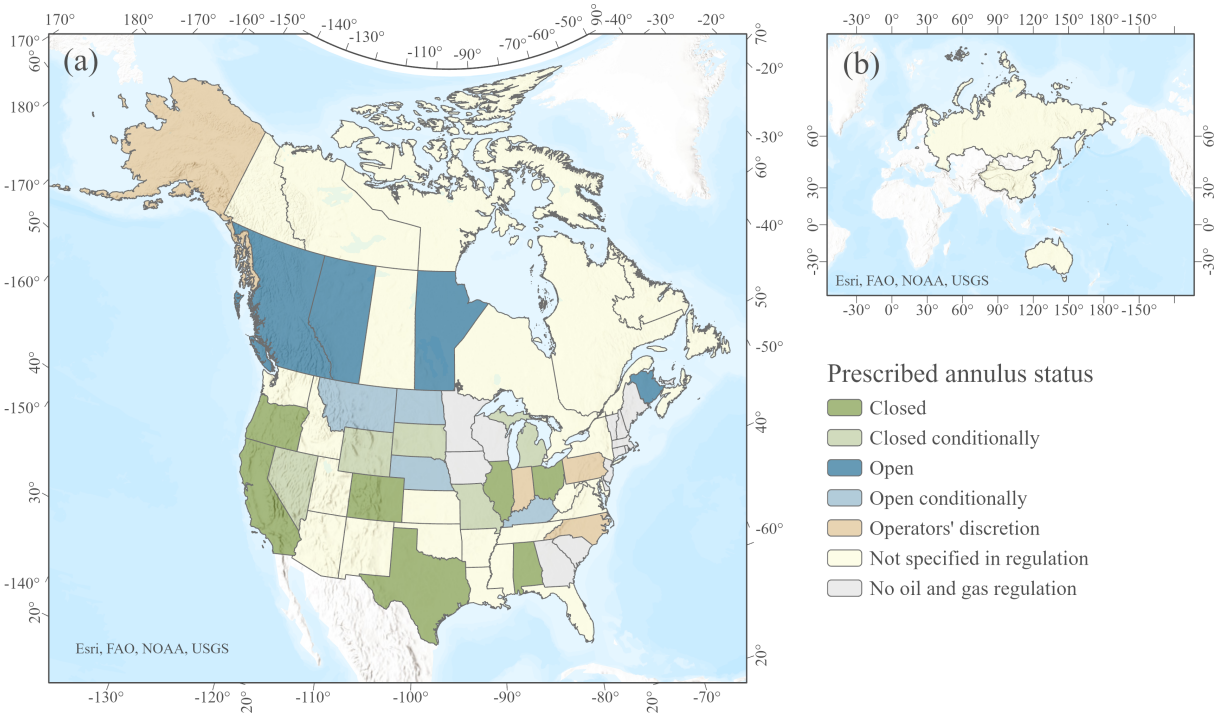


Figure 28: Map of annulus management requirements as outlined in regulations of a) the USA and Canada and b) Norway, Russia, China and Australia. Reproduced from Schulz et al. (2025), shapefiles from Esri (2017, 2022) and Statistics Canada (2023). Projections: a) Albers equal-area conic, b) Mercator

4.2.3 Monitoring

Monitoring for SCP and CVF is another important aspect of well integrity management. It enables the early detection of leaks, which can help to mitigate environmental impacts such as gas emissions and groundwater contamination. Most regulations and guidelines include annulus pressure or flow monitoring (Table 15).

The **USA** offshore regulations describe specific annular monitoring requirements based on the well type (Bureau of Safety and Environmental Enforcement, 2010). Monitoring of all annuli is mandated in fixed platform wells. Subsea wells only require monitoring of the *A* annulus. Hybrid wells (subsea wellhead but surface completion) require monitoring of the *A* and *B* annuli. The recommended monitoring frequency is daily to monthly. Compared to this regulation, the API RP 90 offshore guideline suggests monitoring all annuli monthly to semi-annually (American Petroleum Institute, 2006).

Onshore regulations in the USA are state-dependent and also apply to offshore wells located within state waters, typically extending three geographical miles (≈ 5.6 km) from the shoreline (United States Congress, 1953). Annulus pressure monitoring for onshore wells is mandatory in 18 states and on some federal lands (Figure 29; Supplementary Material 2 of Schulz et al., 2025). Some states require monitoring of specific annuli, whereas others require monitoring of all annuli.

Figure 29 summarizes the state-wise monitoring frequency. Often, monitoring is only prescribed during specific phases like hydraulic fracturing or stimulation. Arkansas, Colorado, New Mexico, Pennsylvania, and Texas are the only jurisdictions in the USA that require routine annulus pressure monitoring (Arkansas Oil and Gas Commission, 2021; Colorado Energy and Carbon Management Commission, 2025; New Mexico Environment Department, 2015; Pennsylvania Department of Environmental Protection, 2017; Railroad Commission of Texas, 2025). Flow rate monitoring is only prescribed in California and Pennsylvania (California Air Resources Board, 2017; Pennsylvania Department of Environmental Protection, 2017). Overall, either pressure or flow monitoring, or both, are required in 38% of U.S. states (Figure 29; Supplementary Material 2 of Schulz et al., 2025).

Russian regulations require routine annulus pressure monitoring during production. However, monitoring frequencies are not specified. After abandonment, annual annulus pressure monitoring and air monitoring for hydrogen sulfide are prescribed (Rostekhnadzor, 2020).

China's guidelines suggest real-time pressure monitoring of annulus A and a daily inspection of the records (China National Offshore Oil Corporation, 2018; China National Petroleum Corporation, 2022).

Canadian regulations do not prescribe routine annulus pressure monitoring. In British Columbia and New Brunswick (15% of provinces and territories), routine flow monitoring

is required (Figure 29; British Columbia Energy Regulator, 2023; Government of New Brunswick, 2021). In British Columbia, gas migration should also be monitored when detected (British Columbia Energy Regulator, 2023). The Canadian IRP 27 guideline suggests monitoring SCVF and annulus pressures during and after remediation (Energy Safety Canada, 2022).

Australia does not prescribe pressure or flow monitoring during well operation. However, annulus pressure reporting is required at well abandonment (NOPSEMA, 2020b).

Norway's regulations mandate pressure monitoring of all annuli in surface-completed wells and the innermost annulus in subsea-completed wells (Petroleum Safety Authority Norway, 2023b). Additionally, pressure monitoring of the next outer annulus is required in the case of hydrocarbon flow in an annulus. Similarly to the regulations, Norwegian guidelines recommend the monitoring of all accessible annuli (Norwegian Oil and Gas Association, 2017; Norwegian Oil Industry Association and Federation of Norwegian Manufacturing Industries, 2021).

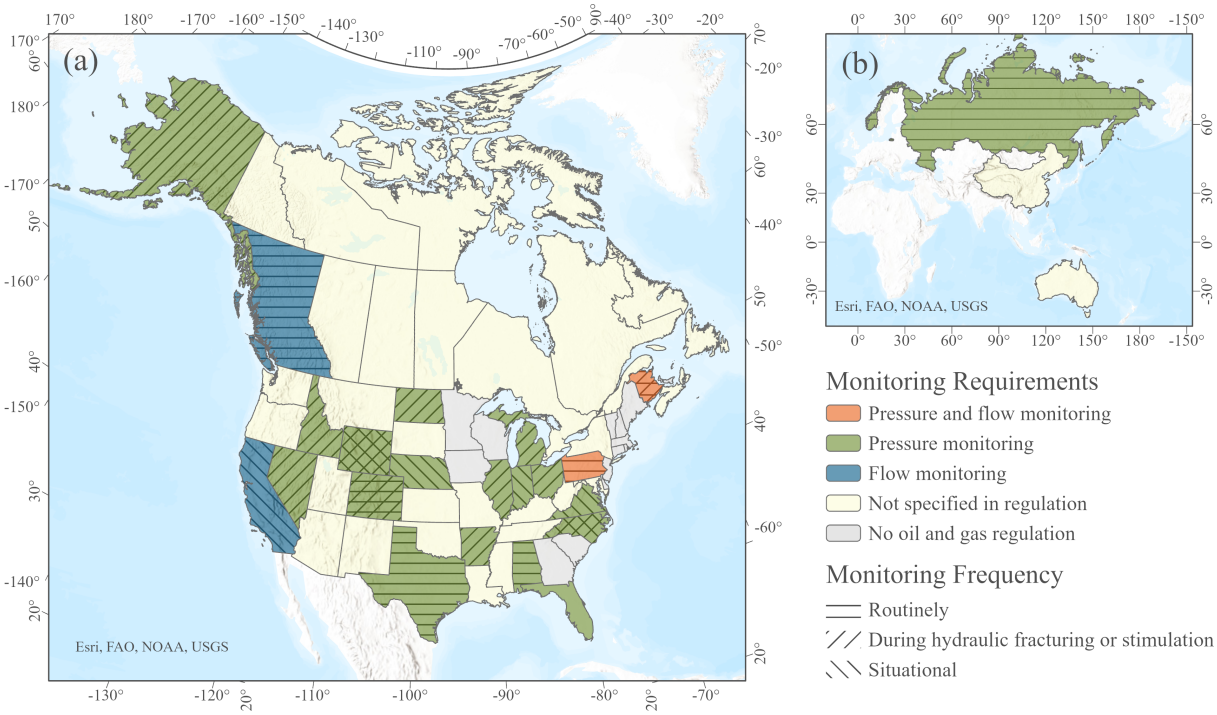


Figure 29: Monitoring requirements as outlined in regulations of a) the USA and Canada and b) Norway, Russia, China and Australia. Reproduced from Schulz et al. (2025), shapefiles from Esri (2017, 2022) and Statistics Canada (2023). Projections: a) Albers equal-area conic, b) Mercator

4.2.4 Diagnostic testing

Diagnostic testing identifies and distinguishes well integrity issues from pressures caused by temperature variations or other effects. Diagnostic testing is initiated at times specified by the regulator or when SCP or CVF is suspected. Through diagnostic testing, information about the leak severity and source can be obtained.

In the USA, diagnostic testing practices vary for offshore and onshore wells. Federal offshore regulations prescribe diagnostic testing if annular pressure is detected and specify reporting requirements (Bureau of Safety and Environmental Enforcement, 2010). These regulations state that operators should follow the diagnostic testing recommendations in the API RP 90 guideline (American Petroleum Institute, 2006). According to API RP 90, diagnostic testing has to be conducted whenever the annulus pressure exceeds 6.9 bar to determine whether the pressure is transient due to thermal effects, or sustained (i.e., rebuilds after it has been bled down) due to a constant leak source in the annulus (Bureau of Safety and Environmental Enforcement, 2010).

The diagnostic test recommended by API RP 90 is the bleed-down/build-up (B/B) test (Figure 30). In this test, gas is released from the annulus being tested through a half-inch needle valve until the annulus pressure equals atmospheric pressure, a predetermined quantity of liquid fluid is recovered, or a specified amount of time has elapsed. Subsequently, the valve is closed, and the annulus pressure development is observed for 24 hours. After B/B tests, further diagnostic actions like analyzing recovered fluids are suggested. The guideline defines three scenarios derived from B/B test results:

1) No leak: When bled down to atmospheric pressure, the annulus pressure does not build up within 24 hours, indicating it was likely thermally induced.

2) Minor leak: The pressure rebuilds to the original pressure or lower within 24 hours after bleeding to atmospheric pressure. In this case, continuous monitoring and periodic re-evaluation are required.

3) Major leak: The annulus pressure cannot be fully bled down to atmospheric pressure or there is pressure communication between annuli. In this scenario, the leak source has to be identified, repairs may be required, and the Maximum Allowable Operating Pressure (MAWOP) has to be recalculated (further explained in Section 4.2.5).

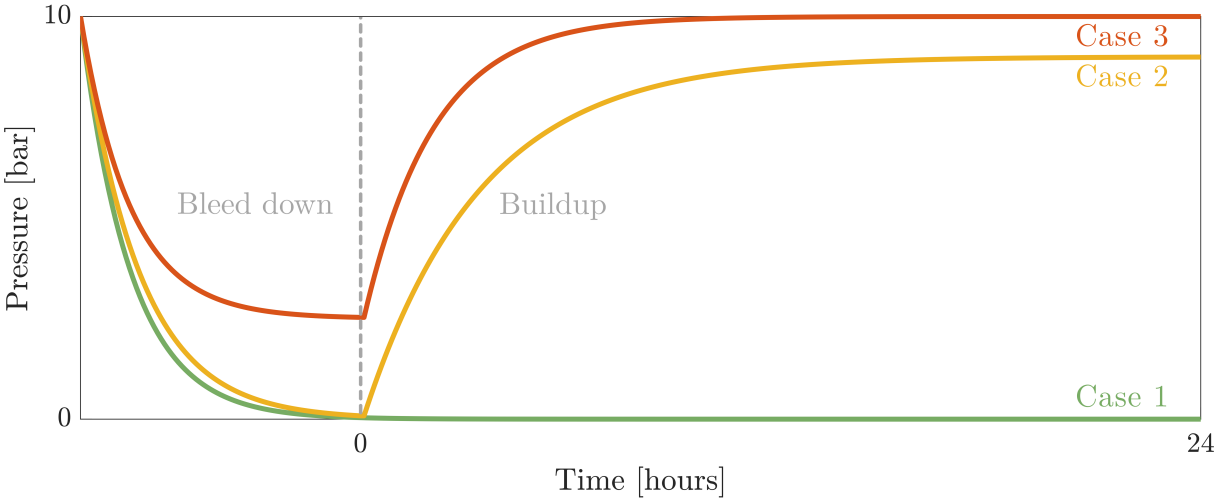


Figure 30: Different cases for *bleed-down/build-up tests* performed at the wellhead by releasing pressure from an annulus and observing the pressure development for 24 hours. Case 1 represents an annulus with a thermally induced or anomalous non-sustained pressure; no pressure build-up is observed after the bleed-down phase. Case 2 is a moderately leaking scenario; Case 3 represents a severe leak. Figure concept based on Kazemi and Wojtanowicz (2022), modified after Schulz et al. (2025)

In contrast to the USA's offshore regulations for federal waters, onshore wells and wells in state waters are regulated by individual states with considerable differences (Figure 31, Supplementary Material 2 of Schulz et al., 2025). Diagnostic pressure testing procedures are mentioned only in five states, usually for all annuli. In Alabama, Alaska and New Mexico, B/B test variations are required, with differing pressure recording practices, bleed-down times, and build-up times (Alaska Oil and Gas Conservation Commission, 2021; New Mexico Energy, Minerals and Natural Resources Department, Oil Conservation Division, 2020; State Oil and Gas Board of Alabama, 2025). Colorado requires the most detailed testing: tubing and casing pressures are recorded; the annulus valve is opened; a fluid sample is taken, if possible; and the tubing and casing pressures are recorded at five-minute intervals for 30 minutes. At the end of the test, the annulus is shut in, the instantaneous pressure is recorded, and an end-of-test fluid sample is collected. The procedure is repeated for all annuli (Colorado Energy and Carbon Management Commission, 2021).

Reporting requirements also vary between states, and reports often have to be filed if certain thresholds are exceeded. In Alaska, Florida and North Carolina, diagnostic flow testing is prescribed, which involves flow rate measurements (Alaska Oil and Gas Conservation Commission, 2021; Florida Department of Environmental Protection, 1996b; North Carolina Department of Environmental Quality, 2015). Overall, either pressure or flow testing, or both, are required in 12% of U.S. states. More information and references for state regulations are compiled in Supplementary Material 2 of Schulz et al. (2025).

China's guidelines suggest a test similar to the API RP 90 B/B test (China National Offshore Oil Corporation, 2018; China National Petroleum Corporation, 2022).

Russian regulations also prescribe diagnostic testing through annulus pressure manipulation (Rostekhnadzor, 2020). The testing method involves pressurizing the annulus with drilling fluid or air. If the annular pressure drops by more than 0.5 MPa within the following 30 minutes, the annulus is considered not tight. However, the regulations do not explicitly state whether an annulus that exhibits such a pressure drop should be classified as experiencing SCP. Leaks must be repaired before abandonment and before any stimulation or other near-wellbore treatments are performed. If any annular pressure due to leaks (SCP) is detected, well operation has to be stopped. The operator is then responsible for identifying and eliminating the causes of SCP and making decisions regarding further well operation.

In **Canada**, operators are often required to continuously vent surface casing annuli to prevent pressure build-up and protect groundwater. Consequently, Canadian regulations focus on SCVF rather than SCP. The provinces of Alberta and British Colombia recommend multiple diagnostic tests for SCVF, including bubble tests (Alberta Energy Regulator, 2022; British Columbia Energy Regulator, 2023). During a bubble test, one end of a hose is connected to the surface casing annulus vent while the other end is submerged in water. If bubbles are observed in the water (or SCVF is detected by other methods), the flow rate through the surface casing vent and the stabilized shut-in surface casing pressure have to be determined in Alberta and British Columbia. Additionally, British Columbia requires build-up pressure tests upon SCVF detection. The suggested bubble test frequency for new wells is yearly (Alberta Energy Regulator, 2022; British Columbia Energy Regulator, 2023).

In Alberta and British Columbia, if SCVF is detected, testing must be repeated annually in the following years (Alberta Energy Regulator, 2022; British Columbia Energy Regulator, 2023). Testing for SCVF is also required in the Northwest Territories, Nunavut and New Brunswick at specific stages in the lifecycle of a well, such as prior to abandonment (Figure 31; Canadian National Energy Board, 2013; Government of New Brunswick, 2021; NWT Office of the Regulator of Oil and Gas Operations, 2022). Overall, 38% of the Canadian provinces and territories require diagnostic testing. The Energy Safety Canada IRP 27 guideline (Energy Safety Canada, 2022) likewise addresses aspects of SCVF testing, focusing on source identification through methods such as carbon isotope data analysis and outlining appropriate remediation techniques.

British Columbia and Alberta also require operators to test wells for gas migration. According to the British Columbia Energy Regulator (2023), gas migration may be identified through surface indications such as bubbles in ponds, stressed vegetation, or unusual gas odours. For gas migration testing, soil samples are taken within a 6 m radius around the well to measure gas concentrations. Both provinces require SCVF and gas migration testing at specific stages in the well lifecycle, such as after drilling-rig release or prior to abandonment.

In Norway, diagnostic testing is not required by regulation. However, the 117 Offshore Norge guideline recommends such tests (Norwegian Oil and Gas Association, 2017). According to this industry guideline, annular pressures correlate with temperatures when the pressure is thermally induced, while a lack of correlation indicates SCP. Once SCP is suspected, the guideline recommends identifying the leak path by manipulating the annulus pressure. For this purpose, bleed-down and pressure-application procedures are suggested, although no further operational details are provided. The document additionally recommends measuring leak rates, maximum stabilized annular pressure, and the volume of flammable hydrocarbons present in annuli. Mitigation and remediation techniques are also described. Furthermore, the guideline advises establishing a maximum allowable pressure-change criterion and recommends halting normal operations if barriers fail, are impaired, or if allowable pressure limits are exceeded. In cases of barrier failure, restoration of the barrier is advised before resuming operations.

Australian regulations do not contain information on diagnostic testing.

The **International** Standard ISO 16530-1 (2017) recommends source identification in case of a high annulus pressure by reviewing the well history, performing B/B tests, or manipulating the neighboring annulus pressures. This standard does not allow leaks to the surface, subsurface, or a well barrier that cannot withstand the new pressures.

4.2.5 Pressure and flow thresholds

Pressure thresholds are recommended or prescribed pressure values that are assumed to be safely applicable to an annulus. These thresholds are usually based on the strength of the weakest well component and incorporate a safety factor. The components included in the threshold calculation vary from country to country.

In the **USA**, thresholds are defined both in regulations and in industry guidelines. The API RP 90 offshore industry guideline considers only the strength of tubulars, such as casings and tubings (American Petroleum Institute, 2006). The guideline recommends calculating the strength of an annulus's inner, outer, and next outer tubular and multiplying these values by a safety factor of less than 1. API RP 90 defines the Maximum Allowable Wellhead Operating Pressure (MAWOP) as the lowest of the resulting values. The same approach is used in offshore regulations issued by the Bureau of Safety and Environmental Enforcement (2009). In contrast, the API industry guideline for onshore wells (API RP 90-2) considers not only tubular strength but also wear and corrosion, wellhead failure, completion equipment failure, and formation fracturing at the casing shoe when determining the MAWOP (American Petroleum Institute, 2016).

Furthermore, the onshore API RP 90-2 guideline recommends establishing upper and lower diagnostic thresholds (DT) as an early-warning system to provide operators sufficient time to respond to pressure changes before they reach critical levels. The upper DT should be

set below the MAWOP to leave enough response time for a bleed off. The lower DT is recommended to be set below the sum of the operator pressure and thermal effects, yet high enough to ensure a prompt response to communication between annuli.

In U.S. onshore regulations, pressure thresholds are specified in 14 states (28%) as well as on public lands (Supplementary Material 2 of Schulz et al., 2025). In four states, the threshold is based on the strength of well components, whereas five other states use absolute pressure values. For example, in Colorado the annular pressure threshold is defined as 30% of the true vertical depth of the surface casing (Colorado Energy and Carbon Management Commission, 2025). This well-specific approach maintains annular pressures below the hydrostatic gradient in the formation at the bottom of the surface casing to prevent gas migration and protect groundwater. If the annular pressure threshold is exceeded, diagnostic testing must follow. There are no flow thresholds in states that require open annuli. However, Florida, North Carolina and New Mexico require remediation or further testing if fluids leak from annuli or if loss of well integrity is discovered (Florida Department of Environmental Protection, 1996a,b; New Mexico Energy, Minerals and Natural Resources Department, Oil Conservation Division, 2020; North Carolina Department of Environmental Quality, 2015). This can be considered a qualitative flow threshold.

In **Canada**, regulations of two jurisdictions include pressure thresholds. In New Brunswick, hydraulic fracturing must cease if an annular pressure increases by more than 35 bar (Government of New Brunswick, 2021). The Northwest Territories use a qualitative threshold: if testing indicates SCP or CVF in any annulus other than the surface casing annulus or annulus A, the regulator must be notified, and remediation is required for suspended and abandoned wells (NWT Office of the Regulator of Oil and Gas Operations, 2022).

Additionally, Canadian regulations classify SCVF and gas migration based on their escalation potential, effectively establishing thresholds. In Alberta and British Columbia, SCVF is categorized as either "serious" or "non-serious", with largely similar criteria, although minor differences exist. These classifications and all of the following associated details for both provinces are drawn from the Alberta Energy Regulator (2022) and British Columbia Energy Regulator (2023).

According to both regulators, a "serious" classification applies when the flow rate exceeds 300 m^3/day[32] or if qualitative criteria are met, such as a public safety risk or casing failure. The criteria for "serious" gas migration are similarly based on qualitative considerations (e.g., public safety risk) in both provinces. If these conditions are not met, SCVF or gas migration is classified "non-serious". In Alberta, "serious" SCVF or gas migration have to

[32]In British Columbia, SCVF must furthermore not exceed 100 m^3/day, which is specified independently of the "serious"/"non-serious" classification (Government of British Columbia, 2023).

be repaired within 90 days. In British Columbia, the regulator has to be contacted for repair work, and "serious" cases require repair as soon as possible. For "non-serious" SCVF and gas migration, repair work can be deferred until abandonment. Similar requirements are outlined in the regulations of New Brunswick and the Northwest Territories (Government of New Brunswick, 2021; NWT Office of the Regulator of Oil and Gas Operations, 2022). Overall, pressure thresholds, flow thresholds, or both are specified in 31% of Canadian provinces and territories.

Several countries apply approaches similar to those used in the USA for the calculation of MAWOPs or Maximum Allowable Annulus Surface Pressures (MAASP). Typically, the strength of well components is included, as outlined in **Chinese** guidelines (China National Offshore Oil Corporation, 2018; China National Petroleum Corporation, 2022). The ISO 16530-1 (2017) and ISO 16530-2 (2014) standards additionally include fluid and rock pressure gradients.

The **Norwegian** 117 Offshore Norge guideline (Norwegian Oil and Gas Association, 2017), as well as ISO 16530-1 (2017) and ISO 16530-2 (2014), also recommend setting diagnostic thresholds. According to the 117 Offshore Norge guideline, leak rates in an annulus of up to 0.42 m^3/day are acceptable. In contrast, the Norwegian NORSOK D-010 guideline considers any leak rate above 0 m^3/day as unacceptable (Norwegian Oil Industry Association and Federation of Norwegian Manufacturing Industries, 2021).

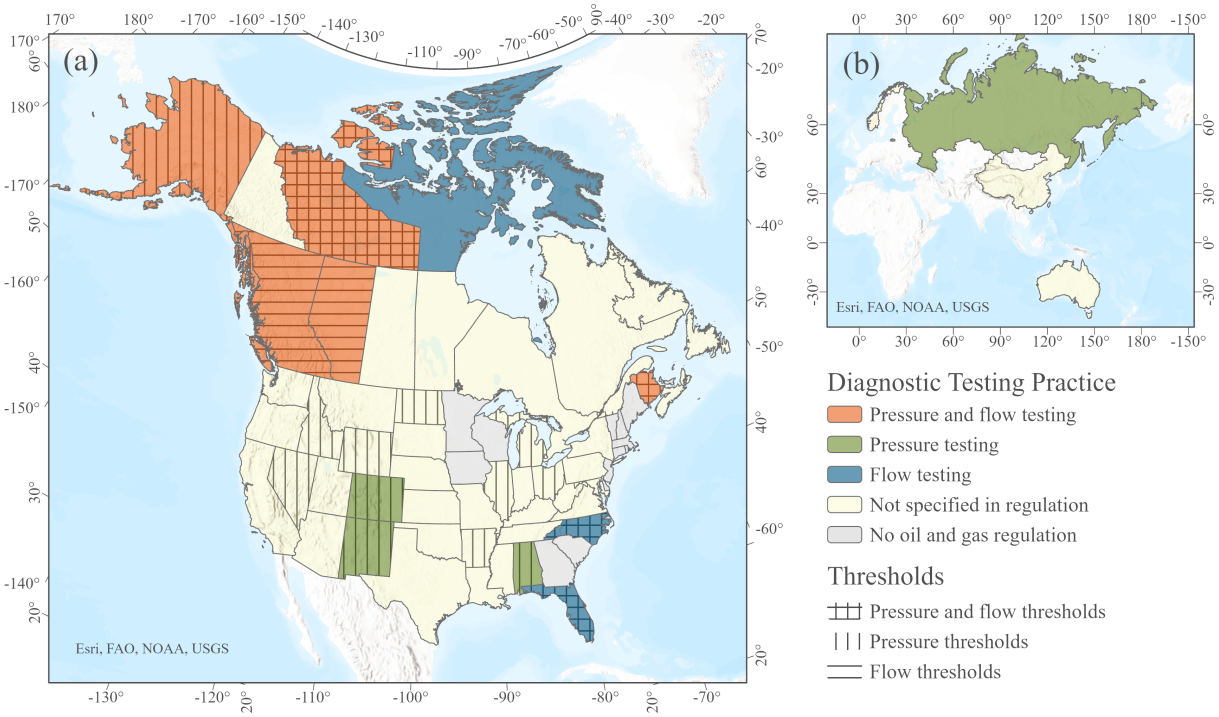


Figure 31: Map of diagnostic testing requirements (Section 4.2.4) and thresholds (Section 4.2.5) as outlined in regulations of a) the USA and Canada and b) Norway, Russia, China and Australia. Reproduced from Schulz et al. (2025), shapefiles from Esri (2017, 2022) and Statistics Canada (2023). Projections: a) Albers equal-area conic, b) Mercator

4.2.6 Barrier classification

Wells are classified in a traffic light system based on barrier integrity in China's and Norway's guidelines (Table 16). Three regulatory documents define both the criteria and recommended actions for each category, escalating from regular protocols to increased monitoring and, if necessary, remediation as barrier integrity declines. While the classifications are similar overall, the details differ between documents.

Table 16: Traffic light classification of wells based on barrier integrity in Chinese and Norwegian guidelines. **C** denotes classification criteria; **R** denotes recommended actions. Reproduced from Schulz et al. (2025)

		China (CNOOC) *China National Offshore Oil Corporation (2018)*	**China (CNPC)** *China National Petroleum Corporation (2022)*	**Norway** *Norwegian Oil and Gas Association (2017)*
Green	**C**	No or minor problems with both barriers	Both barriers intact	No leaks through both barriers and acceptable annulus pressures and leak rates
	R	Follow regular protocols	Follow regular protocols	Follow regular protocols
Yellow	**C**	One barrier intact, the other degraded	The first barrier is intact while the second is damaged, or the first barrier is damaged and the second is compromised with a low risk	One barrier intact, the other degraded
	R	Enhanced monitoring	Maintenance, risk reduction measures, detailed monitoring	Follow regular protocols
Orange	**C**	One barrier failed, the other intact; or both barriers degraded; or a single hazard could cause the failure of both barriers	The first barrier either failed or is damaged, while the second is intact or damaged with a medium risk level	One barrier failed, the other intact, or a single failure may lead to a surface leak
	R	Risk analysis, maintenance and risk reduction measures	Develop an emergency plan, evaluate problems, adjust monitoring, control production, and risk reduction measures	Repair or mitigation (but typically not immediately)
Red	**C**	One barrier failed, the other degraded/not validated, or there is a surface leak	Both barriers failed or are damaged with a high risk, or there is a surface leak	One barrier failed, the other degraded or not verified, or there is a surface leak
	R	Immediate disposal and detailed risk analysis	Develop an emergency plan and implement risk reduction measures immediately	Immediate repair or mitigation

5 Discussion

5.1 Overview

Understanding the occurrence of SCP and CVF and ensuring well integrity involve inherently multi-scale challenges, ranging from physico-chemical processes at material interfaces to field-scale well behavior and the development and implementation of regulatory management strategies. The previous chapters investigated these different scales through experiments, numerical modeling, and a comparative compilation of regulatory approaches.

Building on these findings, this chapter first discusses the experimental and numerical results. The interpretation focuses on the insights that can be derived from the observed behavior, as well as the assumptions and limitations of the numerical model. By examining these processes at laboratory and larger scales, a better quantitative understanding of the mechanisms governing SCP and CVF can be achieved and linked to field-scale well behavior.

Because the implications of leakage extend far beyond the experimental scale, the discussion subsequently broadens toward regulatory and operational aspects of SCP and CVF management. The different regulatory approaches described in Section 4.2 are compared with regard to their scope, enforcement mechanisms, and their respective strengths and limitations. Based on this analysis, recommendations are derived concerning suitable regulatory elements and minimum workflow requirements for effective SCP and CVF management. Combined, these aspects link laboratory-scale leakage processes to practical well integrity challenges and the regulatory strategies intended to address them.

5.2 Evaluation of autoclave experiment results

5.2.1 Background and context

To better understand the mechanisms contributing to annular gap formation and SCP, experimental and modeling results are discussed in the following sections. Previous investigations using the same autoclave system primarily addressed the overall integrity of the cement–steel composite and performed long-term experiments on the corrosion of wellbore sealing systems under CO_2 exposure without cyclic loading (Schilling et al., 2015, 2016). These studies[33] derived gap apertures on the order of 13 µm (Schilling et al., 2015) and 5 µm (Klose et al., 2021), which is consistent with the gap apertures observed at the beginning of experimental series in the present study (Figure 35).

[33]These studies are based on different underlying assumptions. Schilling et al. (2015) assumed an annular gap width w equal to half of the cement–steel interface, whereas Klose et al. (2021) considered the full interface.

Other studies incorporating cyclic loading predominantly investigate the interface between a casing and the surrounding cement sheath, with pressure applied internally to the unfilled casing (Section 1.5). This represents a fundamentally different loading configuration, as it simulates internal casing pressure rather than gas pressure acting on the exposed end of a cement-filled casing, as expected in abandoned wells within active underground gas storage sites. Consequently, the results of these studies are not directly comparable to those obtained in the present work. Nevertheless, the order of magnitude of the gap apertures observed in the present study (typically 5–50 µm) is consistent with values reported in the literature, which generally range from a few micrometers up to approximately 200 µm (Chu et al., 2015; Moghadam et al., 2022; Stormont et al., 2018; Xi et al., 2021).

Experimental investigations specifically addressing cyclic pressure and thermal loading applied to cement-filled casings remain limited. The experimental configuration used in this study therefore provides a novel framework for investigating well integrity degradation mechanisms under conditions representative of gas storage wells. The present study primarily focuses on the effects of cyclic pressure and thermal loading on system permeability and, additionally, examines the interaction between cement aging and cyclic loading. Accordingly, the following discussion evaluates how these factors influence annular gap evolution and the overall sealing performance of the cement–steel system.

5.2.2 Potential cement matrix flow

In the conducted experiments, gas flow through the cement-filled casing may occur via three primary pathways: (1) annular gap between casing and cement, (2) pore space of the cement matrix, or (3) cracks within the cement. The hypothesis tested in this section is that gas flow predominantly occurs through the annular gap, as assumed in the model.

Cement samples used for matrix permeability measurements were examined microscopically to assess the presence of cracks. All investigated samples exhibited some degree of cracking. Representative examples are shown in Figures 32 and 33.

However, no clear correlation between visible crack width and measured matrix permeability is apparent. For example, the autoclave sample of casing 1 shows smaller cracks but a higher measured matrix permeability than the control sample of casing 3 (Figures 32 and 33, Table 11). It should be noted that the prominent crack in Figure 33 was only visible on one side of the sample, suggesting that such cracks may not extend completely through the cement matrix. This may explain the lack of correlation between crack size and measured matrix permeability.

Nevertheless, the possibility of gas flow through cracks cannot be fully excluded based on this observation. Some cracks exhibit dimensions on the same order of magnitude as modeled annular gaps, which could enable gas migration if the cracks are interconnected.

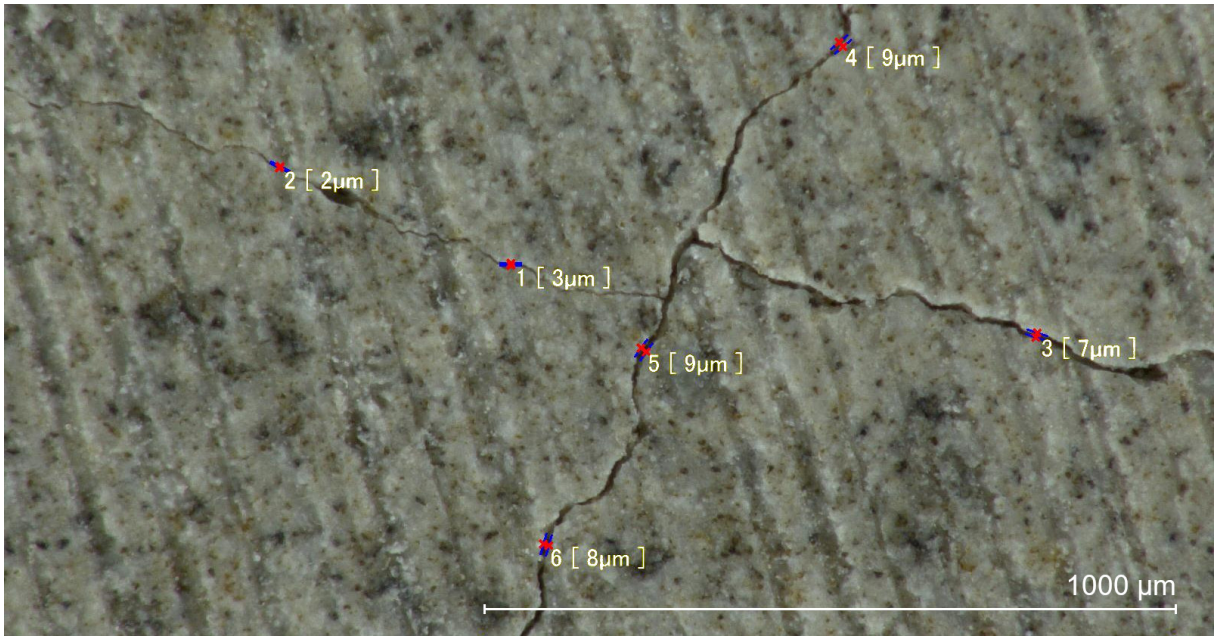


Figure 32: Cracks in the autoclave cement sample of casing 1

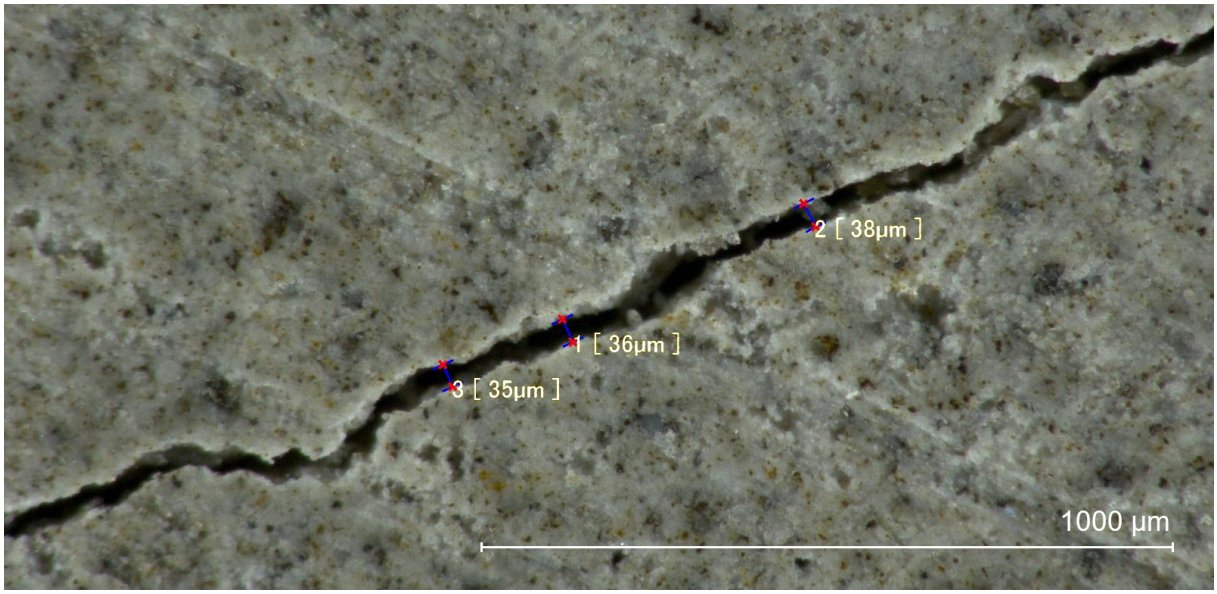


Figure 33: Cracks in the control cement sample of casing 3

However, gas flowing predominantly through cracks or the cement pore space would require sufficiently high matrix permeabilites to match the flow durations observed during the autoclave experiments. The model-derived matrix permeability at the end of an experimental series lies on the order of 10^{-14} – 10^{-13} m^2, which would be expected to match the measured values from the autoclave samples shown in Table 11 if the gas transport were dominated by flow through the cement matrix or cracks. However, all autoclave samples show lower measured matrix permeabilities on the order of 10^{-18} – 10^{-15} m^2 (Figure 34), which fall even below most initial and control samples. This is

unexpected, as autoclave samples, which were flushed with dry gas, would typically be assumed to have higher matrix permeabilities than other samples due to potential drying of the cement.

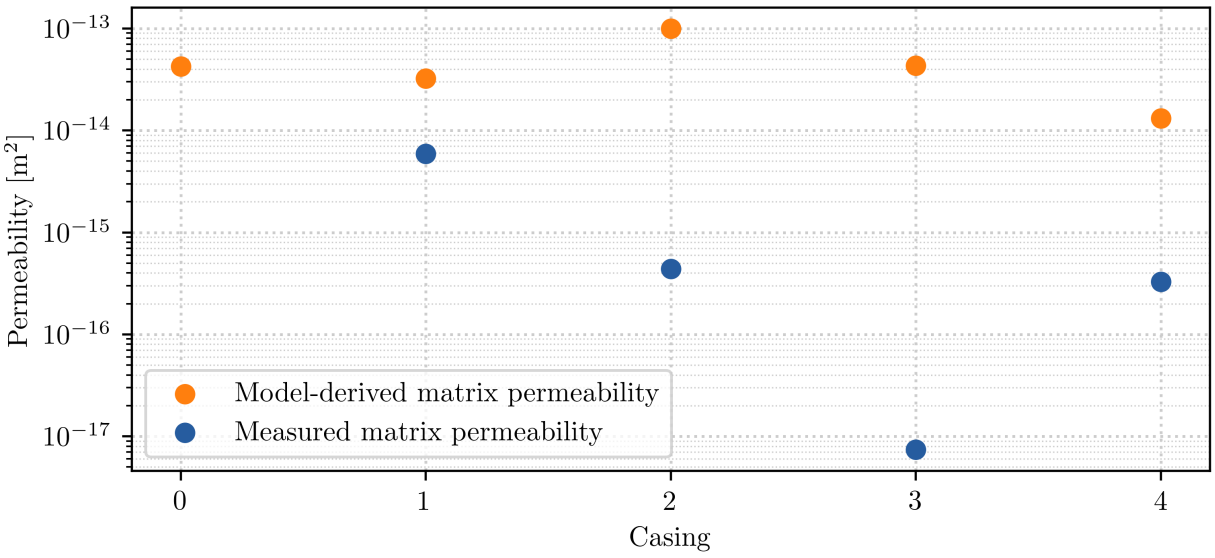


Figure 34: Comparison of model-derived and measured matrix permeabilities. The depicted model-derived permeability is the arithmetic mean of the last ten experiments of each casing, representing the permeability at the end of the experimental series. Similarly, the depicted measured permeability corresponds to the arithmetic mean of the autoclave samples for each casing (Table 11). This means the cement was subjected to cyclic loading in the autoclave system and measured after removal, also representing the end-of-series permeability. For comparison, the literature review by Harooni et al. (2025) suggests that typical Class G and H cement permeabilities are often on the order of 10^{-17} m^2 or lower, which is consistent with the value obtained for the autoclave sample of casing 3.

The inconsistencies in matrix permeability measurements (Table 11) suggest limited reliability of the data, likely due to variations in sample conditioning and associated difficulties in achieving constant weight. Furthermore, mechanical damage introduced during sawing, drilling or conditioning can be considered a likely primary cause of the observed cracks. As such, the actual in-situ matrix permeability of the cement during the experiments was likely lower than the values shown in Table 11.

Moreover, Schilling et al. (2015, 2016) observed carbonation along the lateral surface of the cement inside the casing during earlier, similar experiments involving CO_2. This indicates that CO_2 reacted with the cement along the casing wall and suggests the presence of a gap or imperfect bonding between steel and cement.

Combined, these observations indicate that major gas flow through cracks or the cement matrix is unlikely. Nonetheless, a certain degree of gas flow through cracks cannot be entirely excluded. This may be particularly relevant in early-stage experiments conducted shortly after cement placement, when bonding between casing and cement may still be intact. However, due to the limitations of the available data, the lack of evidence for continuous cracks, and the likely low matrix permeability of the cement matrix, annular

gap apertures are modeled under the assumption that gas flow occurs exclusively through the gap.

In any case, the modeled gap apertures and matrix permeabilities can both be interpreted as quantitative indicators of the system permeability and are therefore suitable for comparative analysis. For future experiments where the relative contributions of crack and gap flow are known or can be better estimated, the model can be adapted accordingly to determine the respective matrix permeabilities and gap apertures.

5.2.3 Effects of thermal loading cycles

This section discusses the effect of cyclic thermal loading on system permeability. The results indicate that thermal loading cycles temporarily decrease the system permeability, as observed in several cases immediately following a thermal loading cycle[34] (Figure 35). Over the course of the subsequent experiments, the system permeability frequently increases again. Notably, such increases can also be observed in cases where no additional loading was applied after a thermal loading had caused an apparent system permeability reduction.

One possible explanation for this behavior is thermally induced volumetric changes of the cement and steel, which temporarily alter the gap aperture. However, these effects are unlikely to produce lasting changes under the present experimental conditions, as all permeability measurements were conducted at approximately 70 °C. Moreover, during cooling, steel contracts more strongly than hardened cement due to its higher thermal expansion coefficient, which would tend to reduce rather than increase the gap aperture (e.g., Bredemann, 2025).

Another explanation is the formation of a water film within the annular gap. The presence of liquid water would hinder gas flow and thereby reduce the apparent system permeability. Although the injected nitrogen was dry, cement generally contains a substantial amount of water. It is therefore plausible that water in the gap originated from the cement. Temperature-dependent dehydration reactions of cementitious phases, however, can be excluded as a dominant mechanism, since these reactions occur only at considerably higher temperatures (e.g., Alonso and Fernandez, 2004; Shui et al., 2009; Zhang and Ye, 2012).

Nevertheless, cement also contains free pore water, and measurements indicate that the cement inside the autoclave lost water during the experimental series (Table 10). This suggests that a fraction of the pore water may have evaporated and contributed to humidity within the autoclave atmosphere.

An explanation for the apparent temporary decrease in system permeability after thermal loading is therefore the condensation of water within the annular gap. Typical tempera-

[34] A thermal loading cycle consists of cooling the gas in the upper chamber from 70 °C to 30 °C and subsequently reheating it to 70 °C (see Section 2.3).

ture changes in the experiments involved cooling from 70 °C to around 30 °C or lower, accompanied by a pressure drop from 60 to 50 bar due to the cooling, while the amount of substance and chamber volume remained constant.

At 30 °C the saturation vapor pressure of water is 4.2 kPa, compared to 31.2 kPa at 70 °C (The Engineering ToolBox, 2004). The critical water vapor mole fraction in the gas necessary for condensation at 30 °C can be estimated from the saturation vapor pressure and total gas pressure of 50 bar as follows (Atkins and de Paula, 2006, ch. 6.3):

$$\text{Critical water vapor fraction} \approx \frac{0.042\ \text{bar}}{50\ \text{bar}} \approx 0.085\%$$

Accordingly, at 30 °C, a water vapor mole fraction as low as 0.085% in the gas is sufficient to initiate condensation.

Furthermore, the critical relative humidity at 70 °C required for condensation upon cooling to 30 °C was determined. Relative humidity is defined according to Equation 43 (Lovell-Smith and Pearson, 2006). Assuming ideal gas behavior at constant amount of substance and constant autoclave volume, Equation 44 follows (Parish and Putnam, 1977). For condensation to occur at 30 °C, the condition $P_{30}^{\mathrm{H_2O}} \geq P_{30}^{\mathrm{sat}}$ must be satisfied, which yields Equation 45.

$$\phi_{70} = \frac{P_{70}^{\mathrm{H_2O}}}{P_{70}^{\mathrm{sat}}} \Rightarrow P_{70}^{\mathrm{H_2O}} = \phi_{70} \cdot P_{70}^{\mathrm{sat}} \tag{43}$$

$$P_{30}^{\mathrm{H_2O}} = P_{70}^{\mathrm{H_2O}} \cdot \frac{T_{30}}{T_{70}} = \phi_{70} \cdot P_{70}^{\mathrm{sat}} \cdot \frac{T_{30}}{T_{70}} \tag{44}$$

$$\phi_{70}^{\mathrm{crit}} \geq \frac{P_{30}^{sat}}{P_{70}^{sat}} \cdot \frac{T_{70}}{T_{30}} \tag{45}$$

ϕ_{70}	Relative humidity at 70 °C [-]
$\phi_{70}^{\mathrm{crit}}$	Critical relative humidity at 70 °C that allows condensation when cooled to 30 °C [-]
$P_{70}^{\mathrm{H_2O}}, P_{30}^{\mathrm{H_2O}}$	Water partial pressures at 70 °C and 30 °C [Pa]
$P_{70}^{\mathrm{sat}}, P_{30}^{\mathrm{sat}}$	Saturation vapor pressures of water at 70 °C and 30 °C [Pa]
T_{70}, T_{30}	Temperatures of 70 °C and 30 °C in Kelvin [K]

It follows from this calculation that a relative humidity of 15.4% at 70 °C is sufficient for condensation to occur upon cooling to 30 °C. Assuming that the according amount of water can be delivered by the cement, condensation during cooling can be expected.

To assess whether the amount of water potentially available for condensation is sufficient to influence the flow behavior in the annular gap, a simple order-of-magnitude estimate was performed. For a gap with a width of 20 cm, a length of 2 m and an aperture of 30 µm, the total gap volume is approximately 12 mL. Assuming that the gas within the

gap is saturated with water vapor at 70 °C, the amount of water that could potentially condense upon cooling can be estimated using the ideal gas equation. The corresponding amount of condensate is on the order of a few microliters (approximately 2.3 µL for the gap volume considered). Although small in absolute terms, such quantities may still accumulate at local constrictions within the narrow annular gap, and thereby temporarily reduce the effective system permeability. In addition, condensation within the upper chamber may allow water to accumulate at the entrance of the annular gap or potentially penetrate into it, which could further contribute to a temporary reduction in effective system permeability.

Because of its high thermal conductivity and small wall thickness, the steel casing is expected to cool more rapidly than the cement and chamber walls. Consequently, condensation is most likely to occur at the casing–cement interface. Upon reheating to 70 °C, the condensed water would normally be expected to evaporate. However, the annular gap is largely isolated from the autoclave chambers, except for small openings at the top and bottom of the casing. As shown by Kolliopoulos et al. (2022), evaporation in confined microchannels is considerably slower than in more open geometries.

The precise geometry of the annular gap and the extent of water saturation are unknown. Nevertheless, as long as no permeability tests or pressure loading cycles are performed, gas circulation is restricted. If water is present in the gap, evaporation is expected to be slow due to the limited gas exchange area. This interpretation is supported by quick reference tests: Ten milliliters of water placed on an open glass surface at 26 °C and 70% relative humidity evaporated within three hours, whereas an equal volume covered by acrylic glass remained almost unchanged after three days.

Therefore, it can be concluded that cooling probably led to condensation of water within the gap, which largely persisted even after reheating. This reduced the apparent system permeability[35] in subsequent experiments. However, during system permeability experiments, gas flow through the gap may have promoted evaporation or physically displaced the condensed water, causing an apparent system permeability increase as gas flow through the gap became less obstructed by water.

This hypothesis is further supported by the observation that a single thermal loading cycle often produced a measurable effect, whereas multiple consecutive thermal cycles without intermediate pressure or non-loading phases (Figure 21) had a substantially reduced impact on the system permeability after the first cycle. Following the initial cycle, condensation likely occurred as described above. Subsequent permeability experiments

[35]Due to the small volume of the gap, only a limited amount of water can condense. However, even a thin film may already be sufficient to hinder gas flow to some extent. Transport processes might also cause water to accumulate at constrictions. The detailed transport processes involved are beyond the scope of this study.

may have partially removed or redistributed the water, but each renewed cooling phase probably effectively reset the process and caused re-condensation within the gap. The same reasoning could further explain why combined pressure-thermal cycles do not exhibit a particularly strong net effect, as the pressure-induced increase in permeability and the thermally induced decrease may partially counteract each other.

Finally, the interpretation presented in this section suggests that maintaining moisture within the cement sheath can be beneficial for reducing gas flow. Building on this, it is conceivable to discuss whether high-viscosity fluids placed above and below the annular gap could additionally impede gas flow. Such fluids would, however, need to penetrate the gap rather than merely overlying the cement sheath. Achieving this would likely require forcing the fluid into the annular gap. In practice, substances that harden after placement are probably more effective and are commonly used for this purpose. Most injection-based remediation operations rely on cement, known as *squeeze cementing* or *cement squeezing*, but resin systems have also been investigated as alternative sealing materials (e.g., Farkas et al., 1999; Izadi and Frigaard, 2026; Wang et al., 2021). Alternatively, instead of squeeze operations, Demirci and Wojtanowicz (2023) have demonstrated that placing a high-density, water-immiscible fluid on top of the cement sheath can also mitigate leakage by increasing the hydrostatic pressure acting on the annulus.

5.2.4 Effects of pressure loading cycles

This section discusses the effect of cyclic pressure loading on the evolution of system permeability. Generally, pressure loading cycles[36] appear to increase the system permeability (e.g., Figure 26). However, the permeability exhibits a saturation-type behavior, with little to no further increase after a certain number of cycles (Figure 35). Assuming the system permeability is exclusively controlled by the annular gap aperture h, it is reasonable to expect that the pressure-induced increase in h approaches a stable maximum. This reflects the physical limit of the space that can be created between cement and steel through pressure-induced debonding, without material erosion or further cement shrinkage.

However, while the gap aperture h is generally assumed to increase with progressing pressure loading cycles (see Section 1.5), it is unlikely to be the only factor governing gap permeability. In particular, the effective gap width w may also evolve during cyclic loading. Rather than assuming that 50% of the interface debonds instantaneously, it appears more plausible that a narrow flow channel forms initially and gradually widens with continued loading. Moreover, debonding is unlikely to occur uniformly along the interface. Instead, spatially heterogeneous gap geometries may develop, with locally wider and narrower sections and intermittent bonded contact zones.

[36] A pressure loading cycle consists of reducing the gas pressure in the upper chamber from 60 bar to atmospheric pressure and subsequently increasing the pressure again to 60 bar (see Section 2.3).

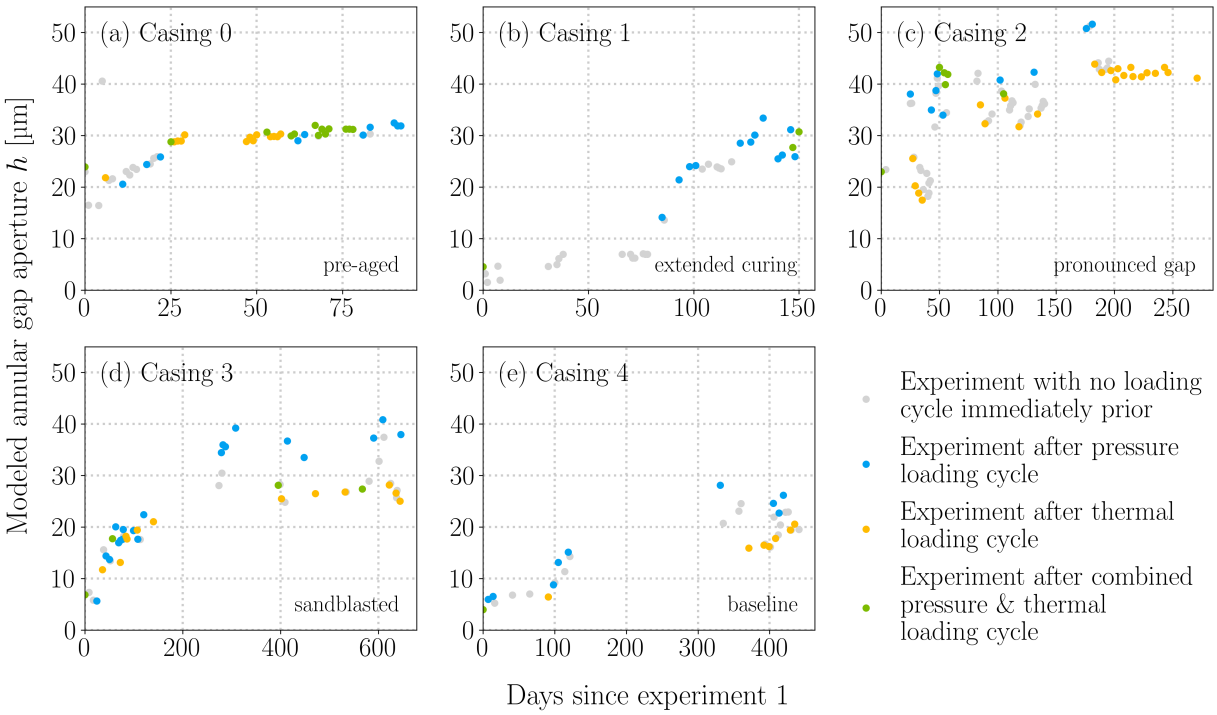


Figure 35: Results of model H based on the experiments that were carried out on all casings (Section 4.1.2). Figure 35 is a compilation of Figures 19 - 23. Casing 0 represents an older casing that had been subjected to loading and aging prior to this study and was filled with cement optimized for minimal shrinkage more than three years before the experiments of this study were conducted (Schilling et al., 2016). The cement of casing 1 underwent an extended curing period of approximately 5 months, while the cement of casings 2–4 cured for 28 days. Casing 2 displayed a pronounced, visible annular gap at the top (discussed in Section 5.2.5). Casing 3 was internally sandblasted to remove scale deposits before it was filled with cement, while casing 4 remained unaltered as a baseline.

Similarly to h, the effective gap width w would also be expected to approach a maximum under cyclic pressure loading, which might even correspond to full interface debonding. Even if this physical limit was not fully reached in the present experiments, both h and w influence the flow rate. Treating both parameters as independent fitting variables would therefore lead to non-unique parameter combinations. For comparability between experiments, w was kept constant in the model. The analysis therefore focuses on the modeled gap aperture h, which enters the flow equations with a cubic dependence and thus dominates the hydraulic resistance of the annular gap. Variations in w have a comparatively weaker effect: for example, doubling w would reduce the modeled value of h by only about 21% to reproduce the same flow rate.

While all casings show an apparent tendency for the modeled gap aperture h to approach a maximum, this behavior is most pronounced for casing 0, which had already been subjected to cyclic pressure loading prior to the experiments conducted in this study. After only three additional pressure cycles and one combined pressure–thermal cycle, the system permeability appears to increase only marginally with further loading (Figure 35a). This suggests that the gap geometry in casing 0 was already close to its upper limit before the

experiments conducted in this study, likely as a result of previous loading and aging. The additional cycles may have induced minor geometric adjustments, resulting in a small system permeability increase before stabilization.

One possible explanation for the comparatively linear increase in the modeled gap aperture h observed for casing 0 during the first 30 days (Figure 35a) is the presence of residual water within the annular gap. In this case, the apparent increase in h could partly reflect the progressive removal of water from the gap during the experiments, as discussed in Section 5.2.3, rather than actual geometric widening of the gap. This interpretation is consistent with the observation that the increase in h for casing 0 appears to occur largely independently of the applied loading type. However, this interpretation is highly speculative. Casing 0 would be expected to contain less residual water than the other casings, as it had been exposed to atmospheric conditions for approximately three years prior to the autoclave experiments, whereas the other casings had been filled with cement only shortly beforehand.

For other casings, the tendency toward a maximum gap aperture is also present, but less distinct. Typically, a steep increase in system permeability occurs at the beginning of an experimental series, followed by fluctuations between the post-increase value and higher values (with the exception of casing 2; see Section 5.2.5). This behavior indicates that an initial irreversible system permeability increase occurs, most likely due to progressive gap opening. Once this stage is reached, the baseline system permeability no longer increases systematically. Instead, reversible variations around a quasi-equilibrium system permeability are superimposed.

A possible explanation is that the gap has reached an effective maximum aperture and width. This established quasi-equilibrium could be temporarily disturbed by loading cycles, for example by increasing the gap aperture slightly on one side while decreasing it on the other. As subsequent loading can revert these changes, the result is not a single maximum gap aperture but rather a range. A narrow range seems possible once the system has stabilized sufficiently, as observed for casing 0.

For casings 3 and 4, pressure loading during the quasi-equilibrium stage was combined with thermal loading. Since thermal cycles tend to temporarily decrease the system permeability, both effects may overlap and partially counteract each other. In contrast, casing 1 was predominantly subjected to pressure loading, with only two combined pressure–thermal cycles during the quasi-equilibrium stage, which supports the interpretation of reversible system permeability fluctuations outlined above.

5.2.5 Additional effects on the system permeability

In addition to the effects of pressure and thermal loading, the evolution of system permeability may also be influenced by several secondary factors. One such factor is time. For all casings, a loading pause was introduced during the experimental series. For casings 0 and 1, this pause occurred before day 100 and did not affect the system permeability considerably (Figure 35a,b). For casing 0, the pause was introduced shortly after the system permeability had reached an approximate maximum, whereas for casing 1 it was implemented at the very beginning, before any loading had been applied or notable changes in system permeability had occurred.

For casings 2, 3, and 4, the pause was introduced after day 100 and was followed by higher system permeability values in the subsequent experiments (Figure 35c,d,e). A possible explanation is cement shrinkage leading to an increase in h, as shrinkage is known to promote the development of an annular gap (e.g., Oyarhossein and Dusseault, 2015). This mechanism likely played no notable role for casing 0 due to the several years old cement, since the majority of shrinkage typically occurs during early curing (e.g., Acker, 2004; Ghanem et al., 2024; Hansen, 1987; Sirtoli et al., 2020). Furthermore, the cement used in casing 0 was optimized for minimal shrinkage (Schilling et al., 2016).

However, for casings 2, 3, and 4 (Figure 35c,d,e) the pauses overlap temporally with the transition toward the quasi-equilibrium stage of the gap aperture described in Section 5.2.4. This overlap, combined with the limited number and duration of pauses, precludes a definitive assessment of time-dependent influences. Moreover, as the pauses were short compared to the preceding curing and experimental phases, substantial shrinkage during these intervals is unlikely. Shrinkage is most pronounced shortly after slurry placement, while the cement had cured for at least 28 days prior to casing installation in the autoclave system.

Nevertheless, shrinkage effects may still have contributed to the observed system permeability evolution. In casing 0, where the cement had undergone years of prior aging, most shrinkage-related deformation had likely been completed. In casings 1–4, some degree of shrinkage may have occurred during the curing phase, implying that even initial values of h were already influenced by early-age volume changes. As the casings were kept wet during curing, drying shrinkage may have commenced after installation in the autoclave system. The minor increase in h observed during the first 80 days of the casing 1 experimental series may reflect this transition (Figure 35b).

Casing 2 exhibits both relatively high initial ($\sim$20 µm) and high final (40–50 µm) values of h (Figures 35c and 36). Casings 1, 3, and 4 show markedly lower initial gap apertures (0–10 µm) and correspondingly lower final values (20–40 µm) (Figures 35b,d,e and 36). The cement of Casing 0 was optimized for minimal shrinkage, yet Casing 0 still exhibits a relatively large initial gap of 20 µm (Figure 35a and 36). This is likely attributable

to prior mechanical loading and aging, as earlier modeling indicated an annular gap of 5–13 µm after a pressure cycle and fluid interactions (Klose et al., 2021; Schilling et al., 2016). Thus, the true initial system permeability of casing 0 at the start of the past study was probably even lower. The final permeability of casing 0 is similar to that of casings 1 and 4.

Collectively, these observations suggest that the magnitude of the initial annular gap aperture exerts a controlling influence on the final gap aperture, with larger initial values tending to result in larger final values. This relationship indicates that the quality of cement placement, early-age curing, and initial bonding conditions may play a decisive role in determining the final system permeability. Proper cement placement therefore appears to be a critical factor, as both the initial and the final system permeability seem to be strongly governed by it. This suggests that achieving good initial bonding and sealing not only benefits the early system permeability but also supports long-term integrity and sealing performance.

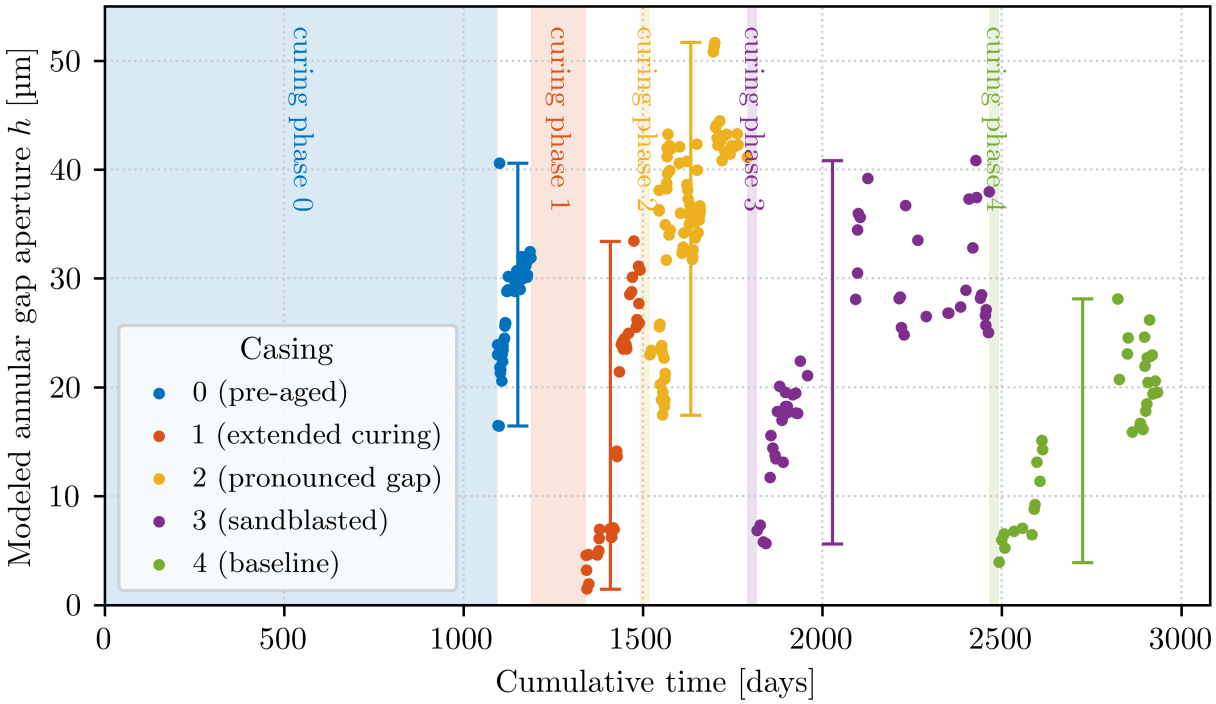


Figure 36: Modeling results and curing times of all casings. Curing phases follow the same indexing scheme as casings (curing phase x belongs to casing x). The vertical lines indicate the range of modeled values for each casing, extending from the minimum to the maximum value. Casing 0 represents an older casing that had been subjected to loading and aging prior to this study and was filled with cement more than three years before the experiments of this study were conducted. The cement of casing 1 had an extended curing period of approximately 5 months, while the cement of casings 2–4 cured for 28 days. Casing 2 displayed a pronounced, visible annular gap at the top (discussed in Section 5.2.5). Casing 3 was internally sandblasted to remove scale deposits before it was filled with cement, while casing 4 remained unaltered as a baseline.

Additionally, sample treatment appears to influence the development of the system permeability. In casing 3, the inner surface was sandblasted to remove the scale layer. Although the overall development of system permeability does not differ much from the other casings in terms of minimum and maximum values, more pressure cycles were required to reach the quasi-equilibrium stage, defined as the point beyond which cyclic loading no longer induces irreversible system permeability changes. This suggests that sandblasting slows down the debonding of cement and steel, but ultimately does not affect the maximum system permeability.

Such a treatment could therefore be beneficial for well operations, particularly if the delayed debonding prevents the maximum gap opening from being reached during the well's lifecycle. However, how this effect translates to hundreds of meters of casing-cement interface would need to be tested under field conditions. In practice, it might even be sufficient to sandblast only parts of the casing string.

The cement of casing 1 underwent a curing period that was 5.5 times longer than that of casings 2–4, whereas the cement of casing 0 had already aged for more than three years and experienced prior cyclic loading. Casing 1 exhibits the lowest initial system permeability of all experimental series, indicating initially favorable bonding conditions. However, the system permeability increases rapidly with pressure cycles, although the maximum permeability attained remains comparatively low. It remains unclear whether this behavior reflects an intrinsic effect of extended curing, such as improved cement microstructure and interfacial bonding, or whether it is primarily a consequence of the limited number of applied pressure cycles. This distinction cannot be resolved conclusively, as casing 4, which was subjected to even fewer cycles, exhibits an even lower final system permeability. Combined, these observations provide no clear evidence that extended curing time alone exerts a dominant control on the evolution or magnitude of system permeability under cyclic loading.

In contrast, casing 2 exhibits both the highest initial and highest final system permeabilities among all casings. It is also the only specimen in which a macroscopic annular gap is directly visible at the cement top (Figure 37), with an aperture of approximately 1 mm already present prior to installation in the autoclave (Figure 37a).

A possible explanation for this observation is the evaporation of water during the curing phase. In all casings, minor sedimentation occurred as denser particles of the slurry settled towards the bottom, resulting in the formation of a thin water layer on top of the cement column. In casing 2, however, this water layer was no longer present when the plastic sealing was removed after 28 days, indicating that evaporation had occurred due to insufficient sealing. The associated drying shrinkage likely induced tensile stresses at the cement–steel interface, ultimately causing interfacial debonding and the formation of the observed annular gap. The absence of a similarly large gap at the bottom of the casing

suggests that drying was spatially limited to the upper section of the cement column, where evaporation was most pronounced.

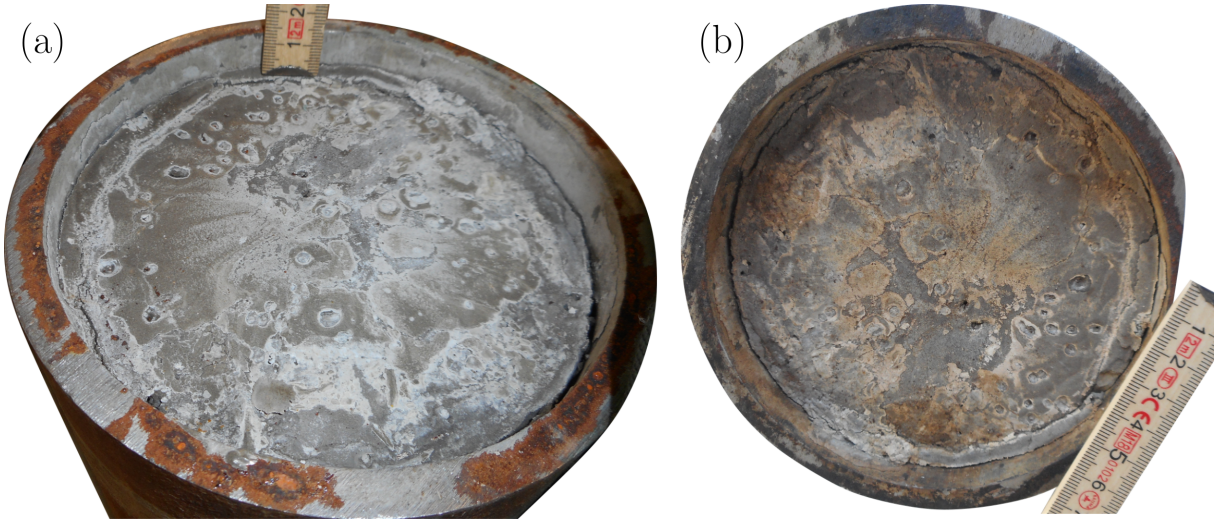


Figure 37: Cement of casing 2 before (a) and after (b) autoclave experiments, showing an annular gap at the cement top

Despite its localized origin, the presence of a large annular gap at the top of the cement column may have had a disproportionate effect on the system permeability evolution. Because this section already provided a hydraulically open pathway, the initial pressurization of the autoclave would have enabled rapid pressure transmission into the annular gap.[37] The elevated pressure within the open top section of the annular gap could then have acted on the cement–steel interface located below, which was not yet debonded. Owing to this locally high pressure, the interface below the initially open gap may have been forced to debond, resulting in the formation of a continuous annular gap from top to bottom before the first system permeability experiment.

The densities and other cement properties of the casing 2 autoclave sample are unremarkable compared with either the initial sample of casing 2 or the autoclave samples of the remaining casings (Table 10). Likewise, mineralogical data reveal no notable differences relative to the other samples (Table 12). However, the autoclave samples used for these analyses were obtained from the central portion of the cement column. Since the missing water at the top most likely affected only the upper section, the measured values do not capture the cement influenced by the assumed drying shrinkage.

[37] In principle, the approximately 1 mm wide opening of the annular gap at the top should be accounted for in the model. If this section is assumed to offer no resistance to gas flow, it could simply be subtracted from the effective height of the cement column. This was not done, however, because the depth extent of the widely opened section is unknown and it is unlikely to extend far downward. Moreover, test calculations showed that, if the open section is shallow, its effect on the results is minimal.

5.2.6 Implications for wells and future research

Practical relevance for wells and SCP

The experiments conducted in this study investigated two meters of cement–casing interface, whereas real wells typically contain hundreds to thousands of meters of such interfaces. Consequently, quantitative differences between laboratory observations and field-scale behavior are expected. Thermal loading effects at the scale of this work are unlikely to play a major role in real wells, primarily because boreholes commonly contain water that limits evaporative and condensational processes. Moreover, even if thermally induced condensation occurs, its influence on the system permeability appears to be transient rather than persistent.

In contrast, cyclic pressure loading was shown to induce permanent system permeability increases, most likely as a result of progressive debonding at the cement–steel interface. At field scale, this process is expected to occur more gradually due to the substantially greater interface length and the correspondingly larger total bonding area. Nevertheless, the cumulative effect of cyclic pressure loading over extended operational periods may still lead to measurable system permeability increases. Furthermore, gas mobility is likely reduced by the presence of fluids within real annular gaps. Additionally, external confining stresses imposed by the surrounding formation and internal casing pressure can reduce gap apertures in real wells (Moghadam et al., 2022; Stormont et al., 2018). Finally, cement formulation and the use of additives may further influence debonding behavior and system permeability evolution under field conditions.

Despite these differences in scale and boundary conditions, the modeling framework developed in this study can be extended to real wells. Given an effective annular gap aperture, the resulting flow rate or pressure build-up at the wellhead can be predicted. Conversely, effective gap apertures can be inferred from measured pressure build-up rates, analogous to the experiments of this work. Similarly, in annuli open to the atmosphere, effective gap apertures can be derived directly from measured gas flow rates.

For example, assuming a 500-meter-long well with a continuous gap aperture of 30 µm, a gap width of 0.2 m, no water in the gap, atmospheric pressure at the wellhead, and a reservoir gas pressure of 50 bar (corresponding to the hydrostatic pressure of a 500 m water column), the model predicts that approximately 24 hours would be required for the wellhead pressure to equilibrate after gas release, given an available gas volume of 5 liters at the wellhead. According to API RP 90, this would qualify as a *minor leak*, as long as the annulus pressure can be bled down to atmospheric pressure through a half-inch needle valve (Figure 30, American Petroleum Institute, 2006). Under the same assumptions, a continuous flow rate on the order of ∼25 L/h would occur if the annulus were open to the atmosphere.

In contrast, a *major leak* according to API RP 90 is defined by the inability to bleed annulus pressure down to atmospheric pressure through a half-inch valve. To evaluate this scenario, the flow capacity of a typical needle valve must first be determined. According to Samson AG (2012), the volumetric gas flow rate through the valve can be calculated using Equation 46 for subsonic flow ($P_{\mathrm{us}} < 2 \cdot P_{\mathrm{ds}}$) or Equation 47 for choked flow ($P_{\mathrm{us}} > 2 \cdot P_{\mathrm{ds}}$). Both equations represent simplified forms of those presented by DIN EN 60534-2-1 (2012).

$$\dot{V}_{\mathrm{G}} = 519 \cdot K_{\mathrm{v}} \cdot \sqrt{\frac{\Delta P_{\mathrm{val}} \cdot P_{\mathrm{ds}}}{\rho_{\mathrm{G}} \cdot T_{\mathrm{us}}}} \tag{46}$$

$$\dot{V}_{\mathrm{G}} = 259.5 \cdot K_{\mathrm{v}} \cdot P_{\mathrm{us}} \cdot \sqrt{\frac{1}{\rho_{\mathrm{G}} \cdot T_{\mathrm{us}}}} \tag{47}$$

$\dot{V}_{\mathrm{G}}$	Volumetric gas flow rate through the needle valve, related to 0 °C and 1.013 bar [m^3/h]
K_{v}	Metric valve flow coefficient; volumetric flow rate of water, expressed in m^3/h, measured at 20 °C under a pressure difference of 1 bar across the valve [-]
ΔP_{val}	Pressure difference across the valve ($P_{\mathrm{us}} - P_{\mathrm{ds}}$) [bar]
P_{us}	Absolute upstream pressure [bar]
P_{ds}	Absolute downstream pressure [bar]
ρ_{G}	Gas density at reference conditions of 0 °C and 1.013 bar [kg/m^3]
T_{us}	Upstream gas temperature [K]

Assuming that the annulus pressure at the wellhead cannot be fully bled down and a residual pressure of 0.5 bar above atmospheric remains, Equation 46 predicts a volumetric gas flow rate of approximately 20 m^3/h from the wellhead to the atmosphere through a typical needle valve with $K_{\mathrm{v}} = 1$. Maintaining such a residual pressure requires a continuous inflow of gas from the annulus at an equivalent rate, thereby establishing steady-state conditions between inflow and outflow.[38]

The gap aperture h required to sustain this flow can be estimated using a discrete Hagen–Poiseuille approach similar to model H, but assuming a constant mass flow rate and without temporal discretization, as the flow is stationary in this case. Accordingly, the annular gap is discretized only spatially and thermal effects are not considered. For each segment, the local volumetric flow rate is calculated from the constant mass flow rate and the gas density at the respective segment. Based on this volumetric flow rate, the

[38]The volumetric flow rate of 20 m^3/h is given at 1 bar and 20 °C. The actual volumetric flow rate into the wellhead is slightly lower than the volumetric flow rate out of the wellhead, because the pressure inside the wellhead exceeds atmospheric pressure. This is accounted for in the calculations.

pressure change across each segment is then determined from reservoir to wellhead using the Hagen–Poiseuille equation (Equation 10).

According to this approach, a gap aperture of approximately 280 µm is required to maintain a residual wellhead pressure of 0.5 bar with an open valve for the 500 m well described above, representing a conservative lower-bound estimate for a major leak. For comparison, maintaining a residual pressure of 49 bar under otherwise identical conditions would require an aperture of approximately 2700 µm. These estimates assume laminar flow and a completely dry annulus. The presence of liquids or turbulent flow components would further increase the required aperture, implying that the presented values represent conservative lower bounds.

In comparison, the maximum effective gap apertures derived from the cyclic loading experiments are approximately 50 µm. Based on the calculations presented above, apertures of 50 µm are insufficient to sustain a persistent wellhead pressure when the annulus is vented through a needle valve. Consequently, annular gaps formed solely as a result of cyclic pressure loading are unlikely to meet the API RP 90 criterion for a major leak. Instead, major leaks likely require the presence of additional high-conductivity pathways, such as mud channels.

This approach can be further condensed into a single equation. For this purpose, the Hagen–Poiseuille equation for stationary incompressible flow (Equation 10) is extended to stationary compressible flow. Under these conditions, an analytical integration along the flow path is possible, such that explicit spatial discretization is no longer required and a single governing equation is obtained.

For the standard Hagen–Poiseuille equation, this conversion from incompressible to compressible flow is, for example, demonstrated by Landau et al. (1987) or Bird et al. (2001) for an isothermal ideal gas. In this context, the pressure gradient $\Delta P/l$ (often also expressed as $\mathrm{d}p/\mathrm{d}x$) can be replaced by $(P_1^2 - P_2^2)/(2 \cdot l \cdot P_{\mathrm{ref}})$, where P_1 and P_2 denote the pressures at both ends of the flow channel, P_{ref} is the reference pressure at which the flow rate is specified, and l is the length of the flow path.

Mathematically, this substitution is justified by accounting for the variation of gas density with pressure under isothermal conditions. Inserting the ideal gas law into the Hagen–Poiseuille equation leads to an integrable form in which the pressure gradient term is proportional to the difference of the squares of the pressures at the channel endpoints.

By following this approach, Equation 10 can be adapted for stationary compressible flow (Equation 48) by replacing the pressure difference between both ends of the channel, ΔP_{cas}, with $(P_{\mathrm{res}}^2 - P_{\mathrm{wh}}^2)/(2 \cdot P_{\mathrm{atm}})$, where P_{res} denotes the reservoir pressure, P_{wh} the annulus pressure at the wellhead, and P_{atm} the atmospheric pressure.

For Darcy flow, an analogous transformation from the incompressible formulation (Equation 37) to the compressible formulation (Equation 9) can be applied (DAfStb, 1991).

Consequently, the effective system permeability for compressible gas flow can be calculated using Equation 49, which represents a well-scale formulation of Equation 9, originally defined for laboratory experiments.

$$h = \left(\frac{24 \cdot \dot{V}_{\text{out}} \cdot \eta \cdot l_{\text{well}} \cdot P_{\text{atm}}}{w \cdot (P_{\text{res}}^2 - P_{\text{wh}}^2)} \right)^{1/3} \tag{48}$$

$$K_{\text{Darcy}}^{\text{sys}} = \frac{2 \cdot \eta \cdot \dot{V}_{\text{out}} \cdot P_{\text{atm}} \cdot l_{\text{well}}}{A_{\text{an}} \cdot (P_{\text{res}}^2 - P_{\text{wh}}^2)} \tag{49}$$

h	Effective annular gap aperture [m]
$\dot{V}_{\text{out}}$	Volumetric flow rate from the annulus at the wellhead to the atmosphere, at atmospheric reference conditions [m^3/s]
η	Dynamic viscosity of the gas at atmospheric reference conditions [$Pa \cdot s$]
l_{well}	Length of the flow path, i.e. depth of the well [m]
P_{atm}	Reference pressure, here equal to atmospheric pressure [Pa]
w	Width of the annular gap [m]
P_{res}	Gas pressure at reservoir depth [Pa]
P_{wh}	Annulus gas pressure at the wellhead [Pa]
$K_{\text{Darcy}}^{\text{sys}}$	Specific system permeability coefficient [m^2]
A_{an}	Cross-sectional area of the annulus permitting gas flow [m^2]; $A_{\text{an}} = \pi \cdot (r_{\text{o}}^2 - r_{\text{i}}^2)$ with r_{o} = inner radius of the outer casing and r_{i} = outer radius of the inner casing

Using Equation 48 or Equation 49, several quantities of interest can be determined. For B/B tests exhibiting a major leak, where the annulus pressure cannot be fully bled down to atmospheric pressure, the effective annular gap aperture or the effective system permeability can be inferred. In this case, $\dot{V}_{\text{out}}$ corresponds to the gas outflow through the needle valve to the atmosphere and may be either measured directly or calculated using Equation 46 or Equation 47. Alternatively, for any arbitrary gap aperture or system permeability, the stabilized annulus pressure P_{wh} at the wellhead can be determined for a B/B test in which a bleed-down to atmospheric pressure is not possible.

Furthermore, Equation 48 and Equation 49 can be applied to annuli that are open to the atmosphere and show no pressure build-up at the wellhead, for example in wells exhibiting CVF. In this case, $\dot{V}_{\text{out}}$ is given by the measured volumetric flow rate from the wellhead to the atmosphere, with $P_{\text{wh}} = P_{\text{atm}}$, and the effective system permeability or gap aperture required to sustain this flow rate can be inferred. Conversely, the expected flow rate can be calculated if a specific gap aperture or system permeability is assumed.

As with all modeling approaches employed in this work, the present formulation represents an approximation of the physical system based on a set of simplifying assumptions. In particular, the compressible Hagen–Poiseuille formulation assumes ideal gas behavior, which is often not strictly valid. For example, under representative reservoir conditions corresponding to a depth of approximately 500 m (50 bar, 40 °C), methane exhibits a real gas factor of approximately $Z = 0.93$ (Wischnewski, 2007), indicating a deviation from ideal gas behavior ($Z = 1$).

Experimental transferability and outlook

In the present experiments, pressure was applied exclusively to the exposed bases of the cement column. In contrast, active wells are not completely filled with cement but contain an inner casing that is also subject to pressurization. When reservoir pressure changes occur in active UGS wells, two distinct effects arise: (i) pressure variations act on the exposed end of the cement sheath at the bottom of the well, and (ii) pressure is transmitted to the inside of the production casing through which gas is injected or extracted, which in turn affects the surrounding cement. Pressure variations at the exposed end of the cement sheath have been shown to increase the system permeability in this work, whereas internal casing pressure loading has been demonstrated to have a similar effect in previous studies (Section 1.5). The combined influence of these two mechanisms therefore constitutes an important subject for future research.

There are, however, two scenarios in which the influence of the production tubular pressure is reduced or negligible. The first scenario is when a tubing is installed (Figure 1) and the A-annulus is filled with a fluid. In this case, the tubing pressure is primarily transmitted to the fluid column rather than to the cement sheath. The second scenario is encountered in former oil or gas fields that are repurposed for UGS, where some wells may be abandoned and filled with cement. These two scenarios more closely resemble the experiments conducted in this work, as pressure is mainly applied to the exposed bottom of the cement.

Furthermore, this study has demonstrated that cement does not remain perfectly sealing, even under highly controlled laboratory conditions. In real wells, cement placements might be less ideal, which can further compromise the sealing performance. Since new concepts for cement alternatives or additives have emerged, it would be valuable to conduct experiments similar to those described in this work using different sealing materials, such as resin-based systems, geopolymers, expanding cements, or cements with specialized additives (e.g., Baumgarte et al., 1999; Ghofrani and Plack, 1993; Kwatia et al., 2019; Morris et al., 2012; Santos et al., 2020; Yakovlev et al., 2023).

Consequently, it is worth discussing whether a transition from conventional cement to sealing systems that incorporate additional or alternative materials is advisable. Although cement remains the industry standard, it does not necessarily represent the optimal choice.

Ensuring well integrity is generally essential, but it becomes particularly critical when leakage could have severe consequences, such as in wells containing hazardous fluids like H_2S. In such cases, incorporating additional barrier systems could enhance well integrity and thus mitigate risks in the long term.

These systems could involve hybrid designs based on cement combined with localized layers of complementary materials. For instance, bismuth-based alloys have been used successfully in remediation, abandonment, or to seal annuli (e.g., Aznor et al., 2025; Carragher et al., 2025; Zhang et al., 2020). It has also been proposed that uncemented annuli between rock and casing may be closed naturally by salt or shale creep (e.g., Enayatpour et al., 2019; Loizzo et al., 2017; Van Oort et al., 2022). Building on this concept, some authors propose removing casings and cement in the caprock section and installing plugs made of bentonite, salt, clay, and/or bitumen (Bracke et al., 2016). These materials can swell or creep, potentially forming a long-term seal, and have demonstrated tightness over geological timescales.

Overall, the development and testing of such alternative or hybrid sealing concepts could play a key role in improving long-term well integrity, particularly in applications where conventional cement systems may reach their technical limitations. A high-quality abandonment using multiple long-term stable materials with complementary properties appears to be a prerequisite for a more safe and sustainable closure of subsurface operations.

5.3 Model considerations and uncertainties

5.3.1 Scope and objectives

The interpretation of the experimental results presented in the previous sections is partly linked to the assumptions and limitations of the applied modeling approach. While the model provides a useful framework for quantifying gap evolution and system permeability, its formulation involves simplifications that may influence the results.

The following sections therefore examine key aspects of the model formulation, evaluate its robustness, and assess associated uncertainties. Particular attention is given to the numerical solution strategy, the selection of fitting parameters, and the validity of the underlying flow assumptions.

5.3.2 Monolithic formulation and comparison to operator splitting

The models described in Section 3.2 are based on an *operator splitting* approach, in which gas flow and thermodynamic calculations are performed separately within each time step and subsequently combined. This approach was chosen to explicitly account for and analyze gas flow and multiple thermal effects on pressure separately. However, operator

splitting introduces numerical splitting errors because the governing processes are not solved simultaneously. A so-called *monolithic* solution, in which all governing equations are solved simultaneously within each time step, would therefore be mathematically more rigorous.

Thus, the aim of this subsection is to assess whether the operator splitting approach yields results comparable to those obtained with a monolithic solution. For this purpose, the following monolithic finite-volume models were developed. All variables used in this section are explained below Equation 55.

Zero-dimensional formulation

The term *zero-dimensional* refers to a formulation in which the annular gap is represented as a single hydraulic element over its full length using the Hagen–Poiseuille relation, i.e., without spatial discretization. The upper chamber is modeled as a single control volume i.e., an open system across whose boundaries mass and energy can be exchanged. The gas pressure in the upper chamber is derived assuming ideal gas behavior (Çengel et al., 2019, ch. 3.6), with the governing equation solved in discrete time steps:

$$P_{\mathrm{uc}}(t) = \frac{m_{\mathrm{uc}}(t) \cdot R_{\mathrm{spec}} \cdot T_{\mathrm{uc}}(t)}{V_{\mathrm{uc}}} \tag{50}$$

Mass enters the upper chamber through the annular gap. The Hagen–Poiseuille equation for compressible, isothermal laminar flow (see Section 5.2.6) yields the following mass balance of the upper chamber:

$$\frac{dm_{\mathrm{uc}}}{dt} = \dot{m}_{\mathrm{uc}} = \frac{h^3 \cdot w}{12 \cdot \eta \cdot l} \cdot \frac{P_{\mathrm{lc}}^2 - P_{\mathrm{uc}}^2}{2 \cdot R_{\mathrm{spec}} \cdot T_{\mathrm{in}}} \tag{51}$$

The temperature evolution follows from the first law of thermodynamics for an open control volume (Çengel et al., 2019, ch. 5.3):

$$\frac{d}{dt}(m_{\mathrm{uc}} \cdot u_{\mathrm{uc}}) = \dot{m}_{\mathrm{uc}} \cdot h_{\mathrm{in}}^{\mathrm{enth}} + \dot{Q}_{\mathrm{uc}} \tag{52}$$

Assuming ideal gas behavior ($u_{\mathrm{uc}} = c_{\mathrm{v}} \cdot T_{\mathrm{uc}}$ and $h_{\mathrm{in}}^{\mathrm{enth}} = c_{\mathrm{p}} \cdot T_{\mathrm{in}}$ according to Çengel et al., 2019, ch. 4.4) and heat transfer between gas and steel wall proportional to the gas–steel temperature difference, Equation 53 is derived from Equation 52:

$$\frac{dT_{\mathrm{uc}}}{dt} = \frac{\dot{m}_{\mathrm{uc}} \cdot c_{\mathrm{p}} \cdot T_{\mathrm{in}} + c \cdot m_{\mathrm{uc}} \cdot c_{\mathrm{v}} \cdot (T_{\mathrm{steel}} - T_{\mathrm{uc}}) - \dot{m}_{\mathrm{uc}} \cdot c_{\mathrm{v}} \cdot T_{\mathrm{uc}}}{m_{\mathrm{uc}} \cdot c_{\mathrm{v}}} \tag{53}$$

Equations (51) and (53) form a coupled system of ordinary differential equations, which is solved simultaneously using the Radau method.

One-dimensional formulation of the gap domain

For improved comparability with the operator-splitting approach, the annular gap is additionally treated as a one-dimensional domain. For the one-dimensional scenario, assuming a constant cross-sectional area, the equation of continuity (Bird et al., 2002, ch. 3.1) reduces to the following one-dimensional mass conservation equation:

$$\frac{\partial \lambda_m(x,t)}{\partial t} + \frac{\partial \dot{m}(x,t)}{\partial x} = 0 \tag{54}$$

This conservation law represents the continuous form of the mass balance and serves as the basis for the finite-volume discretization used in the numerical model. The mass flow along the gap and into the upper chamber is evaluated using the compressible form of the Hagen–Poiseuille relation (see Section 5.2.6 and Equation 51):

$$\dot{m}(x,t) = -\frac{h^3 \cdot w}{24 \cdot \eta \cdot R_{\text{spec}} \cdot T_{\text{in}}} \cdot \frac{\partial P(x,t)^2}{\partial x} \tag{55}$$

In the numerical implementation, this equation is discretized between adjacent control volumes, resulting in mass flow rates proportional to the difference of squared pressures between neighboring cells. The annular gap domain is discretized into N finite volumes. For each control volume, a mass balance equation is obtained by discretizing the continuity equation (Equation 54), while the mass flow rates between adjacent volumes are evaluated using the Hagen–Poiseuille relation (Equation 55) in discretized form.

In the one-dimensional approach, the upper chamber is modeled as an additional control volume with separate mass and energy balance equations. The mass flow rate into the chamber is determined using the Hagen–Poiseuille relation (Equation 55) in discretized form, and the temperature evolution in the upper chamber follows Equation 53. This results in a coupled system of $N + 2$ ordinary differential equations (N gap cell masses, chamber mass, and chamber temperature), which is solved monolithically.

In contrast to the zero-dimensional formulation, the relation underlying Equation 50 is applied to calculate the pressure in each control volume, rather than only in the upper chamber.

In line with operator splitting model H, only the gap aperture h is considered as a fitting parameter in both monolithic models. The modeled pressure evolution in the upper chamber is automatically adjusted to the measured pressure data using a least-squares approach.

The full source code of the monolithic one-dimensional approach is provided in Appendix B, while the main algorithm of the operator splitting model is provided in Appendix A. Variables used in this section are explained below:

c	Heat transfer factor between gas and steel in the upper chamber [1/s]
c_p	Specific heat capacity at constant pressure [J/(kg·K)]
c_v	Specific heat capacity at constant volume [J/(kg·K)]
h	Effective annular gap aperture [m]
$h_\mathrm{in}^\mathrm{enth}$	Specific enthalpy of inflowing gas [J/kg]
l	Length of the flow path [m]
m_uc	Gas mass in the upper chamber [kg]
$\dot{m}_\mathrm{uc}$	Mass flow rate into the upper chamber in 0D [kg/s]
$\lambda_m(x,t)$	Linear mass density [kg/m]; $\lambda_m(x,t) = \rho(x,t) \cdot A$, with ρ being the gas density and A the cross-sectional area.
$\dot{m}(x,t)$	Axial mass flow rate along the annular gap [kg/s]
P_lc	Gas pressure in the lower chamber [Pa]
P_uc	Gas pressure in the upper chamber [Pa]
$P(x,t)$	Gas pressure in a one-dimensional control volume at position x and time t [Pa]
$\dot{Q}_\mathrm{uc}$	Heat flow rate into the upper chamber [W]
R_spec	Specific gas constant of nitrogen [J/(kg · K)]
T_in	Temperature of the inflowing gas [K]
T_steel	Steel temperature of the upper chamber wall [K]
T_uc	Gas temperature in the upper chamber [K]
t	Time [s]
u_uc	Specific internal energy of the gas in the upper chamber [J/kg]
V_uc	Volume of the upper chamber [m^3]
w	Width of the annular gap [m]
x	Spatial coordinate along the annular gap [m]
η	Dynamic viscosity of the gas [Pa · s]

When comparing the results of the monolithic and operator splitting models, all approaches yield similar gap apertures (Table 18). The deviation between the zero-dimensional (0D) and one-dimensional (1D) monolithic models (mean absolute percentage error, MAPE = 1.65%) is even larger than the deviation between the operator splitting and monolithic formulations.

The most appropriate reference for the operator splitting model is the 1D monolithic model, as both approaches employ spatial discretization of the gap domain. Although the modeled gap aperture h differs by approximately 1.4% between these two models (Table 18), the operator splitting formulation can be regarded as a good approximation of the monolithic solution.

Table 18: Comparison of modeled annular gap apertures h from the operator splitting model H (using only h as a fitting parameter) against two monolithic model variants (0D and 1D). N is the number of finite volumes used to discretize the gap. *Cas.* denotes the casing number and *Exp.* the corresponding experiment number. h_{os} denotes the gap aperture derived from operator splitting model H. For each monolithic model, the modeled gap aperture h_{mono} and the relative percentage deviation between operator splitting and monolithic model $\Delta h = 100 \cdot (h_{os} - h_{mono})/h_{mono}$ are given. The MAPE (mean absolute percentage error) is the arithmetic mean of $|\Delta h|$.

			Zero-dimensional		1D, $N = 20$	
Cas.	Exp.	h_{os} [µm]	h_{mono} [µm]	Δh [%]	h_{mono} [µm]	Δh [%]
0	2	23.00	22.66	1.53	23.04	-0.14
0	28	30.71	30.03	2.29	30.53	0.60
0	48	32.47	32.13	1.04	32.68	-0.64
1	10	6.98	7.03	-0.75	7.15	-2.36
1	17	14.13	14.02	0.76	14.26	-0.88
1	18	21.43	20.75	3.25	21.10	1.56
1	33	31.14	31.29	-0.48	31.82	-2.11
2	3	38.10	38.40	-0.78	39.05	-2.43
2	13	19.53	19.44	0.45	19.77	-1.21
2	23	42.01	42.33	-0.77	43.05	-2.43
2	51	42.34	42.48	-0.33	43.20	-2.00
3	8	13.75	13.71	0.23	13.94	-1.40
4	14	28.14	27.91	0.81	28.38	-0.85
MAPE [%]				1.04		1.43

The modeled pressure curves obtained with the monolithic and operator splitting models are nearly indistinguishable (Figure 38a). Both models accurately reproduce the steep initial pressure increase observed in experiments with low gas flow rates.

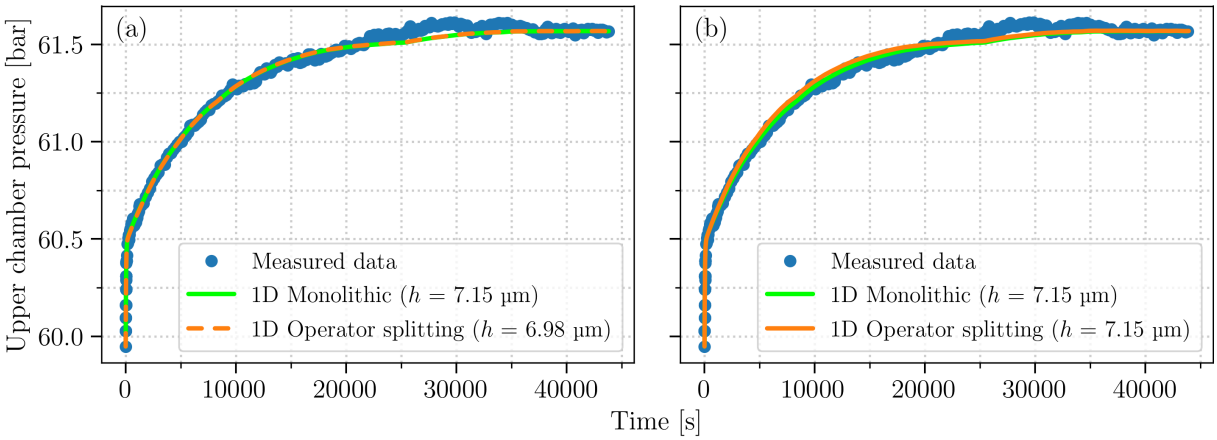


Figure 38: Modeling results for monolithic and operator splitting models based on experiment 10 of casing 1. In (a), the best fit of both model types is shown, while in (b), the best-fit value of h from the monolithic model is applied to the operator splitting model.

When the same gap aperture is applied in both models, small deviations between the resulting pressure curves become visible (Figure 38b). The example shown represents an extreme case, in which the difference between the respective best-fit values of h amounts to approximately 2.4%. For most other experiments, the deviations between the curves are smaller. Overall, the results confirm that the differences between the two models remain minor.

The operator splitting model was used throughout this work to enhance physical interpretability, as it allows individual processes to be analyzed separately and in greater detail than in the monolithic model. In contrast to the monolithic model, where mass and energy balances are solved in a fully coupled manner, the operator splitting approach explicitly represents each physical process in a modular way. This structure made it possible to implement and evaluate individual mechanisms based on the physical understanding developed during the course of the study. Moreover, the operator splitting model reflects the progressive model development conducted in this thesis, as modeling initially started with a simple Hagen–Poiseuille flow equation and was subsequently extended to include thermodynamic processes.

The close agreement between both model types demonstrates that the underlying physical processes were consistently represented. Depending on the intended application, either the monolithic or the operator splitting model can therefore be employed and further adapted.

5.3.3 Selection of the fitting parameters

Although results from all model versions were generated, Section 4 primarily presents the results of operator splitting model H, which uses only the gap aperture h as a fitting parameter (Table 19). This choice was made because the modeled values of h are generally consistent across all models. Introducing additional fitting parameters beyond h mainly improves the agreement between modeled and measured data but has only a minor effect on the resulting values of h and therefore the modeled system permeability. Furthermore, increasing the number of free parameters reduces the comparability of the results. For this reason, an approach with as few independent variables as possible was selected, while still providing an adequate representation of the experimental behavior. The underlying considerations are discussed in the following paragraphs.

Comparison between models H and HC

In addition to h, model HC includes the heat transfer factor c (Equation 26) as a fitting parameter (Table 19). Since the experimental setup, including chamber volume, geometry, and materials, remains largely unchanged throughout this study, heat transfer behavior is expected to be similar across experiments. Consequently, the heat transfer factor c should also exhibit only limited variability. Nevertheless, quantifying its order of magnitude was necessary to represent thermal effects. Therefore, heat transfer factors were estimated directly from selected experiments (Section 3.2.2, page 45 ff.).

Table 19: Fitting parameters used in the different model types. h is the annular gap aperture, c is a heat transfer factor, and P_{min} and P_{max} are the minimum and maximum pressure values encountered during an experiment. The column *Constant parameters* lists only those parameters that were kept constant in a given model but were used as fitting parameters in at least one of the other models. Further details on the different model types are provided in Section 3.2 (page 56 ff.).

Model type	Fitting parameters	Constant parameters
H	h	c, P_{min}, P_{max}
HC	h, c	P_{min}, P_{max}
HP	h, P_{min}, P_{max}	c

As described in Section 3.2.2, reliable estimation of c was only possible for experiments in which heat transfer and gas flow were temporally separated. This condition is fulfilled by ten experiments characterized by sufficiently slow gas flow. For these experiments, incorporating heat transfer substantially improves the agreement between modeled and measured pressure curves, particularly by reproducing the steep initial pressure increase (Figure 39a,b). The resulting estimates of c were subsequently used to derive representative values for the remaining experiments (Section 3.2.2). For experiments with higher gas flow rates, inclusion of heat transfer still improves the agreement between measured and modeled data (Figure 39c,d), although the improvement is less pronounced than for experiments with low gas flow rates (Figure 39a,b).

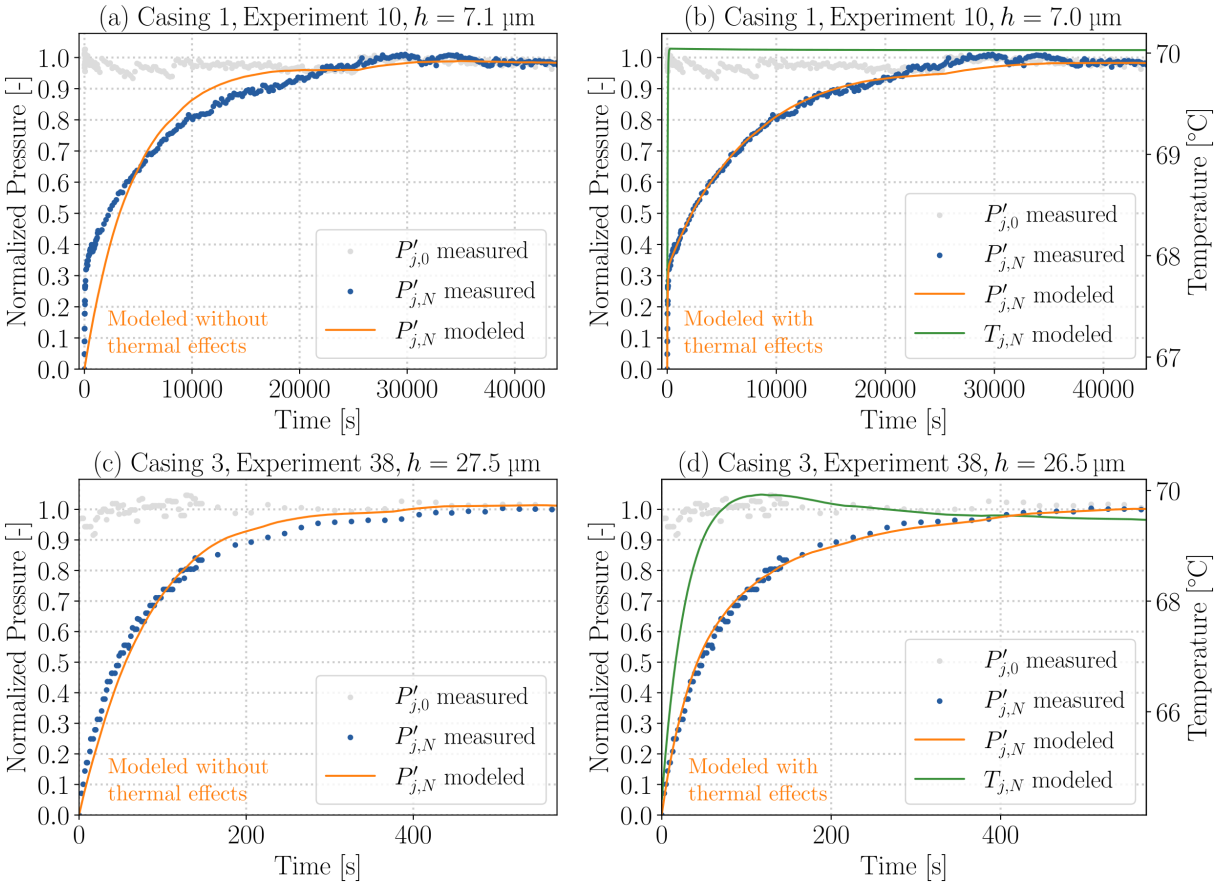


Figure 39: Comparison of modeling results with (b, d) and without (a, c) consideration of thermal effects. In (a) and (c), only the pressure increase due to gas flow is considered in the model. In (b) and (d), heat transfer from the steel of the upper chamber to the gas and the resulting temperature–pressure interactions are additionally included, leading to an improved agreement between measured and modeled data. $P'_{j,0}$ denotes the normalized pressure in the lower chamber, $P'_{j,N}$ the normalized pressure in the upper chamber, $T_{j,N}$ the temperature in the upper chamber and h the modeled aperture of the annular gap.

In principle, c should remain constant for experiments conducted with identical chamber geometry and volume. However, the ten experiments used for its estimation show some variability. For example, casing 3 exhibits values between 0.027 and 0.0317 s^{-1}, casing 1 between 0.0279 and 0.0285 s^{-1}, and casing 4 between 0.0394 and 0.045 s^{-1}. To assess the impact of this variability, model H was executed in two separate simulations using the minimum and maximum observed values of c for these casings (Figure 40a).

The results demonstrate that neglecting heat transfer altogether would influence the modeled values of h (Figure 40b), whereas variations within the observed range of c have only a minor effect (Figure 40a). However, since the estimates of c are based on only ten experiments, their absolute accuracy remains uncertain.[39]

[39] A quantitative assessment of the sensitivity to c is provided in Section 3.3.6.

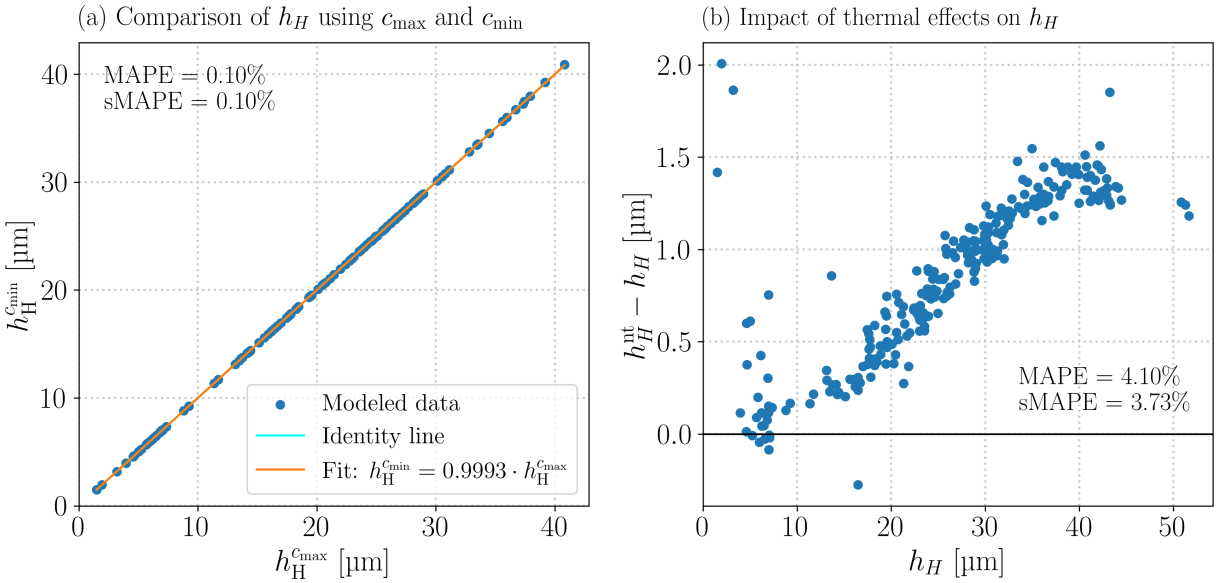


Figure 40: (a) Comparison of h_H, the annular gap aperture derived from model H, using different values of the heat transfer factor c. $h_{\mathrm{H}}^{c_{\max}}$ refers to the value of h_H modeled with the maximum c-value of each casing (instead of the default arithmetic mean), and $h_{\mathrm{H}}^{c_{\min}}$ analogously uses the minimum value. Only casings 1, 3, and 4 are shown because casings 0 and 2 lack experiments with low gas flow rates from which a range of c-values could be determined. The mean absolute percentage error (MAPE) and the symmetric mean absolute percentage error (sMAPE) were determined according to Equations 56 and 57 (Tayman and Swanson, 1999), $h_X = h_{\mathrm{H}}^{c_{\max}}$ and $h_Y = h_{\mathrm{H}}^{c_{\min}}$.

(b) Comparison of h modeled with and without thermal effects. h_{H} denotes the value of h obtained using model H (Section 3.2), which incorporates thermal effects. $h_{\mathrm{H}}^{\mathrm{nt}}$ represents the corresponding value modeled without thermal effects, i.e., assuming purely Hagen–Poiseuille flow. MAPE and sMAPE were determined according to Equations 56 and 57 (Tayman and Swanson, 1999), with $h_X = h_{\mathrm{H}}$ and $h_Y = h_{\mathrm{H}}^{\mathrm{nt}}$.

$$\mathrm{MAPE} = \frac{1}{n} \sum_{k=1}^{n} \left| \frac{h_{X,k} - h_{Y,k}}{h_{X,k}} \right| \cdot 100 \tag{56}$$

$$\mathrm{sMAPE} = \frac{1}{n} \sum_{k=1}^{n} \left| \frac{h_{X,k} - h_{Y,k}}{(h_{X,k} + h_{Y,k})/2} \right| \cdot 100 \tag{57}$$

MAPE	Mean absolute percentage error [%]
sMAPE	Symmetric mean absolute percentage error [%]
h_X, h_Y	h-values to be compared, calculated by different model versions [µm]
k	Index of the data point/experiment [-]
n	Total number of data points/experiments [-]

To further investigate this aspect, model HC was applied with c treated as a fitting parameter over a wide range between 0.001 and 0.25 s^{-1}, substantially exceeding the experimentally derived range. The underlying hypothesis is that model HC may yield

more reliable estimates of c than the estimates obtained from the ten experiments with low gas flow rates, which are subject to considerable uncertainties.

Model HC demonstrates a moderate to strong negative correlation between the modeled values of h and c (Figure 41a), as indicated by Pearson ($r = -0.54$) and Spearman ($r = -0.61$) coefficients (Pearson, 1896; Spearman, 1904). The low p-values indicate a high level of statistical significance. However, the substantial scatter in the data of Figure 41a suggests that the upper chamber volume and h are not the only factors influencing the modeled value of c. Thus, an argument could be made for including c as a fitting parameter.

On the other hand, not using c as a fitting parameter could be considered more reasonable, as c should theoretically remain relatively constant under similar experimental conditions based on physical and thermodynamic principles. Thus, the scatter in the data of Figure 41a is most likely a numerical artifact rather than evidence of unknown factors influencing c considered by model HC.

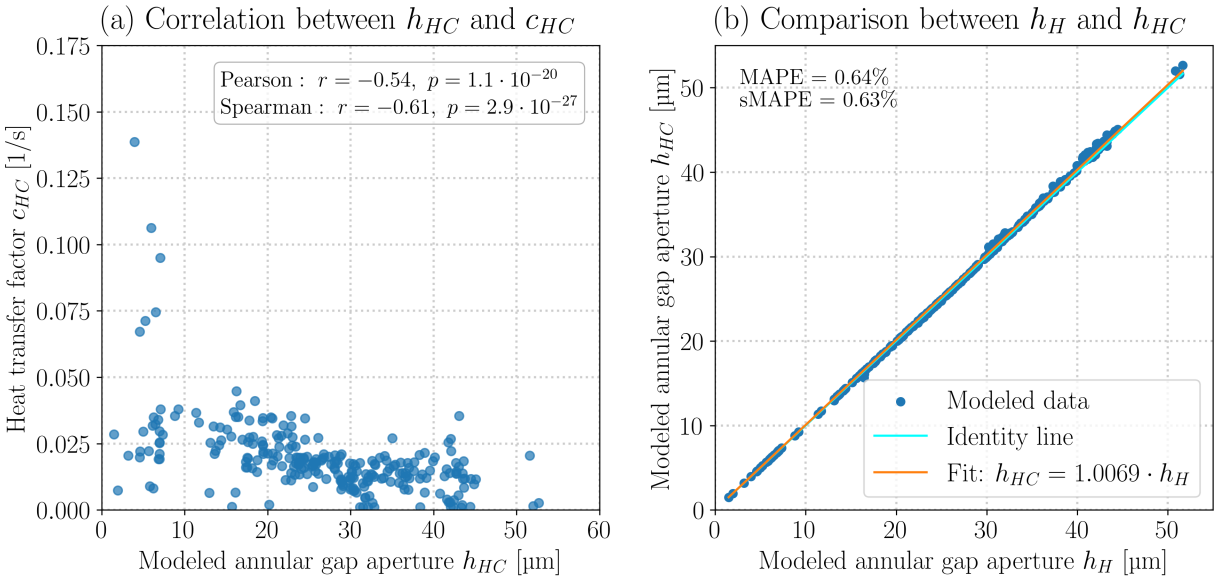


Figure 41: Comparison of modeling results related to using c as a fitting parameter. The parameter h_{HC} denotes the h-value determined by model HC, c_{HC} the c-value determined by model HC and h_H the h-value determined by model H. In subfigure (a), r denotes the Pearson or Spearman correlation coefficient and p the corresponding p-value. In subfigure (b), the mean absolute percentage error (MAPE) and symmetric mean absolute percentage error (sMAPE) were determined according to Equations 56 and 57 (Tayman and Swanson, 1999), with $h_X = h_H$ and $h_Y = h_{HC}$.

Although model HC reduces the arithmetic mean WRMSE by 26% compared to model H, this improvement does not necessarily imply more realistic estimates of h or c. It primarily reflects better agreement between measured and modeled pressure data, which could purely result from increased flexibility due to the additional fitting parameter. Furthermore, increasing the number of fitting parameters tends to reduce the comparability of model results. Lastly, the mean percentage deviation of h between model HC and model H is only 0.6% (Figure 41b). Given the expected physical consistency of c and the negligible

influence on h, treating c as a fitting parameter provides limited additional value. Therefore, model H (using only h as a fitting parameter) was preferred over model HC (using h and c as fitting parameters).

Comparison between models H and HP

In addition to h, model HP also includes $P_{\min}$ and $P_{\max}$ as fitting parameters[40] (Table 19). $P_{\max}$ was included as a fitting parameter because, when used as a fixed value, it is defined by a single measured value. If this value is an outlier, the normalization (Equation 12) becomes distorted (Figure 10). Since both $P_{\min}$ and $P_{\max}$ enter the normalization, they affect all normalized pressure values in the dataset.

Introducing $P_{\min}$ as a fitting parameter was motivated by limitations associated with discrete sampling and sensor response time. Since the pressure is recorded at 2 s intervals and the gas-release phase typically lasts only 1–2 s, the true physical minimum pressure may occur between sampling points.

Model HP was therefore designed to evaluate the impact of allowing $P_{\min}$ and $P_{\max}$ to vary within predefined bounds (bound details in Section 3.2, page 56 ff.). The upper bounds for $P_{\min}$ and $P_{\max}$ are given by their respective measured values. For $P_{\max}$, the lower bound is defined as the measured value minus the absolute pressure corresponding to a normalized offset of 0.025, i.e., 2.5% of the difference between $P_{\max}$ and $P_{\min}$.

Defining the lower bound of $P_{\min}$ is more complex: decreasing $P_{\min}$ in pressure requires a corresponding shift in time. A regression over the first 20 measured pressure-time data points of each experiment was performed to couple the pressure and time offsets of $P_{\min}$, using $P(t) = a - b \cdot e^{-c \cdot t}$ as the regression model. The value of $P_{\min}$ is varied along this regression curve, with the lower bound defined by whichever limit is reached first: a temporal shift of 2 s or a normalized pressure shift of 0.05.[41] Once model HP determines an optimal value of $P_{\min}$, all data points are shifted in time such that the modeled $P_{\min}$ is located at $t = 0$ s. In addition, a change in $P_{\min}$ alters the normalization of all measured pressures, thereby modifying the corresponding normalized values according to Equation 12. Figure 42 illustrates this procedure. This paragraph only describes the basic principles, with full details provided in Section 3.2 (page 56 ff.).

[40] $P_{\min}$ is the minimum pressure occurring during an experiment. In models where $P_{\min}$ is not a fitting parameter, it corresponds to the measured minimum value. $P_{\max}$ is the maximum pressure occurring during an experiment. In models where $P_{\max}$ is not a fitting parameter, it corresponds to the measured maximum value.

[41] This applies only if $P_{\min}$ is recorded during the pressure-increase phase. If it occurs during the gas release phase, a different bound definition applies (Section 3.2, page 56 ff.). This concerns only 10 experiments and has minimal influence on overall results, and is therefore not discussed here in detail.

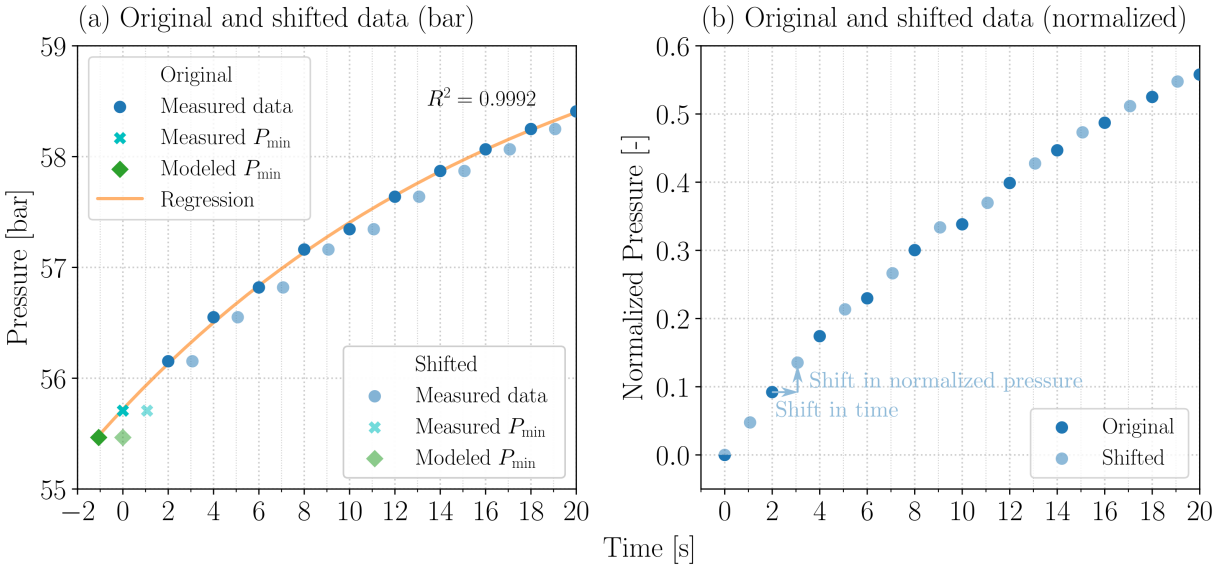


Figure 42: Example illustrating the shifting of P_{min} and P'_{min} in model HP, based on experiment 5 of casing 0. *Shifted* denotes the dataset after the adjustments in time and pressure performed by model HP, whereas *original* refers to the unshifted dataset.
(a) Model HP evaluates combinations of pressure and time and, in this example, identifies the optimal P_{min} at approximately $t = -1$ s, corresponding to a pressure of approximately 55.5 bar. All data are therefore shifted forward in time by ~ 1 s.
(b) As in (a), all data are shifted forward in time by ~ 1 s. Additionally, the normalization changes due to the updated value of P_{min} (Equation 12), placing the modeled P'_{min} at $(0, 0)$ and modifying the normalized pressures accordingly. The two arrows illustrate the shifting process for a single data point as an example. For clarity, all data are shown in blue in (b). Nevertheless, the same data as in (a) are included, now in their normalized form.

The underlying hypothesis for model HP was that using P_{min} and P_{max} as additional fitting parameters would yield more realistic values for both parameters and reduce the WRMSE.

As expected, P_{min} is reduced in 91% of the experiments by model HP. However, in 68% of all experiments, the modeled P_{min} reaches the predefined lower bound (Figure 43a). The frequent convergence to the lower bound indicates that, in these cases, the model would favor an even lower P_{min} if permitted, despite the lower bound already representing a substantial offset in P_{min}.

This indicates that low P_{min} values generally improve the agreement between measured and modeled pressure data. But it does not necessarily imply that the modeled values of P_{min} are more realistic than the measured values. While it is likely that the true P_{min} lies below the measured value, the extent of this difference remains unclear. Since the model consistently favors strong offsets, the resulting P_{min} is often limited by the user-defined bound and is therefore more arbitrary than the measured value.

For P_{max}, 49% of the modeled values remain unchanged at the upper bound, suggesting that the measured P_{max} already provides a good representation of the actual maximum pressure. While 29% of the modeled values of P_{max} reach the lower bound, only 22% of

the values fall between both bounds, indicating that in most cases, P_{max} is not freely optimized between the bounds either (Figure 43b). Furthermore, the arithmetic mean WRMSE of model HP is only reduced by 10% relative to model H. Consistent with this limited improvement, the mean percentage deviation of h between model HP and model H is only 0.9% (Figure 44).

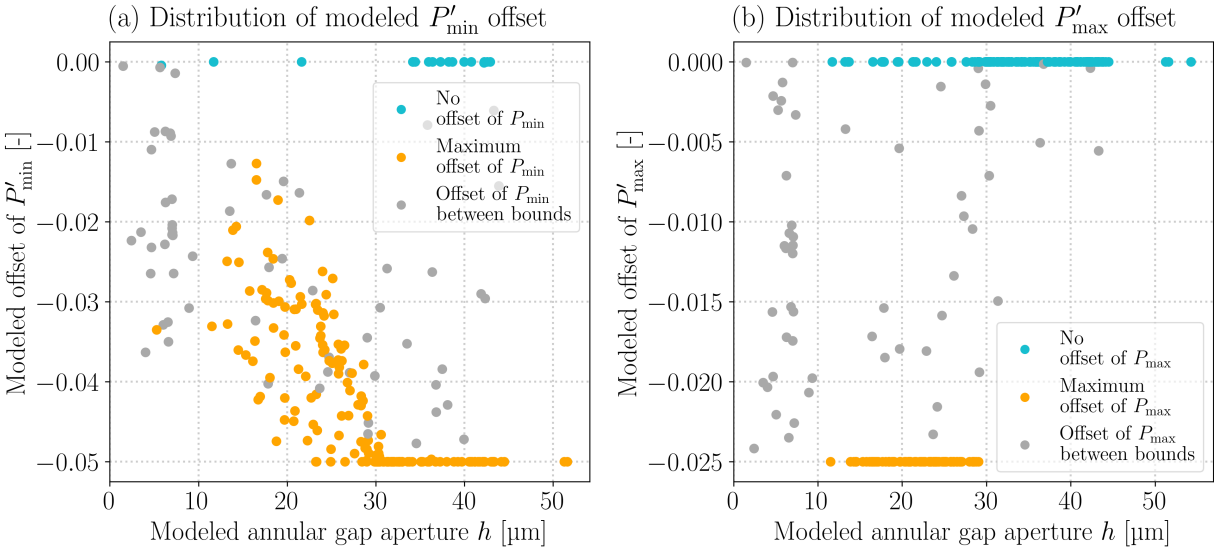


Figure 43: Modeled offsets of P'_{min} (a) and P'_{max} (b) as determined by model HP. In both plots, blue markers indicate that P_{min} or P_{max} reach the upper bound, meaning no offset was applied by model HP. Orange markers indicate that the values reach the lower bound due to the maximum allowed offset. The bound definitions are provided on page 57 ff. In (a), the ten experiments in which P_{min} was recorded during the gas release phase are omitted for clarity, as their bound definitions differ (page 59 ff.). In these ten cases, five values of P_{min} reach the upper bound and five reach the lower bound, with none lying between the bounds.

In conclusion, the differences in both h (0.9%) and WRMSE (10%) between models H and HP are small, considering that model HP uses three fitting parameters whereas model H uses only one. Furthermore, the modeled values of P_{min} and P_{max} in model HP frequently converge to either the upper or the lower bound. Convergence to the upper bound indicates that model HP did not change the original, measured values. Convergence to the lower bound shows that even the generously defined maximum offset was often fully exploited, implying that the model would prefer an even larger, and likely unrealistic, shift of P_{min} and P_{max}.

This does not support the hypothesis that allowing P_{min} and P_{max} to vary freely leads to more realistic estimates compared to the measured values. Consequently, model H (using only h as a fitting parameter) was preferred over model HP (using h, P_{min} and P_{max} as fitting parameters).

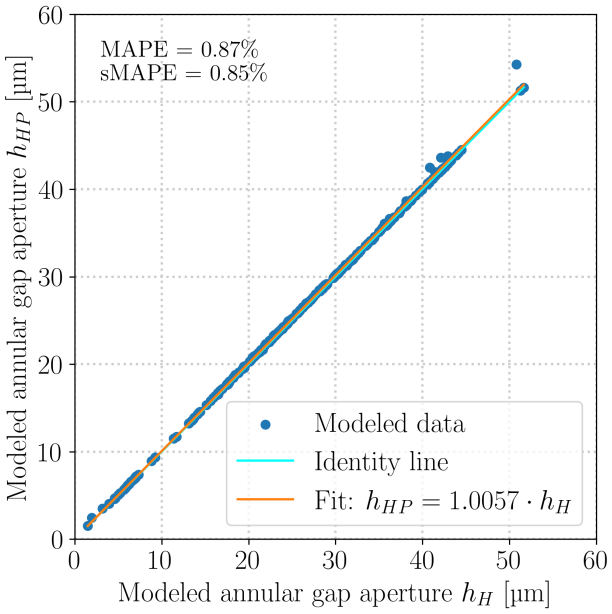


Figure 44: Comparison of modeled gap apertures h between models H and HP. The parameter h_{HP} is the h-value derived from model HP, while h_H is the h-value derived from model H. The mean absolute percentage error (MAPE) and symmetric mean absolute percentage error (sMAPE) were determined according to Equations 56 and 57 (Tayman and Swanson, 1999), with $h_X = h_H$ and $h_Y = h_{HP}$.

Choice of minimization method

This subsection describes the choice of optimization methods used for parameter estimation in the different model variants. Minimization methods from `scipy.optimize` are used in all three model versions to automatically minimize the WRMSE (Equation 39), which represents the difference between measured and modeled pressure values. For models H and HC, local minimization methods are generally sufficient, as h and c each exhibit a single WRMSE minimum for most experiments. Among local methods, the derivative-free `Nelder-Mead` algorithm (Nelder and Mead, 1965) performs well, as it is robust to noise and does not require gradient information. This is an advantage since the WRMSE as a function of c or h is not always numerically smooth or reliably differentiable. In contrast, local gradient-based methods such as `least_squares` (e.g., Branch et al., 1999; Coleman and Li, 1996; Virtanen et al., 2020) can produce slightly higher WRMSE-values in these cases, as they rely on smoothness and may converge to a local minimum instead of the global minimum (Figure 45).

For model HP, however, local minimization alone is insufficient, as there can be multiple local minima for the WRMSE due to the timeshift that occurs with any change in P_{min}. Local minimization methods tend to get trapped in these local minima. Therefore, a combination of global and local minimization is beneficial for model HP (Figure 45).

Since this combined approach also yields slightly lower errors for models H and HC compared to using local methods alone, it is used in all three model versions. First,

the `differential_evolution` method is applied to approximately locate the global minimum of the WRMSE (Storn and Price, 1997). The resulting fitting parameter value(s) at this minimum serve as initial guesses for the `L-BFGS-B` algorithm (Limited-memory Broyden–Fletcher–Goldfarb–Shanno with Bounds), which performs a refined local optimization (e.g., Byrd et al., 1995; Zhu et al., 1997).

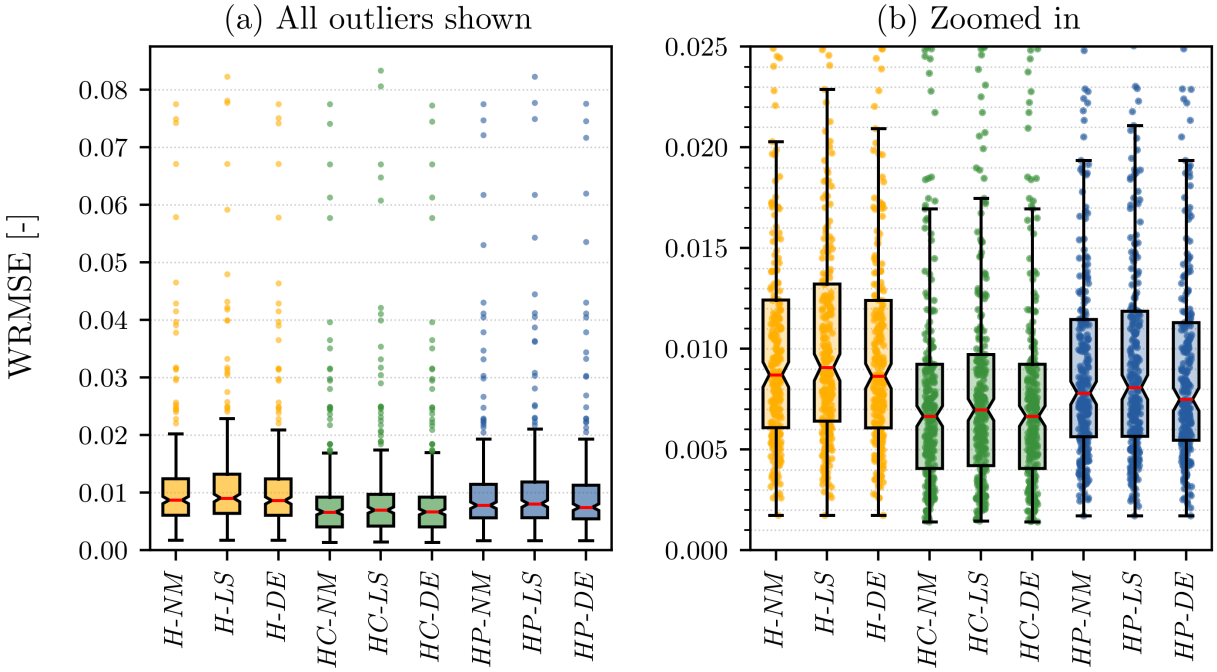


Figure 45: WRMSE boxplots for all models. H, HC, and HP are the model versions. The abbreviations following the model names represent the optimization algorithms: NM stands for Nelder–Mead, LS for least squares, and DE for differential evolution combined with L-BFGS-B. Subfigure (a) displays all outliers. In subfigure (b), the plot is zoomed in along the y-axis, and a swarmplot of the full dataset is overlaid. The red line denotes the median. The notches represent an approximate 95% confidence interval of the median. The box spans the interquartile range (IQR) between the first (Q1) and third quartile (Q3). The whiskers extend to the outermost data points within the range [Q1 − 1.5 · IQR, Q3 + 1.5 · IQR], while data points outside this range are plotted as outliers (Iglewicz, 2025).

5.3.4 Iterations and initial gap aperture

This section primarily addresses the minimization of the required number of iterations. To optimize computational efficiency, the goal is to use as few iterations as possible while ensuring that any inaccuracy introduced by limiting the iteration count remains negligible.

When determining the optimal number of iterations, the key criterion was whether additional iterations would still alter the modeling results. The iteration limits were selected to ensure convergence, as further iterations resulted only in negligible changes to the results, typically on the order of 0.01% or less. Table 20 summarizes the maximum number of iterations used for each model version, as determined from all 256 experiments.

Table 20: Maximum number of allowed iterations for the global (DE – Differential Evolution) and local (L-BFGS-B) minimization algorithms across the different model versions.

Model	Fitting parameters	Allowed iterations DE	L-BFGS-B
H	h	410	300
HC	h, c	820	300
HP	h, P_{min}, P_{max}	132	100

Results for model HP converge rapidly with a small number of iterations, as two of the fitting parameters (P_{min} and P_{max}) typically achieve their best agreement between measured and modeled data at either the upper or lower bound. This is not the case for models H and HC, where the optimal values of the fitting parameters usually lie within the defined bounds. Consequently, models H and HC require more iterations to reach convergence.

The automated model versions require an initial input gap aperture to begin the first calculation. For each experiment, results from previous model runs were used as input apertures, meaning that the initial gap aperture for a given experiment was already close to the modeling result.

Nevertheless, additional tests were performed to evaluate whether the results depend on the choice of the starting value (e.g., Figure 46). These tests serve as a robustness check: if different initial apertures lead to the same result, the model can be considered stable and the resulting gap apertures reliable.

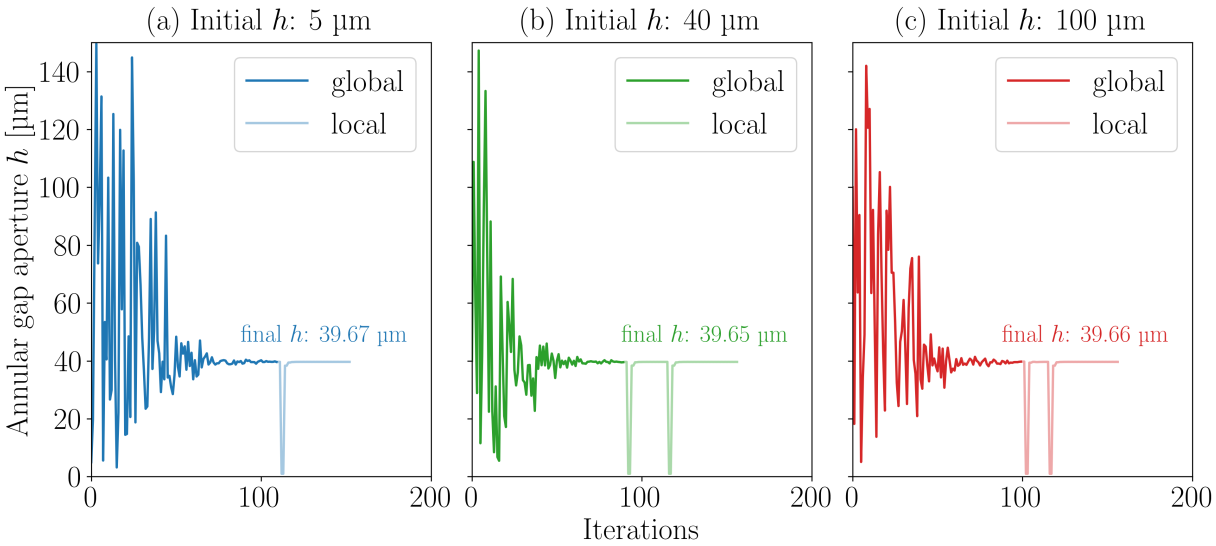


Figure 46: Development of the modeled annular gap aperture h over successive iterations for three different initial apertures (5 µm, 40 µm, and 100 µm), shown here for model H applied to experiment 25 of casing 2. For this test, model H was allowed to vary h between 1 µm and 150 µm for both the global (Differential Evolution) and the local (L-BFGS-B) minimization algorithms. *Final h* refers to the last value obtained from the local minimizer and thus represents the final result of the model run.

The results of these robustness tests demonstrate that the choice of initial aperture indeed has a negligible influence on the final modeling result, as shown in Figure 46. The deviation between model runs with different initial gap apertures generally depends on the number of iterations the model is allowed to perform. In most runs, a few outliers have a higher deviation than the rest. These deviations can typically be reduced by increasing the number of iterations. In all models, the number of iterations (Table 20) was chosen such that this deviation in h remained well below 0.1% in most cases (e.g., final h in Figure 46).

Since the initial gap aperture is already close to the expected solution, the computational time can be further reduced by limiting the range of gap apertures during the optimization. The maximum gap aperture allowed is set to three times the initial aperture, but not lower than 15 µm and not higher than 100 µm. The minimum aperture considered by the model is always 1 µm. After completion of the modeling, all resulting gap apertures were verified to remain far from both the lower and upper bounds.

5.3.5 Agreement between measured and modeled data

In the following, the agreement between measured and modeled data is examined, with particular emphasis on the role of thermal effects and on experiments showing a reduced agreement.

In most experiments, incorporating thermal effects[42] into the flow model leads to a generally good agreement between measured and modeled data (e.g., Figures 47b,d and 48a). In contrast, neglecting thermal effects results in a noticeably poorer agreement between measured and modeled data (Figure 47a,c). This difference in agreement is particularly pronounced in experiments characterized by low system permeability and correspondingly low volumetric gas flow rates (Figure 47a,b). For experiments with high system permeabilities, and thus higher gas flow rates, differences in fit quality between models that include thermal effects (Figure 47d) and those that neglect them (Figure 47c) are still observable, but less pronounced. Despite these differences in agreement between measured and modeled data, the resulting gap apertures h obtained from model versions that include thermal effects (Figure 47b,d) and those that neglect them (Figure 47a,c) do not differ strongly, regardless of the system permeability.

[42] In this work, the term *thermal effects* refers to all processes in which temperature changes influence the pressure evolution or pressure changes influence the temperature evolution in the upper chamber. In other words, thermal effects include all temperature–pressure couplings that contribute to the pressure evolution.

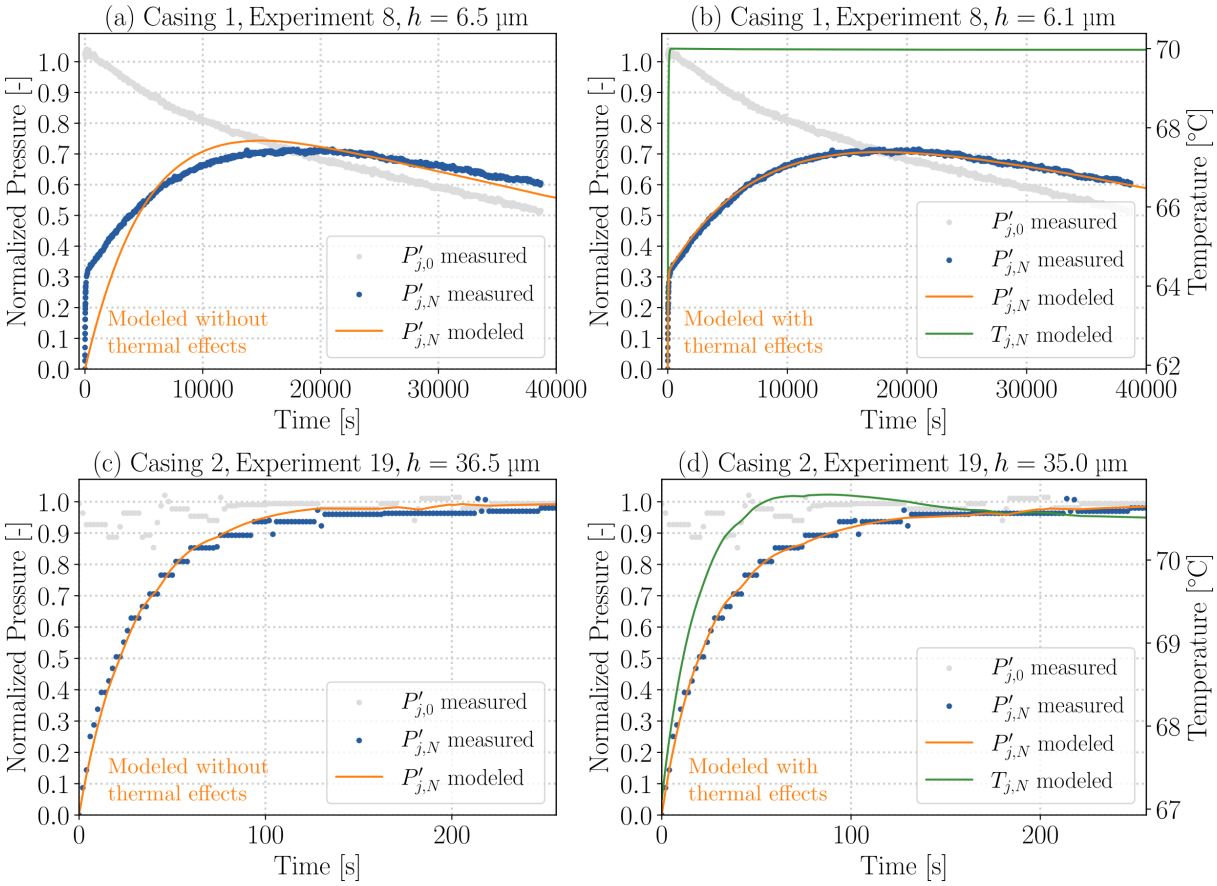


Figure 47: Comparison of modeling results with (b, d) and without (a, c) consideration of thermal effects. In (a) and (c), only pressure increases due to gas flow are considered in the model. In (b) and (d), heat transfer from the steel of the upper chamber to the gas and the resulting temperature–pressure interactions are additionally included, which improves the agreement between measured and modeled pressure. $P'_{j,0}$ denotes the normalized pressure in the lower chamber, $P'_{j,N}$ the normalized pressure in the upper chamber, $T_{j,N}$ the temperature in the upper chamber and h the modeled aperture of the annular gap.

Nevertheless, even with thermal effects included, a small number of experiments exhibit reduced agreement between measured and modeled data. One such example is experiment 3 of casing 4 (Figure 48b). In this experiment, the pressure increases steeply in the beginning, most likely due to thermal effects, followed by a phase of slow pressure increase before the pressure rise accelerates again. In general, after thermal effects have subsided, the pressure is expected to increase monotonically, with a gradually decreasing rate of increase over time, as captured by the modeled pressure in Figure 48b. The non-monotonic behavior observed in the measured data cannot be reproduced by the model, which is not designed to account for such transient deviations.

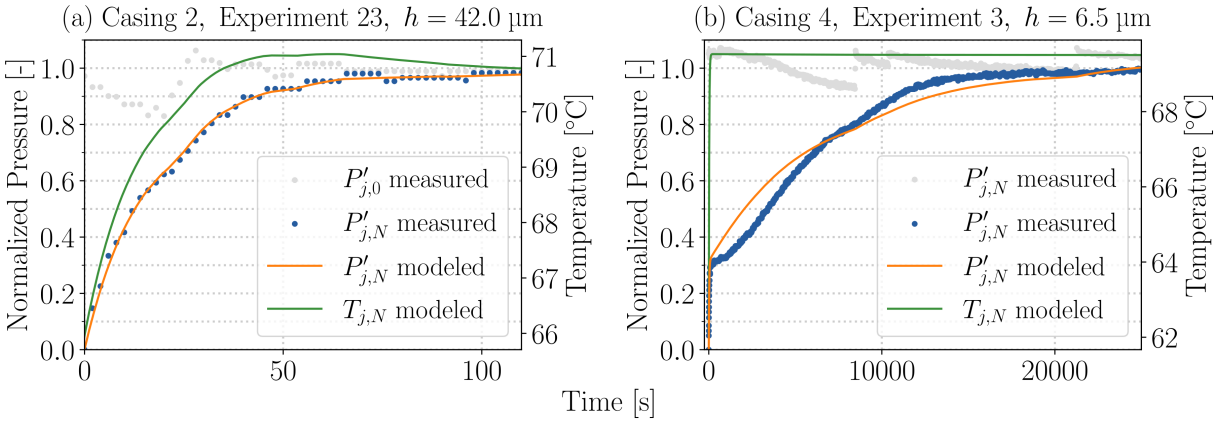


Figure 48: Examples illustrating differences in agreement between measured and modeled data: (a) a good agreement between measured and modeled data with a normalized WRMSE of 0.005, and (b) a suboptimal agreement with a normalized WRMSE of 0.03. $P'_{j,0}$ denotes the normalized pressure in the lower chamber, $P'_{j,N}$ the normalized pressure in the upper chamber, $T_{j,N}$ the temperature in the upper chamber and h the modeled aperture of the annular gap.

While such cases may appear problematic, the reason for their elevated WRMSE becomes clearer when the agreement between measured and modeled data is evaluated systematically across all experiments. For this quantitative assessment, the weighted root mean square error (WRMSE; Equation 39) is used, as shown in Figure 49a for all experiments. The WRMSE represents the weighted root mean square deviation between modeled and measured values. As normalized pressure values between 0 and 1 are used in the model, the WRMSE-values are directly comparable across all experiments in Figure 49a. While the majority of experiments exhibit WRMSE-values below 0.02, several experiments show higher values, indicating a reduced agreement between measured and modeled data.

There are two main factors that contribute to these higher WRMSE-values:

1. Figure 49b shows the WRMSE converted to pressure in bar, obtained by multiplying the normalized WRMSE by the pressure range ($P_{\max} - P_{\min}$) of each experiment. Some experiments with comparatively high normalized WRMSE-values appear less pronounced when expressed in bar instead of their normalized form. This effect is mainly caused by experiments with a small total pressure change (on the order of 1 bar). In such cases, the intrinsic scatter of the measured data (Figure 50) leads to an elevated normalized WRMSE, even though the error in bar remains small. In other words, the normalized WRMSE becomes increasingly sensitive to measurement uncertainty for smaller amounts of released pressure due to the finite measurement resolution.

2. However, a subset of experiments still exhibits distinctly higher WRMSE-values even when expressed in bar (Figure 49b). These experiments are predominantly located at the beginning of a casing series, including experiment 3 of casing 4 (Figure 48b). Several of these early experiments with a high WRMSE-value display a characteristic

pressure evolution: an initially steep, temperature-related pressure increase, followed by a phase of very slow pressure rise, and subsequently a renewed acceleration (e.g., Figure 48b). A plausible explanation for this behavior is the presence of water within the annular gap. In freshly installed casings, residual water may be present at the cement-casing interface. Gas migration through the annulus would then initially have to displace this water, leading to a temporarily reduced pressure increase rate in the upper chamber. Once the water is largely displaced, pressure increases more rapidly. After several experiments, this effect appears to diminish, presumably because the annulus has largely dried out. However, not all experiments with elevated WRMSE-values can be explained by this mechanism.

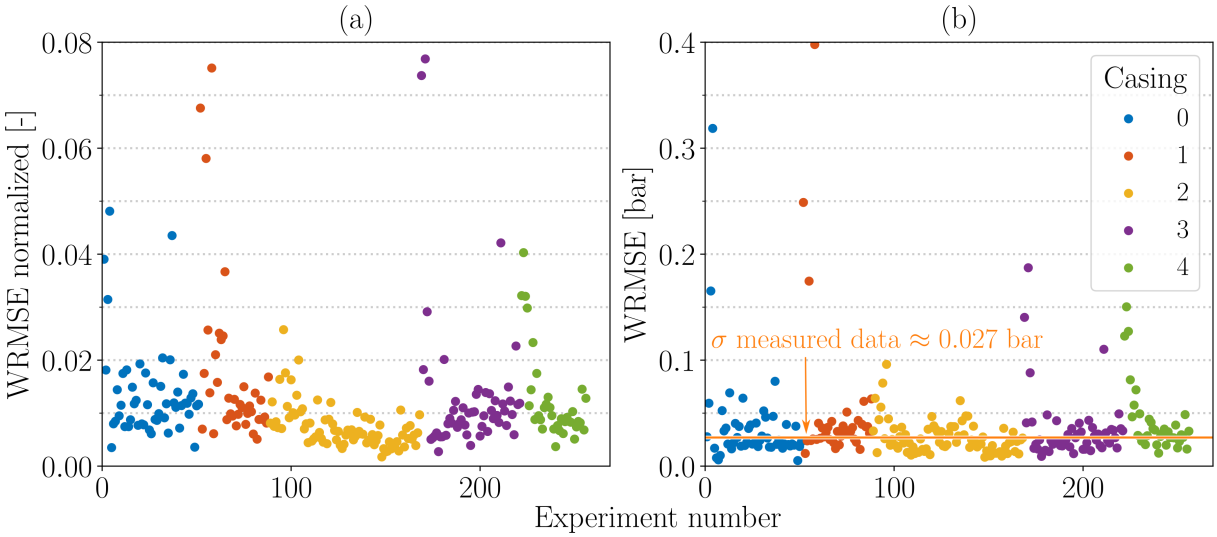


Figure 49: WRMSE (Equation 39) of all experiments. Colors represent different casings. Higher WRMSE-values indicate less agreement between measured and modeled data. The horizontal line in (b) is the standard deviation σ of the raw pressure measurements, which is further explained below.

An important reference for interpreting the WRMSE-values is the scatter of the raw pressure measurements. Figure 50a shows substantial data scatter, while step-like pressure plateaus are clearly visible in Figure 50b. This reflects the finite precision of the pressure measurement, resulting in a standard deviation σ of approximately 0.027 bar. The standard deviation represents the root mean square deviation of the measured values from their mean (Box et al., 2005) and is therefore directly comparable to the WRMSE. While σ can be interpreted as a measure of measurement precision,[43] the WRMSE quantifies how closely the modeled pressure evolution reproduces the measured data.

The standard deviation of the raw measurements is also shown as a reference line in Figure 49b. Most WRMSE-values scatter around this level. As the standard deviation

[43]However, systematic measurement errors cannot be identified from the data scatter alone. For example, a constant offset of all sensors would not be visible in the standard deviation.

represents the intrinsic measurement uncertainty, a WRMSE close to σ indicates an excellent agreement between measured and modeled data. In some cases, the WRMSE even falls below the standard deviation. This is possible because the raw data are averaged prior to modeling, thereby smoothing the step-wise plateaus visible in Figure 50b.

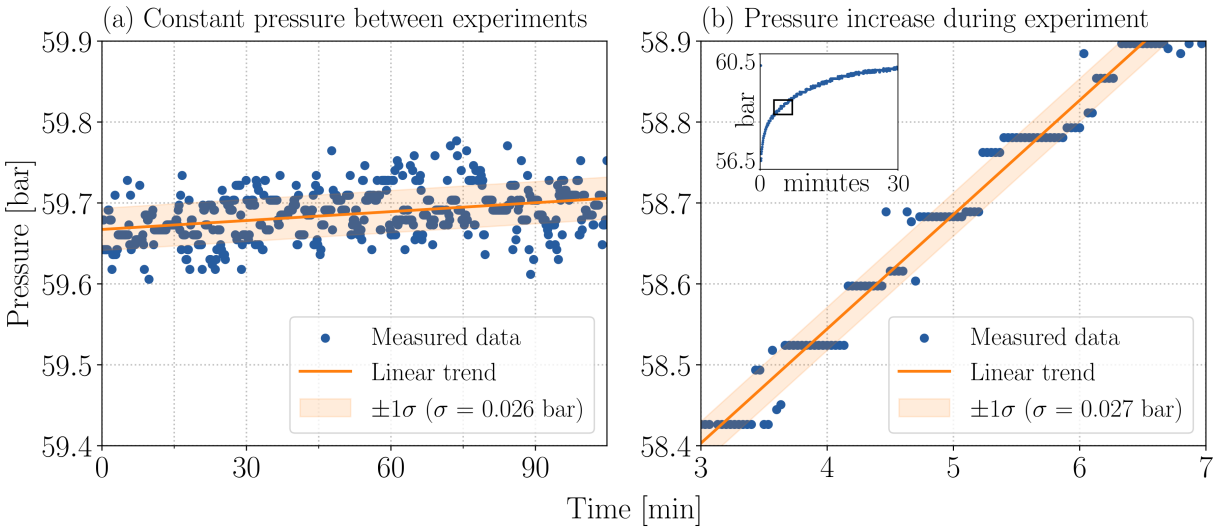


Figure 50: Raw pressure data recorded by the pressure sensor. (a) Measured pressure values between experiments on 29 May 2019; the origin of the time axis (0 min) corresponds to the start of the displayed time window. (b) Excerpt from experiment 6 of casing 3 conducted on 4 September 2020. In (b), 0 min refers to the beginning of the experiment. The inset in the upper left of (b) shows the complete experiment, with the highlighted rectangle indicating the time interval displayed in (b). σ denotes the standard deviation of the data, calculated with respect to a linear regression based on the displayed pressure signal.

In summary, the agreement between measured and modeled data is generally good. The WRMSE-values are typically close to the measurement uncertainty and only rarely significantly higher. Elevated WRMSE-values can largely be attributed to experiments with a small amount of released pressure or to transient effects, such as the presence of water in the annular gap during early experiments. More generally, elevated WRMSE-values may indicate that the effective hydraulic properties or geometry of the annular gap changed during the experiment. Since the model assumes a constant effective gap aperture throughout an experiment, transient changes caused by processes such as water displacement, drying, or thermally induced shrinkage and expansion during an experiment cannot be captured and may therefore contribute to higher WRMSE-values.

5.3.6 Applicability of the Hagen–Poiseuille equation to compressible, non-ideal fluids under unsteady flow conditions

This section examines the hypothesis that the gas flow may be described as laminar under the experimental conditions. The Hagen–Poiseuille equation (Equation 15) is strictly valid only for incompressible fluids, whereas compressible gas was used in the experiments. However, as discussed in Section 5.2.6, Equation 15 can be reformulated for compressible flow by replacing the linear pressure difference $P_{j,i-1} - P_{j,i}$ between two segments with $(P_{j,i-1}^2 - P_{j,i}^2)/(2\,P_{\mathrm{ref}})$, where P_{ref} denotes the reference pressure at which the volumetric flow rate is defined.

Using the compressible formulation within the model explicitly accounts for the pressure dependence of gas density, resulting in a smaller volumetric flow rate leaving a higher-pressure segment than entering the adjacent lower-pressure segment, while conserving mass flow rate. The compressible formulation therefore allows a more physically consistent representation of volumetric flow by assigning segment-specific reference pressures rather than relying on implicit averaged[44] conditions.

However, the compressible formulation assumes ideal gas behavior, which is only an approximation under the experimental conditions. Furthermore, the modeled gap apertures obtained using both formulations differ by a mean absolute percentage error of less than 0.5 %. Consequently, although neither formulation is strictly exact, the choice of formulation has only a minor influence on the modeling results. This is most likely because the gas behaves nearly ideally under the experimental pressure and temperature conditions, and the relative pressure differences between lower and upper chamber were small.

Furthermore, the compressibility factor Z describes the deviation of a real gas from ideal gas behavior in terms of compressibility and varies with both pressure and temperature. Among other applications, it is often used to adjust thermodynamic calculations to account for real gas compressibility. While some of the equations employed are based on ideal-gas assumptions, Z reaches at most 1.01 for the typical temperature and pressure values encountered during the experiments (Wischnewski, 2007), indicating that deviations from ideal gas behavior are minor. Incorporating Z into the equations would require determining its value for each time step and segment under the corresponding pressure and temperature conditions. Moreover, real-gas parameters (κ, c_{p}, c_{v}, γ, η) as well as the measured pressures and temperatures already reflect real-gas behavior, so applying an explicit Z-adjustment could lead to overcorrection with negligible benefit. Consequently, Z was not used to correct the respective equations.

[44] Using the incompressible Hagen–Poiseuille equation is mathematically equivalent to applying the compressible formulation at a reference pressure corresponding to the arithmetic mean pressure of adjacent segments. The incompressible formulation can therefore be interpreted as a special case of the compressible formulation with an averaged reference pressure.

Another aspect concerns the assumption of steady (stationary) flow inherent to the Hagen–Poiseuille equation. In reality, the volumetric flow rate varies continuously as pressures in the annular gap and the chambers evolve over time. However, in the model, the Hagen–Poiseuille equation is not applied globally over the entire casing length and experiment duration. Instead, the annular gap is discretized spatially into segments and temporally into time steps (Equation 15). At the beginning of each time step, the pressure difference between two adjacent segments is evaluated and used to calculate the volumetric flow rate between these segments for that time step. Consequently, the flow is treated as locally steady between adjacent segments within one time step, while the overall flow behavior remains unsteady over the length of the casing and the duration of the experiment. For sufficiently small segment lengths and time steps, this quasi-steady approach appears to provide a good approximation of the actual transient flow.

5.3.7 Laminar and turbulent flow

The Hagen–Poiseuille equation applies only to laminar flow. To distinguish between laminar and turbulent flow, the Reynolds number is often used, based on the experiments of Reynolds (1883) and calculated according to Equation 58 (White, 2011). The hydraulic diameter D_h required for this calculation is defined in Equation 59 (White, 2011), with $D_\mathrm{h} \approx 2h$ in this work.

$$Re = \frac{\rho_{Re} \cdot v \cdot D_\mathrm{h}}{\eta} \tag{58}$$

$$D_\mathrm{h} = \frac{2 \cdot h \cdot w}{h + w} \tag{59}$$

Re	Reynolds number [-]
ρ_{Re}	Density of the flowing gas [kg/m^3]
v	Mean flow velocity [m/s]
D_h	Hydraulic diameter [m]
η	Dynamic viscosity of the flowing gas [Pa $\cdot$ s]
h	Aperture of the annular gap [m]
w	Width of the annular gap [m]

Based on the work of Rotta (1956), the transition from laminar to turbulent flow is commonly assumed to begin at a critical Reynolds number of approximately 2300 (White, 2011). However, this threshold applies to regular pipe flow. For microchannels, as investigated in this work, the critical Reynolds number appears to lie in a similar range. According to Kandlikar (2013), the transition in channels with widths of 1–200 µm occurs at Reynolds numbers of approximately 2200 for square cross sections and 2500 for flow between parallel plates, the latter being more representative of the annular gap studied in

this work. Nonetheless, there is no clear consensus in the literature and critical Reynolds numbers for microchannels vary widely. While many values are close to 2000, some studies report transitions at values as low as 300, as reviewed by Hetsroni et al. (2005) and Morini (2004).

Reynolds numbers in this work are determined by first calculating the amount of substance flowing due to the pressure difference using the ideal gas law. From this, the mass is derived based on the molar mass (28 g/mol for N_2), and the volume is calculated via the gas density. With the flow time and cross-sectional area, the mean velocity can be determined. Alternatively, velocity can be obtained from the numerical model directly, but the experimental data were preferred. Once velocity is known, the Reynolds number can be determined using Equation 58.

The highest flow velocity observed in this study occurs at the beginning of experiment 59 (casing 2), for which one of the largest gap apertures (51.3 µm) is obtained from model H. In this experiment, pressure equalization was completed within only 50 seconds, driven by a comparatively large initial pressure difference of approximately 5 bar. The pressure in the upper chamber increased approximately linearly by 3 bar during the first 10 seconds. These are ideal circumstances for a conservative upper-bound estimation. A Reynolds number of 700 is determined for this 10-second interval.

In contrast, the Reynolds number determined for experiment 3 (casing 2) is only 110, although it is derived from the steepest part of the pressure increase as well and the system permeability is still relatively high for this experiment, with a modeled gap aperture of 38.1 µm. This suggests that the Reynolds number remains below 100 for most of the experiments. For example, a typical experiment with a modeled gap aperture of 20 µm yields an arithmetic mean Reynolds number of only 15. Furthermore, these estimations conservatively assume that the pressure increase is caused exclusively by gas flow, without any thermal effects.

Even the highest Reynolds numbers determined for the autoclave experiments remain far below the transition threshold of approximately 2000, which is commonly assumed to mark the onset of flow transition from laminar to turbulent conditions (e.g., Hetsroni et al., 2005; Kandlikar, 2013; Morini, 2004; White, 2011). The largest value obtained in this study (≈ 700) therefore still lies well within the laminar regime. Given that the vast majority of experiments yield Reynolds numbers below 100, and many even below 20, it is reasonable to assume predominantly laminar flow for the conditions investigated here, based solely on the Reynolds number.

However, the literature suggests that the critical Reynolds number for flow transition can decrease with increasing channel surface roughness (e.g., Kandlikar, 2013; Peiyi and Little, 1983). In other words, roughness can influence the onset of turbulence alongside fluid properties, velocity, and hydraulic diameter. To account for roughness in flow calculations, the relative roughness ε_{rel}, as defined in Equation 60, is commonly used (Guo

and Ghalambor, 2005). It is based on the absolute roughness ε_{abs}, which describes the average height of surface irregularities.

$$\varepsilon_{\text{rel}} = \frac{\varepsilon_{\text{abs}}}{D_{\text{h}}} \tag{60}$$

ε_{rel} Relative roughness [m]
ε_{abs} Absolute roughness [m]
D_{h} Hydraulic diameter as defined in Equation 59 [m]

A common way to calculate turbulent flow while accounting for surface roughness is the Darcy–Weisbach equation, which can be rearranged to express velocity and adapted to the model used in this work, as shown in Equation 61 (Chanson, 2004):

$$v = \sqrt{\frac{2 \cdot \Delta P'_{j,i} \cdot D_{\text{h}}}{f \cdot l_{\text{sg}} \cdot \rho}} \tag{61}$$

v Mean flow velocity [m/s]
$\Delta P'_{j,i}$ Normalized pressure difference between segment i and $i-1$ (point i and $i-1$) at the beginning of time step j [-]; equals $P'_{j,i-1} - P'_{j,i}$
D_{h} Hydraulic diameter as defined in Equation 59 [m]
f Darcy friction factor [-]
l_{sg} Length of an annular gap segment [m]
ρ Fluid density [kg/m^3]

The relative roughness ε_{rel} (Equation 60) is a key parameter for determining the friction factor f in Equation 61. Various formulations for determining f exist, as demonstrated by Zeghadnia et al. (2019), who reviewed 33 different equations. However, these are typically only valid for relatively high Reynolds numbers (often above 2300 or 4000) and for small relative roughnesses below 0.05. Moreover, turbulent flow behavior has been more extensively studied at the scale of commercial pipes than on the microscale - especially for systems involving cement interfaces.

Nevertheless, given the potentially high relative roughness in cement–steel annuli, which could lead to turbulence, an approach was made to simulate an extreme case where the laminar Hagen–Poiseuille flow in the model was replaced by the turbulent formulation of Equation 61. The volumetric flow rate was determined from the flow velocity and cross-sectional area. The friction factor was estimated according to Chen (1979), representing a worst-case scenario of fully rough, turbulent flow. In this simulation, the annular gap aperture required to match the pressure increase was found to be a factor of five smaller than in the laminar case. However, this is most likely inaccurate. First, the absolute

roughness ε_{abs} was arbitrarily assumed to be 50 µm. Second, it is highly questionable whether standard friction factor and turbulent flow equations are applicable under the conditions of this work at all, as discussed in the following paragraphs.

A general issue is that surface roughness is typically characterized either for commercial pipes or for microchannels made from glass. In both cases, the relative roughness is rather small due to the large diameters in pipes and the smooth surfaces in glass channels. Thus, relative roughness values above 0.05 are rarely considered. For gaps between cement and casing, no published roughness data is available. It is plausible that the relative roughness in such systems exceeds 0.05 by far, placing it well outside the range commonly investigated.

Additionally, microchannel flow is often studied using simple circular or rectangular geometries, typically with moderate aspect ratios. In comparison, the geometry in this work is rather extreme, with the channel width w several hundred times greater than the gap aperture h. This strongly deviates from the flow conditions common equations were developed for. Therefore, it is doubtful that a roughness or friction factor expressed in one single value is sufficient for such geometries. Moreover, the roughness shape may play a critical role: a sawtooth-like roughness may lead to different flow behavior than slowly varying constrictions, especially at this scale.

In conclusion, while Reynolds numbers suggest laminar flow, it remains uncertain whether roughness could locally induce turbulence. Corina et al. (2021) also assume laminar flow for cement–steel annuli, but propose that nonlinear corrections might be required depending on the gap geometry. Garcia Fernandez et al. (2019) also suggest that the geometry of a real gap can differ considerably from the assumption of a gap between parallel plates.

However, the good agreement between the modeled laminar pressure evolution and the experimental measurements suggests that the flow is predominantly laminar under the conditions investigated here. This is particularly evident from the good agreement observed even for experiments with the largest modeled annular gap apertures, corresponding to comparatively high flow rates (Figure 51). Furthermore, given the small annular gap apertures and low flow rates considered in this study, it is unlikely that turbulent flow dominates. Therefore, purely laminar flow is assumed throughout this work as a first-order approximation, which is sufficient to resolve and interpret the relevant effects investigated here. A more precise assessment of the effects of surface roughness and gap geometry would require detailed information on the actual surface structure of the cement–steel interface for each annular gap. Addressing this would require extensive experimental investigation of cement–steel interfaces, which is beyond the scope of the present study.

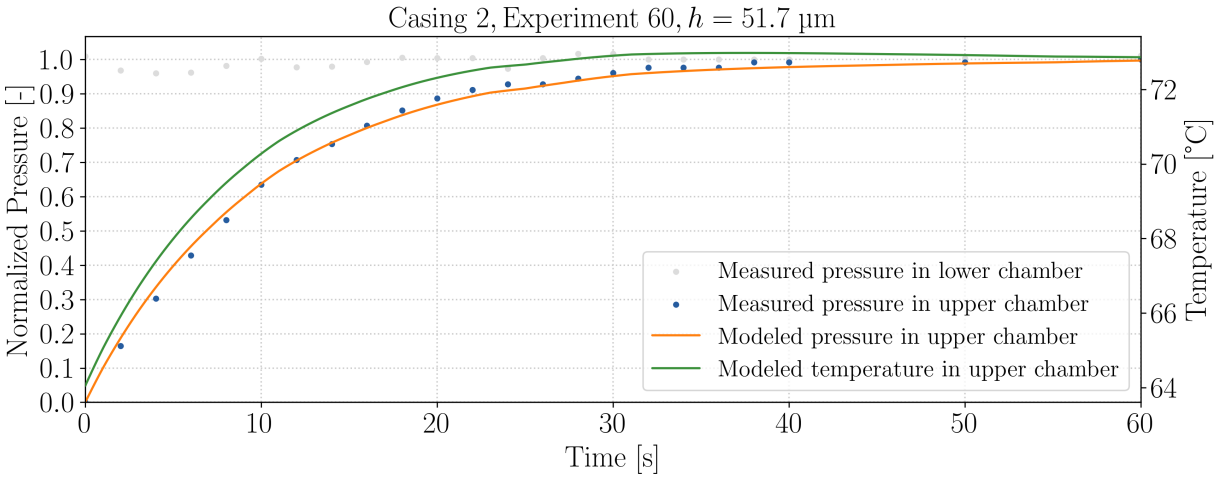


Figure 51: Pressure and temperature evolution in the upper chamber for the experiment with the largest modeled annular gap aperture h. The good agreement between measured and modeled pressure data, even for this experiment with comparatively high flow velocities, indicates that the flow remains predominantly laminar.

5.3.8 Synthesis of model uncertainties and sensitivities

In this study, a physics-based numerical model was applied to represent the underlying mechanism of gas transport through an annular gap. While efforts were made to quantify uncertainties and assess the sensitivity of the model to key assumptions, some uncertainties inevitably remain. For example, flow within the annular gap may locally deviate from purely laminar conditions, and real annular gaps are unlikely to exhibit perfectly uniform apertures or widths along their entire length.

Consequently, the modeled annular gap apertures should be interpreted as effective values that reproduce the observed pressure response rather than as exact geometric properties. The same applies when these apertures are converted into equivalent system permeabilities, which likewise represent effective parameters.

Provided that the general model assumptions are valid, the cumulative uncertainty arising from input parameters, numerical discretization in time and space, and simplifications of the physical system is expected to be on the order of a few percent (Section 3.3). This level of uncertainty does not affect the principal conclusions drawn from the modeling results.

5.4 Annular pressure and flow regulations

5.4.1 From experimental insights to regulation

The experimental and modeling findings discussed above provide insight into mechanisms governing annular gap development, system permeability evolution, and fluid migration in well systems. However, the implications of these processes extend beyond the experimental and modeling scale and directly relate to challenges in well integrity management.

These challenges are addressed in practice through regulatory frameworks that aim to prevent leakage, with annular pressure and gas flow serving as indicators. The following sections therefore discuss the rationale and content of such regulations, with particular focus on different regulatory approaches and their effectiveness in light of the findings of this study.

5.4.2 Rationale for regulation

Before any regulation or guideline is written, it is important to understand why it is necessary in the first place. In the context of wells, regulations are usually introduced to mitigate specific risks. The United Nations Office for Disaster Risk Reduction defines a *disaster risk* as "the potential loss of life, injury, or destroyed or damaged assets which could occur to a system, society or a community in a specific period of time, determined probabilistically as a function of hazard[45], exposure, vulnerability and capacity[46]" (UNDRR, 2017b).

Applying this framework to the context of wells highlights that not every risk poses a threat to public safety or the environment. Some well-related risks primarily affect operator costs and companies already have intrinsic incentives to minimize the expenses associated with such risks. Consequently, such risks are generally of limited relevance from a regulatory perspective.

The risks that are more relevant to regulatory and licensing authorities are those related to *health, safety, and the environment (HSE)*. Health risks concern the potential impact on human health, for example by exposing workers or residents living near a well to toxic gases (Epstein, 2015). Environmental risks include threats to ecosystems, the contamination of groundwater, soil, or surface environments, as well as climate-related risks such as unintended emissions of greenhouse gases (e.g., Dakhaeva and Magomaev, 2022; Forde et al., 2019). These risks may manifest locally, for example through the pollution of drinking

[45]According to the UNDRR (2017d), a *hazard* is defined as "a process, phenomenon or human activity that may cause loss of life, injury or other health impacts, property damage, social and economic disruption or environmental degradation".

[46]*Capacity*, *exposure* and *vulnerability* are defined in UNDRR (2017a,c,e)

water resources, or globally, through cumulative contributions to atmospheric greenhouse gas concentrations. Safety risks, in contrast, are typically associated with sudden, *acute* hazards, such as accidents that can occur during drilling, completion, production, or well intervention activities (Tamim et al., 2019). These accidents can lead to both immediate health consequences and environmental damage.

In addition to identifying the risks that regulations aim to prevent, it is equally important to ensure that compliance is effectively monitored. Regulators must be able to verify that the prescribed practices are actually being followed, for example through routine inspections. Otherwise, the regulations have little practical value. Furthermore, violations must be subject to meaningful consequences. For example, if the penalty for non-compliance is lower than the cost of preventing the violation, it may be economically rational for an operator to ignore the regulation, which undermines the overall intent of risk mitigation.

Accordingly, effective regulation appears to rely on at least three essential pillars.

1. Regulations must ensure that operators adhere to the current state of technology and best practices (Veer and Kumar, 2024).

2. Regulatory frameworks should confirm that operators possess the necessary technical competence and sufficient financial capacity to remediate potential damages (e.g., Fogleman, 2020; Guven et al., 2020).

3. The responsible authorities must be equipped with both the expertise and the legal means to monitor compliance and enforce sanctions that are sufficiently dissuasive to ensure meaningful adherence (Walters et al., 2021).

Only when all three conditions are fulfilled can regulations achieve their intended purpose of minimizing HSE risks.

5.4.3 Direct and indirect regulations

The studied countries regulate SCP and CVF using two different approaches: (1) Direct regulations with specific requirements, as in the USA, Canada, and Russia, and (2) indirect regulations that outline risks to be avoided, as in Australia and Norway, without specifying mitigation measures. China follows an intermediate approach, as the guidelines of state-owned companies are not official regulations.

Direct and indirect approaches each have advantages and disadvantages. Direct regulations establish clear rules and boundaries that operators have to follow. They ensure a minimum standard for all wells in a jurisdiction, some containing hundreds of thousands of wells. However, prescriptive regulations must be regularly updated to keep pace with technological developments and evolving scientific understanding. If regulations are not revised, they may continue to prescribe outdated practices. Moreover, once a well has been approved

and licensed under a given regulatory framework, regulators often have limited ability to impose additional requirements retroactively, even when new technological solutions or scientific insights become available. Furthermore, purely direct regulations struggle to capture the variability of well types and geological settings. Every well is, to some degree, unique, and there is an argument that regulations should reflect this complexity.

Indirect regulations do not apply requirements widely to all wells. The Australian approach requires operators to design a well operations management plan and present it to the regulator for approval (NOPSEMA, 2020a). This indirect approach allows for more regulatory flexibility, as regulators can tailor their requirements to individual wells or well types. Thus, stricter requirements can be enforced in specific cases, which is not the case for general, direct regulations. However, the Australian approach leaves room for human error and subjectivity and may not be feasible in jurisdictions that manage large numbers of wells. Norwegian regulations place responsibility on the operator, based on the assumption that they have the optimal expertise to handle specific well integrity challenges (Petroleum Safety Authority Norway, 2017). This reliance on industry knowledge and standards is common across many jurisdictions and has led some to incorporate industry guidelines into official regulations. For example, U.S. federal offshore regulations directly mandate compliance with the API RP 90 guideline (American Petroleum Institute, 2006; Bureau of Safety and Environmental Enforcement, 2010).

A notable advantage of indirect regulations is that, by specifying only the risks to be avoided, operators are implicitly required to use all reasonable measures to prevent them. In the event of an incident, regulators can question why available best practices were not applied. In contrast, under direct regulation, operators may only be required to demonstrate compliance with the written rule. Thus, while it may seem counter intuitive, indirect regulations can result in a higher level of safety, because they require operators to justify their decisions relative to the state of knowledge, rather than merely comply with a fixed list of requirements that could become outdated over time.

Thus, it seems advantageous to follow an indirect regulatory approach, in which the risks to be avoided are clearly defined and compliance with best practices is required. However, it is advisable to include at least one directly regulated element: mandatory data reporting. Regulators should require operators to routinely submit monitoring results, diagnostic testing data, and other relevant operational information directly to the competent authority in a predefined format.[47] It is also advisable that regulators establish a database for this data, which should be accessible to the public, comparable to the Netherlands Oil and Gas Portal (Geological Survey of the Netherlands, n.d.). This ensures transparency, reduces the

[47]In jurisdictions with a large number of wells, regulators may choose to reduce the reporting frequency (e.g., one averaged daily value instead of continuous data) or allow operators to host the data in an accessible database. At the very least, operators should be required to provide the data upon request.

risk of data loss, and supports environmental and well integrity research.[48] Furthermore, it allows state agencies to efficiently identify potential well-integrity issues and contact operators when data indicate possible anomalies.

Although an indirect regulatory approach is favored here, a *minimum standard workflow* for SCP and CVF management is proposed based on the current state of knowledge (see Section 5.4.4). This workflow can be combined with an indirect regulatory framework to provide a basic, common foundation, or, more importantly, it can be incorporated into direct regulations in jurisdictions that do not intend to adopt an indirect approach. Such jurisdictions might favor a direct approach because it can reduce administrative complexity for regulators, for example by potentially accelerating approval processes through a fixed set of requirements.

5.4.4 Suggested minimum standard workflow

If a prescriptive approach through direct regulations is chosen, it is reasonable to ensure that, at minimum, monitoring, diagnostic testing, and basic provisions for remediation are included. As compiled in Section 4.2, existing regulations do not always cover all of these three elements. In several jurisdictions, for example, only monitoring requirements are prescribed. However, monitoring alone does not prevent or resolve well integrity issues; it merely documents the presence of pressure or flow, which may or may not indicate a leak or harmful conditions. When pressure or flow is detected during monitoring, diagnostic testing is necessary to determine whether these measurements are caused by a leak and to assess leak severity. Remediation may be required where loss of integrity is confirmed. Without these components, regulations risk being formally compliant yet practically ineffective in mitigating HSE risks.

A minimum standard workflow for basic HSE risk mitigation based on these considerations is illustrated in Figure 52. Continuous monitoring of all accessible annuli throughout the well's lifecycle is recommended, combined with data recording (continuous electronic recording preferred) and an early warning system based on threshold values. Analog pressure gauges should be used for safety redundancy and reviewed periodically.

Regulators should establish an annulus pressure or flow threshold that triggers diagnostic testing when exceeded. If a threshold is surpassed, B/B tests can serve as a starting point for identifying well integrity issues, with further testing or modeling depending on the test results. Routine diagnostic testing is also recommended for all wells, at least annually. When SCP is detected, operators should inform regulators immediately and suggest remediation options.

[48] For example, flow rate data are especially important for the estimation of emissions in the context of CVF (e.g., Bowman et al., 2023; Seymour et al., 2024).

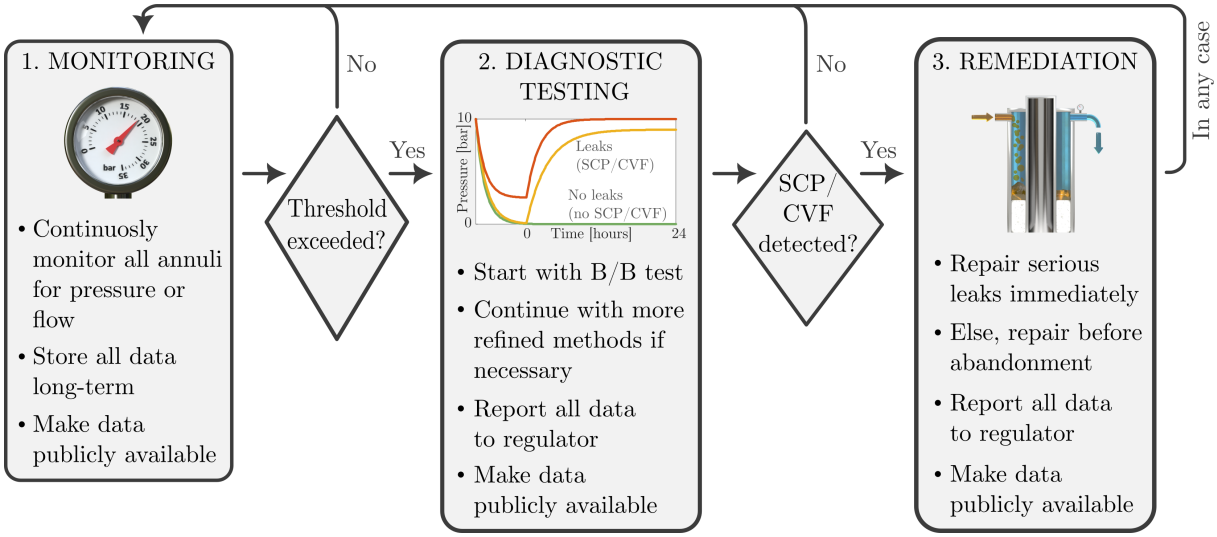


Figure 52: Recommended minimum standard workflow for SCP/CVF management, including 1) monitoring, 2) diagnostic testing, and 3) remediation. Modified after Schulz et al. (2025)

Monitoring for gas migration can be equally important and may start with a visual inspection for distressed vegetation, if vegetation is available. Alternatively, infrared cameras, portable hydrocarbon detectors, or drone sensing can, for example, be effective options (e.g., Burgués and Marco, 2020; Jońca et al., 2022; Massie et al., 2006; Ravikumar et al., 2017; Zimmerle et al., 2020). If gas migration is detected, diagnostic testing (e.g., soil testing) and remediation should follow, similar to procedures for SCP or CVF detection. As discussed, mandatory reporting requirements for all testing data to regulators are also recommended.

Similar workflows that cover monitoring and diagnostic testing are suggested in API RP 90 (American Petroleum Institute, 2006). Designed for direct field use, these API workflows include explicit threshold values and require MAWOP (Maximum Allowable Wellhead Operating Pressure) recalculations in case of pressure communication between annuli. However, they do not address reporting or remediation directly; instead, wells that do not bleed down to atmospheric pressure during testing are handled on a case-by-case basis. Furthermore, they provide detailed guidance for different well types and specific scenarios. In contrast, the workflow suggested here outlines only minimum requirements for safe annulus pressure and flow management: monitoring, diagnostic testing, and remediation. Due to its generic nature, it is designed to be applicable across most jurisdictions, particularly those without mandatory or comprehensive SCP/CVF workflows.

Since the workflow covers minimum requirements, it can be adjusted and expanded based on the specific characteristics of a jurisdiction or serve as a foundation for a more tailored or optimized workflow. For example, regulators might choose to mandate geochemical

sampling of annular fluids alongside diagnostic testing, require continuous electronic monitoring, or demand higher testing frequencies in high-risk scenarios.

As suggested by Kinik and Wojtanowicz (2011) and Kazemi and Wojtanowicz (2022), the B/B test could also be refined in a more optimized workflow. For example, removing the 24-hour time limit and allowing both bleed-down and build-up pressures to reach steady states would capture the true minimum and maximum pressures. Otherwise, if an annulus cannot be bled down to zero bar, it is unclear whether this is due to a major leak or simply because the bleed-down was halted prematurely. Moreover, the standard B/B test procedure does not consider that a pressure build-up stabilizing at a low value may also be the result of pressure loss due to subsurface leakage. Thus, an optimized workflow could include a more in-depth examination of these cases.

5.4.5 Open and closed annuli

Another key decision in well integrity and pressure management involves balancing uncontrolled gas emissions through CVF in open annuli against the consequences of SCP in closed annuli. Ideally, effective SCP/CVF monitoring would detect issues early enough that the choice of annular management approach is of lesser importance.

However, to combine the benefits of open and closed annuli, it seems advantageous to use *closed annuli with emergency release valves* where feasible. The valves can be installed at the wellhead and contain trigger springs that release gas only if a certain pressure threshold is reached, such as the MAWOP (maximum allowable wellhead operating pressure) minus a safety margin. To provide additional redundancy and prevent valve malfunction (e.g., due to corrosion of the spring mechanism), the valves should also be equipped with rupture discs designed to burst at a pressure above the spring release threshold, but still well below the MAWOP.

In the case of open annuli, quantifying leakage rates for CVF wells is crucial for understanding their contribution to global oil and gas sector emissions, and to estimate effective cement and system permeabilities. Furthermore, gaining a deeper understanding of the integrity issues experienced by a well can enhance the chances of successful remediation. To support this, recording the flow rates during the depressurization phase of B/B tests can provide additional information for further analysis.

5.4.6 Abandoned wells

The regulations and guidelines discussed primarily apply to active wells and often do not specify SCP, CVF, or gas migration monitoring requirements for abandoned wells. To ensure well integrity after abandonment, it would be advisable to prescribe diagnostic testing prior to abandonment and to perform remediation measures if integrity issues are

detected, as for example mandated in Alberta and British Columbia (Alberta Energy Regulator, 2022; British Columbia Energy Regulator, 2023). However, studies have shown that abandoned wells can also lose integrity after plugging (e.g., Cahill et al., 2023). Furthermore, subsurface leakage from abandoned wells can result in aquifer contamination or gas emissions, similar to active wells (e.g., Li et al., 2023; Williams et al., 2021). Therefore, adopting a long-term perspective seems essential, as cement-plugged abandoned wells may not remain impermeable indefinitely and leakage or contamination may only become apparent after extended periods of time.

Consequently, this study recommends long-term monitoring of abandoned wells. Where annuli are accessible, pressure or flow monitoring represent suitable options, ideally using electric gauges or flow meters to enable remote surveillance. If annuli are inaccessible, infrared cameras, portable hydrocarbon detectors, or drone-based sensing, as discussed above for gas migration, provide alternative approaches. Some of these methods, however, require on-site personnel, which underscores the complexity of the issue: every well requires monitoring for essentially an indefinite period, and each method still necessitates regular evaluation of well-specific data. As new wells are drilled, the cumulative monitoring effort and associated workload will inevitably continue to increase.

One potential solution is large-area emission monitoring using aircraft or satellite-based systems. Although these technologies offer comparatively low spatial resolution, they remain effective at identifying major emission sources, even in remote areas (e.g., Cusworth et al., 2019; Jervis et al., 2021). And ultimately, detecting the largest emitters is of primary importance. However, these methods are limited to atmospheric emissions and are not suitable for detecting subsurface impacts such as groundwater contamination, which would require more extensive and targeted sampling efforts. For example, nearby groundwater monitoring wells can be sampled to test for subsurface gas migration. Finally, leakage from abandoned wells remains an active field of research (O'Malley et al., 2024), making the development of practical long-term monitoring solutions a valuable subject for future research.

5.4.7 Relation to experimental observations

There is a clear relation between B/B tests and the experiments conducted in this work. Between loading cycles, when gas was released from the upper chamber, the procedure essentially resembles a B/B test. As in B/B tests, the subsequent pressure increase at the top of the cement column was monitored. However, while B/B tests are typically evaluated qualitatively and classified into three categories (no leak, minor leak, major leak), the experimental results presented here allow for a more detailed and quantitative assessment.

Consequently, some of the insights obtained may be transferable to the interpretation of B/B tests. Depending on the gas volume above the cement, volumetric flow rates, and the prevailing pressure and temperature conditions, thermal effects may also influence B/B test outcomes. However, these effects are likely less pronounced in B/B tests, as gas release typically occurs over a longer timespan than in the experiments described in this study. Consequently, the temperatures of the wellhead steel and the slowly expanding gas are expected to largely equilibrate during the bleed-down phase, with less heat transfer occurring during the build-up phase. As some heat transfer will still occur, particularly during bleed-down, it may be of interest to investigate how thermal effects influence the pressure–time response of B/B tests in real wells. Since the heat-transfer factors derived from the autoclave experiments are only valid for those experimental conditions, such an analysis would require data from real wells.

6 Conclusions

Wells are essential infrastructure elements for subsurface energy extraction, storage, and utilization. Sustained casing pressure (SCP) and casing vent flow (CVF) describe unintended pressure build-up at the wellhead and unintended gas flow to the atmosphere, respectively. Both are common problems caused by loss of well integrity that can compromise the safety of wells or lead to aquifer pollution and greenhouse gas emissions. In many cases, the cement–steel compound represents a critical mechanical weakness within the well barrier system.

Given the complexity of well integrity, the topic was investigated across multiple scales in this study. Large-scale experiments supported by laboratory-scale experiments were conducted to improve the understanding of leakage mechanisms, with a particular focus on underground gas storage wells operated under highly cyclic loading conditions associated with fluctuating renewable energy supply. In addition, international regulations and industry practices related to SCP and CVF were reviewed to evaluate how well integrity is managed in the field.

The large-scale experimental investigations were conducted on five cement-filled steel casings, each 2 m in length, to examine the effects of cyclic pressure and thermal loading on the casing-cement interface. For this purpose, each cement-filled casing was installed between two autoclave chambers, allowing gas pressure to be applied and independently controlled from both sides of the specimen. The experiments simulated operating conditions of underground gas storage wells at pressures of 60 bar and temperatures of 70 °C. Pressure loading was applied by releasing and reapplying gas pressure, while thermal loading was induced by activation and deactivation of heating mats. Between loading cycles, the system permeability was quantified by stimulating gas flow through the cement-filled casing. Gas flow was initiated by releasing gas from the upper autoclave chamber, thereby creating a pressure difference across the cement-filled casing. This procedure is conceptually comparable to a bleed-down/build-up (B/B) test. However, the pressure is not fully released. As a result, the pressure gradient along the short 2 m casing is closer to pressure gradients encountered in real wells than would be the case for a complete pressure release.

The experiments demonstrate that repeated pressure cycling can increase the effective system permeability of the cement-filled casing, most likely due to progressive debonding at the casing–cement interface. This finding suggests that cyclic operation promotes the formation or reactivation of leakage pathways in the form of annular gaps between steel and cement.

Notably, the permeability increase is limited to the first few loading cycles, typically fewer than ten. Subsequent cycling does not seem to cause further irreversible changes, indicating that the interfacial gap aperture approaches a mechanically stable state beyond which additional debonding is negligible and has no significant effect on system permeability.

Thermal loading appears to temporarily reduce the system permeability, an effect that may be attributed to condensation of water within the annular gap. Subsequent gas flow likely removes this water, explaining the transient nature of the permeability reduction. If this interpretation is correct, thermal loading is expected to be of limited relevance in wells where annular gaps are already liquid-filled. This observation suggests that the permeability of annular gaps may be further reduced through the presence of fluids with appropriately selected density and viscosity, together with actively maintaining a continuous fluid column on top of each annulus to prevent drying out.

During gas release from the autoclave to initiate flow through the cement-filled casing, a pronounced coupling between pressure and temperature can be observed. Gas release from the upper chamber initially causes rapid depressurization, which in turn leads to cooling of the remaining gas. Subsequently, heat transfer from the surrounding steel to the gas results in reheating, with thermal equilibration in the upper chamber occurring after approximately 200 s. This temperature increase alone induced a partial pressure recovery in the upper chamber. In parallel, gas inflow into the upper chamber contributed to both pressure and temperature increases.

The heat flow from the steel to the gas strongly influences the observed pressure build-up in the upper chamber. At low flow rates due to low system permeabilities, where negligible gas inflow occurs during the first 200 s, approximately 30% of the initially released pressure are recovered solely due to heat exchange between the gas and the surrounding steel. With increasing gas flow rates, the relative contribution of thermal effects diminishes, as the pressure build-up becomes increasingly dominated by mass inflow.

At the field scale, however, such thermal effects are expected to be of minor relevance. Pressure changes in wells typically occur over much longer timescales than in laboratory experiments, allowing the gas to remain close to thermal equilibrium with its surroundings. By comparison, pressure release from the autoclave occurred within approximately 2 s, whereas bleeding an annulus at the wellhead through a needle valve may take several hours.

To complement the experiments, numerical modeling was applied to quantify the evolution of the system permeability as a function of loading cycles, assuming gas migration occurs predominantly through an annular gap between steel and cement. A finite difference approach based on the Hagen–Poiseuille flow equation (Equation 10) was chosen, including thermal effects described above.

The modeled effective annular gap apertures inferred at the end of an experimental series of a casing range between approximately 25 and 45 µm (Figure 35), assuming the casing-cement interface is debonded along half of the casing circumference. These values are representative of abandoned wells in pore storage settings, although they were derived for cement sheath lengths of only 2 m. The model can, however, be adapted to real well geometries and conditions (Section 5.2.6), including wells exhibiting SCP or CVF.

As an example, the model was applied to simulate pressure bleed-down/build-up (B/B) tests (Figure 53), which represent a common diagnostic approach for SCP. In such tests, annular pressure at the wellhead is released and the subsequent pressure recovery is observed over a period of 24 hours. According to API RP 90, if pressure can be bled down to atmospheric conditions but subsequently rebuilds, the leak is classified as minor (American Petroleum Institute, 2006). For a simulated 500 m well with a reservoir pressure of 50 bar, assuming hydrostatic conditions, and a dry annular gap (described in more detail in Section 5.2.6), the modeled pressure evolution for different gap apertures is shown in Figure 53. For the same scenarios, the corresponding steady gas outflow rates at the wellhead, assuming the valve is open to the atmosphere, would be approximately 120 L/h for $h = 50\,\mu$m, 25 L/h for $h = 30\,\mu$m, and 0.1 L/h for $h = 5\,\mu$m.

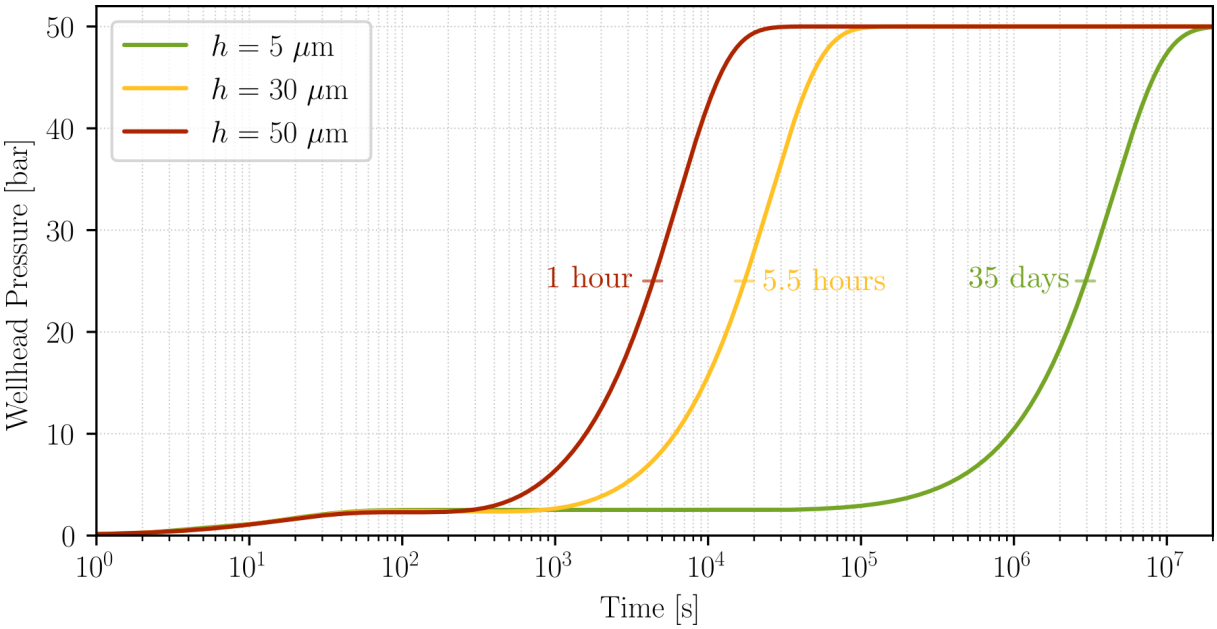


Figure 53: Modeled pressure build-up curves during bleed-down/build-up (B/B) tests for three different annular gap apertures h in a 500 m deep well. For a continuous aperture of $h = 50\,\mu$m, the wellhead pressure reaches 50 bar after approximately 5.5 hours, for $h = 30\,\mu$m after about one day, and for $h = 5\,\mu$m after approximately 230 days. The results are highly sensitive to the available wellhead volume, the assumed gap geometry, and the assumption that no gas is lost elsewhere along the flow path.

Furthermore, API RP 90 defines a major leak as a condition in which the annular pressure cannot be fully bled down to atmospheric pressure through a half-inch needle valve (American Petroleum Institute, 2006). Modeling this scenario shows that gap apertures of at least approximately 280 µm would be required to maintain even a residual pressure of 0.5 bar above atmospheric pressure with the needle valve open. If such gap apertures are required to produce a major leak, it appears unlikely that cyclic loading alone can be responsible, as the largest annular gap apertures obtained in all modeled experiments are on the order of only 50 µm.

Moreover, the gap aperture required to sustain a residual pressure at the wellhead with an open valve (e.g., the 280 µm case discussed above) can also be obtained without numerical modeling by means of a first-order analytical estimate. Equation 48 directly relates the annular gap aperture required to sustain a given wellhead pressure to the outflow through an open needle valve and yields gap apertures consistent with the numerical model, with deviations on the order of 0.1%. An analogous formulation (Equation 49) allows the effective system permeability to be estimated instead of the effective annular gap aperture. Both equations are equally applicable to wells exhibiting CVF and can be used to estimate the gap aperture or permeability required to sustain a given CVF rate.

These findings demonstrate that both the numerical model and simplified analytical approaches are applicable to SCP and CVF scenarios and consistently indicate that annular gaps generated by cyclic loading alone are unlikely to produce what API RP 90 defines as a major leak. This is attributed to the assumption that the annular gap aperture approaches a mechanically stable upper limit, which in turn limits the leakage rate. From the perspective of underground gas storage operations, this behavior is favorable. This further suggests that, under conditions of high-quality cementation, the likelihood of major leaks may be low.

Nevertheless, even minor leaks may pose long-term risks, particularly in the context of well abandonment. Each well represents a permanent subsurface opening that may become a leakage pathway in the future. From the perspectives of climate change mitigation, groundwater protection, and long-term liability, each well is therefore associated with enduring costs.

Accordingly, in addition to monitoring abandoned wells, further research into alternative sealing materials appears warranted. While cement is relatively inexpensive and widely used, it is not necessarily the most reliable long-term sealing material. Hybrid sealing concepts combining cement for mechanical stability with additional sealing layers, such as bentonite, rock plugs, bitumen, or bismuth alloys, may offer improved long-term performance. In particular, self-sealing concepts appear promising, such as the placement of clay plugs within clay caprock formations after abandonment, relying solely on lithological sealing rather than on steel or cement components.

However, beyond the technical insights gained, it is also essential to consider how SCP and CVF are managed in practice. In major oil- and gas-producing regions, approximately 10–30% of wells exhibit SCP or CVF. Against this background, this study reviewed governmental regulations and industry guidelines addressing SCP and CVF in major gas producing countries, including the United States, Russia, China, Canada, Australia, and Norway (Schulz et al., 2025).

This review reveals substantial differences in regulatory approaches. Countries such as the United States, Canada, and Russia apply relatively direct regulations, whereas Norway and Australia rely on indirect frameworks that place responsibility on operators to manage

annular pressures and flows. China similarly does not regulate SCP explicitly but operators follow guidelines issued by state-owned companies. In the United States and Canada, regulatory requirements vary considerably between jurisdictions.

While a strict, highly prescriptive regulatory approach might initially appear preferable for ensuring well safety, it remains debatable whether it represents the most effective strategy for managing SCP and the associated risks. These direct regulations place the burden on regulators to anticipate all possible scenarios and to continuously update requirements. Alternatively, defining unacceptable risks and obligating operators to apply best practices may lead to improved safety outcomes, even if this approach appears counterintuitive at first. In such frameworks, responsibility rests with the operator, who must demonstrate adherence to evolving best practices that often exceed regulatory standards.

Against this regulatory background, the review further examined how SCP and CVF are addressed in terms of monitoring, diagnostic testing, and intervention criteria. Monitoring requirements for annular pressure or flow are mandated in 38% of U.S. states, 15% of Canadian provinces and territories, as well as in Norway and Russia. In contrast, China and Australia do not require monitoring by regulation. Diagnostic testing to assess whether abnormal pressures or flows indicate integrity issues is explicitly required in 12% of U.S. states, 38% of Canadian provinces and territories, and in Russia. Threshold values triggering regulatory action are prescribed in 28% of U.S. states and 31% of Canadian provinces and territories, while in other countries they are typically suggested in guidelines. These findings indicate opportunities to strengthen regulatory frameworks, particularly by incorporating systematic monitoring and diagnostic testing to enable early detection of integrity loss.

Consequently, this study proposes a minimum workflow for SCP/CVF management in regulatory frameworks that rely on direct requirements, beginning with routine monitoring throughout the entire well lifecycle. When abnormal pressures or flows are detected, diagnostic testing should be initiated. Initial diagnostics may include simple tests such as bleed-down/build-up (B/B) tests, in which pressure is released from an annulus at the wellhead and the subsequent pressure recovery is observed, or bubble tests, where a hose connected to an annulus outlet is submerged in water to visually detect gas leakage. These basic diagnostic techniques may be supplemented by further methods, such as leak-rate quantification, fluid analysis, or numerical modeling, depending on the severity and persistence of the observed anomalies. Additionally, wells should be tested for SCP and CVF before abandonment and monitoring should continue indefinitely thereafter. In general, remediation measures should be implemented if diagnostic results indicate the presence of leakage. Finally, comprehensive documentation and reporting of SCP/CVF data are essential to prevent the loss of information that is critical for understanding a well's integrity history.

Despite these insights, significant challenges remain regarding the understanding and management of well integrity at a global scale. Given the large number of wells exhibiting integrity issues worldwide, extensive research remains essential. The present work represents a small contribution toward improving the understanding of well integrity. Future studies could expand the experimental program to include alternative sealing materials and apply the modeling framework to real well data. Regulations and field practices might also be further optimized.

Ultimately, even in a hypothetical future without hydrocarbon production, where all hydrocarbon wells are abandoned and no new wells are drilled, understanding and managing the integrity of the millions of wells that already exist today will remain an important challenge.

Glossary

Mathematical symbols and variables

This section contains only those symbols and variables that are used repeatedly throughout the document. Symbols and variables that appear exclusively in a specific context (e.g., within Section 2.5 or in Figure 5) are defined directly at the point of use and are not referred to elsewhere. For the sake of clarity and conciseness, these context-specific definitions are not included in the glossary.

$\boldsymbol{\gamma}$	Adiabatic index, heat capacity ratio of the gas [-]
$\boldsymbol{\Delta h}$	Percentage change in the annular gap opening aperture h, used for comparison in different contexts [%]
$\boldsymbol{\Delta P_{\mathrm{cas}}}$	Pressure difference between the two ends of the cement column inside the casing [Pa]
$\boldsymbol{\Delta P_{j,N}^{\mathrm{inflow}}}$	Pressure increase in the upper chamber solely due to $\dot{V}_{j,N}$, the gas flow from segment/grid point $N-1$ into the upper chamber at time step j [Pa]; see Equation 18 for normalized form
$\boldsymbol{\Delta P_{\mathrm{Z}}}$	Pressure difference over which ΔZ is determined [Pa]
$\boldsymbol{\Delta P'_{j,i}}$	Normalized pressure difference between segment i and $i-1$ (point i and $i-1$) at the beginning of time step j [-]; equals $P'_{j,i-1} - P'_{j,i}$
$\boldsymbol{\Delta P'^{\mathrm{inflow}}_{j,i}}$	Normalized pressure change in segment i due to gas flow from grid point $i-1$ to i at time step j [-]
$\boldsymbol{\Delta P'^{\mathrm{inflow}}_{j,N}}$	Normalized pressure change in segment N (in the upper chamber) due to gas flow from grid point $N-1$ to N at time step j [-]
$\boldsymbol{\Delta P'^{\mathrm{outflow}}_{j,i}}$	Normalized pressure change in segment i due to gas flow from grid point i to $i+1$ at time step j [-]
$\boldsymbol{\Delta P'^{\mathrm{warm}}_{j,N}}$	Normalized pressure increase in the upper chamber due to heat flow from steel to gas at time step j [-]
$\boldsymbol{\Delta t}$	Time step width used in the model [s]
$\boldsymbol{\Delta T_{j,N}}$	Difference between the saturation temperature $T_{\max}$ and the last modeled temperature $T_{j-1,N}$; decreases with increasing j [K]
$\boldsymbol{\Delta T^{\mathrm{flow}}_{j,N}}$	Temperature increase in the upper chamber at time step j, caused by the gas flow into the chamber and the resulting pressure increase [K]
$\boldsymbol{\Delta T^{\mathrm{gap}}_{j,N}}$	Temperature difference between the gas entering the upper chamber from the gap and the gas already present in the upper chamber at the moment of mixing during time step j [K]
$\boldsymbol{\Delta T^{\mathrm{gap}}}$	A constant temperature difference between the gas entering the upper chamber from the gap and the gas already present in the upper chamber at the moment of mixing during all time steps [K]

$\boldsymbol{\Delta Z}$	Change in compressibility factor Z of nitrogen corresponding to ΔP_{Z} [-]
$\boldsymbol{\eta}$	Dynamic viscosity of the flowing fluid [Pa·s]
$\boldsymbol{\kappa}$	Compressibility of the flowing fluid [Pa^{-1}]
$\boldsymbol{\kappa^{(\mathrm{S})}}$	Isentropic compressibility of the flowing fluid [Pa^{-1}]
$\boldsymbol{\kappa^{(\mathrm{T})}}$	Isothermal compressibility of the flowing fluid [Pa^{-1}]
$\boldsymbol{\kappa^{(\mathrm{S})}_{j,N}}$	Isentropic compressibility of the gas in segment N and time step j [Pa^{-1}]
$\boldsymbol{\kappa^{(\mathrm{T})}_{j,i}}$	Isothermal compressibility of the gas in segment i and time step j [Pa^{-1}]
$\boldsymbol{\kappa^{(\mathrm{T})}_{j,N}}$	Isothermal compressibility of the gas in segment N and time step j [Pa^{-1}]
$\boldsymbol{a}$	Maximum temperature that can be reached during the heating process as $t \to \infty$ [K]; equals the temperature before the gas release and after the full heating process is completed
$\boldsymbol{A}$	Base area of the cement column [m^2]
$\boldsymbol{b}$	Difference between the temperatures immediately before and after gas release with $b = a - T(0) = T_{\max} - T_{\min}$ [K]
$\boldsymbol{c}$	Growth rate constant of the bounded growth equation; controls the rate at which heat is exchanged between the steel of the upper chamber and the gas inside and can therefore be regarded as a continuous heat transfer factor [1/s]
$\boldsymbol{c_{\mathrm{p}}}$	Heat capacity of gas at constant pressure [J/(kg·K)]
$\boldsymbol{c_{\mathrm{v}}}$	Heat capacity of gas at constant volume [J/(kg·K)]
$\boldsymbol{F_{\Delta t}}$	Additional factor to manually decrease Δt [-]
$\boldsymbol{h}$	Aperture of the annular gap [m]; see Figure 4
$\boldsymbol{i}$	Index for intervals/segments/grid points [-]; $i = 1, 2, \ldots, N$ for intervals and $i = 0, 1, 2, \ldots, N$ for segments/grid points
$\boldsymbol{j}$	Time steps assigned to modeled data, $j = 1, 2, \ldots, J$ [-]
$\boldsymbol{J}$	Total number of time steps assigned to modeled data [-]
$\boldsymbol{k}$	Discrete heat transfer factor based on c and Δt [-]
$\boldsymbol{K_{\mathrm{HP}}}$	Shape factor accounting for the channel geometry [-]; since w is 4–5 orders of magnitude greater than h in this work, K_{HP} is close to 1.
$\boldsymbol{K^{\mathrm{model}}_{\mathrm{Darcy}}}$	Modeled equivalent cement matrix permeability assuming only cross-sectional flow [m^2]
$\boldsymbol{l}$	Length of the annular gap [m]; see Figure 4
$\boldsymbol{l_{\mathrm{sg}}}$	Length of an annular gap segment, equals l/N [m]
$\boldsymbol{m}$	Time steps assigned to measured data, $m = 1, 2, \ldots, M$ [-]
$\boldsymbol{M}$	Total number of time steps assigned to measured data [-]
$\boldsymbol{N}$	Total number of intervals. Total number of segments/grid points = N + 1, with grid point N representing the upper chamber and grid point 0 representing the lower chamber [-]

$\boldsymbol{p}$	The p-value [-] is the probability of obtaining the observed result (or a more extreme one) under the null hypothesis. Conventionally, a p-value greater than 0.05 suggests that the observed effect is not statistically significant.
$\boldsymbol{P_{\mathrm{phys}}}$	Physical, non-normalized pressure value [Pa]
$\boldsymbol{P_{j,0}}$	Measured pressure in the lower chamber at the end of time step j
$\boldsymbol{P_{j,i}}$	Calculated pressure in segment i at the end of time step j [bar]
$\boldsymbol{P_{j-1,i}}$	Calculated pressure in segment i at the end of time step $j-1$ and thus at the beginning of time step j [bar]
$\boldsymbol{P_{j-1,N}}$	Calculated pressure in the upper chamber at the end of time step $j-1$ and thus at the beginning of time step j [Pa]; $P_{0,N} = P_{\min}$
$\boldsymbol{P_{j,N}^{\mathrm{warm}}}$	Calculated pressure in the upper chamber at time step j, including the pressure increase from heating at time step j, but not the pressure increase due to gas flow from the lower chamber at time step j [Pa]; the difference between $P_{j,N}^{\mathrm{warm}}$ and $P_{j-1,N}$ is solely caused by the heating of the gas due to the warmer surrounding steel; $P_{0,N}^{\mathrm{warm}} = P_{\min}$
$\boldsymbol{P_m}$	Measured pressure in the upper chamber at time step m [Pa]; $P_0 = P_{\min}$
$\boldsymbol{P_{\mathrm{max}}}$	Measured maximum pressure in the upper chamber that can be reached during the pressure build-up, equals pressure before the gas release [Pa]
$\boldsymbol{P_{\mathrm{min}}}$	Measured minimum pressure in the upper chamber reached at the end of the gas release [Pa]; $P_{\min} = P_{0,N}$
$\boldsymbol{P_Z}$	Pressure at which the compressibility is calculated [Pa]
$\boldsymbol{P'}$	Normalized pressure value [-]
$\boldsymbol{P'_{0,i}}$	Normalized pressure in segment i at the beginning of the modeling [-]
$\boldsymbol{P'_{j,0}}$	Normalized measured pressure in the lower chamber at the end of time step j [-]
$\boldsymbol{P'_{j,i}}$	Normalized pressure in segment i at the end of time step j, after the gas flows $\dot{V}_{j,i}$ and $\dot{V}_{j,i+1}$ have concluded [-]
$\boldsymbol{P'_{j,N}}$	Normalized pressure in the upper chamber at the end of time step j, including both heating and gas flow shares [-]; $P'_{0,N} = 0$
$\boldsymbol{P'_{j-1,i}}$	Normalized pressure in segment i at the end of time step $j-1$, and thus at the beginning of time step j [-]
$\boldsymbol{P'^{\mathrm{warm}}_{j,N}}$	Normalized value of $P_{j,N}^{\mathrm{warm}}$ [-]; $P'^{\mathrm{warm}}_{0,N} = 0$
$\boldsymbol{r}$	Inner radius of the casing [m]
$\boldsymbol{t}$	Time that has passed since the beginning of the experiment [s]
$\boldsymbol{T_{j,N}}$	Calculated temperature in the upper chamber (segment N) at the end of time step j, including both heating and gas flow shares [K]; $T_{0,N} = T_{\min}$
$\boldsymbol{T_{j-1,N}}$	Calculated temperature in the upper chamber at the end of time step $j-1$ and thus at the beginning of time step j, calculated according to Equation 36 [K]

$\boldsymbol{T_{j,N}^{\text{flow}}}$	Calculated temperature in the upper chamber at time step j, including the temperature increase from gas flow at time step j, but not the temperature increase due to heat flow from steel to gas at time step j [K]; $T_{0,N}^{\text{flow}} = T_{\min}$
$\boldsymbol{T_{j,N}^{\text{warm}}}$	Calculated temperature in the upper chamber at time step j, accounting for heat flow from gas to steel during time step j. The temperature change caused by gas flow during time step j is not included [K]
$\boldsymbol{T_m}$	Calculated temperature in the upper chamber at time step m [K]; $T_0 = T_{\min}$
$\boldsymbol{T_{\text{max}}}$	Measured temperature in the upper chamber before the gas release [K]
$\boldsymbol{T_{\text{min}}}$	Calculated minimum temperature in the upper chamber immediately after the gas release [K]
$\boldsymbol{T(t)}$	Temperature in the upper chamber at time t [K]
$\boldsymbol{V_{\text{sg}}}$	Volume of a gap segment [m^3]
$\boldsymbol{V_{\text{uc}}}$	Volume of the upper chamber (segment N) [m^3]
$\boldsymbol{\dot{V}}$	Volumetric flow rate [m^3/s]
$\boldsymbol{\dot{V}_{j,i}}$	Volumetric flow rate between grid point $i-1$ and grid point i during time step j; can be positive (gas flow from point $i-1$ to point i) or negative (gas flow from point i to point $i-1$) [$\frac{m^3}{Pa \cdot s}$]
$\boldsymbol{\dot{V}'_{j,i}}$	Volumetric flow rate (pressure-normalized) between grid point $i-1$ and grid point i during time step j; can be positive (gas flow from point $i-1$ to point i) or negative (gas flow from point i to point $i-1$) [$\frac{m^3}{Pa \cdot s}$]; $\dot{V}'_{j,i} \cdot (P_{\max} - P_{\min}) = \dot{V}_{j,i}$
$\boldsymbol{w}$	Width of the straightened annular gap [m]; see Figure 4
$\boldsymbol{w_m}$	Weight assigned to time step m in the WRMSE calculation [-]
WRMSE	Weighted root mean square error [-]
$\boldsymbol{y_m}$	True (measured) normalized pressure in the upper chamber at time step m [-]
$\boldsymbol{\hat{y}_m}$	Predicted (modeled) normalized pressure in the upper chamber at time step m [-]
$\boldsymbol{Z}$	Compressility factor of nitrogen at the pressure P_Z and temperature T at which the compressibility is calculated [-]

Chemical symbols

$\mathbf{CaCl_2}$	Calcium chloride
$\mathbf{CaCO_3}$	Calcium carbonate
$\mathbf{Ca(OH)_2}$	Portlandite
$\mathbf{Ca_2(Al,Fe)_2O_5}$	Brownmillerite (C_4AF in cement notation)
$\mathbf{Ca_2SiO_4}$	Belite (C_2S in cement notation)
$\mathbf{Ca_3Al_2O_6}$	Tricalcium aluminate (C_3A in cement notation)

Ca_3SiO_5	Alite (C_3S in cement notation)
CO_2	Carbon dioxide
CO_3^{2-}	Carbonate ion
C–S–H	Calcium silicate hydrates (cement notation)
Fe/Fe^+	Iron (elemental/cationic form)
FeS	Iron(II) sulfide
H_2/H^+	Hydrogen (molecular/cationic form)
H_2CO_3	Carbonic acid
HCO_3^-	Bicarbonate
HCl	Hydrogen chloride
H_2O	Water
H_2S	Hydrogen sulfide
N_2	Nitrogen

Abbreviations

API	**American Petroleum Institute** Issues industry standards
B/B test	**Bleed-down/build-up test** Diagnostic test based on a pressure release (bleed-down) of an annulus and the following rise (build-up) of the pressure curve within 24 hours
CVF	**Casing Vent Flow** Gas or liquid flow through an open annulus
DE	**Differential evolution** Optimization algorithm
H	**Model version H** Automated model that uses the gap aperture h as a fitting parameter
HC	**Model version HC** Automated model that uses the gap aperture h and the heat transfer factor c as fitting parameters
HP	**Model version HP** Automated model that uses the gap aperture h, the minimum pressure $P_{\min}$, and the maximum pressure $P_{\max}$ as fitting parameters
LS	**Least squares** Optimization algorithm
L-BFGS-B	**Limited-memory Broyden–Fletcher–Goldfarb–Shanno with Bounds** Optimization algorithm

MAASP	**Maximum Allowable Annulus Surface Pressure** Maximum pressure that is allowed at the wellhead, calculated for each annulus
MAWOP	**Maximum Allowable Wellhead Operating Pressure** Maximum operating pressure that is allowed at the wellhead, calculated for each annulus
NM	**Nelder-Mead method** Optimization algorithm
NOPSEMA	**The National Offshore Petroleum Safety and Environmental Management Authority** Australian authority
NORSOK	**The Norwegian Shelf's Competitive Position** Issues industry standards
SCP	**Sustained Casing Pressure** Pressure in annuli that rebuilds when it is bled down and that is not caused by thermal fluctuations or the operator
SCVF	**Surface Casing Vent Flow** Gas or liquid flow through the open surface casing annulus
UGS	**Underground Gas Storage** Caverns, depleted oil and gas fields, or other subsurface structures used to store gas in the underground
WOMP	**Well Operations Management Plan**
WRMSE	Weighted root mean square error
XRD	**X-ray diffraction** A method used to identify crystalline phases by measuring the diffraction pattern of X-rays passing through a sample.

Acknowledgements

First and foremost, I would like to thank Frank Schilling for his supervision, support and continuous guidance throughout my doctoral studies as well as for the trust placed in me. Without him, this work would obviously not have been possible. In a similar manner, I would like to thank Birgit Müller and Thomas Röckel for their ongoing support.

For the experimental part of this work, I especially wish to thank Hagen Steger, who was always available to help whenever urgent issues or questions arose, and Kevin Altinger, whose skill and efficiency in manufacturing components and supporting the modification of the experimental setups were indispensable. I further thank Felix Voß for his assistance with laboratory experiments on cement parameters and Olaf Ukelis for his support during the cementing of the casings. I would also like to remember Roland Tremmel, who sadly passed away during the course of this work. He greatly supported the experimental part of this thesis, in particular through his help with the reconstruction of the autoclave setups. His dedication and kindness will be remembered.

I would also like to acknowledge Janine Wagner for her support with XRD and sample preparation, and Kirsten Drüppel, who carried out the Rietveld refinement of the XRD data. My thanks also go to Petra Schlager, Astrid Hirsch and Sebastian Schwarz for their help with permeability measurements and cement related issues. Special thanks are also due to Lukas Zimmermann who encouraged me to look into thermal effects.

I am very grateful to Mayukh Talukdar, Isabelle Pfander, Greg Lackey, Andrew Wojtanowicz, and Philipp Blum for their contributions, valuable input, and stimulating discussions during the preparation of our joint publication (Schulz et al., 2025).

I also wish to thank the following colleagues and experts from regulatory authorities and research institutions: Sergey Khafizov, Alik Ismail-Zadeh, Natalya Zeinalova, Halvard Hedland, Roar Sognnes, Erin Barillaro, Alyx Guarin, San Aung, Justin Forster, Wang Minliuyan, Zhouji Liang, Bo Zhang, Jonathan Woods and Chantelle. Their support was invaluable in gathering and understanding international SCP regulations and guidelines.

I would also like to thank my dear friend Natalya Zeinalova again for proofreading and for many helpful discussions, as well as Alik Ismail-Zadeh for his support with mathematical questions.

I am also deeply grateful to the Earthquake Research Institute in Tokyo, in particular to Masa Kinoshita, in whose group I was hosted and from whom I learned a lot, and to Yoko Teruhara, who kindly handled administrative matters and was always ready to help with any issues. I further thank JAMSTEC for providing insights into practical drilling, especially Adam Wspanialy for patiently answering my many questions. Special thanks go to Andreas Schenk, Diana Lieber, and the GRACE team in general for generously funding this trip to Japan.

Furthermore, I want to thank Sean Holland for providing me with computer equipment for my home workspace, which made the writing process much more pleasant. I am also grateful to Anna Bahß and Benjamin Lampe for taking over the organization and coordination of our regular activities during the final phase of my doctoral studies, which allowed me to focus on completing this dissertation.

I would also like to thank my parents, Monika and Volker Schulz, and my sister, Leyla Langauf, for their continuous support and encouragement throughout my doctoral studies.

This work was made possible through funding provided by the Federal Ministry for Economic Affairs and Energy of Germany (BMWE, formerly BMWK) under the project $SAMUH_2$ (grant number 03EI3051A), and by the Federal Ministry of Research, Technology and Space of Germany (BMFTR, formerly BMBF) under the project SUBI (grant number 03G0869). I am also grateful to the members of the $SAMUH_2$ and SUBI project teams for the excellent collaboration and inspiring discussions.

Finally, I want to thank Luisa Röckel for everything she has done to support me, whether by rendering Figures 1, 3, 4, 5 and 6, discussing content, helping me with Python, or simply providing encouragement and mental support.

I also wish to acknowledge the use of artificial intelligence tools, primarily for correcting grammar and spelling. DeepL Write, ChatGPT, and Microsoft Copilot were used for these purposes. The latter two were also employed in other ways: I occasionally posed questions or presented problems to verify whether their conclusions or solutions aligned with mine. Additionally, I used them to resolve programming errors and to accelerate coding tasks where the results could be easily verified. This mainly applied to small programs, such as for simple data merging and processing.

An Unexpected Observation

„Moria! Moria! Wonder of the Northern world! Too deep we delved there, and woke the nameless fear." (Tolkien, 1954)[49]

Surprisingly, J.R.R. Tolkien may have been more knowledgeable about well integrity than commonly assumed. How else could we interpret *delving too deep* and awakening the *Flame of Udûn* if not as a fire caused by gas migrating to the surface? Tolkien is even more specific regarding the evil awakened in the depths: the Balrog, a fiery being that is quite literally burning. The Balrog of Morgoth was eventually halted by Gandalf the *Grey* with the famous words: "You cannot pass." Considering both the color of cement and its purpose of preventing fluid migration, it seems obvious that Gandalf represents the cement barrier, while the Balrog represents gas attempting to migrate upward. Indeed, the Balrog migrates from the underground toward the surface, pursued by Gandalf, until it is finally defeated and thrown back down from the peak of Zirakzigil.

After the battle, Gandalf the Grey becomes Gandalf the White. This transformation likely represents remedial well intervention (perhaps placing a – rather white – salt plug?), as no competent well engineer would continue to rely on a barrier that had already allowed a Balrog to pass.

[49]Tolkien, J.R.R. (1954): *The Fellowship of the Ring.* London: George Allen & Unwin

References

Abboud, J. M.; Watson, T. L.; Ryan, M. C. (2021): Fugitive Methane Gas Migration around Alberta's Petroleum Wells. In: *Greenhouse Gases: Science and Technology* 11.1, pp. 37–51. ISSN: 2152-3878, 2152-3878. DOI: 10.1002/ghg.2029. URL: https://onlinelibrary.wiley.com/doi/10.1002/ghg.2029 (visited on 08/23/2024).

Acker, P. (2004): Swelling, Shrinkage and Creep: A Mechanical Approach to Cement Hydration. In: *Materials and Structures* 37.4, pp. 237–243. ISSN: 1359-5997, 1871-6873. DOI: 10.1007/BF02480632. URL: http://link.springer.com/10.1007/BF02480632 (visited on 11/21/2025).

Ahmed, Shawgi and Salehi, Saeed (2021): Failure Mechanisms of the Wellbore Mechanical Barrier Systems: Implications for Well Integrity. In: *Journal of Energy Resources Technology* 143.7. ISSN: 0195-0738, 1528-8994. DOI: 10.1115/1.4050694.

Alaska Oil and Gas Conservation Commission (2021): Industry Guidance Bulletin 21-001, No-Flow Test Guidance. Anchorage. URL: https://www.commerce.alaska.gov/web/Portals/18/pub/StatutesAndRegulations/Industry%20Guidance%20Bulletin%2021-001.pdf (visited on 05/18/2026).

Alberta Energy Regulator (2022): Directive 087: Well Integrity Management. URL: https://static.aer.ca/prd/documents/directives/directive-087.pdf.

Allahvirdizadeh, Payam (2020): A Review on Geothermal Wells: Well Integrity Issues. In: *Journal of Cleaner Production* 275, p. 124009. ISSN: 09596526. DOI: 10.1016/j.jclepro.2020.124009. URL: https://linkinghub.elsevier.com/retrieve/pii/S0959652620340543 (visited on 08/12/2025).

Alonso, C. and Fernandez, L. (2004): Dehydration and Rehydration Processes of Cement Paste Exposed to High Temperature Environments. In: *Journal of Materials Science* 39.9, pp. 3015–3024. ISSN: 0022-2461, 1573-4803. DOI: 10.1023/B:JMSC.0000025827.65956.18. URL: https://link.springer.com/10.1023/B:JMSC.0000025827.65956.18 (visited on 11/24/2025).

American Petroleum Institute (2006): API Recommended Practice 90: Annular Casing Pressure Management for Offshore Wells. URL: https://www.apiwebstore.org/standards/90 (visited on 10/13/2022).

American Petroleum Institute (2016): API Recommended Practice 90-2: Annular Casing Pressure Management for Onshore Wells. URL: https://www.apiwebstore.org/standards/90-2 (visited on 10/13/2022).

Anya, Alexander; Emadi, Hossein; Watson, Marshall; Kolawole, Oladoyin; Altawati, Faisal (2023): An Investigation of Fatigue Response of Well Cement under Cyclic Loading and Impact on Zonal Isolation Performance. In: *Geoenergy Science and Engineering* 230, p. 212172. ISSN: 29498910. DOI: 10.1016/j.geoen.2023.212172. URL: https://linkinghub.elsevier.com/retrieve/pii/S2949891023007595 (visited on 08/13/2025).

Arkansas Oil and Gas Commission (2021): Arkansas Administrative Code, Title 15, Chapter XV, Part 275. URL: https://www.aogc.state.ar.us/rules/rulesregs.aspx (visited on 05/11/2026).

Atkins, Peter and de Paula, Julio (2006): Atkins' Physical Chemistry. 8th ed. New York: W. H. Freeman and Company. ISBN: 0-7167-8759-8.

Aznor, M. Z. B; Lucas, A.; Sim, C. S.; Mokhtar, M. K. B. M; Abdullah, M. B. B. M.; Zainuddin, A. A. B.; Chadwick, M.; Berry, P.; Choi, Y. X.; Carragher, P.; Nor, M. A. B. M.; Khalid, M. I. B. (2025): Remediation of Post-Abandonment Sustained Annular Pressure and Gas Migration Using Bismuth Alloy Plugs. In: *SPE Symposium - Asia Pacific Decommissioning and Well P&A*. SPE Symposium - Asia Pacific Decommissioning and Well P&A. Perth, Australia: SPE, D021S007R001. DOI: 10.2118/228564-MS. URL: https://onepetro.org/SPESM02/proceedings/26SA04/26SA04/D021S007R001/793806 (visited on 11/24/2025).

Bachu, Stefan (2017): Analysis of Gas Leakage Occurrence along Wells in Alberta, Canada, from a GHG Perspective – Gas Migration Outside Well Casing. In: *International Journal of Greenhouse Gas Control* 61, pp. 146–154. ISSN: 17505836. DOI: 10.1016/j.ijggc.2017.04.003. URL: https://linkinghub.elsevier.com/retrieve/pii/S175058361630593X (visited on 04/02/2024).

Bachu, Stefan and Watson, Theresa L. (2009): Review of Failures for Wells Used for CO2 and Acid Gas Injection in Alberta, Canada. In: *Energy Procedia* 1.1, pp. 3531–3537. ISSN: 18766102. DOI: 10.1016/j.egypro.2009.02.146. URL: https://linkinghub.elsevier.com/retrieve/pii/S1876610209007899 (visited on 08/04/2025).

Bai, Mingxing; Zhang, Zhichao; Fu, Xiaofei (2016): A Review on Well Integrity Issues for CO 2 Geological Storage and Enhanced Gas Recovery. In: *Renewable and Sustainable Energy Reviews* 59, pp. 920–926. ISSN: 13640321. DOI: 10.1016/j.rser.2016.01.043. URL: https://linkinghub.elsevier.com/retrieve/pii/S1364032116000733 (visited on 08/14/2024).

Baumgarte, C.; Thiercelin, M.; Klaus, D. (1999): Case Studies of Expanding Cement To Prevent Microannular Formation. In: *SPE Annual Technical Conference and Exhibition*. SPE Annual Technical Conference and Exhibition. Houston, Texas: SPE, SPE-56535–MS. DOI: 10.2118/56535-MS. URL: https://onepetro.org/SPEATCE/proceedings/99ATCE/99ATCE/SPE-56535-MS/60267 (visited on 08/28/2025).

Baumgartner, A.W. (1962): Microbiological Corrosion What Causes It and How It Can Be Controlled. In: *Journal of Petroleum Technology* 14.10, pp. 1074–1078. ISSN: 0149-2136, 1944-978X. DOI: 10.2118/391-PA. URL: https://onepetro.org/JPT/article/14/10/1074/162705/Microbiological-Corrosion-What-Causes-It-and-How (visited on 08/05/2025).

Bellarby, Jonathan (2009): 10.3. Packers. In: *Well Completion Design*. 1st ed. Developments in Petroleum Science v. 56. Amsterdam, Netherlands Boston, Mass: Elsevier. ISBN: 978-0-444-53210-7.

Benchiheub, Omar; Mechachti, Said; Serrai, S.; Khalifa, M.G. (2010): Elaboration of Iron Powder from Mill Scale. In: *Journal of Materials and Environmental Science* 1.4, pp. 267–276. URL: https://www.jmaterenvironsci.com/Document/vol1/31-JMES-22-2010-Benchibeub.pdf (visited on 10/08/2025).

Bertness, T.A.; Chilingarian, George V.; Al-Bassam, Moayed (1989): Chapter 8 Corrosion in Drilling and Producing Operations. In: *Developments in Petroleum Science*. Vol. 19. Elsevier, pp. 283–317. ISBN: 978-0-444-42677-2. DOI: 10.1016/S0376-7361(08)70507-7. URL: https://linkinghub.elsevier.com/retrieve/pii/S0376736108705077 (visited on 08/04/2025).

Bird, R. Byron; Stewart, Warren E.; Lightfoot, Edwin N. (2002): Transport Phenomena. 2nd, Wiley international ed. New York: J. Wiley. 895 pp. ISBN: 978-0-471-41077-5.

Bird, Robert Byron; Stewart, Warren E.; Lightfoot, Edwin N. (2001): §2.3 Flow through a Circular Tube. In: *Transport Phenomena*. 2. ed. New York Weinheim: Wiley. ISBN: 978-0-471-41077-5.

Bittleston, S.H.; Ferguson, J.; Frigaard, I.A. (2002): Mud Removal and Cement Placement during Primary Cementing of an Oil Well – Laminar Non-Newtonian Displacements in an Eccentric Annular Hele-Shaw Cell. In: *Journal of Engineering Mathematics* 43.2/4, pp. 229–253. ISSN: 00220833. DOI: 10.1023/A:1020370417367. URL: http://link.springer.com/10.1023/A:1020370417367 (visited on 02/07/2025).

Boettcher, Christian; Garg, Amit; Mbuthi, Paul Nzomo; Oliver, Steven J.; Quadrelli, Roberta; Randles, Cynthia Ann; Souza, Raquel Rodrigues de; Singh, Ajay Kumar; Strogies, Michael; Tadlya, Kostyantyn; Uvarova, Nina; Watterson, John D.; Weitz, Melissa M.; Yamba, Francis Davison; Yu, Shengmin; Zhu, Songli; Dawidowski, Laura E.; Kolmogortseva, Oleksandra; Okazaki, Teruo; Pinho, Ingrid Person Rocha e; Smyth, Steven C.; Witi, Jongikhaya (2019): 2019 Refinement to the 2006 IPCC Guidelines for National Greenhouse Gas Inventorie, Volume 2: Energy, Chapter 4: Fugitive Emissions. In: Switzerland. ISBN 978-4-88788-232-4: Intergovernmental Panel on Climate Change (IPCC). ISBN: 978-4-88788-232-4. URL: https://www.ipcc-nggip.iges.or.jp/public/2019rf/vol2.html.

Bourgoyne, Adam T.; Scott, Stuart L.; Manowski, Wojciech (1999): A Review of Sustained Casing Pressure Occuring on the OCS. Submitted to: US Department of Interior - Minerals Management Service. Technical Report Contract Number 14-35-001-30749. Baton Rouge, Louisiana, USA: Luisiana State University. URL: https://www.bsee.gov/sites/bsee.gov/files/tap-technical-assessment-program/008de.pdf (visited on 10/11/2022).

Bowman, Lauren V.; El Hachem, Khalil; Kang, Mary (2023): Methane Emissions from Abandoned Oil and Gas Wells in Alberta and Saskatchewan, Canada: The Role of Surface Casing Vent Flows. In: *Environmental Science & Technology* 57.48, pp. 19594–19601. ISSN: 0013-936X, 1520-5851. DOI: 10.1021/acs.est.3c06946. URL: https://pubs.acs.org/doi/10.1021/acs.est.3c06946 (visited on 08/16/2024).

Box, George E. P.; Hunter, J. Stuart; Hunter, William Gordon (2005): Chapter 2.4: Measures of Location and Spread. In: *Statistics for Experimenters: Design, Innovation, and Discovery*. 2nd ed. Wiley Series in Probability and Statistics. Hoboken, N.J: Wiley-Interscience. ISBN: 978-0-471-71813-0.

Bracke, Guido; Charlier, Frank; Geckeis, Horst; Harms, Ulrich; Heidbach, Oliver; Kienzler, Bernhard; Liebscher, Axel; Müller, Birgit; Prevedel, Bernhard; Röckel, Thomas; Schilling, Frank; Sperber, Axel (2016): Tiefe Bohrlöcher. Auftrags-Nr.: 565 000. GRS – Gesellschaft für Anlagen- und Reaktorsicherheit, im Auftrag der Kommission Lagerung hochradioaktiver Abfallstoffe. URL: https://www.bundestag.de/resource/blob/413166/73c4148a71bb98611305958662204e23/kmat_52-data.pdf (visited on 11/25/2025).

Branch, Mary Ann; Coleman, Thomas F.; Li, Yuying (1999): A Subspace, Interior, and Conjugate Gradient Method for Large-Scale Bound-Constrained Minimization Problems. In: *SIAM Journal on Scientific Computing* 21.1, pp. 1–23. ISSN: 1064-8275, 1095-7197. DOI: 10.1137/S1064827595289108. URL: http://epubs.siam.org/doi/10.1137/S1064827595289108 (visited on 03/20/2026).

Bredemann, Scott (2025): Misumi Mech Lab: Linear Thermal Expansion Coefficient of Materials Chart. URL: https://us.misumi-ec.com/blog/thermal-expansion-coefficients/ (visited on 04/07/2026).

British Columbia Energy Regulator (2023): Oil and Gas Activity Operations Manual. URL: https://www.bc-er.ca/energy-professionals/operations-documentation/oil-and-gas-activity-operations-manual/ (visited on 11/30/2023).

Broni-Bediako, Eric; Joel, Ogbonna F.; Ofori-Sarpong, Grace (2016): Oil Well Cement Additives: A Review of the Common Types. In: *Oil & Gas Research* 02.02. ISSN: 24720518. DOI: 10.4172/2472-0518.1000112. URL: https://www.omicsonline.org/open-access/oil-well-cement-additives-a-review-of-the-common-types-ogr-1000112.php?aid=74018 (visited on 08/01/2025).

Brunner, Edgar and Munzel, Ullrich (2000): The Nonparametric Behrens-Fisher Problem: Asymptotic Theory and a Small-Sample Approximation. In: *Biometrical Journal* 42.1, pp. 17–25. ISSN: 0323-3847, 1521-4036. DOI: 10.1002/(SICI)1521-4036(200001)42:1<17::AID-BIMJ17>3.0.CO;2-U. URL: https://onlinelibrary.wiley.com/doi/10.1002/(SICI)1521-4036(200001)42:1%3C17::AID-BIMJ17%3E3.0.CO;2-U (visited on 10/13/2025).

Bruus, Henrik (2008): Poiseuille Flow, Section 3.4, Equation 3.57d. In: *Theoretical Microfluidics*. Oxford Master Series in Physics 18. Oxford ; New York: Oxford University Press. ISBN: 978-0-19-923508-7 978-0-19-923509-4.

Bureau of Safety and Environmental Enforcement (2009): Notice to Lessees and Operators of Federal Oil and Gas Leases in the Outer Continental Shelf, Gulf of Mexico OCS Region. NTL No. 2009-G01. URL: https://www.bsee.gov/sites/bsee.gov/

files/notices-to-lessees-ntl/notices-to-lessees/09-g01.pdf (visited on 08/27/2024).

Bureau of Safety and Environmental Enforcement (2010): 30 CFR Part 250 Subpart E - Casing Pressure Management. URL: https://www.ecfr.gov/current/title-30/chapter-II/subchapter-B/part-250/subpart-E/subject-group-ECFR7cee4c12995e05d (visited on 02/01/2024).

Burgués, Javier and Marco, Santiago (2020): Environmental Chemical Sensing Using Small Drones: A Review. In: *Science of The Total Environment* 748, p. 141172. ISSN: 00489697. DOI: 10.1016/j.scitotenv.2020.141172.

Byrd, Richard H.; Lu, Peihuang; Nocedal, Jorge; Zhu, Ciyou (1995): A Limited Memory Algorithm for Bound Constrained Optimization. In: *SIAM Journal on Scientific Computing* 16.5, pp. 1190–1208. ISSN: 1064-8275, 1095-7197. DOI: 10.1137/0916069. URL: http://epubs.siam.org/doi/10.1137/0916069 (visited on 03/20/2026).

Cahill, Aaron G.; Joukar, Mohammad; Sefat, Morteza; Van Geloven, Chelton (2023): Evaluating Methane Emissions From Decommissioned Unconventional Petroleum Wells in British Columbia, Canada. In: *Geophysical Research Letters* 50.24, e2023GL106496. ISSN: 0094-8276, 1944-8007. DOI: 10.1029/2023GL106496. URL: https://agupubs.onlinelibrary.wiley.com/doi/10.1029/2023GL106496 (visited on 08/27/2024).

California Air Resources Board (2017): California Code of Regulations, Title 17, Division 3, Chapter 1, Subchapter 10 Climate Change, Article 4. URL: https://ww2.arb.ca.gov/sites/default/files/2020-03/2017%20Final%20Reg%20Orders%20GHG%20Emission%20Standards.pdf (visited on 05/12/2026).

Canadian National Energy Board (2013): Filing Requirements for Onshore Drilling Operations Involving Hydraulic Fracturing, No. NE23-175/2013E. Calgary, Alta. ISBN: 978-1-100-22558-6. URL: https://www.cer-rec.gc.ca/en/about/acts-regulations/other-acts/filing-requirements-onshore-drilling/?=undefined&wbdisable=true (visited on 05/18/2026).

Cao, Vui Van; Le, Quoc Dinh; Nguyen, Phuoc Trong (2020): Experimental Behaviour of Concrete-Filled Steel Tubes under Cyclic Axial Compression. In: *Advances in Structural Engineering* 23.1, pp. 74–88. ISSN: 1369-4332, 2048-4011. DOI: 10.1177/1369433219866107. URL: https://journals.sagepub.com/doi/10.1177/1369433219866107 (visited on 08/12/2025).

Carragher, P.; Talapatra, D.; Morales, J. (2025): Deployment and Performance Evaluation of Bismuth Alloy-Based Thermally Deformable Annular Packer (TDAP) for Mitigating Gas Migration in Casing Annuli. In: *SPE Offshore Europe Conference & Exhibition*. SPE Offshore Europe Conference & Exhibition. Aberdeen, Scotland, UK: SPE, D031S010R008. DOI: 10.2118/226747-MS. URL: https://onepetro.org/SPEOE/proceedings/25OE/25OE/D031S010R008/789366 (visited on 11/24/2025).

Carroll, Susan; Carey, J. William; Dzombak, David; Huerta, Nicolas J.; Li, Li; Richard, Tom; Um, Wooyong; Walsh, Stuart D.C.; Zhang, Liwei (2016): Review: Role of Chem-

istry, Mechanics, and Transport on Well Integrity in CO2 Storage Environments. In: *International Journal of Greenhouse Gas Control* 49, pp. 149–160. ISSN: 17505836. DOI: 10.1016/j.ijggc.2016.01.010.

Çengel, Yunus A.; Boles, Michael A.; Kanoglu, Mehmet (2019): Thermodynamics: An Engineering Approach. Ninth edition. New York, NY: McGraw-Hill Education. 984 pp. ISBN: 978-1-259-82267-4.

Chai, T. and Draxler, R. R. (2014): Root Mean Square Error (RMSE) or Mean Absolute Error (MAE)? – Arguments against Avoiding RMSE in the Literature. In: *Geoscientific Model Development* 7.3, pp. 1247–1250. ISSN: 1991-9603. DOI: 10.5194/gmd-7-1247-2014. URL: https://gmd.copernicus.org/articles/7/1247/2014/ (visited on 10/13/2025).

Chanson, Hubert (2004): Physical Modelling of Hydraulics. In: *Hydraulics of Open Channel Flow*. Elsevier, pp. 253–274. ISBN: 978-0-7506-5978-9. DOI: 10.1016/B978-075065978-9/50021-0. URL: https://linkinghub.elsevier.com/retrieve/pii/B9780750659789500210 (visited on 07/30/2025).

Chen, Jie; Chao, Du; Deyi, Jiang; Jinyang, Fan; Yi, He (2016): The Mechanical Properties of Rock Salt under Cyclic Loading-Unloading Experiments. In: *Geomechanics and Engineering* 10.3, pp. 325–334. DOI: 10.12989/GAE.2016.10.3.325. URL: https://doi.org/10.12989/GAE.2016.10.3.325 (visited on 10/26/2023).

Chen, Ning Hsing (1979): An Explicit Equation for Friction Factor in Pipe. In: *Industrial & Engineering Chemistry Fundamentals* 18.3, pp. 296–297. ISSN: 0196-4313, 1541-4833. DOI: 10.1021/i160071a019. URL: https://pubs.acs.org/doi/abs/10.1021/i160071a019 (visited on 07/30/2025).

Chenevert, M. E. and Shrestha, B. K. (1991): Chemical Shrinkage Properties of Oilfield Cements. In: *SPE Drilling Engineering* 6.01, pp. 37–231. ISSN: 0885-9744. DOI: 10.2118/16654-pa. URL: https://onepetro.org/DC/article/6/01/37/52267/Chemical-Shrinkage-Properties-of-Oilfield-Cements (visited on 07/22/2025).

China National Offshore Oil Corporation (2018): Q/HS 14031—2017, Well Integrity Requirements for Offshore Wells, Corporate Standards of China National Offshore Oil Corporation Co., Ltd.

China National Petroleum Corporation (2022): Q/SY 01037-2019, Specification for Well Integrity of HPHT & High H2S Content Wells, China National Petroleum Corporation Corporate Standards.

Chu, Wei; Shen, Jiyun; Yang, Yunfei; Li, Yong; Gao, Deli (2015): Calculation of Micro-Annulus Size in Casing-Cement Sheath-Formation System under Continuous Internal Casing Pressure Change. In: *Petroleum Exploration and Development* 42.3, pp. 414–421. ISSN: 18763804. DOI: 10.1016/S1876-3804(15)30033-1. URL: https://linkinghub.elsevier.com/retrieve/pii/S1876380415300331 (visited on 08/12/2025).

Cirimello, Pablo. G.; Otegui, Jose L.; Carfi, Guillermo; Morris, Walter (2017): Failure and Integrity Analysis of Casings Used for Oil Well Drilling. In: *Engineering Failure*

Analysis 75, pp. 1–14. ISSN: 13506307. DOI: 10.1016/j.engfailanal.2016.11.008. URL: https://linkinghub.elsevier.com/retrieve/pii/S1350630716307889 (visited on 08/04/2025).

Claessens, Michel (2023): The Future of Energy. In: *ITER: The Giant Fusion Reactor*. Cham: Springer International Publishing, pp. 1–10. ISBN: 978-3-031-37761-7 978-3-031-37762-4. DOI: 10.1007/978-3-031-37762-4_1. URL: https://link.springer.com/10.1007/978-3-031-37762-4_1 (visited on 10/02/2025).

Colborn, Theo; Schultz, Kim; Herrick, Lucille; Kwiatkowski, Carol (2014): An Exploratory Study of Air Quality Near Natural Gas Operations. In: *Human and Ecological Risk Assessment: An International Journal* 20.1, pp. 86–105. ISSN: 1080-7039, 1549-7860. DOI: 10.1080/10807039.2012.749447. URL: http://www.tandfonline.com/doi/abs/10.1080/10807039.2012.749447 (visited on 06/27/2024).

Coleman, Thomas F. and Li, Yuying (1996): An Interior Trust Region Approach for Nonlinear Minimization Subject to Bounds. In: *SIAM Journal on Optimization* 6.2, pp. 418–445. ISSN: 1052-6234, 1095-7189. DOI: 10.1137/0806023. URL: http://epubs.siam.org/doi/10.1137/0806023 (visited on 03/20/2026).

Colorado Energy and Carbon Management Commission (2021): EMC Operator Guidance: Bradenhead Monitoring, Testing, Management, Mitigation and Reporting. URL: https://ecmc.state.co.us/documents/reg/OpGuidance/ECMC_operator_guidance_Bradenhead_Monitoring_Testing_Reporting.pdf (visited on 05/11/2026).

Colorado Energy and Carbon Management Commission (2025): Colorado Code of Regulations, 2 CCR 404-1-419: Bradenhead Monitoring, Testing, and Reporting. URL: https://ecmc.colorado.gov/regulation/rules.

Corina, Anisa Noor; Skorpa, Ragnhild; Sangesland, Sigbjørn; Vrålstad, Torbjørn (2021): Simulation of Fluid Flow through Real Microannuli Geometries. In: *Journal of Petroleum Science and Engineering* 196, p. 107669. ISSN: 09204105. DOI: 10.1016/j.petrol.2020.107669. URL: https://linkinghub.elsevier.com/retrieve/pii/S0920410520307361 (visited on 07/30/2025).

Cornot-Gandolphe, Sylvie (2019): Underground Gas Storage in the World - 2019 Status. In: *Cedigaz Insights* 35. URL: https://www.cedigaz.org/shop-with-selector/?type=publications&search=Underground%20Gas%20Storage%20in%20the%20World (visited on 08/11/2025).

Cusworth, Daniel H.; Jacob, Daniel J.; Varon, Daniel J.; Miller, Christopher Chan; Liu, Xiong; Chance, Kelly; Thorpe, Andrew K.; Duren, Riley M.; Miller, Charles E.; Thompson, David R.; Frankenberg, Christian; Guanter, Luis; Randles, Cynthia A. (2019): Potential of Next-Generation Imaging Spectrometers to Detect and Quantify Methane Point Sources from Space. In: *Atmospheric Measurement Techniques* 12.10, pp. 5655–5668. ISSN: 1867-8548. DOI: 10.5194/amt-12-5655-2019.

Daccord, Gerard; Guillot, Dominique; Nilsson, Frederik (2006): Mud Removal, Chapter 5. In: *Well Cementing*. 2. ed. Sugar Land, Tex: Schlumberger. ISBN: 978-0-9788530-0-6.

DAfStb (1991): Deutscher Ausschuss für Stahlbeton, Heft 422: Prüfung von Beton, Empfehlung und Hinweise als Ergänzung zu DIN 1048 (German Committee for Reinforced Concrete, Booklet 422: Testing of concrete, recommendation and notes as a supplement to DIN 1048). 1st ed. DE: Beuth Verlag. ISBN: 978-3-410-65622-7. URL: https://doi.org/10.2366/3708068 (visited on 11/04/2024).

Dakhaeva, Fatima and Magomaev, Tamerlan (2022): Environmental and Economic Risks of the Oil and Gas Sector. In: *RT&A* 17 (Special Issue № 4 (70)), pp. 530–536.

Darcy, Henry (1856): Les Fontaines Publiques de La Ville de Dijon: Exposition et Application Des Principes a Suivre et Des Formulesa Employer Dans Les Questions de Distribution d'Eau. Paris: Dalmont. 647 pp.

Davies, Richard J.; Almond, Sam; Ward, Robert S.; Jackson, Robert B.; Adams, Charlotte; Worrall, Fred; Herringshaw, Liam G.; Gluyas, Jon G.; Whitehead, Mark A. (2014): Oil and Gas Wells and Their Integrity: Implications for Shale and Unconventional Resource Exploitation. In: *Marine and Petroleum Geology* 56, pp. 239–254. ISSN: 02648172. DOI: 10.1016/j.marpetgeo.2014.03.001.

Dehli, Martin; Doering, Ernst; Schedwill, Herbert (2023): Real Gases and Vapors. In: *Fundamentals of Technical Thermodynamics*. Wiesbaden: Springer Fachmedien Wiesbaden, pp. 151–212. ISBN: 978-3-658-38909-3 978-3-658-38910-9. DOI: 10.1007/978-3-658-38910-9_5. URL: https://link.springer.com/10.1007/978-3-658-38910-9_5 (visited on 10/17/2025).

Demirci, Efecan and Wojtanowicz, Andrew K. (2023): Design and Field-Scale Demonstration of the Buoyant-Kill Process for Restoring Integrity of Wells with Sustained Casing Pressure. In: *Frontiers in Energy Research* 11, p. 1309207. ISSN: 2296-598X. DOI: 10.3389/fenrg.2023.1309207. URL: https://www.frontiersin.org/articles/10.3389/fenrg.2023.1309207/full (visited on 12/18/2023).

DIN 18125-1 (2010): Baugrund, Untersuchung von Bodenproben – Bestimmung Der Dichte Des Bodens – Teil 1: Laborversuche (Soil, Investigation and Testing – Determination of Density of Soil – Part 1: Laboratory Tests).

DIN 18129 (2011): Baugrund, Untersuchung von Bodenproben - Kalkgehaltsbestimmung (Soil, Investigation and Testing - Determination of Lime Content).

DIN 66139 (2012): Porengrößenanalyse – Darstellung von Porengrößenverteilungen (Pore Size Analysis – Representation of Pore Size Distributions).

DIN EN 1015-3 (2007): Prüfverfahren Für Mörtel Für Mauerwerk – Teil 3: Bestimmung Der Konsistenz von Frischmörtel (Mit Ausbreittisch); Deutsche Fassung EN 1015-3:1999+A1:2004+A2:2006 (Methods of Test for Mortar for Masonry – Part 3: Determination of Consistence of Fresh Mortar (by Flow Table); German Version EN 1015-3:1999+A1:2004+A2:2006).

DIN EN 1015-6 (2006): Prüfverfahren Für Mörtel Für Mauerwerk – Teil 6: Bestimmung Der Rohdichte von Frischmörtel; Deutsche Fassung EN 1015-6:1998+A1:2006 (Methods

of Test for Mortar for Masonry – Part 6: Determination of Bulk Density of Fresh Mortar; German Version EN 1015-6:1998+A1:2006).

DIN EN 12350-7 (2022): Prüfung von Frischbeton – Teil 7: Luftgehalt – Druckverfahren; Deutsche Fassung EN 12350-7:2019 + AC:2022 (Testing Fresh Concrete – Part 7: Air Content – Pressure Methods; German Version EN 12350-7:2019 + AC:2022).

DIN EN 60534-2-1 (2012): Stellventile Für Die Prozessregelung – Teil 2-1: Durchflusskapazität – Bemessungsgleichungen Für Fluide Unter Betriebsbedingungen (IEC 60534-2-1:2011); Deutsche Fassung EN 60534-2-1:2011 (Industrial-process Control Valves – Part 2-1: Flow Capacity – Sizing Equations for Fluid Flow under Installed Conditions (IEC 60534-2-1:2011); German Version EN 60534-2-1:2011).

Dunn, Olive Jean (1964): Multiple Comparisons Using Rank Sums. In: *Technometrics* 6.3, pp. 241–252. ISSN: 0040-1706, 1537-2723. DOI: 10.1080/00401706.1964.10490181. URL: http://www.tandfonline.com/doi/abs/10.1080/00401706.1964.10490181 (visited on 10/13/2025).

Dusseault, Maurice B.; Gray, Malcolm N.; Nawrocki, Pawel A. (2000): Why Oilwells Leak: Cement Behavior and Long-Term Consequences. In: *International Oil and Gas Conference and Exhibition in China*. International Oil and Gas Conference and Exhibition in China. Beijing, China: SPE, SPE-64733–MS. DOI: 10.2118/64733-MS. URL: https://onepetro.org/SPEIOGCEC/proceedings/00IOGCEC/00IOGCEC/SPE-64733-MS/132512 (visited on 02/07/2025).

DVV Media Group GmbH (2023): Untertage Gasspeicherung in Deutschland (Stand: 1.1.2023); Underground Gas Storage in Germany. In: EEK- Erdöl Erdgas Kohle 139.11. URL: https://www.lbeg.niedersachsen.de/energie_rohstoffe/erdoel_und_erdgas/untertagegasspeicher/publikation_untertageerdgaspeicherung/publikation-zur-untertage-erdgasspeicherung-in-der-zeitschrift-eek-898.html (visited on 08/11/2025).

DVV Media Group GmbH (2025): Untertage Gasspeicherung in Deutschland (Stand: 1.1.2024); Underground Gas Storage in Germany. In: EEK- Erdöl Erdgas Kohle 141.2. URL: https://www.lbeg.niedersachsen.de/energie_rohstoffe/erdoel_und_erdgas/untertagegasspeicher/publikation_untertageerdgaspeicherung/publikation-zur-untertage-erdgasspeicherung-in-der-zeitschrift-eek-898.html (visited on 08/11/2025).

Economides, Michael J. and Wood, David A. (2009): The State of Natural Gas. In: *Journal of Natural Gas Science and Engineering* 1.1–2, pp. 1–13. ISSN: 18755100. DOI: 10.1016/j.jngse.2009.03.005. URL: https://linkinghub.elsevier.com/retrieve/pii/S187551000900002X (visited on 06/27/2024).

Enayatpour, Saeid; Thombare, Akshay; Aldin, Munir; Van Oort, Eric (2019): Exploiting Shale Creep Deformation to Create Annular Barriers for Well Plugging and Abandonment: Experimental Investigation and Numerical Simulation. In: *SPE Annual Technical Conference and Exhibition*. SPE Annual Technical Conference and Exhibition. Cal-

gary, Alberta, Canada: SPE, D011S010R004. DOI: 10.2118/195966-MS. URL: https://onepetro.org/SPEATCE/proceedings/19ATCE/19ATCE/D011S010R004/217583 (visited on 11/24/2025).

Enerdata (2024): World Energy and Climate Statistics - Yearbook 2024. URL: https://yearbook.enerdata.net/ (visited on 11/30/2023).

Energy Safety Canada (2022): DACC IRP 27: Wellbore Decommissioning - An Industry Recommended Practice (IRP) for the Canadian Oil and Gas Industry, Volume 27 – 2022. URL: https://www.energysafetycanada.com/Resource/DACC-IRP-Volumes/DACC-IRP-VOLUME-27-WELLBORE-DECOMMISSIONING (visited on 04/10/2024).

Epstein, Anne (2015): Health and Environment Risks from Oil and Gas Development. In: *Hydraulic Fracturing Impacts and Technologies*. Ed. by Venkatesh Uddameri; Audra Morse; Kay Tindle. CRC Press, pp. 101–114. ISBN: 978-1-4987-2117-2 978-1-4987-2121-9. DOI: 10.1201/b18581-7. URL: http://www.crcnetbase.com/doi/10.1201/b18581-7 (visited on 11/12/2025).

Esri (2017): US State Boundaries. URL: https://hub.arcgis.com/datasets/1612d351695b467eba75fdf82c10884f/explore?showTable=true (visited on 12/21/2023).

Esri (2022): World Countries Generalized. URL: https://hub.arcgis.com/datasets/esri::world-countries-generalized/explore (visited on 06/14/2023).

Fan, Jinyang; Chen, Jie; Jiang, Deyi; Chemenda, Alexandre; Chen, Junchao; Ambre, Julien (2017): Discontinuous Cyclic Loading Tests of Salt with Acoustic Emission Monitoring. In: *International Journal of Fatigue* 94, pp. 140–144. ISSN: 01421123. DOI: 10.1016/j.ijfatigue.2016.09.016. URL: https://linkinghub.elsevier.com/retrieve/pii/S0142112316302900 (visited on 10/26/2023).

Fan, Jinyang; Chen, Jie; Jiang, Deyi; Ren, Song; Wu, Jianxun (2016): Fatigue Properties of Rock Salt Subjected to Interval Cyclic Pressure. In: *International Journal of Fatigue* 90, pp. 109–115. ISSN: 01421123. DOI: 10.1016/j.ijfatigue.2016.04.021. URL: https://linkinghub.elsevier.com/retrieve/pii/S0142112316300755 (visited on 10/26/2023).

Farkas, R. F.; England, K. W.; Roy, M. L.; Dickinson, M.; Samuel, M.; Robert, E. Hart (1999): New Cementing Technology Cures 40-Year-Old Squeeze Problems. In: *SPE Annual Technical Conference and Exhibition*. SPE Annual Technical Conference and Exhibition. Houston, Texas: SPE, SPE-56537–MS. DOI: 10.2118/56537-MS. URL: https://onepetro.org/SPEATCE/proceedings/99ATCE/99ATCE/SPE-56537-MS/60155 (visited on 11/25/2025).

Feder, Judy (2001): Casing and Cementing. 3. ed. Rotary Drilling Series Unit 2, Normal Drilling Operations Lesson 4. Austin, Tex: Petroleum Extension Service, Continuing & Extended Education, University of Texas at Austin. 109 pp. ISBN: 978-0-88698-191-4.

Federal Network Agency (2026): Bundesnetzagentur: Verlauf Der Speicherfüllstände in Prozent. URL: https://www.bundesnetzagentur.de/DE/Gasversorgung/aktuelle_

gasversorgung/_svg/Gasspeicher_Fuellstand/Speicherfuellstand.html (visited on 06/28/2026).

Fibbi, Gabriele; Del Soldato, Matteo; Fanti, Riccardo (2022): Review of the Monitoring Applications Involved in the Underground Storage of Natural Gas and CO2. In: *Energies* 16.1, p. 12. ISSN: 1996-1073. DOI: 10.3390/en16010012. URL: https://www.mdpi.com/1996-1073/16/1/12 (visited on 10/07/2025).

Figgener, Jan; Hecht, Christopher; Haberschusz, David; Bors, Jakob; Spreuer, Kai Gerd; Kairies, Kai-Philipp; Stenzel, Peter; Sauer, Dirk Uwe (2022): The Development of Battery Storage Systems in Germany: A Market Review (Status 2023). Version 3. DOI: 10.48550/ARXIV.2203.06762. URL: https://arxiv.org/abs/2203.06762 (visited on 08/07/2025). Pre-published.

Fink, Johannes Karl (2011): Chapter 10: Cement Additives. In: *Petroleum Engineer's Guide to Oil Field Chemicals and Fluids*. 1st ed. Amsterdam Boston: Elsevier Gulf Professional Publishing. ISBN: 978-0-12-383844-5.

Fleming, Patrik (2025): 5.8 Adiabatic Compressibility. In: *Physical Chemistry*. California State University East Bay: LibreTexts. URL: https://chem.libretexts.org/Bookshelves/Physical_and_Theoretical_Chemistry_Textbook_Maps/Physical_Chemistry_%28Fleming%29/05%3A_The_Second_Law/5.08%3A_Adiabatic_Compressibility (visited on 10/17/2025).

Florida Department of Environmental Protection (1996a): Florida Administrative Code, Chapter 62C-28: Conservation of Oil and Gas: Production and Flowlines, Rule 62C-28.001: Wellhead Equipment. URL: https://flrules.org/gateway/ChapterHome.asp?Chapter=62C-28 (visited on 05/13/2026).

Florida Department of Environmental Protection (1996b): Florida Administrative Code, Chapter 62C-29: Conservation of Oil and Gas: Injection Wells, Well Workovers, and Abandonments, Rule 62C-29.007 Pressure Tests. URL: https://flrules.org/gateway/ChapterHome.asp?Chapter=62C-28 (visited on 05/13/2026).

Fogleman, Valerie (2020): Improving Financial Security in the Context of the Environmental Liability Directive. No 07.0203/2018/789239/SER/ENV.E.4. European Commission, Directorate - General for Environment, Directorate E - Implementation, Support to member States, Unit 4 - Compliance, and Better Regulation. URL: https://circabc.europa.eu/ui/group/3b48eff1-b955-423f-9086-0d85ad1c5879/library/01708073-da51-4db7-8049-6e7141c901f4/details?download=true (visited on 11/18/2025).

Forde, O.N.; Mayer, K.U.; Hunkeler, D. (2019): Identification, Spatial Extent and Distribution of Fugitive Gas Migration on the Well Pad Scale. In: *Science of The Total Environment* 652, pp. 356–366. ISSN: 00489697. DOI: 10.1016/j.scitotenv.2018.10.217. URL: https://linkinghub.elsevier.com/retrieve/pii/S004896971834110X (visited on 11/12/2025).

Fuenkajorn, Kittitep and Phueakphum, Decho (2010): Effects of Cyclic Loading on Mechanical Properties of Maha Sarakham Salt. In: *Engineering Geology* 112.1–4, pp. 43–52. ISSN: 00137952. DOI: 10.1016/j.enggeo.2010.01.002. URL: https://linkinghub.elsevier.com/retrieve/pii/S0013795210000037 (visited on 10/26/2023).

Gao, Peike and Fan, Keyan (2023): Sulfur-Oxidizing Bacteria (SOB) and Sulfate-Reducing Bacteria (SRB) in Oil Reservoir and Biological Control of SRB: A Review. In: *Archives of Microbiology* 205.5, p. 162. ISSN: 0302-8933, 1432-072X. DOI: 10.1007/s00203-023-03520-0. URL: https://link.springer.com/10.1007/s00203-023-03520-0 (visited on 09/17/2025).

Garcia Fernandez, Serafin; Matteo, Edward N.; Taha, Mahmoud Reda; Stormont, John C. (2019): Characterization of Wellbore Microannuli. In: *Journal of Natural Gas Science and Engineering* 62, pp. 13–25. ISSN: 18755100. DOI: 10.1016/j.jngse.2018.12.003. URL: https://linkinghub.elsevier.com/retrieve/pii/S1875510018305316 (visited on 08/13/2025).

Gas Infrastructure Europe (2026): Aggregated Gas Storage Inventory (AGSI). URL: https://agsi.gie.eu/ (visited on 03/24/2026).

Gasda, Sarah E.; Bachu, Stefan; Celia, Michael A. (2004): Spatial Characterization of the Location of Potentially Leaky Wells Penetrating a Deep Saline Aquifer in a Mature Sedimentary Basin. In: *Environmental Geology* 46.6–7, pp. 707–720. ISSN: 0943-0105, 1432-0495. DOI: 10.1007/s00254-004-1073-5. URL: http://link.springer.com/10.1007/s00254-004-1073-5 (visited on 08/13/2024).

Geological Survey of the Netherlands (n.d.): Netherlands Oil and Gas Portal (NLOG). Ministry of Economic Affairs and Climate Policy. URL: https://www.nlog.nl/datacenter/?lang=en (visited on 10/01/2024).

Ghabezloo, Siavash (2011): Effect of the Variations of Clinker Composition on the Poroelastic Properties of Hardened Class G Cement Paste. In: *Cement and Concrete Research* 41.8, pp. 920–922. ISSN: 00088846. DOI: 10.1016/j.cemconres.2011.03.022. URL: https://linkinghub.elsevier.com/retrieve/pii/S0008884611000986 (visited on 08/01/2025).

Ghanem, Hassan; Ramadan, Rawan; Khatib, Jamal; Elkordi, Adel (2024): A Review on Chemical and Autogenous Shrinkage of Cementitious Systems. In: *Materials* 17.2, p. 283. ISSN: 1996-1944. DOI: 10.3390/ma17020283. URL: https://www.mdpi.com/1996-1944/17/2/283 (visited on 11/21/2025).

Ghofrani, Reza and Plack, Heiko (1993): CaO- and/or MgO-Swelling Cements: A Key for Providing a Better Annular Sealing? In: *SPE/IADC Drilling Conference*. SPE/IADC Drilling Conference. Amsterdam, Netherlands: SPE, SPE-25697–MS. DOI: 10.2118/25697-MS. URL: https://onepetro.org/SPEDC/proceedings/93DC/93DC/SPE-25697-MS/55654 (visited on 08/28/2025).

Gomez, Steven P.; Sobolik, Steve R.; Matteo, Edward N.; Reda Taha, Mahmoud; Stormont, John C. (2017): Investigation of Wellbore Microannulus Permeability under Stress via

Experimental Wellbore Mock-up and Finite Element Modeling. In: *Computers and Geotechnics* 83, pp. 168–177. ISSN: 0266352X. DOI: 10.1016/j.compgeo.2016.10.001. URL: https://linkinghub.elsevier.com/retrieve/pii/S0266352X16302300 (visited on 08/13/2025).

Goodwin, K. J. and Crook, R. J. (1992): Cement Sheath Stress Failure. In: *SPE Drilling Engineering* 7.04, pp. 291–296. ISSN: 0885-9744. DOI: 10.2118/20453-pa. URL: https://onepetro.org/DC/article/7/04/291/70415/Cement-Sheath-Stress-Failure (visited on 07/21/2025).

Goodwin, Melissa J.; Musa, Osama M.; Steed, Jonathan W. (2015): Problems Associated with Sour Gas in the Oilfield Industry and Their Solutions. In: *Energy & Fuels* 29.8, pp. 4667–4682. ISSN: 0887-0624, 1520-5029. DOI: 10.1021/acs.energyfuels.5b00952. URL: https://pubs.acs.org/doi/10.1021/acs.energyfuels.5b00952 (visited on 05/23/2026).

Government of British Columbia (2023): British Columbia Oil and Gas Activities Act - Drilling and Production Regulation B.C. Reg. 282/2010, Last Amended January 1, 2023 by B.C. Reg. 266/2022, Consolidated Regulations of British Columbia. URL: https://www.bclaws.gov.bc.ca/civix/document/id/complete/statreg/282_2010 (visited on 02/20/2023).

Government of New Brunswick (2021): Responsible Environmental Management of Oil and Natural Gas Activities in New Brunswick. URL: https://www2.gnb.ca/content/dam/gnb/Departments/en/pdf/ong-rules-for-industry.pdf (visited on 06/12/2026).

Government of Western Australia (2015): Petroleum and Geothermal Energy Resources (Resource Management and Administration) Regulations 2015. URL: https://www.legislation.wa.gov.au/legislation/statutes.nsf/main_mrtitle_13656_homepage.html (visited on 11/30/2023).

Grotzinger, John and Jordan, Thomas (2017): Mensch und Umwelt. In: *Press/Siever Allgemeine Geologie*. Berlin, Heidelberg: Springer Berlin Heidelberg, pp. 643–678. ISBN: 978-3-662-48341-1 978-3-662-48342-8. DOI: 10.1007/978-3-662-48342-8_23. URL: http://link.springer.com/10.1007/978-3-662-48342-8_23 (visited on 10/06/2025).

Guo, Boyun and Ghalambor, Ali (2005): Chapter 11: Transportation. In: *Natural Gas Engineering Handbook*. Elsevier, pp. 219–262. ISBN: 978-1-933762-41-8. DOI: 10.1016/B978-1-933762-41-8.50018-6. URL: https://linkinghub.elsevier.com/retrieve/pii/B9781933762418500186 (visited on 07/30/2025).

Guven, Brooke; Toldano, Perrine; Johnson, Lise (2020): Preparing Legal Frameworks for Environmental Disasters: Practical Considerations for Host States. Columbia Center on Sustainable Development. URL: https://ccsi.columbia.edu/sites/ccsi.columbia.edu/files/content/docs/Preparing-Legal-Frameworks-for-Environmental-Disasters.pdf (visited on 11/18/2025).

Habibzadeh, Farrokh (2025): The *P* Value: What It Is and What It Is Not. In: *Journal of Korean Medical Science* 40.44, e321. ISSN: 1011-8934, 1598-6357. DOI: 10.3346/jkms.2025.40.e321. URL: https://jkms.org/DOIx.php?id=10.3346/jkms.2025.40.e321 (visited on 04/02/2026).

Hachem, Khalil El and Kang, Mary (2023): Reducing Oil and Gas Well Leakage: A Review of Leakage Drivers, Methane Detection and Repair Options. In: *Environmental Research: Infrastructure and Sustainability* 3.1, p. 012002. ISSN: 2634-4505. DOI: 10.1088/2634-4505/acbced. URL: https://iopscience.iop.org/article/10.1088/2634-4505/acbced (visited on 02/07/2025).

Hansen, Will (1987): Drying Shrinkage Mechanisms in Portland Cement Paste. In: *Journal of the American Ceramic Society* 70.5, pp. 323–328. ISSN: 0002-7820, 1551-2916. DOI: 10.1111/j.1151-2916.1987.tb05002.x. URL: https://ceramics.onlinelibrary.wiley.com/doi/10.1111/j.1151-2916.1987.tb05002.x (visited on 08/22/2025).

Hao, Haiyang; Wang, Shuai; Wang, Jianbin; Wang, Yiteng; He, Jibiao; Yang, Xiaodong (2024): Study on Mechanical Strength and Deformation Properties of Rubberized Cement Sheath Barrier Reinforced with Inorganic Hybrid Fibers. In: *Construction and Building Materials* 434, p. 136692. ISSN: 09500618. DOI: 10.1016/j.conbuildmat.2024.136692. URL: https://linkinghub.elsevier.com/retrieve/pii/S0950061824018336 (visited on 08/14/2025).

Harooni, Ali Barati; Sedeh, Mehran Sohrabi; Farzaneh, Seyed Amir; Fahimpour, Jalal (2025): Experimental Investigation of Gas Permeability and Flow Behaviour in Wellbore Cements. In: *International Journal of Greenhouse Gas Control* 147, p. 104489. ISSN: 17505836. DOI: 10.1016/j.ijggc.2025.104489. URL: https://linkinghub.elsevier.com/retrieve/pii/S1750583625001872 (visited on 11/10/2025).

Heintz, Andreas (2017): Das Volumen als Zustandsfunktion. In: *Thermodynamik*. Berlin, Heidelberg: Springer Berlin Heidelberg, pp. 45–93. ISBN: 978-3-662-49921-4 978-3-662-49922-1. DOI: 10.1007/978-3-662-49922-1_3. URL: http://link.springer.com/10.1007/978-3-662-49922-1_3 (visited on 10/17/2025).

Hetsroni, G.; Mosyak, A.; Pogrebnyak, E.; Yarin, L.P. (2005): Fluid Flow in Micro-Channels. In: *International Journal of Heat and Mass Transfer* 48.10, pp. 1982–1998. ISSN: 00179310. DOI: 10.1016/j.ijheatmasstransfer.2004.12.019. URL: https://linkinghub.elsevier.com/retrieve/pii/S0017931005000244 (visited on 07/30/2025).

Holm, Sture (1979): A Simple Sequentially Rejective Multiple Test Procedure. In: *Scandinavian Journal of Statistics* 6.2, pp. 65–70. JSTOR: 4615733. URL: https://www.jstor.org/stable/4615733 (visited on 10/13/2025).

Ibukun, Matthew; Elyan, Eyad; Amish, Mohamed; Njuguna, James; Oluyemi, Gbenga F. (2024): A Review of Well Life Cycle Integrity Challenges in the Oil and Gas Industry and Its Implications for Sustained Casing Pressure (SCP). In: *Energies* 17.22, p. 5562.

ISSN: 1996-1073. DOI: 10.3390/en17225562. URL: https://www.mdpi.com/1996-1073/17/22/5562 (visited on 08/12/2025).

Iglewicz, Boris (2025): Summarizing Data with Boxplots. In: *International Encyclopedia of Statistical Science*. Ed. by Miodrag Lovric. Berlin, Heidelberg: Springer Berlin Heidelberg, pp. 2741–2745. ISBN: 978-3-662-69358-2 978-3-662-69359-9. DOI: 10.1007/978-3-662-69359-9_669. URL: https://link.springer.com/10.1007/978-3-662-69359-9_669 (visited on 04/30/2026).

Ingraffea, Anthony R.; Wells, Martin T.; Santoro, Renee L.; Shonkoff, Seth B. C. (2014): Assessment and Risk Analysis of Casing and Cement Impairment in Oil and Gas Wells in Pennsylvania, 2000-2012. In: *Proceedings of the National Academy of Sciences of the United States of America* 111.30, pp. 10955–10960. DOI: 10.1073/pnas.1323422111.

ISO 16530-1 (2017): Petroleum and Natural Gas Industries - Well Integrity - Part 1: Life Cycle Governance (ISO 16530-1:2017 by the International Organization for Standardization).

ISO 16530-2 (2014): Well Integrity - Part 2: Well Integrity for the Operational Phase (ISO/TS 16530-2:2014 by the International Organization for Standardization).

ISO 17892-1 (2014): Geotechnical Investigation and Testing - Laboratory Testing of Soil - Part 1: Determination of Water Content. In.

ISO 17892-2 (2014): Geotechnical Investigation and Testing - Laboratory Testing of Soil - Part 2: Determination of Bulk Density. In.

ISO 17892-3 (2015): Geotechnical Investigation and Testing - Laboratory Testing of Soil - Part 3: Determination of Particle Density. In.

Iyer, Jaisree; Lackey, Greg; Edvardsen, Laura; Bean, Andrew; Carroll, Susan A.; Huerta, Nicolas; Smith, Megan M.; Torsæter, Malin; Dilmore, Robert M.; Cerasi, Pierre (2022): A Review of Well Integrity Based on Field Experience at Carbon Utilization and Storage Sites. In: *International Journal of Greenhouse Gas Control* 113, p. 103533. ISSN: 17505836. DOI: 10.1016/j.ijggc.2021.103533.

Izadi, M. and Frigaard, I.A. (2026): Effects of Microannulus Geometry and Slurry Particle Size on Squeeze Cementing Effectiveness. In: *Geoenergy Science and Engineering* 257, p. 214262. ISSN: 29498910. DOI: 10.1016/j.geoen.2025.214262. URL: https://linkinghub.elsevier.com/retrieve/pii/S2949891025006207 (visited on 11/25/2025).

Jackson, P. B. and Murphey, C. E. (1993): Effect of Casing Pressure on Gas Flow through a Sheath of Set Cement. In: *SPE/IADC Drilling Conference*. SPE/IADC Drilling Conference. Amsterdam, Netherlands: SPE, SPE-25698–MS. DOI: 10.2118/25698-MS. URL: https://onepetro.org/SPEDC/proceedings/93DC/93DC/SPE-25698-MS/55682 (visited on 08/12/2025).

Jackson, R. E. and Dusseault, M. B. (2014): Gas Release Mechanisms from Energy Wellbores. Paper Presented at the 48th U.S. Rock Mechanics/Geomechanics Symposium, Minneapolis, Minnesota, June 2014. Paper Number: ARMA-2014-7753. In: vol. All

Days. U.S. Rock Mechanics/Geomechanics Symposium. URL: https://onepetro.org/ARMAUSRMS/proceedings-abstract/ARMA14/All-ARMA14/123952.

Jackson, Robert B. (2014): The Integrity of Oil and Gas Wells. In: *Proceedings of the National Academy of Sciences of the United States of America* 111.30, pp. 10902–10903. DOI: 10.1073/pnas.1410786111.

Jervis, Dylan; McKeever, Jason; Durak, Berke O. A.; Sloan, James J.; Gains, David; Varon, Daniel J.; Ramier, Antoine; Strupler, Mathias; Tarrant, Ewan (2021): The GHGSat-D Imaging Spectrometer. In: *Atmospheric Measurement Techniques* 14.3, pp. 2127–2140. ISSN: 1867-8548. DOI: 10.5194/amt-14-2127-2021.

Jiang, Wu (2021): Casing String and Design. In: *Applied Well Cementing Engineering*. Elsevier, pp. 17–67. ISBN: 978-0-12-821956-0. DOI: 10.1016/B978-0-12-821956-0.00007-9. URL: https://linkinghub.elsevier.com/retrieve/pii/B9780128219560000079 (visited on 02/05/2025).

Jońca, Justyna; Pawnuk, Marcin; Bezyk, Yaroslav; Arsen, Adalbert; Sówka, Izabela (2022): Drone-Assisted Monitoring of Atmospheric Pollution—A Comprehensive Review. In: *Sustainability* 14.18, p. 11516. ISSN: 2071-1050. DOI: 10.3390/su141811516.

Joule, J.P. and Thomson, W. (1852): LXXVI. *On the Thermal Effects Experienced by Air in Rushing through Small Apertures*. In: *The London, Edinburgh, and Dublin Philosophical Magazine and Journal of Science* 4.28, pp. 481–492. ISSN: 1941-5982, 1941-5990. DOI: 10.1080/14786445208647169. URL: https://www.tandfonline.com/doi/full/10.1080/14786445208647169 (visited on 02/20/2025).

Kandlikar, Satish G. (2013): Transition to Turbulence in Microchannels. In: *Encyclopedia of Microfluidics and Nanofluidics*. Boston, MA: Springer US, pp. 1–4. ISBN: 978-3-642-27758-0. DOI: 10.1007/978-3-642-27758-0_1622-3. URL: https://link.springer.com/10.1007/978-3-642-27758-0_1622-3 (visited on 07/29/2025).

Kazemi, Mohammad and Wojtanowicz, Andrew K. (2022): Improved Method for Testing Integrity Loss of Wells with Sustained Casing Pressure. In: *Energies* 15.10, p. 3632. ISSN: 1996-1073. DOI: 10.3390/en15103632. URL: https://www.mdpi.com/1996-1073/15/10/3632.

Keeley, Deborah (2008): Failure Rates for Underground Gas Storage, RR671; Prepared by the Health and Safety Laboratory. In: *HSE Books*. URL: https://www.hse.gov.uk/research/rrpdf/rr671.pdf (visited on 10/24/2023).

Kentucky Energy and Environment Cabinet (2020): 805 KAR 1:060: Plugging Wells. URL: https://apps.legislature.ky.gov/law/kar/titles/805/001/060/ (visited on 05/11/2026).

Khaledi, Kavan; Mahmoudi, Elham; Datcheva, Maria; Schanz, Tom (2016): Stability and Serviceability of Underground Energy Storage Caverns in Rock Salt Subjected to Mechanical Cyclic Loading. In: *International Journal of Rock Mechanics and Mining Sciences* 86, pp. 115–131. ISSN: 13651609. DOI: 10.1016/j.ijrmms.2016.04.010. URL:

https://linkinghub.elsevier.com/retrieve/pii/S1365160916300612 (visited on 10/26/2023).

Kim, Jihoon; Moridis, George J.; Martinez, Eduardo R. (2016): Investigation of Possible Wellbore Cement Failures during Hydraulic Fracturing Operations. In: *Journal of Petroleum Science and Engineering* 139, pp. 254–263. ISSN: 0920-4105. DOI: 10.1016/j.petrol.2016.01.035. URL: https://linkinghub.elsevier.com/retrieve/pii/S0920410516300353 (visited on 07/22/2025).

King, George E. and King, Daniel E. (2013): Environmental Risk Arising From Well Construction Failure: Difference Between Barrier and Well Failure, and Estimates of Failure Frequency Across Common Well Types, Locations and Well Age. In: *SPE Annual Technical Conference and Exhibition*. SPE Annual Technical Conference and Exhibition. New Orleans, Louisiana, USA: SPE, D031S044R001. DOI: 10.2118/166142-MS. URL: https://onepetro.org/SPEATCE/proceedings/13ATCE/13ATCE/D031S044R001/172417 (visited on 09/16/2025).

Kinik, K. and Wojtanowicz, Andrew K. (2011): Identifying Environmental Risk of Sustained Casing Pressure. In: *SPE Americas E&P Health, Safety, Security, and Environmental Conference*. SPE. DOI: 10.2118/143713-MS.

Kiran, Raj; Teodoriu, Catalin; Dadmohammadi, Younas; Nygaard, Runar; Wood, David; Mokhtari, Mehdi; Salehi, Saeed (2017): Identification and Evaluation of Well Integrity and Causes of Failure of Well Integrity Barriers (A Review). In: *Journal of Natural Gas Science and Engineering* 45, pp. 511–526. ISSN: 18755100. DOI: 10.1016/j.jngse.2017.05.009.

Klose, Tim; Chaparro, M. Carme; Schilling, Frank; Butscher, Christoph; Klumbach, Steffen; Blum, Philipp (2021): Fluid Flow Simulations of a Large-Scale Borehole Leakage Experiment. In: *Transport in Porous Media* 136.1, pp. 125–145. ISSN: 0169-3913. DOI: 10.1007/s11242-020-01504-y.

Kolliopoulos, Panayiotis; Jochem, Krystopher S.; Francis, Lorraine F.; Kumar, Satish (2022): Capillary Flow of Evaporating Liquid Solutions in Open Rectangular Microchannels. In: *Journal of Fluid Mechanics* 938, A22. ISSN: 0022-1120, 1469-7645. DOI: 10.1017/jfm.2022.140. URL: https://www.cambridge.org/core/product/identifier/S0022112022001409/type/journal_article (visited on 08/15/2025).

Koloo, Farhad Ahadi; Badakhshan, Armin; Fallahnejad, Hossein; Jamkhaneh, Mehdi Ebadi; Ahmadi, Masoud (2018): Investigation of Proposed Concrete Filled Steel Tube Connections under Reversed Cyclic Loading. In: *International Journal of Steel Structures* 18.1, pp. 163–177. ISSN: 1598-2351, 2093-6311. DOI: 10.1007/s13296-018-0313-6. URL: http://link.springer.com/10.1007/s13296-018-0313-6 (visited on 08/12/2025).

Kremieniewski, Marcin; Wiśniowski, Rafał; Stryczek, Stanisław; Łopata, Paweł (2021): Comparison of Efficient Ways of Mud Cake Removal from Casing Surface with Traditional and New Agents. In: *Energies* 14.12, p. 3653. ISSN: 1996-1073. DOI: 10.3390/

en14123653. URL: https://www.mdpi.com/1996-1073/14/12/3653 (visited on 07/22/2025).

Kreyszig, Erwin; Kreyszig, Herbert; Norminton, E. J. (2011): Chapter 1.3: Separable ODEs. Modeling. In: *Advanced Engineering Mathematics*. 10th ed. Hoboken, NJ: John Wiley. ISBN: 978-0-470-45836-5.

Kruskal, William H. and Wallis, W. Allen (1952): Use of Ranks in One-Criterion Variance Analysis. In: *Journal of the American Statistical Association* 47.260, pp. 583–621. ISSN: 0162-1459, 1537-274X. DOI: 10.1080/01621459.1952.10483441. URL: http://www.tandfonline.com/doi/abs/10.1080/01621459.1952.10483441 (visited on 10/13/2025).

Kuanhai, Deng; Yue, Yuan; Yi, Hao; Zhonghui, Li; Yuanhua, Lin (2020): Experimental Study on the Integrity of Casing-Cement Sheath in Shale Gas Wells under Pressure and Temperature Cycle Loading. In: *Journal of Petroleum Science and Engineering* 195, p. 107548. ISSN: 09204105. DOI: 10.1016/j.petrol.2020.107548. URL: https://linkinghub.elsevier.com/retrieve/pii/S0920410520306197 (visited on 08/13/2025).

Kwatia, George; Al Ramadan, Mustafa; Salehi, Saeed; Teodoriu, Catalin (2019): Enhanced Cement Composition for Preventing Annular Gas Migration. In: *Volume 8: Polar and Arctic Sciences and Technology; Petroleum Technology*. ASME 2019 38th International Conference on Ocean, Offshore and Arctic Engineering. Glasgow, Scotland, UK: American Society of Mechanical Engineers, V008T11A067. ISBN: 978-0-7918-5887-5. DOI: 10.1115/OMAE2019-95589. URL: https://asmedigitalcollection.asme.org/OMAE/proceedings/OMAE2019/58875/Glasgow,%20Scotland,%20UK/1068063 (visited on 08/28/2025).

Lackey, Greg; Pfander, Isabelle; Gardiner, James; Sherwood, Owen A.; Rajaram, Harihar; Ryan, Joseph N.; Dilmore, Robert M.; Thomas, Burt (2022): Composition and Origin of Surface Casing Fluids in a Major US Oil- and Gas-Producing Region. In: *Environmental Science & Technology* 56.23, pp. 17227–17235. ISSN: 0013-936X, 1520-5851. DOI: 10.1021/acs.est.2c05239. URL: https://pubs.acs.org/doi/10.1021/acs.est.2c05239 (visited on 06/27/2024).

Lackey, Greg and Rajaram, Harihar (2019): Modeling Gas Migration, Sustained Casing Pressure, and Surface Casing Vent Flow in Onshore Oil and Gas Wells. In: *Water Resources Research* 55.1, pp. 298–323. ISSN: 0043-1397. DOI: 10.1029/2018WR024066.

Lackey, Greg; Rajaram, Harihar; Bolander, James; Sherwood, Owen A.; Ryan, Joseph N.; Shih, Chung Yan; Bromhal, Grant S.; Dilmore, Robert M. (2021): Public Data from Three US States Provide New Insights into Well Integrity. In: *Proceedings of the National Academy of Sciences* 118.14, e2013894118. ISSN: 0027-8424, 1091-6490. DOI: 10.1073/pnas.2013894118. URL: https://pnas.org/doi/full/10.1073/pnas.2013894118 (visited on 07/02/2024).

Landau, Lev Davidovič; Lifšic, Evgenij Mihailovič; Sykes, John Bradbury; Reid, William Hill (1987): §17 Flow in a Pipe. In: *Fluid Mechanics*. 2nd ed. Course of Theoretical Physics 6. Oxford: Pergamon press. ISBN: 978-0-08-033933-7.

Li, Huayao; Zhang, Fawang; Du, Xinqiang; Tian, Dezhi; Jiao, Shan; Zhu, Jiliang; Dai, Fenggang (2023): Identification of the Pollution Mechanisms and Remediation Strategies for Abandoned Wells in the Karst Areas of Northern China. In: *Sustainability* 15.23, p. 16458. ISSN: 2071-1050. DOI: 10.3390/su152316458. URL: https://www.mdpi.com/2071-1050/15/23/16458 (visited on 11/19/2025).

Li, Juan; Su, Donghua; Tang, Shizhong; Li, Zaoyuan; Wu, Hua; Huang, Sheng; Sun, Jinfei (2021): Deformation and Damage of Cement Sheath in Gas Storage Wells under Cyclic Loading. In: *Energy Science & Engineering* 9.4, pp. 483–501. ISSN: 2050-0505, 2050-0505. DOI: 10.1002/ese3.869. URL: https://onlinelibrary.wiley.com/doi/10.1002/ese3.869 (visited on 08/12/2025).

Li, Jun; Xi, Yan; Tao, Qian; Li, Yumei; Qu, Guohui (2020): Experimental Investigation and Numerical Simulation of the Emergence and Development of Micro-Annulus in Shale Gas Wells Subjected to Multistage Fracturing. In: *Journal of Natural Gas Science and Engineering* 78, p. 103314. ISSN: 18755100. DOI: 10.1016/j.jngse.2020.103314. URL: https://linkinghub.elsevier.com/retrieve/pii/S1875510020301682 (visited on 08/13/2025).

Liang, Weiguo; Zhang, Chuanda; Gao, Hongbo; Yang, Xiaoqin; Xu, Suguo; Zhao, Yangsheng (2012): Experiments on Mechanical Properties of Salt Rocks under Cyclic Loading. In: *Journal of Rock Mechanics and Geotechnical Engineering* 4.1, pp. 54–61. ISSN: 16747755. DOI: 10.3724/SP.J.1235.2012.00054. URL: https://linkinghub.elsevier.com/retrieve/pii/S1674775515301591 (visited on 10/26/2023).

Lin, Tiejun; Zhang, Qiang; Lian, Zhanghua; Chang, Xuejun; Zhu, Kuanliang; Liu, Yonghui (2016): Evaluation of Casing Integrity Defects Considering Wear and Corrosion – Application to Casing Design. In: *Journal of Natural Gas Science and Engineering* 29, pp. 440–452. ISSN: 18755100. DOI: 10.1016/j.jngse.2016.01.029. URL: https://linkinghub.elsevier.com/retrieve/pii/S1875510016300294 (visited on 08/04/2025).

Liu, Kui; Gao, Deli; Zeng, Jing; Wang, Zhengxu (2018a): Study on Cement Sheath Integrity in Horizontal Wells During Hydraulic Fracturing Process. In: 52nd U.S. Rock Mechanics/Geomechanics Symposium, ARMA-2018–1267. URL: https://onepetro.org/ARMAUSRMS/proceedings-abstract/ARMA18/All-ARMA18/ARMA-2018-1267/124102 (visited on 07/21/2025).

Liu, Ming-wei; Zhang, Fang-hua; Su, Guang-quan (2018b): Test Method Research on Weakening Interface Strength of Steel - Concrete under Cyclic Loading. In: *IOP Conference Series: Earth and Environmental Science* 113, p. 012161. ISSN: 1755-1307, 1755-1315. DOI: 10.1088/1755-1315/113/1/012161. URL: https://iopscience.iop.org/article/10.1088/1755-1315/113/1/012161 (visited on 08/12/2025).

Loizzo, Matteo; Bonnier, Nicolas; Maurin, Christian; Guenel, Louis; Singh, Kamaljeet (2020): Extending the Life of a Storage Field Through Full Integrity Characterization. In: *Abu Dhabi International Petroleum Exhibition & Conference*. Abu Dhabi International Petroleum Exhibition & Conference. Abu Dhabi, UAE: SPE, D031S095R004. DOI: 10.2118/203195-MS. URL: https://onepetro.org/SPEADIP/proceedings/20ADIP/20ADIP/D031S095R004/452166 (visited on 08/06/2025).

Loizzo, Matteo; Lecampion, Brice; Mogilevskaya, Sofia (2017): The Role of Geological Barriers in Achieving Robust Well Integrity. In: *Energy Procedia* 114, pp. 5193–5205. ISSN: 18766102. DOI: 10.1016/j.egypro.2017.03.1673. URL: https://linkinghub.elsevier.com/retrieve/pii/S187661021731874X (visited on 11/24/2025).

Lovell-Smith, J W and Pearson, H (2006): On the Concept of Relative Humidity. In: *Metrologia* 43.1, pp. 129–134. ISSN: 0026-1394, 1681-7575. DOI: 10.1088/0026-1394/43/1/018. URL: https://iopscience.iop.org/article/10.1088/0026-1394/43/1/018 (visited on 08/15/2025).

Ma, Lei; Zhang, Kui; Xie, Junfeng; Yuan, Liang; Geng, Hailong; Ning, Kun (2020): Research Progress and Prospect of Well Integrity Technology. In: *Journal of Power and Energy Engineering* 08.07, pp. 45–54. ISSN: 2327-588X, 2327-5901. DOI: 10.4236/jpee.2020.87004. URL: https://www.scirp.org/journal/doi.aspx?doi=10.4236/jpee.2020.87004 (visited on 08/12/2025).

Ma, Xinhua; Luo, Jinhuan; Li, Lifeng; Wang, Jianjun; Chen, Hongjian (2022): Wellbore Monitoring and Tubing-Casing Annulus Protection. In: *Handbook of Underground Gas Storages and Technology in China*. Ed. by Xinhua Ma. Singapore: Springer Singapore. ISBN: 978-981-334-733-5 978-981-334-734-2. DOI: 10.1007/978-981-33-4734-2. URL: https://link.springer.com/10.1007/978-981-33-4734-2 (visited on 05/28/2026).

Maharaj, G. (1996): Thermal Well Casing Failure Analysis. In: *SPE Latin America/-Caribbean Petroleum Engineering Conference*. SPE Latin America/Caribbean Petroleum Engineering Conference. Port-of-Spain, Trinidad: SPE, SPE-36143–MS. DOI: 10.2118/36143-MS. URL: https://onepetro.org/SPELACP/proceedings/96LACPEC/96LACPEC/SPE-36143-MS/58667 (visited on 08/04/2025).

Manceau, J. C.; Tremosa, J.; Audigane, P.; Lerouge, C.; Claret, F.; Lettry, Y.; Fierz, T.; Nussbaum, C. (2015): Well Integrity Assessment under Temperature and Pressure Stresses by a 1:1 Scale Wellbore Experiment. In: *Water Resources Research* 51.8, pp. 6093–6109. ISSN: 0043-1397, 1944-7973. DOI: 10.1002/2014WR016786. URL: https://agupubs.onlinelibrary.wiley.com/doi/10.1002/2014WR016786 (visited on 08/12/2025).

Massie, Crawford; Stewart, George; McGregor, George; Gilchrist, John R. (2006): Design of a Portable Optical Sensor for Methane Gas Detection. In: *Sensors and Actuators B: Chemical* 113.2, pp. 830–836. ISSN: 09254005. DOI: 10.1016/j.snb.2005.03.105.

Maytal, Ben-Zion and Pfotenhauer, John M. (2013): The Joule-Thomson Effect, Its Inversion and Other Expansions. In: *Miniature Joule-Thomson Cryocooling*. New York, NY: Springer New York, pp. 39–72. ISBN: 978-1-4419-8284-1 978-1-4419-8285-8. DOI: 10.1007/978-1-4419-8285-8_2. URL: http://link.springer.com/10.1007/978-1-4419-8285-8_2 (visited on 02/20/2025).

Meng, Meng; Frash, Luke P.; Carey, J. William; Mehana, Mohamed; Li, Wenfeng; Chen, Bailian (2024): Effect of Stress-Dependent Microannulus Aperture on Well Leakage. In: *Journal of Rock Mechanics and Geotechnical Engineering* 16.6, pp. 1967–1976. ISSN: 16747755. DOI: 10.1016/j.jrmge.2024.02.004. URL: https://linkinghub.elsevier.com/retrieve/pii/S167477552400091X (visited on 08/13/2025).

Michalski, Jan; Bünger, Ulrich; Crotogino, Fritz; Donadei, Sabine; Schneider, Gregor-Sönke; Pregger, Thomas; Cao, Karl-Kiên; Heide, Dominik (2017): Hydrogen Generation by Electrolysis and Storage in Salt Caverns: Potentials, Economics and Systems Aspects with Regard to the German Energy Transition. In: *International Journal of Hydrogen Energy* 42.19, pp. 13427–13443. ISSN: 03603199. DOI: 10.1016/j.ijhydene.2017.02.102. URL: https://linkinghub.elsevier.com/retrieve/pii/S0360319917306109 (visited on 10/07/2025).

Moghadam, Al; Castelein, Koen; Ter Heege, Jan; Orlic, Bogdan (2022): A Study on the Hydraulic Aperture of Microannuli at the Casing–Cement Interface Using a Large-Scale Laboratory Setup. In: *Geomechanics for Energy and the Environment* 29, p. 100269. ISSN: 23523808. DOI: 10.1016/j.gete.2021.100269. URL: https://linkinghub.elsevier.com/retrieve/pii/S235238082100037X (visited on 08/14/2025).

Montana Secretary of State (2011): Administrative Rules of Montana (ARM), Rule 36.22.1106: Safety and Well Control Requirements – Hydraulic Fracturing. URL: https://rules.mt.gov/browse/collections/aec52c46-128e-4279-9068-8af5d5432d74/sections/961f5df6-e107-4193-a9c2-fb24648fd8b0 (visited on 05/11/2026).

Morais, Carlos H. B.; Abreu, Danilo T. M. P.; Santos, Joaquim; Maturana, Marcos C.; Colombo, Danilo; Martins, Marcelo R. (2019): The Influence of Non-Prescriptive Legislation in the Evolution of Offshore Well Integrity Practices: An Exploratory Review. In: *Volume 3: Structures, Safety, and Reliability*. ASME 2019 38th International Conference on Ocean, Offshore and Arctic Engineering. Glasgow, Scotland, UK: American Society of Mechanical Engineers, V003T02A082. ISBN: 978-0-7918-5878-3. DOI: 10.1115/OMAE2019-96269. URL: https://asmedigitalcollection.asme.org/OMAE/proceedings/OMAE2019/58783/Glasgow,%20Scotland,%20UK/1067625 (visited on 08/12/2025).

Morais, Tiago A.; Fleming, Neil A.; Attalage, Dinu; Mayer, Bernhard; Mayer, K.U.; Ryan, M. Cathryn (2024): Field Investigation of the Transport and Attenuation of Fugitive Methane in Shallow Groundwater around an Oil and Gas Well with Gas Migration. In: *Science of The Total Environment* 908, p. 168246. ISSN: 00489697. DOI:

10.1016/j.scitotenv.2023.168246. URL: https://linkinghub.elsevier.com/retrieve/pii/S0048969723068730 (visited on 04/01/2024).

Morini, Gian Luca (2004): Laminar-to-Turbulent Flow Transition in Microchannels. In: *Microscale Thermophysical Engineering* 8.1, pp. 15–30. ISSN: 1089-3954, 1091-7640. DOI: 10.1080/10893950490272902. URL: http://www.tandfonline.com/doi/abs/10.1080/10893950490272902 (visited on 07/30/2025).

Morris, Kay A.; Deville, Jay P.; Jones, Paul (2012): Resin-Based Cement Alternatives for Deepwater Well Construction. In: *SPE Deepwater Drilling and Completions Conference*. SPE Deepwater Drilling and Completions Conference. Galveston, Texas, USA: SPE, SPE-155613–MS. DOI: 10.2118/155613-MS. URL: https://onepetro.org/SPEDDC/proceedings/12DDC/12DDC/SPE-155613-MS/157322 (visited on 08/28/2025).

Mubarak, Ghadeer; Verma, Chandrabhan; Barsoum, Imad; Alfantazi, Akram; Rhee, Kyong Yop (2023): Internal Corrosion in Oil and Gas Wells during Casings and Tubing: Challenges and Opportunities of Corrosion Inhibitors. In: *Journal of the Taiwan Institute of Chemical Engineers* 150, p. 105027. ISSN: 18761070. DOI: 10.1016/j.jtice.2023.105027. URL: https://linkinghub.elsevier.com/retrieve/pii/S1876107023003565 (visited on 08/04/2025).

Nebraska Oil and Gas Conservation Commission (2017): Nebraska Administrative Code, Title 267, Ch. 3, § 042 - Hydraulic Fracturing. URL: http://www.nogcc.ne.gov/Publications/NE_CodeChapter3.pdf (visited on 05/11/2026).

Nelder, J. A. and Mead, R. (1965): A Simplex Method for Function Minimization. In: *The Computer Journal* 7.4, pp. 308–313. ISSN: 0010-4620, 1460-2067. DOI: 10.1093/comjnl/7.4.308. URL: https://academic.oup.com/comjnl/article-lookup/doi/10.1093/comjnl/7.4.308 (visited on 03/20/2026).

Nelson, Erik B., ed. (2006): Well Cementing. 2. ed. Sugar Land, Tex: Schlumberger. 773 pp. ISBN: 978-0-9788530-0-6.

New Mexico Energy, Minerals and Natural Resources Department, Oil Conservation Division (2020): Memorandum (3-20-01) 2020 District III Bradenhead Test Schedule. URL: https://www.emnrd.nm.gov/wp-content/uploads/sites/6/2020BHTCompletew-attachments.pdf (visited on 05/12/2026).

New Mexico Environment Department (2015): New Mexico Administrative Code, 20.6.2.5204: Mechanical Integrity for Class I and Class III Wells. URL: https://www.srca.nm.gov/wp-content/uploads/attachments/20.006.0002.pdf (visited on 05/12/2026).

NOPSEMA (2020a): Well Operations Management Plan – Content and Level of Detail: N-04600-GN1602 A461074. URL: https://www.nopsema.gov.au/offshore-industry/well-integrity (visited on 05/02/2022).

NOPSEMA (2020b): Well Operations Management Plan – Lifecycle Management: N-04600-GN1601 A462131. URL: https://www.nopsema.gov.au/offshore-industry/well-integrity (visited on 05/02/2022).

North Carolina Department of Environmental Quality (2015): 15A NCAC 05H .1613: Well Stimulation Requirements. URL: http://reports.oah.state.nc.us/ncac/title%2015a%20-%20environmental%20quality/chapter%2005%20-%20mining%20-%20mineral%20resources/subchapter%20h/subchapter%20h%20rules.pdf (visited on 05/12/2026).

North Dakota Industrial Commission (2010): North Dakota Administrative Code (NDAC), Chapter 43-02-03-27. Perforating, Fracturing, and Chemically Treating Wells. URL: https://ndlegis.gov/information/acdata/pdf/43-02-03.pdf (visited on 05/11/2026).

Norwegian Oil and Gas Association (2017): 117 Norwegian Oil and Gas Association Recommended Guidelines for Well Integrity, Rev. 6. URL: https://www.offshorenorge.no/en/faginnhold/guidelines/guidelines/drilling/117-recommended-guidelines-for-well-integrity-/ (visited on 02/14/2025).

Norwegian Oil Industry Association and Federation of Norwegian Manufacturing Industries (2021): NORSOK Standard D-010: Well Integrity in Drilling and Well Operations. URL: https://standard.no/en/sectors/petroleum/norsok-standards/d-drilling (visited on 12/10/2023).

NWT Office of the Regulator of Oil and Gas Operations (2022): Well Suspension and Abandonment Guidelines and Interpretation Notes. URL: https://www.orogo.gov.nt.ca/sites/default/files/resources/2022-05-25_-_revised_well_suspension_and_abandonment_guidelines_and_interpretation_notes.pdf (visited on 05/12/2026).

Nygaard, Runar; Salehi, Saeed; Weideman, Benjamin; Lavoie, Robert Guy (2014): Effect of Dynamic Loading on Wellbore Leakage for the Wabamun Area CO2-Sequestration Project. In: *Journal of Canadian Petroleum Technology* 53.01, pp. 69–82. ISSN: 0021-9487. DOI: 10.2118/146640-PA.

O'Malley, Daniel; Delorey, Andrew A.; Guiltinan, Eric J.; Ma, Zhiwei; Kadeethum, Teeratorn; Lackey, Greg; Lee, James; E. Santos, Javier; Follansbee, Emily; Nair, Manoj C.; Pekney, Natalie J.; Jahan, Ismot; Mehana, Mohamed; Hora, Priya; Carey, J. William; Govert, Andrew; Varadharajan, Charuleka; Ciulla, Fabio; Biraud, Sebastien C.; Jordan, Preston; Dubey, Mohit; Santos, Andre; Wu, Yuxin; Kneafsey, Timothy J.; Dubey, Manvendra K.; Weiss, Chester J.; Downs, Christine; Boutot, Jade; Kang, Mary; Viswanathan, Hari (2024): Unlocking Solutions: Innovative Approaches to Identifying and Mitigating the Environmental Impacts of Undocumented Orphan Wells in the United States. In: *Environmental Science & Technology* 58.44, pp. 19584–19594. ISSN: 0013-936X, 1520-5851. DOI: 10.1021/acs.est.4c02069. URL: https://pubs.acs.org/doi/10.1021/acs.est.4c02069 (visited on 02/13/2025).

Obot, Ime Bassey; Sorour, Ahmad A.; Verma, Chandrabhan; Al-Khaldi, Turki A.; Rushaid, Anas S. (2023): Key Parameters Affecting Sweet and Sour Corrosion: Impact on Corrosion Risk Assessment and Inhibition. In: *Engineering Failure Analysis* 145,

p. 107008. ISSN: 13506307. DOI: 10.1016/j.engfailanal.2022.107008. URL: https://linkinghub.elsevier.com/retrieve/pii/S135063072200975X (visited on 08/05/2025).

Office of Parliamentary Counsel, Canberra (2023): Offshore Petroleum and Greenhouse Gas Storage (Resource Management and Administration) Regulations 2011. URL: https://www.legislation.gov.au/Details/F2023C00260 (visited on 11/30/2023).

Opedal, N.; Lavrov, A.; Todorovic, J.; Torsæter, M. (2018): The Importance of Shale Caprock Damage for Well Integrity. In: *International Journal of Greenhouse Gas Control* 74, pp. 182–190. ISSN: 17505836. DOI: 10.1016/j.ijggc.2018.04.007.

Opedal, Nils Van Der Tuuk; Torsæter, Malin; Vrålstad, Torbjørn; Cerasi, Pierre (2014): Potential Leakage Paths along Cement-formation Interfaces in Wellbores; Implications for CO2 Storage. In: *Energy Procedia* 51, pp. 56–64. ISSN: 18766102. DOI: 10.1016/j.egypro.2014.07.007. URL: https://linkinghub.elsevier.com/retrieve/pii/S1876610214008698 (visited on 10/26/2023).

Oyarhossein, M. and Dusseault, M. B. (2015): Wellbore Stress Changes and Microannulus Development Because of Cement Shrinkage. In: 49th U.S. Rock Mechanics/Geomechanics Symposium, ARMA-2015–118.

Ozturk, Merve and Dincer, Ibrahim (2021): A Comprehensive Review on Power-to-Gas with Hydrogen Options for Cleaner Applications. In: *International Journal of Hydrogen Energy* 46.62, pp. 31511–31522. ISSN: 03603199. DOI: 10.1016/j.ijhydene.2021.07.066. URL: https://linkinghub.elsevier.com/retrieve/pii/S0360319921027075 (visited on 10/07/2025).

Parish, O. O. and Putnam, T. W. (1977): Equations for the Determination of Humidity from Dewpoint and Psychrometric Data. NASA TN D-8401. Edwards, California, USA: NASA Dryden Flight Research Center, NASA Technical Note. URL: https://ntrs.nasa.gov/api/citations/19770009916/downloads/19770009916.pdf.

Pearson, Karl (1896): VII. Mathematical Contributions to the Theory of Evolution.—III. Regression, Heredity, and Panmixia. In: *Philosophical Transactions of the Royal Society of London. Series A, Containing Papers of a Mathematical or Physical Character* 187, pp. 253–318. ISSN: 0264-3952, 2053-9258. DOI: 10.1098/rsta.1896.0007. URL: https://royalsocietypublishing.org/doi/10.1098/rsta.1896.0007 (visited on 10/13/2025).

Peiyi, Wu and Little, W.A. (1983): Measurement of Friction Factors for the Flow of Gases in Very Fine Channels Used for Microminiature Joule-Thomson Refrigerators. In: *Cryogenics* 23.5, pp. 273–277. ISSN: 00112275. DOI: 10.1016/0011-2275(83)90150-9. URL: https://linkinghub.elsevier.com/retrieve/pii/0011227583901509 (visited on 07/30/2025).

Pelipenko, S. and Frigaard, I.A. (2004): Mud Removal and Cement Placement during Primary Cementing of an Oil Well – Part 2; Steady-State Displacements. In: *Journal of Engineering Mathematics* 48.1, pp. 1–26. ISSN: 0022-0833. DOI: 10.1023/B:ENGI.

0000009499.63859.f0. URL: http://link.springer.com/10.1023/B:ENGI.0000009499.63859.f0 (visited on 02/07/2025).

Peng, Ding-Yu and Robinson, Donald B. (1976): A New Two-Constant Equation of State. In: *Industrial & Engineering Chemistry Fundamentals* 15.1, pp. 59–64. ISSN: 0196-4313, 1541-4833. DOI: 10.1021/i160057a011. URL: https://pubs.acs.org/doi/abs/10.1021/i160057a011 (visited on 02/20/2025).

Pennsylvania Department of Environmental Protection (2017): Pennsylvania Code Title 25: Environmental Protection, Chapter 78: Oil and Gas Wells. URL: https://www.pacodeandbulletin.gov/Display/pacode?file=/secure/pacode/data/025/chapter78/chap78toc.html&d= (visited on 04/01/2026).

Petroleum Safety Authority Norway (2017): Safety and Responsibility. Understanding the Norwegian Regime. Stavanger, Norway: Havtil. URL: https://www.havtil.no/contentassets/0079bf5eb8824beb969fd0f217f395b7/safety--and-responsibilit_nett.pdf (visited on 05/13/2026).

Petroleum Safety Authority Norway (2023a): Regulations Relating to Conducting Petroleum Activities: The Activities Regulations. URL: https://www.ptil.no/en/regulations/all-acts/?forskrift=613 (visited on 07/12/2022).

Petroleum Safety Authority Norway (2023b): Regulations Relating to Design and Outfitting of Facilities, Etc. in the Petroleum Activities: The Facilities Regulations. URL: https://www.ptil.no/en/regulations/all-acts/?forskrift=634#par54 (visited on 07/13/2022).

Petroleum Safety Authority Norway (2023c): Regulations Relating to Health, Safety and the Environment in the Petroleum Activities and at Certain Onshore Facilities. URL: https://www.havtil.no/en/regulations/all-acts/?forskrift=158#par11 (visited on 08/09/2024).

Powers, T. (1935): Absorption of Water by Portland Cement Paste during the Hardening Process. In: *Industrial & Engineering Chemistry* 27.7, pp. 790–794. ISSN: 0019-7866, 1541-5724. DOI: 10.1021/ie50307a011. URL: https://pubs.acs.org/doi/abs/10.1021/ie50307a011 (visited on 06/15/2026).

Queensland Government (2004): Petroleum and Gas (Production and Safety) Act 2004. URL: https://www.legislation.qld.gov.au/view/whole/html/inforce/current/act-2004-025 (visited on 05/28/2024).

Railroad Commission of Texas (2025): Texas Administrative Code, Title 16, Part 1, Chapter 3: Oil and Gas Division. URL: https://www.rrc.texas.gov/media/jfqhzm1y/chapter3-all-effective-july1-2025.pdf (visited on 06/12/2026).

Ravikumar, Arvind P.; Wang, Jingfan; Brandt, Adam R. (2017): Are Optical Gas Imaging Technologies Effective For Methane Leak Detection? In: *Environmental Science & Technology* 51.1, pp. 718–724. ISSN: 0013-936X. DOI: 10.1021/acs.est.6b03906.

Reynolds, Osborne (1883): XXIX. An Experimental Investigation of the Circumstances Which Determine Whether the Motion of Water Shall Be Direct or Sinuous, and of the

Law of Resistance in Parallel Channels. In: *Philosophical Transactions of the Royal Society of London* 174, pp. 935–982. ISSN: 0261-0523, 2053-9223. DOI: 10.1098/rstl.1883.0029. URL: https://royalsocietypublishing.org/doi/10.1098/rstl.1883.0029 (visited on 07/28/2025).

Ritchie, Hannah (2020): Sector by Sector: Where Do Global Greenhouse Gas Emissions Come From? URL: https://ourworldindata.org/ghg-emissions-by-sector (visited on 04/01/2024).

Rød, Kristian Ottestad (2017): An Investigation of Sustained Casing Pressure Occurring on the NCS (Master Thesis). University of Stavanger, Norway. HDL: 11250/2734707. URL: https://hdl.handle.net/11250/2734707 (visited on 07/02/2024).

Rostekhnadzor (2020): Federal Service for Environmental, Technological and Nuclear Supervision: Federal Norms and Rules in the Field of Industrial Safety "Safety Rules in the Oil and Gas Industry" (as Amended on January 19, 2022). URL: http://base.safework.ru/law?doc&nd=33300114&nh=0&ssect=0 (visited on 11/30/2023).

Rotta, J. (1956): Experimenteller Beitrag zur Entstehung turbulenter Strömung im Rohr. In: *Ingenieur-Archiv* 24.4, pp. 258–281. ISSN: 0020-1154, 1432-0681. DOI: 10.1007/bf00536526. URL: http://link.springer.com/10.1007/BF00536526 (visited on 07/28/2025).

Samson AG (2012): Application Notes KV Coefficient · Valve Sizing. AB 05 EN, Edition March 2012. Frankfurt am Main, Germany. URL: https://www.samsongroup.com/document/t00050en.pdf (visited on 01/15/2025).

SAMUH$_2$ consortium (2022): Projekt SAMUH$_2$ - Sichere Und Innovative Erschließungskonzepte Für Ausbau, Nachnutzung Und Monitoring von Untergrundspeichern Für Wasserstoff - BMWE Förderkennzeichen 03EI3051A. URL: https://www.samuh2.de/ (visited on 08/11/2025).

Santos, Livio; Dahi Taleghani, Arash; Li, Guoqiang (2020): Smart Expandable Fiber Additive To Prevent Formation of Microannuli. In: *SPE Drilling & Completion* 35.03, pp. 490–502. ISSN: 1064-6671, 1930-0204. DOI: 10.2118/201100-PA. URL: https://onepetro.org/DC/article/35/03/490/450749/Smart-Expandable-Fiber-Additive-To-Prevent (visited on 08/28/2025).

Schilling, Frank R.; Bieberstein, Andreas; Eckhardt, Jörg-Detlef; Haist, Michael; Hirsch, Astrid; Klumbach, Steffen; Kromer, Marco; Mühlbach, Josephin; Müller, Birgit I. R.; Müller, Harald S.; Neumann, Thomas; Schläger, Stefan; Triantafyllidis, Theodoros (2015): Long-Term Safety of Well Abandonment: First Results from Large Scale Laboratory Experiments (COBRA). In: *Geological Storage of CO2 – Long Term Security Aspects: GEOTECHNOLOGIEN Science Report No. 22*. Ed. by Axel Liebscher and Ute Münch. Cham: Springer International Publishing, pp. 115–138. ISBN: 978-3-319-13930-2. DOI: 10.1007/978-3-319-13930-2_6. URL: https://doi.org/10.1007/978-3-319-13930-2_6.

Schilling, Frank R.; Müller, Harald S.; Eckhardt, Jörg-Detlef; Haist, Michael; Triantafyllidis, Theodoros; Bieberstein, Andreas; Neumann, Thomas; Scheuermann, Alexander; Balthasar, Karl; Hirsch, Astrid; Klumbach, Steffen; Kromer, Marco; Mühlbach, Josephin (2016): CO2-Speicherung-Bohrlochsimulator, Akronym COBRA (CO2 Bohrlochverschluss Versuchsanlage), Sonderprogramm Geotechnologien III, Abschlussbericht, Gefördert Durch Das Bundesministerium Für Bildung Und Forschung. 03G0763A. Karlsruhe, p. 183. URL: https://edocs.tib.eu/files/e01fb17/879188170.pdf (visited on 11/20/2025).

Schulz, Marcel; Talukdar, Mayukh; Pfander, Isabelle; Lackey, Greg; Röckel, Luisa; Wojtanowicz, Andrew; Schilling, Frank; Blum, Philipp (2025): Global Regulations and Practices for Well Integrity Management: A Review. In: *Journal of Petroleum Exploration and Production Technology* 15.5. ISSN: 2190-0558, 2190-0566. DOI: 10.1007/s13202-025-01997-7. URL: https://link.springer.com/10.1007/s13202-025-01997-7 (visited on 07/25/2025).

Seymour, Scott P.; Xie, Donglai; Kang, Mary (2024): Highly Uncertain Methane Leakage from Oil and Gas Wells in Canada Despite Measurement and Reporting. In: *Energy & Fuels*, acs.energyfuels.4c00908. ISSN: 0887-0624, 1520-5029. DOI: 10.1021/acs.energyfuels.4c00908. URL: https://pubs.acs.org/doi/10.1021/acs.energyfuels.4c00908 (visited on 06/17/2024).

Al-Shafi, Manal; Massarweh, Osama; Abushaikha, Ahmad S.; Bicer, Yusuf (2023): A Review on Underground Gas Storage Systems: Natural Gas, Hydrogen and Carbon Sequestration. In: *Energy Reports* 9, pp. 6251–6266. ISSN: 23524847. DOI: 10.1016/j.egyr.2023.05.236. URL: https://linkinghub.elsevier.com/retrieve/pii/S2352484723009794 (visited on 08/11/2025).

Shapiro, S. S. and Wilk, M. B. (1965): An Analysis of Variance Test for Normality (Complete Samples). In: *Biometrika* 52.3–4, pp. 591–611. ISSN: 0006-3444, 1464-3510. DOI: 10.1093/biomet/52.3-4.591. URL: https://academic.oup.com/biomet/article-lookup/doi/10.1093/biomet/52.3-4.591 (visited on 10/13/2025).

Sherwin, Evan D.; Rutherford, Jeffrey S.; Zhang, Zhan; Chen, Yuanlei; Wetherley, Erin B.; Yakovlev, Petr V.; Berman, Elena S. F.; Jones, Brian B.; Cusworth, Daniel H.; Thorpe, Andrew K.; Ayasse, Alana K.; Duren, Riley M.; Brandt, Adam R. (2024): US Oil and Gas System Emissions from Nearly One Million Aerial Site Measurements. In: *Nature* 627.8003, pp. 328–334. ISSN: 0028-0836, 1476-4687. DOI: 10.1038/s41586-024-07117-5. URL: https://www.nature.com/articles/s41586-024-07117-5 (visited on 03/27/2024).

Shui, Zhonghe; Xuan, Dongxing; Chen, Wei; Yu, Rui; Zhang, Rui (2009): Cementitious Characteristics of Hydrated Cement Paste Subjected to Various Dehydration Temperatures. In: *Construction and Building Materials* 23.1, pp. 531–537. ISSN: 09500618. DOI: 10.1016/j.conbuildmat.2007.10.016. URL: https://linkinghub.elsevier.com/retrieve/pii/S0950061807002516 (visited on 11/24/2025).

Siddig, Osama; Mahmoud, Ahmed Abdulhamid; Elkatatny, Salaheldin (2020): A Review of Different Approaches for Water-Based Drilling Fluid Filter Cake Removal. In: *Journal of Petroleum Science and Engineering* 192, p. 107346. ISSN: 0920-4105. DOI: 10.1016/j.petrol.2020.107346. URL: https://linkinghub.elsevier.com/retrieve/pii/S0920410520304228 (visited on 07/22/2025).

Sirtoli, Davide; Wyrzykowski, Mateusz; Riva, Paolo; Lura, Pietro (2020): Autogenous and Drying Shrinkage of Mortars Based on Portland and Calcium Sulfoaluminate Cements. In: *Materials and Structures* 53.5, p. 126. ISSN: 1359-5997, 1871-6873. DOI: 10.1617/s11527-020-01561-1. URL: https://link.springer.com/10.1617/s11527-020-01561-1 (visited on 11/21/2025).

Song, Haipeng; Zhang, Hao; Fu, Donghui; Zhang, Qian (2016): Experimental Analysis and Characterization of Damage Evolution in Rock under Cyclic Loading. In: *International Journal of Rock Mechanics and Mining Sciences* 88, pp. 157–164. ISSN: 13651609. DOI: 10.1016/j.ijrmms.2016.07.015. URL: https://linkinghub.elsevier.com/retrieve/pii/S1365160916301435 (visited on 08/13/2025).

Song, Jianjian; Chen, Rongyao; Wu, Zhongtao; Yin, Zhong; Xu, Mingbiao (2024): A Review of Research Methods for Oil Well Cement Corroded by Carbon Dioxide. In: *Geoenergy Science and Engineering* 232, p. 212469. ISSN: 29498910. DOI: 10.1016/j.geoen.2023.212469. URL: https://linkinghub.elsevier.com/retrieve/pii/S2949891023010564 (visited on 08/06/2025).

Spearman, C. (1904): The Proof and Measurement of Association between Two Things. In: *The American Journal of Psychology* 15.1, p. 72. ISSN: 00029556. DOI: 10.2307/1412159. JSTOR: 1412159. URL: https://www.jstor.org/stable/1412159?origin=crossref (visited on 10/13/2025).

Stark, Jochen and Wicht, Bernd (2013): Zement. In: *Dauerhaftigkeit von Beton*. Berlin, Heidelberg: Springer Berlin Heidelberg, pp. 27–101. ISBN: 978-3-642-35277-5 978-3-642-35278-2. DOI: 10.1007/978-3-642-35278-2_2. URL: https://link.springer.com/10.1007/978-3-642-35278-2_2 (visited on 08/01/2025).

State Oil and Gas Board of Alabama (2025): Oil and Gas Report 1: Rules and Regulations Governing the Conservation of Oil and Gas in Alabama, Rule 400-2-6-.08: Wellhead Equipment and Testing Procedures. URL: https://gsa.state.al.us/ogb/rules (visited on 05/12/2026).

Statistics Canada (2023): 2021 Census – Boundary Files. URL: https://www12.statcan.gc.ca/census-recensement/2021/geo/sip-pis/boundary-limites/index2021-eng.cfm?Year=21 (visited on 12/21/2023).

Stormont, John C.; Fernandez, Serafin Garcia; Taha, Mahmoud R.; Matteo, Edward N. (2018): Gas Flow through Cement-Casing Microannuli under Varying Stress Conditions. In: *Geomechanics for Energy and the Environment* 13, pp. 1–13. ISSN: 23523808. DOI: 10.1016/j.gete.2017.12.001. URL: https://linkinghub.elsevier.com/retrieve/pii/S2352380817300436 (visited on 11/24/2025).

Storn, Rainer and Price, Kenneth (1997): Differential Evolution – A Simple and Efficient Heuristic for Global Optimization over Continuous Spaces. In: *Journal of Global Optimization* 11.4, pp. 341–359. ISSN: 0925-5001, 1573-2916. DOI: 10.1023/A:1008202821328. URL: https://link.springer.com/10.1023/A:1008202821328 (visited on 03/20/2026).

SUBI consortium (2017): Projekt SUBI - Sicherheit von Untergrundspeichern Bei Zyklischer Belastung: Funktionalität Und Integrität von Speichern Und Bohrungen - BMBF Förderkennzeichen 03G0869. URL: https://www.subi-ugs.de/ (visited on 08/11/2025).

Sun, Dandan; Wu, Kai; Shi, Huisheng; Miramini, Saeed; Zhang, Lihai (2019): Deformation Behaviour of Concrete Materials under the Sulfate Attack. In: *Construction and Building Materials* 210, pp. 232–241. ISSN: 09500618. DOI: 10.1016/j.conbuildmat.2019.03.050.

Syed, Talibuddin and Cutler, Thor (2010): Well Integrity Technical and Regulatory Considerations for CO2 Injection Wells. In: *SPE International Conference on Health, Safety and Environment in Oil and Gas Exploration and Production*. SPE International Conference on Health, Safety and Environment in Oil and Gas Exploration and Production. Rio de Janeiro, Brazil: SPE, SPE-125839–MS. DOI: 10.2118/125839-MS. URL: https://onepetro.org/SPEHSE/proceedings/10HSE/10HSE/SPE-125839-MS/105950 (visited on 08/11/2025).

Tamim, Nafiz; Mannan, M. Sam; Karim, M. Nazmul; O'Connor, Mary Kay (2019): An Analysis of Offshore Safety Incidents in the Last 50 Years and a Look into the Current Perspectives. In: *Hazards 29 – Symposium Series No. 166*. Hazards 29 – Symposium. Vol. 166. Symposium Series. College Station, TX, USA: Texas A&M University. URL: https://www.icheme.org/media/19465/hazards-29-poster-17.pdf (visited on 11/12/2025).

Tao, Ye; He, Youbin; Zhao, Zhongxiang; Wu, Dongsheng; Deng, Qiao (2023): Sealing of Oil-Gas Reservoir Caprock: Destruction of Shale Caprock by Micro-Fractures. In: *Frontiers in Earth Science* 10. ISSN: 2296-6463. DOI: 10.3389/feart.2022.1065875.

Tayman, Jeff and Swanson, David A. (1999): On the Validity of MAPE as a Measure of Population Forecast Accuracy. In: *Population Research and Policy Review* 18.4, pp. 299–322. ISSN: 0167-5923, 1573-7829. DOI: 10.1023/A:1006166418051. URL: https://link.springer.com/10.1023/A:1006166418051 (visited on 10/13/2025).

The Engineering ToolBox (2004): Water Vapor Saturation Pressure: Data, Tables & Calculator. URL: https://www.engineeringtoolbox.com/water-vapor-saturation-pressure-d_599.html (visited on 08/14/2025).

Thomas, Tim and Johnson, Raymond L. (2019): An Assessment Of The Current Regulatory Frameworks For Onshore, Upstream, Unconventional Well Integrity And Strategies For Improvement. In: *SPE Annual Technical Conference and Exhibition*. SPE Annual Technical Conference and Exhibition. Calgary, Alberta, Canada: SPE, D021S031R006.

DOI: 10.2118/195967-MS. URL: https://onepetro.org/SPEATCE/proceedings/19ATCE/19ATCE/D021S031R006/217590 (visited on 08/11/2025).

Ugarte, Esteban R. and Salehi, Saeed (2022): A Review on Well Integrity Issues for Underground Hydrogen Storage. In: *Journal of Energy Resources Technology* 144.4. ISSN: 0195-0738. DOI: 10.1115/1.4052626.

Uliasz-Misiak, Barbara and Misiak, Jacek (2024): Underground Gas Storage in Saline Aquifers: Geological Aspects. In: *Energies* 17.7, p. 1666. ISSN: 1996-1073. DOI: 10.3390/en17071666. URL: https://www.mdpi.com/1996-1073/17/7/1666 (visited on 10/07/2025).

Umweltbundesamt (2025a): Endenergieverbrauch Nach Energieträgern Und Sektoren. URL: https://www.umweltbundesamt.de/daten/energie/energieverbrauch-nach-energietraegern-sektoren#allgemeine-entwicklung-und-einflussfaktoren (visited on 08/07/2025).

Umweltbundesamt (2025b): Energieverbrauch Für Fossile Und Erneuerbare Wärme. URL: https://www.umweltbundesamt.de/daten/energie/energieverbrauch-fuer-fossile-erneuerbare-waerme (visited on 08/07/2025).

Umweltbundesamt (2025c): Stromverbrauch. URL: https://www.umweltbundesamt.de/daten/energie/stromverbrauch#entwicklung-des-stromverbrauchs (visited on 08/07/2025).

UNDRR (2017a): United Nations Office for Disaster Risk Reduction (UNDRR), The Sendai Framework Terminology on Disaster Risk Reduction. "Capacity". URL: https://www.undrr.org/terminology/capacity (visited on 11/11/2025).

UNDRR (2017b): United Nations Office for Disaster Risk Reduction (UNDRR), The Sendai Framework Terminology on Disaster Risk Reduction. "Disaster Risk". URL: https://www.undrr.org/terminology/disaster-risk (visited on 11/11/2025).

UNDRR (2017c): United Nations Office for Disaster Risk Reduction (UNDRR), The Sendai Framework Terminology on Disaster Risk Reduction. "Exposure". URL: https://www.undrr.org/terminology/exposure (visited on 11/11/2025).

UNDRR (2017d): United Nations Office for Disaster Risk Reduction (UNDRR), The Sendai Framework Terminology on Disaster Risk Reduction. "Hazard". URL: https://www.undrr.org/terminology/hazard (visited on 11/11/2025).

UNDRR (2017e): United Nations Office for Disaster Risk Reduction (UNDRR), The Sendai Framework Terminology on Disaster Risk Reduction. "Vulnerability". URL: https://www.undrr.org/terminology/vulnerability (visited on 11/11/2025).

United States Congress (1953): Submerged Lands Act §1301-§1315. United States Code, Title 43 - Public Lands, Chapter 29 - Submerged Land. URL: https://uscode.house.gov/view.xhtml?path=/prelim@title43/chapter29&edition=prelim (visited on 02/09/2026).

Van Oort, Eric; Juenger, Maria; Aldin, Munir; Thombare, Akshay; McDonald, Michael; Lucas, Alexander; Ditlevsen, Frederik (2022): Simplifying Well Abandonments Using

Shale as a Barrier. In: *SPE Drilling & Completion* 37.04, pp. 282–294. ISSN: 1064-6671, 1930-0204. DOI: 10.2118/199654-PA. URL: https://onepetro.org/DC/article/37/04/282/485175/Simplifying-Well-Abandonments-Using-Shale-as-a (visited on 11/24/2025).

Van Kleef, R. P. A. R. (1989): Optimized Slurry Design for Salt Zone Cementations. In: *SPE/IADC Drilling Conference*. SPE/IADC Drilling Conference. New Orleans, Louisiana: SPE. DOI: 10.2118/18620-ms. URL: https://onepetro.org/SPEDC/proceedings/89DC/89DC/SPE-18620-MS/63464 (visited on 07/22/2025).

Veer, Karan and Kumar, Ravinder (2024): Standards for Industrial Safety: Challenges and Prospects. In: *National Academy Science Letters*. ISSN: 0250-541X, 2250-1754. DOI: 10.1007/s40009-024-01579-x. URL: https://link.springer.com/10.1007/s40009-024-01579-x (visited on 11/18/2025).

Vignes, Birgit and Aadnoy, Bernt S. (2008): Well-Integrity Issues Offshore Norway. In: *All Days*. IADC/SPE Drilling Conference. Orlando, Florida, USA: SPE, SPE-112535–MS. DOI: 10.2118/112535-MS. URL: https://onepetro.org/SPEDC/proceedings/08DC/All-08DC/SPE-112535-MS/143821 (visited on 07/02/2024).

Vignes, Birgit and Aadnøy, Bernt S. (2010): Well-Integrity Issues Offshore Norway. In: *SPE Production & Operations* 25.02, pp. 145–150. ISSN: 1930-1855, 1930-1863. DOI: 10.2118/112535-PA. URL: https://onepetro.org/PO/article/25/02/145/191952/Well-Integrity-Issues-Offshore-Norway (visited on 08/12/2025).

Virtanen, Pauli et al. (2020): SciPy 1.0: Fundamental Algorithms for Scientific Computing in Python. In: *Nature Methods* 17.3, pp. 261–272. ISSN: 1548-7091, 1548-7105. DOI: 10.1038/s41592-019-0686-2. URL: https://www.nature.com/articles/s41592-019-0686-2 (visited on 03/20/2026).

Vrålstad, Torbjørn; Saasen, Arild; Fjær, Erling; Øia, Thomas; Ytrehus, Jan David; Khalifeh, Mahmoud (2019): Plug & Abandonment of Offshore Wells: Ensuring Long-Term Well Integrity and Cost-Efficiency. In: *Journal of Petroleum Science and Engineering* 173, pp. 478–491. ISSN: 09204105. DOI: 10.1016/j.petrol.2018.10.049.

Wagner-Menghin, Michaela M. (2005): Binomial Test. In: *Encyclopedia of Statistics in Behavioral Science*. Ed. by Brian S. Everitt and David C. Howell. 1st ed. Wiley. ISBN: 978-0-470-86080-9 978-0-470-01319-9. DOI: 10.1002/0470013192.bsa743. URL: https://onlinelibrary.wiley.com/doi/10.1002/0470013192.bsa743 (visited on 10/13/2025).

Wallace, Gary; Kiddie, Neil; Kearns, John; Robinson, Peter (2008): A Compliance-based Approach to Well Integrity Management. In: *SPE Annual Technical Conference and Exhibition*. SPE Annual Technical Conference and Exhibition. Denver, Colorado, USA: SPE, SPE-115585–MS. DOI: 10.2118/115585-MS. URL: https://onepetro.org/SPEATCE/proceedings/08ATCE/08ATCE/SPE-115585-MS/144817 (visited on 08/12/2025).

Walters, David; Johnstone, Richard; Bluff, Elizabeth; Limborg, Hans Jørgen; Gensby, Ulrik (2021): Improving Compliance with Occupational Safety and Health Regulations:

An Overarching Review. Commissioned by the European Agency for Safety and Health at Work (EU-OSHA). URL: https://osha.europa.eu/sites/default/files/Improving_compliance_OSH_regulatons_lit%20review.pdf (visited on 11/18/2025).

Wan, Renpu (2011): Advanced Well Completion Engineering. Elsevier. ISBN 978-0-12-385868-9. https://doi.org/10.1016/C2010-0-66820-9. ISBN: 978-0-12-385868-9. DOI: 10.1016/C2010-0-66820-9. URL: https://linkinghub.elsevier.com/retrieve/pii/C20100668209 (visited on 02/05/2025).

Wang, Yangang; Feng, Yongcun; Zhao, Yingxiao; Li, Saxing; Su, Feiyu; Gu, Chenwang; Li, Xiaorong (2024): Experimental Study on Cement Sheath Integrity of UGS Wells under Cyclic Loading. In: *Geoenergy Science and Engineering* 239, p. 212958. ISSN: 29498910. DOI: 10.1016/j.geoen.2024.212958. URL: https://linkinghub.elsevier.com/retrieve/pii/S2949891024003282 (visited on 08/13/2025).

Wang, Ying; Zheng, Xin; Li, Li; Yuan, Jianbo; Vo, Minh; Reading, Richard; Zhang, Junliang (2021): Resin Squeeze Operation to Successfully Seal Micro-Channels and Eliminate Sustained Casing Pressure of a Sour Gas Well. In: *IADC/SPE Asia Pacific Drilling Technology Conference*. IADC/SPE Asia Pacific Drilling Technology Conference. Virtual: SPE, D011S005R002. DOI: 10.2118/201008-MS. URL: https://onepetro.org/SPEAPDT/proceedings/20APDT/20APDT/D011S005R002/463660 (visited on 11/25/2025).

Wang, Zhechao; Li, Shucai; Qiao, Liping; Zhang, Qingsong (2015): Finite Element Analysis of the Hydro-Mechanical Behavior of an Underground Crude Oil Storage Facility in Granite Subject to Cyclic Loading during Operation. In: *International Journal of Rock Mechanics and Mining Sciences* 73, pp. 70–81. ISSN: 13651609. DOI: 10.1016/j.ijrmms.2014.09.018. URL: https://linkinghub.elsevier.com/retrieve/pii/S1365160914002627 (visited on 10/26/2023).

Watson, Theresa L. and Bachu, Stefan (2009): Evaluation of the Potential for Gas and CO2 Leakage Along Wellbores. In: *SPE Drilling & Completion* 24.01, pp. 115–126. ISSN: 1064-6671, 1930-0204. DOI: 10.2118/106817-pa. URL: https://onepetro.org/DC/article/24/01/115/191763/Evaluation-of-the-Potential-for-Gas-and-CO2 (visited on 07/22/2025).

Webb, Paul A. and Orr, Clyde (1997): Analytical Methods in Fine Particle Technology. 1. ed., 2. print. Norcross, Ga: Micromeritics Instrument Corp. 301 pp. ISBN: 978-0-9656783-0-8 978-0-9656783-1-5.

WellDatabase (2025): WellDatabase.Com. URL: https://welldatabase.com (visited on 01/27/2025).

WellWiki (2021): WellWiki.Org Main Page. URL: https://www.wellwiki.org/wiki/Main_Page (visited on 01/27/2025).

White, Frank M. (2011): Chapter 6: Viscous Flow in Ducts. In: *Fluid Mechanics*. 7. ed. McGraw-Hill Series in Mechanical Engineering. New York: McGraw-Hill. ISBN: 978-0-07-352934-9 978-0-07-741908-0 978-0-07-742241-7.

Williams, James P.; Regehr, Amara; Kang, Mary (2021): Methane Emissions from Abandoned Oil and Gas Wells in Canada and the United States. In: *Environmental Science & Technology* 55.1, pp. 563–570. ISSN: 0013-936X. DOI: 10.1021/acs.est.0c04265. URL: https://doi.org/10.1021/acs.est.0c04265.

Wischnewski, Berndt (2007): Peace Software. URL: https://www.peacesoftware.de/einigewerte/stickstoff.html (visited on 02/21/2025).

Wisen, Joshua; Chesnaux, Romain; Werring, John; Wendling, Gilles; Baudron, Paul; Barbecot, Florent (2020): A Portrait of Wellbore Leakage in Northeastern British Columbia, Canada. In: *Proceedings of the National Academy of Sciences of the United States of America* 117.2, pp. 913–922. DOI: 10.1073/pnas.1817929116.

Witherspoon, P.A.; Mueller, T.D.; Donovan, R.W. (1962): Evaluation of Underground Gas-Storage Conditions In Aquifers Through Investigations of Groundwater Hydrology. In: *Journal of Petroleum Technology* 14.05, pp. 555–561. ISSN: 0149-2136, 1944-978X. DOI: 10.2118/162-PA. URL: https://onepetro.org/JPT/article/14/05/555/162486/Evaluation-of-Underground-Gas-Storage-Conditions (visited on 10/07/2025).

Wojtanowicz, Andrew K.; Nishikawa, Somei; Rong, Xu (2001): Diagnosis and Remediation of Sustained Casing Pressure in Wells: Final Report, Submitted to: US Department of Interior - Minerals Management Service. Baton Rouge, Louisiana, USA: Luisiana State University. URL: https://www.bsee.gov/sites/bsee.gov/files/tap-technical-assessment-program/008dk.pdf (visited on 10/11/2022).

Wood, David A. (2024): Well Integrity for Underground Gas Storage Relating to Natural Gas, Carbon Dioxide, and Hydrogen. In: *Sustainable Natural Gas Drilling*. Elsevier, pp. 551–576. ISBN: 978-0-443-13422-7. DOI: 10.1016/B978-0-443-13422-7.00019-2. URL: https://linkinghub.elsevier.com/retrieve/pii/B9780443134227000192 (visited on 08/14/2024).

Wyckoff, R. D.; Botset, H. G.; Muskat, M.; Reed, D. W. (1933): The Measurement of the Permeability of Porous Media for Homogeneous Fluids. In: *Review of Scientific Instruments* 4.7, pp. 394–405. ISSN: 0034-6748, 1089-7623. DOI: 10.1063/1.1749155. URL: https://pubs.aip.org/rsi/article/4/7/394/304042/The-Measurement-of-the-Permeability-of-Porous (visited on 07/01/2025).

Xi, Yan; Li, Jun; Tao, Qian; Guo, Boyun; Liu, Gonghui (2020): Experimental and Numerical Investigations of Accumulated Plastic Deformation in Cement Sheath during Multistage Fracturing in Shale Gas Wells. In: *Journal of Petroleum Science and Engineering* 187, p. 106790. ISSN: 09204105. DOI: 10.1016/j.petrol.2019.106790. URL: https://linkinghub.elsevier.com/retrieve/pii/S0920410519312082 (visited on 08/14/2025).

Xi, Yan; Lian, Wei; Fan, Lifeng; Tao, Qian; Guo, Xueli (2021): Research and Engineering Application of Pre-Stressed Cementing Technology for Preventing Micro-Annulus Caused by Cyclic Loading-Unloading in Deep Shale Gas Horizontal Wells. In: *Journal of Petroleum Science and Engineering* 200, p. 108359. ISSN: 09204105. DOI: 10.1016/j.petrol.2021.108359. URL: https://linkinghub.elsevier.com/retrieve/pii/S0920410521000188 (visited on 08/13/2025).

Xu, Rong and Wojtanowicz, Andrew K. (2017): Pressure Buildup Test Analysis in Wells with Sustained Casing Pressure. In: *Journal of Natural Gas Science and Engineering* 38, pp. 608–620. ISSN: 18755100. DOI: 10.1016/j.jngse.2016.12.033.

Yakoot, Mostafa S.; Elgibaly, Ahmed A.; Ragab, Adel M. S.; Mahmoud, Omar (2021): Well Integrity Management in Mature Fields: A State-of-the-Art Review on the System Structure and Maturity. In: *Journal of Petroleum Exploration and Production Technology* 11.4, pp. 1833–1853. ISSN: 2190-0558, 2190-0566. DOI: 10.1007/s13202-021-01154-w. URL: https://link.springer.com/10.1007/s13202-021-01154-w (visited on 08/11/2025).

Yakovlev, Andrey; Lafitte, Valerie; Kapoor, Saurabh; Meade, Mark; Smith, William; Fischer, Nathan; Parton, Chris; Richter McDonald, Veronica; Nenjerama, Yeukayi; Wei, Xia; Landry, Geoff (2023): An Innovative and Sustainable Portland Cement Alternative for Oil and Gas Wells. In: *SPE International Conference on Oilfield Chemistry*. SPE International Conference on Oilfield Chemistry. The Woodlands, Texas, USA: SPE, D011S006R001. DOI: 10.2118/213805-MS. URL: https://onepetro.org/SPEOCC/proceedings/23OCC/23OCC/D011S006R001/521063 (visited on 08/28/2025).

Yang, Hanzhi; Wang, Lei; Yang, Chunhe; Zhao, Jian; Huang, Guangping; Guo, Yintong; Liu, Wei Victor (2024): Mechanical Performance of Oil-Well Cement Slurries Cured and Tested under High-Temperatures and High-Pressures for Deep-Well Applications. In: *Cement and Concrete Research* 175, p. 107355. ISSN: 00088846. DOI: 10.1016/j.cemconres.2023.107355. URL: https://linkinghub.elsevier.com/retrieve/pii/S0008884623002697 (visited on 08/13/2025).

Yao, Theodore and Wojtanowicz, Andrew K. (2017): Criteria and Risk of Integrity Loss for Wells with Sustained Casing Pressure. In: *AGH Drilling, Oil, Gas* 34.2, p. 639. ISSN: 1507-0042. DOI: 10.7494/drill.2017.34.2.639.

Yousuf, Navid; Olayiwola, Olatunji; Guo, Boyun; Liu, Ning (2021): A Comprehensive Review on the Loss of Wellbore Integrity Due to Cement Failure and Available Remedial Methods. In: *Journal of Petroleum Science and Engineering* 207, p. 109123. ISSN: 09204105. DOI: 10.1016/j.petrol.2021.109123. URL: https://linkinghub.elsevier.com/retrieve/pii/S0920410521007786 (visited on 02/10/2025).

Yuan, Zhaoguang; Teodoriu, Catalin; Schubert, Jerome (2013): Low Cycle Cement Fatigue Experimental Study and the Effect on HPHT Well Integrity. In: *Journal of Petroleum Science and Engineering* 105, pp. 84–90. ISSN: 09204105. DOI: 10.1016/

j.petrol.2013.03.006. URL: https://linkinghub.elsevier.com/retrieve/pii/S0920410513000600 (visited on 08/14/2025).

Zeghadnia, Lotfi; Robert, Jean Loup; Achour, Bachir (2019): Explicit Solutions for Turbulent Flow Friction Factor: A Review, Assessment and Approaches Classification. In: *Ain Shams Engineering Journal* 10.1, pp. 243–252. ISSN: 20904479. DOI: 10.1016/j.asej.2018.10.007. URL: https://linkinghub.elsevier.com/retrieve/pii/S2090447919300176 (visited on 07/30/2025).

Zeng, Yijin; Liu, Rengguang; Li, Xiaojiang; Zhou, Shiming; Tao, Qian; Lu, Peiqing (2019): Cement Sheath Sealing Integrity Evaluation under Cyclic Loading Using Large-Scale Sealing Evaluation Equipment for Complex Subsurface Settings. In: *Journal of Petroleum Science and Engineering* 176, pp. 811–820. ISSN: 09204105. DOI: 10.1016/j.petrol.2019.02.014. URL: https://linkinghub.elsevier.com/retrieve/pii/S092041051930141X (visited on 08/13/2025).

Zhang, Chuanchuan; Li, Julun; Yu, Miao; Lu, Yue; Liu, Shizhong (2024a): Mechanism and Performance Control Methods of Sulfate Attack on Concrete: A Review. In: *Materials* 17.19, p. 4836. ISSN: 1996-1944. DOI: 10.3390/ma17194836. URL: https://www.mdpi.com/1996-1944/17/19/4836 (visited on 08/06/2025).

Zhang, Hua; Ramakrishnan, T. S.; Elias, Quincy K.; Perez, Albert (2020): Evaluation of Bismuth-Tin Alloy for Well Plug and Abandonment. In: *SPE Production & Operations* 35.01, pp. 111–124. ISSN: 1930-1855, 1930-1863. DOI: 10.2118/199363-PA. URL: https://onepetro.org/PO/article/35/01/111/448259/Evaluation-of-Bismuth-Tin-Alloy-for-Well-Plug-and (visited on 11/24/2025).

Zhang, Qi and Ye, Guang (2012): Dehydration Kinetics of Portland Cement Paste at High Temperature. In: *Journal of Thermal Analysis and Calorimetry* 110.1, pp. 153–158. ISSN: 1388-6150, 1572-8943. DOI: 10.1007/s10973-012-2303-9. URL: http://link.springer.com/10.1007/s10973-012-2303-9 (visited on 11/24/2025).

Zhang, Weicheng; Eckert, Andreas; Liu, Xiaolong (2017): Numerical Simulation of Micro-annuli Generation by Thermal Cycling. In: ARMA 17-354. URL: https://www.researchgate.net/publication/318116522_Numerical_Simulation_of_Micro-annuli_Generation_by_Thermal_Cycling/stats (visited on 08/13/2025).

Zhang, Xiaoyu; Wang, Lei; Bi, Zhenhui; Guo, Yintong; Yang, Chunhe; Yang, Hanzhi; Chang, Xin (2022): Mechanical Analysis on Cement Sheath Integrity under Asymmetric Load. In: *Journal of Petroleum Exploration and Production Technology* 12.1, pp. 135–146. ISSN: 2190-0558, 2190-0566. DOI: 10.1007/s13202-021-01346-4. URL: https://link.springer.com/10.1007/s13202-021-01346-4 (visited on 08/14/2025).

Zhang, Zhen; Yuan, Zhongtao; Ye, Sutao; Li, Yang; Yang, Lvchao; Pang, Xueyu; Lv, Kaihe; Sun, Jinsheng (2024b): The Influence of Cyclic Loading on the Mechanical Properties of Well Cement. In: *Energies* 17.15, p. 3856. ISSN: 1996-1073. DOI: 10.3390/en17153856. URL: https://www.mdpi.com/1996-1073/17/15/3856 (visited on 08/13/2025).

Zhou, Peng; Gao, Shuaizhi; Lv, Yue; Zhao, Ge (2022): Energy Transition Management towards a Low-Carbon World. In: *Frontiers of Engineering Management* 9.3, pp. 499–503. ISSN: 2095-7513, 2096-0255. DOI: 10.1007/s42524-022-0201-9. URL: https://link.springer.com/10.1007/s42524-022-0201-9 (visited on 10/02/2025).

Zhou, Shiming; Liu, Rengguang; Zeng, Hao; Zeng, Yijin; Zhang, Linhai; Zhang, Jiaying; Li, Xiaojiang (2019): Mechanical Characteristics of Well Cement under Cyclic Loading and Its Influence on the Integrity of Shale Gas Wellbores. In: *Fuel* 250, pp. 132–143. ISSN: 00162361. DOI: 10.1016/j.fuel.2019.03.131. URL: https://linkinghub.elsevier.com/retrieve/pii/S0016236119305150 (visited on 08/12/2025).

Zhu, Ciyou; Byrd, Richard H.; Lu, Peihuang; Nocedal, Jorge (1997): Algorithm 778: L-BFGS-B: Fortran Subroutines for Large-Scale Bound-Constrained Optimization. In: *ACM Transactions on Mathematical Software* 23.4, pp. 550–560. ISSN: 0098-3500, 1557-7295. DOI: 10.1145/279232.279236. URL: https://dl.acm.org/doi/10.1145/279232.279236 (visited on 03/20/2026).

Zimmerle, Daniel; Vaughn, Timothy; Bell, Clay; Bennett, Kristine; Deshmukh, Parik; Thoma, Eben (2020): Detection Limits of Optical Gas Imaging for Natural Gas Leak Detection in Realistic Controlled Conditions. In: *Environmental Science & Technology* 54.18, pp. 11506–11514. ISSN: 0013-936X. DOI: 10.1021/acs.est.0c01285.

Appendix

A) Operator splitting algorithm

Here, the main algorithm implemented in Python 3.9 is provided. It represents the programmatic implementation of the mathematical description given in Section 3.2. The full source code and all experimental data are included on the supplementary CD accompanying the physical copy of this document and are also available through *KITopen* (DOI: 10.35097/ybrjg8rd9dupktum).

```
    """ Hagen-Poiseuille function """
    # Calculation of the volumetric flow rate through a rectangular cross-section
    # according to Hagen-Poiseuille (finite difference model)
    # If/Else statement to capture unrealistic flow rates, usually caused due to
    # large time steps
    def Q_HP(DeltaP, DeltaZ, Eta, K, TubeHeight, TubeWidth):
        try:
            Vdot = K*TubeHeight**3*TubeWidth/(12*Eta)*DeltaP/DeltaZ
        except:
            Vdot = 0.0
            print("Error while calculating --> Vdot set to 0")

        if Vdot < np.inf:
            Vdot = Vdot
        else:
            Vdot = 0.0
            print(DeltaP,DeltaZ,"Error while calculating --> Vdot runs to infinity")
            time.sleep(4)
        return Vdot




    """ Main algorithm """
    k = 1 - np.exp(-c*dt) # Heat transfer factor
    VolumeAutoclave = VolumeAutoclave + 0.5*VolumeSegment
    const_gap = dt/VolumeSegment
    const_autoclave = dt/VolumeAutoclave

    # For each modeled data, the closest pressure (lowerP_values) and
    # temperature (lowerT_values) in the lower chamber are identified
    closestIndices = timeIndices["closestIndex"].astype(int).values
    lowerP_values = LowerChamber.iloc[closestIndices, 1].values
    lowerT_values = LowerChamber.iloc[closestIndices, 0].values


    # HAGEN-POISEUILLE GAS FLOW:

    for j in np.arange(1, lengthOfTime, 1): # lengthOfTime = number of time steps

        #Lower chamber
        Pi[0] = lowerP_values[j-1]
        closestTime[j] = lowerT_values[j-1]
        # Regression-based isothermal compressibility
        kappa[0] = (-0.000000002973239 * (Pi[0]*(P0-P1)+P1) + 0.000000342476357)

```

```
47
48          # Gap segments:
49          for i in range(1,N,1):
50              DeltaP = Pi[i-1]-Pi[i] # Pressure difference
51              DeltaZ = dl # Flow length
52              # Regression-based isothermal compressibility
53              kappa[i] = (-0.000000002973239 * (Pi[i]*(P0-P1)+P1) + 0.000000342476357)
54              # Hagen-Poiseuille flow
55              Qi[i] = Q_HP(DeltaP, DeltaZ, Viscosity, K, TubeHeight, TubeWidth)
56              dPi[i] = Qi[i]*const_gap/kappa[i]
57              Pi[i] = Pi[i] + dPi[i]
58              Pi[i-1] = Pi[i-1]-Qi[i]*const_gap/kappa[i-1]
59
60          # Upper chamber:
61          # Regression-based isentropic compressibility
62          kappa[N] = ((-0.000000002973239 * (Pi[N]*(P0-P1)+P1)
63                       + 0.000000342476357)/Adiabatic_Index)
64          # Hagen-Poiseuille flow
65          Qi[N] = Q_HP(Pi[N-1]-Pi[N],dl,Viscosity, K, TubeHeight, TubeWidth)
66          dPi[N] = Qi[N]*const_autoclave/kappa[N]
67          PAutoclave[j] = PAutoclave[j-1] + dPi[N]
68          Pi[N-1] = Pi[N-1]-Qi[N]*const_gap/kappa[N-1]
69
70
71      # THERMAL EFFECTS (upper chamber only):
72
73          # Non-normaized pressure at beginning of time step j
74          PAutoclave_abs_start_j = PAutoclave[j-1]*(P0-P1)+P1
75          # Current temperature difference between steel and gas (upper chamber)
76          Delta_T[j] = a - T_Curve_k[j-1]
77          # Temperature evolution due to heat exchange between steel and gas
78          T_Curve_k[j] = T_Curve_k[j-1] + (Delta_T[j] * k)
79
80          # Pressure increase due to heat transfer from steel to gas:
81          # Calculate pressure from heat flow (isochoric, upper chamber)
82          P_from_T_abs[j] = PAutoclave_abs_start_j/T_Curve_k[j-1]*T_Curve_k[j]
83          P_from_T[j] = (P_from_T_abs[j]-P1)/(P0-P1) # Normalization
84
85          # Pressure difference from heat flow (upper chamber), which is later
86          # added to the total pressure
87          Delta_P_from_T[j] = P_from_T[j] - PAutoclave[j-1]
88
89          # Temperature change due to gas flow induced pressure changes in the
90          # upper chamber (isentropic):
91          T_from_gasflow[j] = (T_Curve_k[j-1] *
92                               (PAutoclave_abs_start_j
93                               /(PAutoclave[j]*(P0-P1)+P1))
94                               **((1-Adiabatic_Index)/Adiabatic_Index))
95          Delta_T_from_gasflow[j] = T_from_gasflow[j] - T_Curve_k[j-1]
96
97          # Add gas flow induced temperature change to temperature curve
98          T_Curve_k[j] = T_Curve_k[j] + Delta_T_from_gasflow[j]
99          # Add heat flow induced pressure change to pressure curve
100         PAutoclave[j] = PAutoclave[j] + Delta_P_from_T[j]
101         Pi[N] = PAutoclave[j]
```

B) Monolithic model

The full monolithic 1D model implemented in Python 3.9 and described in Section 5.3.2 is provided below.

```
# -*- coding: utf-8 -*-
"""
Monolithic 1D finite-volume model
Automated fitting and reading of input data
"""
import numpy as np
import matplotlib.pyplot as plt
from scipy.integrate import solve_ivp
from scipy.optimize import least_squares
import pandas as pd
import os

# ------------------------------------------------------------
#                          Read excel data
# ------------------------------------------------------------
# Adjust input folder and file if necessary
# Expected columns:
# "Time [s]", "P_uc [bar]", "P_lc [bar]", "T0 [deg C]", "T1 [K]", "V_uc [m^3]", "c [1/s]", "l [m]"

folder = r"D:\Modeling_Data"
filename = "C2_V51.xlsx"
path = os.path.join(folder, filename)

df = pd.read_excel(path)

# Time series (continuous) - upper and lower chamber pressures
t_exp = df["Time [s]"].to_numpy(dtype=float)
p_top_exp = df["P uc [bar]"].to_numpy(dtype=float) * 1e5    # in Pa
p_bot_exp = df["P lc [bar]"].to_numpy(dtype=float) * 1e5    # in Pa

# Individual values (first valid entry from the respective column)
def first_valid(colname):
    vals = df[colname].dropna().to_numpy()
    if len(vals) == 0:
        raise ValueError(f"Column '{colname}' does not contain valid values.")
    return float(vals[0])

T0_C = first_valid("T0 [deg C]")
T0 = T0_C + 273.15
T1 = first_valid("T1 [K]")
V_chamber = first_valid("V_uc [m^3]")
c = first_valid("c [1/s]")
L = first_valid("l [m]")
DiameterWell = first_valid("Diameter [m]")

# ------------------------------------------------------------
#                  Physical parameters for N2
# ------------------------------------------------------------
R = 296.8
cp = 1109.6
cv = 754.38
mu = 20.7e-6

```

```
    # Temperature when gas enters chamber
    T_in = T0

    # ------------------------------------------------------
    #                        Geometry
    # ------------------------------------------------------
    w = 0.5*np.pi*DiameterWell # [m] gap width (transverse to the longitudinal
        direction)

    # 1D FV discretization
    N = 20
    dx = L / N

    # ------------------------------------------------------------------
    #       Interpolation p_bot(t): linear; constant outside
    # ------------------------------------------------------------------
    def p_bot_of_t(t):
        return np.interp(t, t_exp, p_bot_exp, left=p_bot_exp[0], right=p_bot_exp[-1])

    # ------------------------------------------------------
    #                 Starting conditions
    # ------------------------------------------------------
    P1 = p_top_exp[0]  # first measured pressure in upper chamber

    def build_initial_state(h):
        V_cell = w * h * dx
        # Linear pressure distribution in the gap between p_bot(t=0) and P1
        p_init = np.linspace(p_bot_exp[0], P1, N)
        m_cells = p_init * V_cell / (R * T_in)
        m_chamber = P1 * V_chamber / (R * T1)
        return np.hstack([m_cells, m_chamber, T1])

    # ------------------------------------------------------------
    #                  Simulation for given h
    # ------------------------------------------------------------
    def simulate_pressure(h):
        V_cell = w * h * dx
        # Hagen-Poiseuille coefficient per cell (Squared form for compressible/
            isotherma)
        C_HP_cell = (h**3 * w) / (12.0 * mu * dx)

        y0 = build_initial_state(h)

        def rhs_fit(t, y):
            m_cells = y[:N]
            m_ch = y[N]
            T = y[N+1]

            # time-dependent lower chamber pressure
            p_bot_t = p_bot_of_t(t)

            # Pressures
            p_cells = m_cells * R * T_in / V_cell
            p_ch = m_ch * R * T / V_chamber

            # Mass flow (p^2-form)
            mdot = np.zeros(N+1)
            mdot[0] = C_HP_cell * (p_bot_t**2 - p_cells[0]**2) / (2.0 * R * T_in)
            for i in range(1, N):
                mdot[i] = C_HP_cell * (p_cells[i-1]**2 - p_cells[i]**2) / (2.0 * R *
                    T_in)
```

```
112             mdot[N] = C_HP_cell * (p_cells[N-1]**2 - p_ch**2) / (2.0 * R * T_in)
113
114             dmdt_cells = mdot[:-1] - mdot[1:]
115             mdot_in = mdot[N]  # Flow into upper chamber
116
117             # Energy balance upper chamber
118             if m_ch <= 0:
119                 Tdot = 0.0
120             else:
121                 Tdot = (mdot_in * cp * T_in + c * m_ch * cv * (T0 - T) - mdot_in * cv
                        * T) / (m_ch * cv)
122
123             return np.hstack([dmdt_cells, mdot_in, Tdot])
124
125         sol = solve_ivp(
126             rhs_fit,
127             [float(t_exp[0]), float(t_exp[-1])],
128             y0,
129             method="Radau",
130             max_step=0.5
131         )
132
133         m_ch = sol.y[N]
134         T_ch = sol.y[N+1]
135         p_ch = m_ch * R * T_ch / V_chamber
136
137         # Interpolation at measurement times
138         p_interp = np.interp(t_exp, sol.t, p_ch)
139         return p_interp
140
141     # ------------------------------------------------------
142     #               Function for fitting
143     # ------------------------------------------------------
144     def residuals(h_array):
145         h = float(h_array[0])
146         p_model = simulate_pressure(h)
147         return (p_model - p_top_exp) / 1e5  # scale to bar
148
149     # ------------------------------------------------------
150     #                         Fit
151     # ------------------------------------------------------
152     h_initial = 30e-6
153     result = least_squares(
154         residuals,
155         x0=[h_initial],
156         bounds=(1e-6, 100e-6)
157     )
158     h_fit = float(result.x[0])
159     print(f"\nFitted gap height ({filename}, 1D):")
160     print(f"h = {h_fit*1e6:.10f} 10E-6 m\n")
161
162     # ------------------------------------------------------
163     #             Final simulation with fitted h
164     # ------------------------------------------------------
165     p_fit = simulate_pressure(h_fit)
166
167     # ------------------------------------------------------
168     #                         Plot
169     # ------------------------------------------------------
170     # Adjust output folder if necessary
171     plt.figure(figsize=(7,4))
```

```
172     plt.plot(t_exp, p_top_exp/1e5, 'o', label="Experiment (P_uc)")
173     plt.plot(t_exp, p_fit/1e5, label=f"1D FV monolithic (h = {h_fit*1e6:.2f} 10E-6 m)
            ")
174     plt.xlabel("Time [s]")
175     plt.ylabel("Upper chamber pressure [bar]")
176     plt.legend()
177     plt.grid(True)
178 
179     # Safe figure
180     out_path = rf"C:\Users\Marcel\Desktop\temp\monolithic_{filename}_n={N}.png"
181     plt.savefig(out_path, dpi=300)
```